ENVIRONMENTAL RESEARCH REPORT 1980-1

A Public Service of

Syncrude Canada Ltd.

DISPERSION MODELING OF A PLUME IN THE TAR SANDS AREA

P.R. Slawson, G.A. Davidson and C.S. Maddukuri

Envirodyne Ltd.

DISPERSION MODELING OF A PLUME IN THE TAR SANDS AREA

by

P.R. Slawson, G.A. Davidson

and C.S. Maddukuri

of

ENVIRODYNE LIMITED,

Waterloo, Ontario.

for

SYNCRUDE CANADA LIMITED,

Edmonton, Alberta

December, 1979.

FOREWORD

Syncrude Canada Ltd. is producing synthetic crude oil from a surface mine in the Athabasca Tar Sands area of North-eastern Alberta. This present report was commissioned to develop a physical-mathematical plume dispersion model as part of the development of an Air Quality Prediction System. Such a system could substantially reduce the yearly frequency of potential violations of the short-term air quality standards by predicting the onset of adverse weather conditions in advance of real time.

Syncrude's Environmental Research Monographs are published verbatim from the final reports of professional environmental consultants. Only proprietary technical or budget-related information is withheld. Because we do not necessarily base our decisions on just one consultant's opinion, recommendations found in the text should not be construed as commitments to action by Syncrude.

Syncrude Canada Ltd. welcomes public and scientific interest in its environmental activities. Scientists interested in working with the raw data contained in the Appendices referred to in this report may write requesting access to these data. Please address any questions or comments to Syncrude Environmental Affairs, 10030 - 107 Street, Edmonton, Alberta, T5J 3E5.

This report may be referred to as:

Slawson, P.R., G.A. Davidson and C.S. Maddukuri. 1980. Dispersion modeling of a plume in the tar sands area. Syncrude Environmental Research Report 1980-1. 316pp.

SUMMARY

The plume rise, spread and supporting meterological and source data given in Slawson et al (1978) were further analyzed in order to provide a more suitable data set upon which a site-tuned plume dispersion model could be developed. This dispersion model was considered to consist of a buoyant plume rise and growth phase followed by an atmospheric (Gaussian) dispersion phase. Since a truly predictive plume dispersion model is ultimately required for use in emission limitation control programs some effort was spent in developing and testing a predictive one dimensional planetary boundary layer model.

Both analytical and simple numerical integration plume rise and growth models are described in some detail and tested against a reduced set of observed time-mean plume behavior. The numerical integration plume rise models (NIM) proved to be superior to the analytical models for the G.C.O.S. plume as: (1) non-linear temperature and wind fields were more easily incorporated, (2) the Boussinesq approximation (which proved to be significant) was not required, and (3) low windspeed predictions were improved. Thus, a NIM is recommended for plume rise and growth in the buoyant phase.

Considerable time was spent on re-analyzing the aircraft in-plume transect data in an attempt to reduce scatter and obtain more consistent standard deviations of plume spread (sigmas) and their

rates of growth under various atmospheric stability conditions so that a better comparison with several typing schemes could be made. Plume cross-section isopleths were constructed from the aircraft transect data for all cross-sections flown and are contained in an Appendix. The sigma data abstracted from the isopleths had less scatter than that found previously and correct trends in the data were noted. A sigma typing scheme due to Briggs (1975) was selected as best representative of that observed in the absence of cross-wind shear. Since an equivalent Gaussian plume dispersion model was required a tentative empirical formulation for the effects of cross-wind shear enhanced diffusion was extracted from the data. Also, a model that incorporates the effect of plume distortion directly into a modified Gaussian plume model is described and tested against some of the observed plume cross-sections.

A plume rise and Gaussian dispersion model based on these measurements of the G.C.O.S. plume is described and tested against observed ground plane aircraft transect data. This model may form the basis for a subsequent Syncrude plume model.

All computer codes developed during this study including the plume rise and growth, plume spread and planetary boundary layer models are given in an Appendix which is presented as a separate volume.

It is highly unlikely and probably impossible to develop a truly predictive plume dispersion model that satisfactorily describes the resulting ground level concentration field under all atmospheric conditions, time scales, source conditions and terrain for even a very specific site. Thus further work on the more critical aspects of a predictive dispersion model is recommended.

Table of Contents

List of Figures

List of Tables

1. INTRODUCTION

An investigation into the plume rise and dispersion of the Great Canadian Oil Sands plant plume (G.C.O.S.) was initiated by Syncrude Canada Limited in January 1977. Subsequently, four seasonal, intensive field studies were carried out during 1977 to obtain observational data on the G.C.O.S. plume. The experimental method, resulting data and a limited analysis of that data was reported by Slawson et al[12] (1978).

The objective of the work outlined in this report is to re-analyze the Syncrude Canada Limited plume rise and dispersion data in order to develop, to the extent possible, a site-tuned plume rise and dispersion model for the G.C.O.S. plume. Also, since a truly predictive dispersion model is ultimately required, a planetary boundary layer model is to be developed and tested such that predictions of the temperature and wind field may be made some six hours in advance. The dispersion model is to account for such effects as, atmospheric stratification, stability, and wind speed and directional shear.

The dispersion model is considered to consist of two phases: (1) a buoyant plume rise and growth phase, and (2) an atmospheric phase. Since ground level concentrations from industrial stacks are particularly sensitive to the effective height of release of the contaminants, the plume rise part of the dispersion model is very

important. Subsequently, a great deal of research on the behaviour of buoyant plumes has been carried out in the past and thus the physics and therefore the theory of plume rise is at present fairly well understood. Thus, one of our tasks here is to organize and classify the plume rise and supporting source and atmospheric data so that the effects of various atmospheric and source conditions on plume behaviour may be identified. One may then proceed to develop a site-tuned plume rise and growth model with the data set. The availability of both the large plume rise data base from the field study of 1977 and the well understood buoyant plume theory should provide the basis for a sound plume rise model of the G.C.O.S. plume.

There is much more uncertainty associated with the atmospheric dispersion phase data than the plume rise data, as illustrated in the report by Slawson et al[12] (1978). Also, the theoretical basis for the atmospheric phase is not as well established as that for the buoyant phase. A very popular model for the atmospheric phase and one that has enjoyed some success is the Gaussian plume model. However, considerable empirical input is required in the form of a suitable set of sigma curves which describe the rate of diffusion of the plume. Thus our main task for the atmospheric phase model development is to reanalyze the in-plume transect data in order to try and reduce uncertainty and scatter (error) in the sigma data. Subsequently, this hopefully better sigma data can then be compared with some of the current sigma typing schemes with similarities and differences noted.

Further details on the results of the work on the plume rise and atmospheric dispersion phases may be found in the appropriate sections of the report that follows.

As mentioned above, in order to make any plume dispersion model truly predictive requires apriori knowledge of the various input variables. Also, for such a predictive model to be used as an operational or emission limitation control tool one requires the input information far enough in advance to allow for the time required to affect the control on emission. Thus, a further task of this report is to provide some insight into the capability of a state of the art planetary boundary layer model to provide this advance information on the atmospheric input variables.

2. PLUME RISE AND GROWTH

2.1 INTRODUCTION

The plume rise and growth component of the dispersion model (Fig. 2.1, Ref. 12) is very important due to the strong dependence of predicted maximum ground level concentration on plume rise. Also, (fortunately) the data base of plume rise observations is of a much better quality in terms of accuracy than plume spread (sigma) data. Thus, one can at least hope to achieve a well documented site-tuned plume rise model for the G.C.O.S. plume where on the other hand, an appropriate well-defined sigma typing scheme may prove to be elusive with the present data base.

In the report by Slawson et al[12] (1978) some 450 time-mean plume observations were abstracted from the data base. Of these a net of 366 were subsequently used for comparison with a simple analytical plume rise model. In the comparisons, no attempt was made to separate, or group plume rise observations according to ambient conditions. Thus, inherent in the comparisons are those that compare a theory with certain assumptions and limitations (particularly as regards wind conditions) with observations that do not satisfy these limitations. The result is, of course, to increase the scatter and error when predictions are compared with observations. In spite of this shortcoming (necessary due to the magnitude of the data base and limited time for

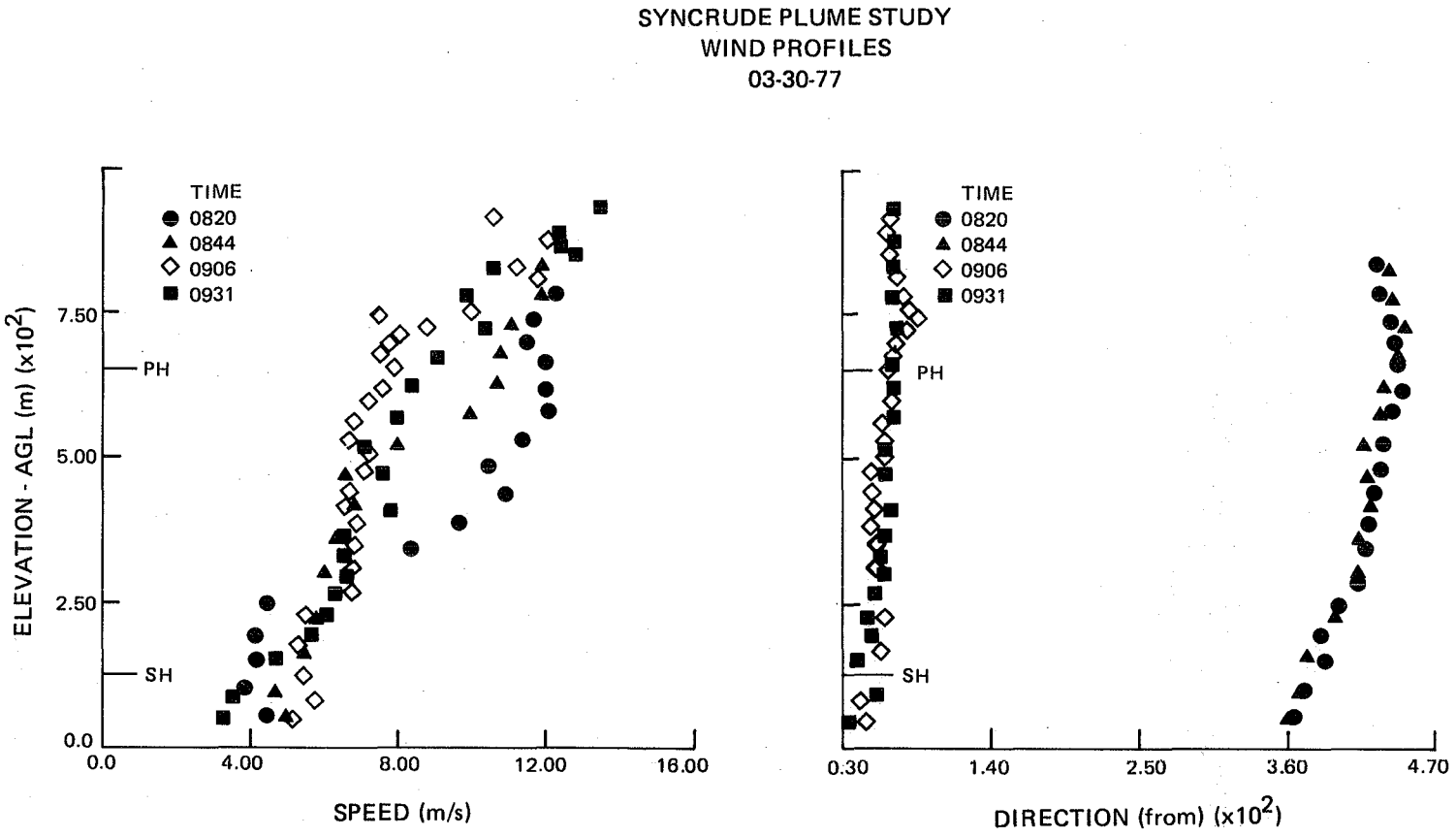

Figure 2.1. A typical pibal data plot.

analysis) an average entrainment constant of 0.53 resulted with a corresponding average predicted trajectory error of less than 25% on 155 of the time-mean plumes. Thus, considerable improvement in the plume rise prediction could possibly be made by careful matching of a given plume rise model to that part of the data set where model assumptions are valid.

The analytical model used in the 1978 report assumes a constant wind speed and linear temperature profile over the plume rise region. Therefore, it was suggested in the previous report that (a) some method for choosing the average wind speed over the plume rise region in the presence of vertical wind speed shear be investigated, or (b) plume rise theory incorporating a numerical integration of the governing equations be employed so that the model would accept the observed or predicted wind and temperature distributions.

In the following sections, several closed form integral plume rise and growth models are compared with time-mean plume observations. The objectives of these comparisons are (i) to determine which model best predicts plume trajectory and growth in the buoyant phase, and (ii) to compare and contrast the successes and failures of the various models tested.

2.2 SCOPE OF WORK ON PLUME RISE MODELLING

From the results of the work on plume rise in the report by Slawson et al (1978), the general scope of work for this present work evolved and is outlined below:

(i) Abstract from the existing data base of time-mean plumes, a reduced set corresponding to appropriate sampling times during which ambient and source conditions could be considered to be steady.

(ii) Separate the data in (i) into groups corresponding to cases having, (a) uniform wind and linear temperatures, (b) wind speed shear (no directional wind shear) and linear temperature profiles, (c) wind speed shear (no directional shear) and non linear temperature profiles (inversions), (d) wind speed and directional shear and linear temperature profiles, (e) wind speed and directional shear and non-linear temperature profiles, (f) low wind speed cases.

(iii) For a given plume rise model determine the optimum entrainment constants by tuning the models to the data in group (ii) (a) above.

(iv) With the optimum (uniform wind) entrainment constant, determine a method for choosing the appropriate "constant" wind speed to be used in an analytical plume rise model to account for wind speed shear.

(v) Evaluate the need for the direct incorporation of wind shears (speed and direction) into analytical or numerical (integral) plume rise models.

(vi) Test subsequent models in calm wind conditions and recommend an appropriate model.

In addition to the above, an attempt was to be made to determine whether the data base reflected effects of terrain on observed plume rise.

2.3 SUMMARY OF PLUME RISE MODEL DEVELOPMENT

As outlined in the scope of work above, the time-mean plume observations were subsequently reduced to a data set consisting of 62 time-mean plumes (over about a 1-hour time base). The windfields of 25 of the 62 data sets exhibited significant directional shear, and, as discussed in section 2.4.2, these cases were not used in model evaluations. The remaining 37 data sets, which contained windfields with approximately constant direction profiles, were subdivided into the three groups described in section 2.4.2.1.

2.3.1 Effect of Wind Speed Shear

The effect of wind speed shear on plume rise is to reduce the rise over that found in a uniform wind. This is illustrated in Slawson (1978) and in section 2.4 in this report. A discussion of estimating an appropriate uniform wind speed to be used in an analytical plume rise model to account for wind speed shear effects is given in the paper by Davidson, Slawson and Djurfors[11] (1978) and is presented as Appendix A.4. Different approaches to incorporating wind speed shear into a plume rise model are discussed in section 2.4.

2.3.2 Effect of Wind Direction Shear

The effect of wind speed shear on plume rise is readily seen by running a numerical integration model (NIM) for plume rise with uniform and wind speed shear input. The effect of wind direction shear can also easily be incorporated into a NIM for plume rise. Howroyd (1979) has done this by simply replacing the circular plume cross-sectional shape assumption by a square, and incorporating the relative cross-wind displacements of the top and bottom of the plume about the plume trajectory (center). The qualitative effect is to reduce plume rise. The magnitude of this effect when such a model is run against some of the G.C.O.S. time-mean plumes proves to be small for the observed wind directional shears (see McCormick, 1979). A similar result was found by Howroyd (1979).

2.3.3 Effect of Terrain on Plume Rise

In order to assess the effects of terrain on plume rise, a number of normalized observed near neutral final rises (z_F/l_B), where l_B is a buoyancy length scale, were plotted as a function of wind direction. It was hoped that by choosing observations taken in a near neutral atmosphere that stability effects would be a minimum and thus any wind direction (terrain) effects on plume rise might materialize. It was found that a very weak (insignificant) correlation of plume rise with wind direction existed in this data base. There did seem to be some indication that the largest observed rises were associated with south easterly winds. This is a qualitatively expected result, based on the assessment of geographical effects on plume rise given in the report by Slawson et al[12] (1978). It was shown that plume rise should be reduced slightly when winds blow from the plateau out over the river valley.

2.3.4 Comparison of Analytical and Various Numerical Models for Plume Rise

Section 2.4 outlines in detail a description of, and resulting comparisons of various plume rise models. Four closed form integration models (analytical) and seven numerical integration models (NIM) are discussed and compared with the reduced set of 37 time-mean plumes. A recommendation for a predictive plume rise model is given

in Section 2.5. The recommended model is a NIM with two entrainment constants and no Boussinesq assumption. The performance of this model in the presence of wind directional shear over the plume rise region is illustrated in Appendix A.2.

2.4 PLUME RISE MODEL DEVELOPMENT

2.4.1 Formulation of the Problem

The initial rise of a plume of exhaust gases emitted into the atmosphere may be described mathematically using statements of conservation of mass, horizontal momentum, vertical momentum, and energy. These statements simplify and become one-dimensional if it is assumed that the plume variables follow a specified profile (top-hat or Gaussian) normal to the plume direction, and that the plume cross-section is circular. In Appendix 1, the one dimensional conservation equations, on which integral models of plume rise are based, are shown to be:

$$\frac{d}{dt}(\rho_p R^2 V) = 2\rho_a R V v_e \tag{2.1}$$

$$\frac{d}{dt}(\rho_p R^2 V v_x) = 2\rho_a R V v_e U + C_D \rho_a R V V_R (U - v_x) \tag{2.2}$$

$$\frac{d}{dt}(\rho_p R^2 V w) = g R^2 V(\rho_a - \rho_p) - C_D \rho_a R V V_R w \tag{2.3}$$

$$\frac{d}{dt}[g R^2 V(\rho_a - \rho_p)] = - \rho_a N^2 R^2 V w \tag{2.4}$$

where ρ_p and ρ_a are plume and air densities respectively; R is plume cross-sectional radius; V is absolute plume velocity, which has horizontal component V_x and vertical component w; U is the (horizontal) windspeed; V_R is the relative velocity between the plume and the atmosphere, which has horizontal component $(v_x - U)$ and vertical component w; N is the Brunt-Vaisala frequency; g is the acceleration of gravity; C_D is the drag coefficient; and t is downwind travel time. As the plume rises, turbulence, generated in the velocity shear zone between the plume and the atmosphere, causes the plume radius to grow. Following Taylor[1], an entrainment velocity v_e is introduced to describe this rate of growth.

Additional relationships are necessary to enable the solution of equations (2.1) to (2.4) for plume radius and centerline altitude as functions of downwind distance from the stack. These relationships are (i) the hydrostatic pressure law, which may be written as (see Appendix A.1)

$$\frac{d}{dt}(\rho_p T_p) = -\frac{7}{2}\gamma_d \rho_a w \qquad (2.5)$$

where T_p is plume temperature and $\gamma_d = 0.0098$ °C/m is the dry adiabatic lapse rate;

(ii) the kinematic equations

$$\frac{ds}{dt} = V \tag{2.6}$$

$$\frac{dz}{dt} = w \tag{2.7}$$

$$\frac{dx}{dt} = v_x \tag{2.8}$$

which relate plume arc length s, centerline altitude z, and downwind distance x to plume velocity components; and

(iii) the plume velocity definition

$$V^2 = v_x^2 + w^2 \tag{2.9}$$

Equations (2.1) to (2.9) represent nine equations for the nine unknowns ρ_p, R, V, v_x, w, T_p, s, z, and x as functions of travel time t. Solution is therefore possible once the parameters v_e and C_D are specified along with atmospheric parameters $\rho_a(z)$, $N^2(z)$, and U(z), and plume source parameters. The principal assumptions contained in these nine equations have already been noted; the plume variables follow a top-hat profile normal to the plume direction, the plume is circular in cross-section, and plume generated turbulence may be characterized by v_e. No other major assumption is necessary in the derivation.

Two views on the drag coefficient C_D appear in the literature. Briggs[2] presents mathematical arguments to show that no drag forces should appear in the one-dimensional conservation equations; the analytical plume rise models which he recommends accordingly have $C_D = 0$. Hoult, Fay and Forney[3] and Escudier[4] also develop models with $C_D = 0$, citing laboratory studies by Jordinson[5] as proof that drag is not an important factor in plume rise. On the other hand, such authors as Abraham[6], Ooms[7], and Slawson[8] have developed plume rise models with C_D values of the order of 0.5, on the basis that agreement between model predictions and measurements is improved when the drag force is retained. For specified atmospheric and source conditions and specified v_e, plume rise and spread at any given t is reduced as C_D is increased.

Of the many expressions that have been used for v_e (see the review by Briggs[2]), the derivation by Hoult, Fay and Forney[3] has the most appealing physical background. The entrainment velocity in the plume rise region is a measure of the turbulence generated due to the relative velocity between the plume and the surrounding atmosphere, and is therefore assumed to be proportional to this relative velocity. Tangential to the plume direction, the relative velocity component is

$$V_t = V - U\cos\theta \qquad (2.10)$$

where θ is slope angle of the plume to the horizontal, which can be related to the plume velocity components by

$$\theta = \tan^{-1}(w/v_x) \tag{2.11}$$

Normal to the plume direction, the relative velocity component becomes

$$V_n = U \sin \theta \tag{2.12}$$

Hoult, Fay, and Forney, therefore, suggest an entrainment hypothesis

$$\begin{aligned} v_e &= \alpha|V_t| + \beta|V_n| \\ &= \alpha\left|V - U\frac{v_x}{V}\right| + \beta\left|\frac{Uw}{V}\right| \end{aligned} \tag{2.13}$$

where α and β are constants to be determined empirically.

When $U = 0$, equation (2.13) reduces to

$$v_e = \alpha|V| \tag{2.14}$$

which is the expression applied successfully by Morton, Taylor, and Turner[9] (with $\alpha \simeq 0.13$) to describe a jet spreading in a quiescent fluid. When $v_x \simeq U$ and $w << V$, equation (2.13) reduces to

$$v_e = \beta|w| \tag{2.15}$$

which is the expression applied successfully by Slawson and Csanady[10] and recommended by Briggs[2] (with $\beta \simeq 0.6$) to describe a bent-over plume. Equation (2.13) therefore, attempts to account for the entrainment associated with a jet as well as that associated with a bent-over plume.

There is a question, however, as to whether the V_t and V_n terms should be simply added together. Near the source of a jet entering a cross-flow, $v_x \simeq 0$ and $w \simeq V$, so that equation (2.13) becomes

$$v_e = \alpha|V| + \beta|U| \tag{2.14)(a}$$

Plume-type entrainment, therefore, adds to jet-type entrainment right at the source. Abraham[6], Ooms[7] and others have forced only jet-type entrainment to occur near the source by introducing a weighting factor into equation (2.13):

$$v_e = \alpha\left|V - \frac{Uv_x}{V}\right| + \beta\,\frac{v_x}{V}\left|\frac{Uw}{V}\right| \tag{2.15)(a}$$

The factor $\frac{v_x}{V} = \cos\theta$ was chosen arbitrarily to force $v_e = \alpha|V|$ near the source while maintaining $v_e = \beta|w|$ downwind. Other weighting factors could easily be devised to produce the same effect while altering the rate at which source and downwind limits are approached. Another

possibility is to combine V_t and V_n in a vector sum, with or without weighting factors. Equation (2.13) would become, for example,

$$v_e = \{\alpha^2(V - \frac{Uv_x}{V})^2 + \beta^2(\frac{Uw}{V})^2\}^{1/2} \qquad (2.16)$$

which has the effect of reducing the influence of the V_n term near the source and of the V_t term downwind.

2.4.2 Scope of This Work

The aim of this work is to test several integral plume rise models developed from the preceding equations against plume trajectory data from the 106 m high, 5.8 m diameter powerhouse stack of the Great Canadian Oil Sands (G.C.O.S.) plant in northern Alberta. For four seasonal periods in 1977, plume rise was recorded photographically, while source data were monitored, and wind and temperature profiles were obtained by regular pibal and minisonde releases. Details of the measurement program may be found in References 11 and 12.

Hoult, Fay, and Forney have identified two major sources of error in plume rise measurements. The first problem arises from the determination of true average plume boundaries from instantaneous photographs of randomly fluctuating outlines. Our averaging procedure, in which outlines from up to 35 consecutive slides are superimposed to produce one time-mean plume outline, reduces this type of error.

However, additional errors are introduced, since a single average wind and temperature field must be taken to apply over the entire interval of the time-mean plume. Even when atmospheric conditions stay reasonably steady, measurements of these profiles can be expected on average to contain root-mean-square errors of about 15 to 20 percent[3]. Any non-steady atmospheric conditions during the time-mean plume interval would compound this difficulty.

The second source of error is identified as the accurate determination of downwind distance for the plume trajectory during periods when the wind field exhibits appreciable directional shear through the plume mixing layer. Halitsky[13] has shown that these errors remain small if directional shear is less than about 20 degrees across the plume rise region.

To reduce measurement errors as much as possible, attention in this chapter will be focused on data collected during intervals when atmospheric conditions were reasonably steady and when little or no directional shear was evident in the windfield. Several data sets with appreciable directional shear are, however, considered in Appendix A.2. Thirty-seven time-mean plume data sets which satisfy the above criteria have been extracted from the raw data base.

2.4.2.1 Grouping of Plume Rise Data. In subsequent sections on model validation, the 37 time-mean plume data sets are grouped as follows:

(i) A (12 cases): wind profile shows no directional shear and no speed shear; temperature profile is linear.

(ii) B (17 cases): wind field shows no directional shear, but has appreciable speed shear; various temperature profiles.

(iii) C (8 cases): low windspeed cases; no directional shear; various temperature profiles.

A typical data set contains source variables, wind speed and direction profiles, a temperature profile, and measured plume centerline co-ordinates, all averaged over about a 40 to 70 minute period. An example is shown in Table 2.1. Atmospheric parameters for this case were obtained from the pibal data of Figures 2.1 and 2.2, while plume measurements were obtained following the procedure outlined in Reference 12. Measured co-ordinate points on the plume upper and lower boundaries during the time-mean plume intervals were also available for comparison with predicted outlines, but these measurements were not included in the actual time-mean plume data set. Appendix A.3 contains the data sets used in this report. The corresponding pibal and minisonde plots are contained in Appendix D.

Table 2.1. A Typical Time-Mean Plume Data Set.

Mar. 30 0918-0954 (Group B case)

T_{p_o} = 263.0°C w_o = 18.8 m/s

Windfield (3 points)*

z (m)	: 0	210	700
speed (m/s)	: 2.0	5.7	8.6
direction (degrees from)	:60	60	60

Temperature profile (2 points)*

z (m)	: 0	600
temperature (°C)	: 2.3	-3.8

Measured Plume Centerline Coordinates

x (m)	: 0	50	200	400	600	800	1000	1200	1400	1600
z (m)	: 0	43	101	161	206	240	267	288	304	313

*Atmospheric parameters are assumed to follow linear profiles between whatever points are specified in the data set.

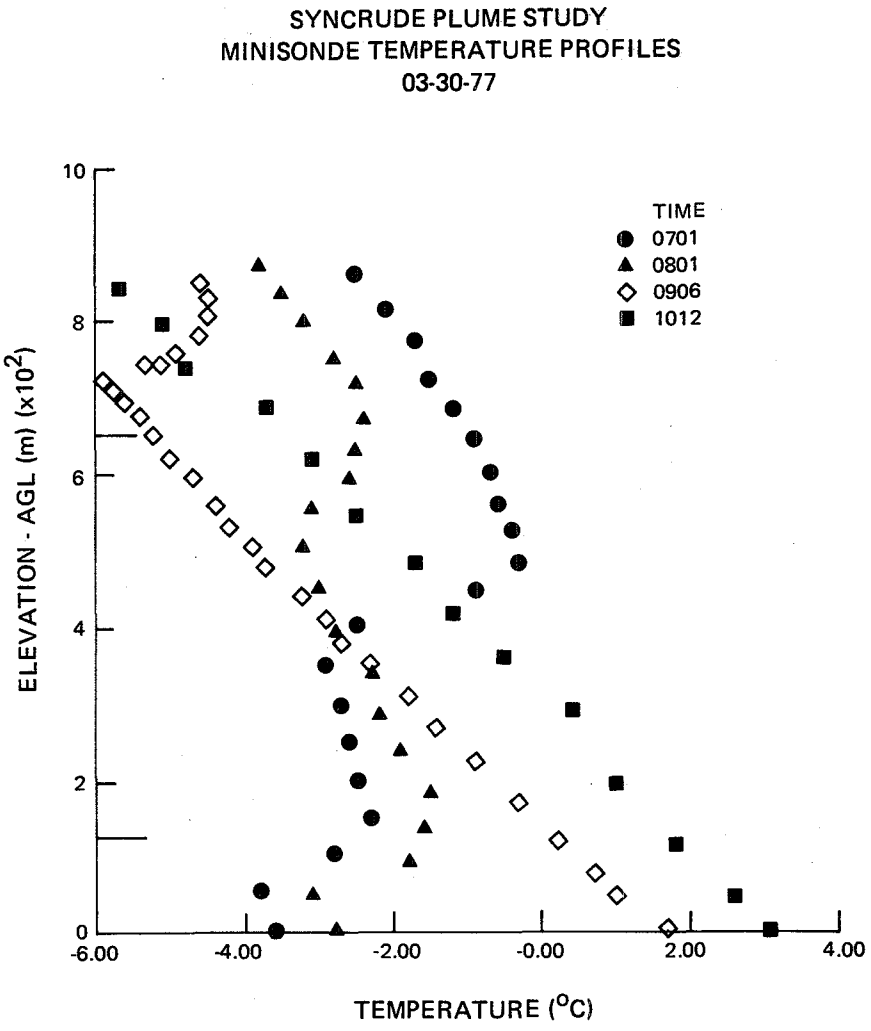

Figure 2.2. A typical minisonde data plot.

Plume rise models will be evaluated by computing the root-mean-square errors between measured and predicted plume centerline co-ordinates:

$$\varepsilon_{RMS} = \sqrt{\frac{1}{m} \sum_{i=1}^{m} \left[\frac{z(x_i)^{model} - z(x_i)^{measured}}{z(x_i)^{measured}} \right]^2} \qquad (2.17)$$

where m is the number of comparison points (usually about 10) selected at arbitrary intervals along the measured trajectory. Plume centerline rather than boundary co-ordinates are used in equation (2.17) both because true plume edges are more difficult to define than the centerline, and also because the centerline trajectory is the more important variable to fix for downwind dispersion calculations. Trajectory errors were considered rather than just final rise errors both because we wish to investigate the detailed effects of the assumptions made in the development of the various models, and because the data base on plume trajectory is larger and more reliable than that on final rise alone. Some comparisons with final rise data are made, however, in section 2.5.

The first step in the model evaluation process is to tune a particular model by selecting values of the empirical constants to minimize ε_{RMS}. Performing this calculation for any one time-mean plume, however, may lead to unreliable estimates for the constants,

since the minimum point for ε_{RMS} is sensitive to any errors in the time-mean plume data set. Errors in U(z), which, as has been mentioned previously, are likely to be of the order of 15 to 20 percent, are particularly important. To overcome this problem, the empirical constants will be chosen to minimize ε_{RMS} averaged over the entire set of twelve Group A data sets.

Once the optimum constants have been selected, there are several performance indicators for the tuned plume rise model:

(i) the actual minimum value of ε_{RMS} averaged over the Group A cases;

(ii) the variation of ε_{RMS} among the twelve Group A cases;

(iii) a comparison of measured and predicted plume spread (outlines) in addition to centerline trajectory;

(iv) the performance of the tuned model against Group B and C data sets;

(v) a comparison of measured and predicted final rises.

2.4.3 Analytical Models

2.4.3.1 Model A1 Derivation. Analytical solutions for R and z may be obtained from the conservation equations (2.1) to (2.9) by introducing the simplifications:

(i) $\rho_a = \rho_p$ = constant, except in density difference terms (the Boussinesq approximation)

(ii) $v_x = U$, $w << V$ (the bent-over plume assumption)

(iii) U = constant with altitude

(iv) $C_D = 0$

along with the bent-over plume entrainment hypothesis

$$v_e = \beta|w| \tag{2.18}$$

The time variable is replaced using $\frac{d}{dt} = U \frac{d}{dx}$, and the governing equations reduce to

$$U \frac{dR}{dx} = \beta \left| \frac{M}{UR^2} \right| \tag{2.19}$$

$$U \frac{dM}{dx} = F \tag{2.20}$$

$$U \frac{dF}{dx} = - MN^2 \tag{2.21}$$

$$\frac{dz}{dx} = \frac{w}{U} \tag{2.22}$$

which represent four equations for the four unknowns R, z, vertical momentum flux $M = UR^2w$ and buoyancy flux $F = UR^2g(T_p - T_a)/T_a$, where T_a is the air temperature.

For stable conditions ($N^2 > 0$), the solution of equations (2.19) to (2.22) may be shown to be

$$R = R_o + \beta z \tag{2.23}$$

$$z = \{\frac{3}{U\beta^2N^2}\left[F_o \left(1-\cos \frac{Nx}{U}\right) + NM_o \sin \frac{Nx}{U} \right] + \left(\frac{R_o}{\beta} \right)^3\}^{1/3} - \frac{R_o}{\beta} \tag{2.24}$$

where R_o, F_o, and M_o are the values of R, F, and M at the source ($x = 0$). Corresponding expressions for neutral conditions ($N^2 = 0$) are equations (2.23) and

$$z = \{\frac{3}{2\beta^2}\left[\frac{F_o}{U^3} x^2 + 2 \frac{M_o}{U^2} x \right] + \left(\frac{R_o}{\beta} \right)^3\}^{1/3} - \frac{R_o}{\beta} \tag{2.25}$$

An exponential solution for z (x) may also be derived for unstable conditions ($N^2 < 0$), but equation (2.25) is usually applied to give a conservative rise estimate for these situations. For a plume with negligible M_o and R_o, equation (2.25) reduces to the well established $\frac{2}{3}$ law;

$$z = \left(\frac{3F_o}{2\beta^2 U^3}\right)^{1/3} x^{2/3} \tag{2.26}$$

which also approximates equation (2.24) for the x range which satisfies $\frac{Nx}{U} << 1$. It is important to note that, to be consistent with the bent-over plume assumption, the initial fluxes in the above expressions must be defined as

$$M_o = UR_o^2 w_o \tag{2.27}$$

$$F_o = UR_o^2 g(Tp_o - T_{a_o})/T_{a_o} \tag{2.28}$$

following the definition of M and F. These initial fluxes are generally smaller than the true initial fluxes, $M_o = R_o^2 w_o^2$ and $F_o = R_o^2 w_o g(T_{p_o} - T_{a_o})/T_{a_o}$.

For this analytical model, the plume rise is allowed to continue until a final, constant rise height is reached. Under stable conditions, the final rise height is taken to occur beyond the first peak of the oscillatory solution (2.24); that is, for downwind distances

$$x \geq \frac{(\pi-\theta)U}{N} \tag{2.29}$$

$$\text{where } \theta = \tan^{-1}\frac{NM_o}{F_o} \tag{2.30}$$

For neutral conditions, Brigg's correlation[2] is applied, under which the final, constant rise height occurs for

$$x \geq 3.5\ x^* \tag{2.31}$$

$$\text{where } x^* = 34 \mathcal{F}_o^{2/5} \tag{2.32}$$

Note that Brigg's definition of buoyancy flux, equation (2.38), is employed in equation (2.32).

2.4.3.2 Model A1 Performance.

Group A Data Sets. The performance of Model A1 (equations 2.23 to 2.25, with equations 2.29 to 2.32) against Group A data sets, for which model assumptions are reasonable, is summarized in Table 2.2 and Figure 2.3. The minimum average ε_{RMS} occurs at $\beta = 0.64$, while the minimum error of 13.5% is of the same order as that reported in previous studies.[3,14] Model A1 with $\beta = 0.64$ predicts trajectories for all twelve cases reasonably well, the worst error being about 25% for the April 1 case.

A typical plume outline prediction is compared with experimental data in Figure 2.4. Both the trajectory and rate of spread are well represented by the $\beta = 0.64$ entrainment constant.

Table 2.2. Model A1 Performance for Group A Data Sets.
R.M.S. Trajectory Errors versus Beta.

Date		Beta=0.50	0.55	0.60	0.65	0.70
Jan. 25	1138-1235	0.098	0.114	0.146	0.179	0.212
Apr. 1	0859-1005	0.135	0.177	0.216	0.252	0.283
July 12	1400-1440	0.219	0.160	0.115	0.089	0.086
July 20	1935-2026	0.111	0.059	0.048	0.078	0.114
July 21	1618-1658	0.166	0.153	0.159	0.177	0.200
July 21	1954-2040	0.060	0.075	0.113	0.151	0.187
July 25	1545-1628	0.111	0.108	0.128	0.157	0.187
Oct. 18	1602-1634	0.288	0.216	0.156	0.107	0.072
Oct. 19	1616-1700	0.197	0.138	0.098	0.083	0.094
Oct. 20	1538-1612	0.294	0.223	0.164	0.116	0.081
Oct. 24	0930-1002	0.238	0.177	0.132	0.105	0.099
Oct. 24	1046-1120	0.304	0.234	0.175	0.128	0.094
Average		0.185	0.153	0.138	0.135	0.142

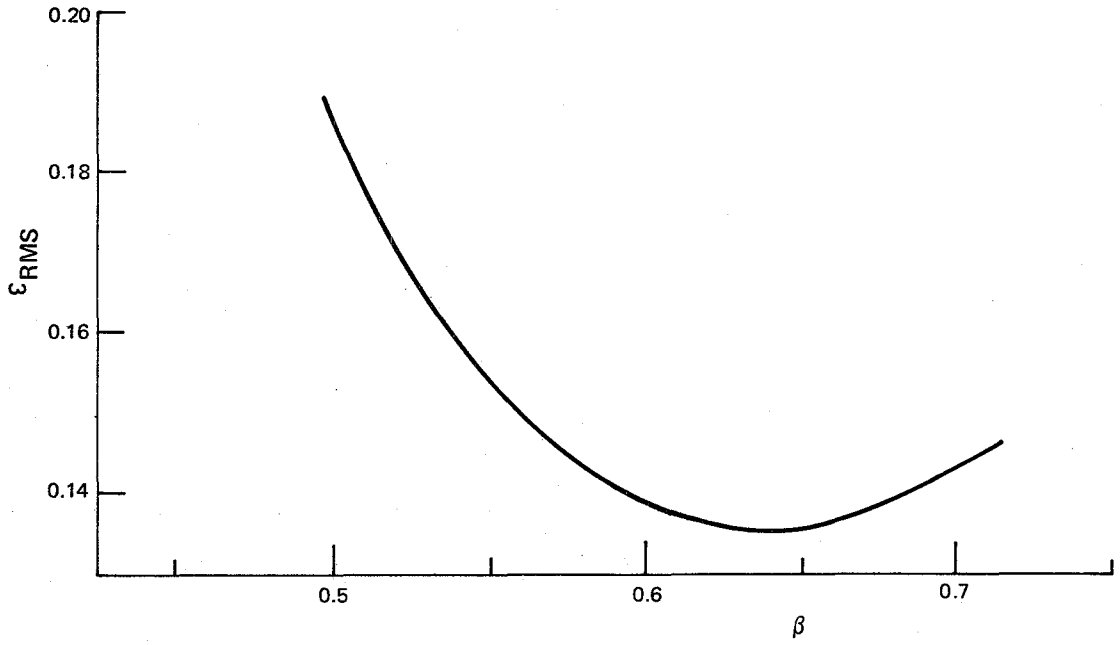

Figure 2.3. Model A1 average trajectory error for Group A data sets.

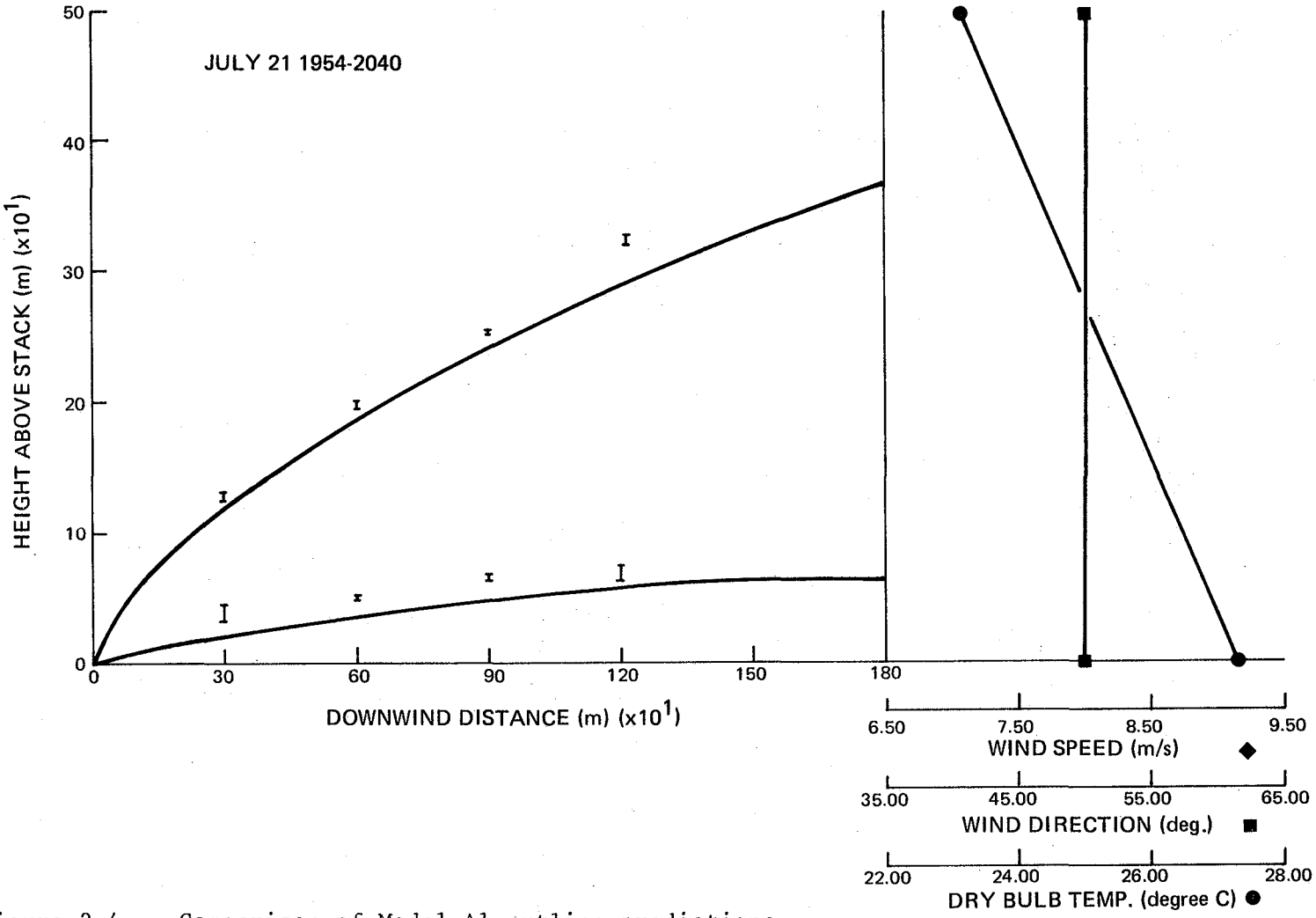

Figure 2.4. Comparison of Model A1 outline predictions (β = 0.64) with photographic data.

Group B and C Data Sets. In Tables 2.3 and 2.4, the tuned model A1 is tested against Group B and C data sets. When wind speed shear and/or a nonlinear temperature profile was evident in a data set, the model was applied twice: iteration 1 was performed using the windspeed and lapse rate at stack exit, while iteration 2 was performed using an average windspeed and lapse rate calculated over the plume mixing layer given by iteration 1. This averaging procedure is similar to the method suggested by Slawson[15].

The average error in applying model A1 to Group B conditions is about 19% for iteration 1, and about 26% for iteration 2, and in a number of cases, plume rise is underpredicted. The velocity averaging procedure generally leads to poorer predictions since the underestimated rise height of iteration 1 is reduced even further by a windspeed increase for iteration 2. The largest error for both iteration 1 and 2 is about 40%.

The performance of model A1 against Group C data sets (low winds) deteriorates further since the bent-over plume assumption and corresponding entrainment hypothesis become invalid for these low windspeed cases. For iteration 1, the predicted trajectory underestimates the centerline measurements by about 38% on average, while the corresponding average error for iteration 2, is about 40%. In both cases, the worst ε_{RMS} is about 50%.

Table 2.3. Model A1 Performance for Group B Data Sets. R.M.S. Trajectory Errors for Beta = 0.64 Ambient Parameters: IT1 - Stack Top; IT2 - Average.

Date		Temp. Profile	IT1	IT2
Jan. 26	1138-1212	Inv. at 600 m	0.303	0.420
Jan. 26	1316-1407	Inv. at 600 m	0.202	0.203
Mar. 30	0840-0934	Linear	0.198	0.271
Mar. 30	0918-0954	Linear	0.121	0.355
Apr. 1	0659-0758	Inv. at 620 m	0.253	0.339
July 13	1524-1614	Kink at 700 m	0.146	0.171
July 23	2116-2202	Linear	0.052	0.295
Oct. 17	1548-1624	Linear	0.168	0.099
Oct. 17	1626-1700	Linear	0.333	0.288
Oct. 19	0920-1011	Inv. at 270 m	0.104	0.218
Oct. 19	1110-1144	Inv. at 470 m	0.235	0.228
Oct. 20	0956-1032	Linear	0.407	0.167
Oct. 25	0918-0956	Kink at 500 m	0.173	0.199
Oct. 25	0958-1030	Inv. at 460 m	0.146	0.322
Oct. 25	1056-1137	Inv. at 350 m	0.170	0.413
Oct. 25	1546-1640	Inv. at 620 m	0.170	0.213
Oct. 27	1516-1548	Linear	0.117	0.253
Average			0.194	0.262

Table 2.4. Model A1 Performance for Group C Data Sets. R.M.S. Trajectory Errors for Beta = 0.64. Ambient Parameters: IT1 - Stack Top; IT2 - Average.

Date		Temp. Profile	IT1	IT2
Jan. 25	1418-1455	Kink at 500 m	0.497	0.497
Jan. 25	1505-1545	Kink at 500 m	0.425	0.436
Mar. 28	1818-1852	Inv. at 320 m	0.369	0.520
July 15	0615-0700	Inv. at 210 m	0.341	0.474
July 15	1608-1652	Linear	0.429	0.470
July 18	0600-0623	Kink at 300 m	0.236	0.236
July 25	1630-1708	Linear	0.309	0.098
July 26	0615-0702	Inv. at 100 m	0.407	0.443
Average			0.377	0.397

2.4.3.3 Model A2 Derivation. As was pointed out in section 2.4.3.1, analytical model A1 is derived under the bent-over plume assumption, which implies that incorrect initial fluxes M_o and F_o are used. Hanna[16] has suggested that a simple modification of model A1, in which an initial radius correction

$$R_o^* = R_o \sqrt{\frac{w_o}{U}} \tag{2.33}$$

is introduced, can recover the correct initial fluxes. Slawson[15] has used this flux correction along with the correction for windspeed shear outlined above to predict cooling tower plume behavior. The neutral plume rise model becomes, for example

$$R = R_o^* + \beta z \tag{2.34}$$

$$z = \left\{ \frac{3}{2\beta^2} \left[\frac{F_o^*}{U^3} x^2 + 2 \frac{M_o^*}{U^2} x \right] + \left(\frac{R_o^*}{\beta} \right)^3 \right\}^{1/3} - \frac{R_o^*}{\beta} \tag{2.35}$$

where $M_o^* = UR_o^{*2} w_o = R_o^2 w_o^2$ (2.36)

and $F_o^* = UR_o^{*2} g(T_{p_o} - T_{a_o})/T_{a_o} = R_o^2 w_o g(T_{p_o} - T_{a_o})/T_{a_o}$ (2.37)

Correct initial fluxes are thereby obtained at the expense of an initial radius error appearing in both equations (2.34) and (2.35). Model A2 is identical to model A1 except for the introduction of R_o^*, M_o^*, and F_o^* in the analytical solutions.

2.4.3.4 Model A2 Performance.

Group A Data Sets. The performance of model A2 against Group A data sets is summarized in Table 2.5 and Figure 2.5. The minimum average ε_{RMS} of 12.4% occurs at $\beta = 0.88$ which is considerably larger than the optimum β for model A1. Physically, higher entrainment is necessary in model A2 to offset the increased initial fluxes M_o^* and F_o^*. Trajectories for all the Group A cases are predicted slightly better by model A2 than by model A1, the worst error being about 19% for the October 20 case.

A typical model A2 plume outline prediction is compared with experimental data in Figure 2.6, where it is evident that the rate of spread is overestimated. Correction of the initial fluxes in an analytical bent-over plume model therefore leads to slightly better centerline but poorer growth rate predictions.

Group B and C Data Sets. In Tables 2.6 and 2.7, the tuned model A2 is tested against Group B and C data sets, following the iterative procedure outlined in 2.4.3.2 to allow for windspeed shear and nonlinear temperature profiles. The average error in applying model A2 to Group B conditions is about 27% for iteration 1, and about 17% for iteration 2. While the performance of the model does deteriorate when wind shear is present, the averaging procedure reduces the iteration 1 error considerably. The success of the procedure for

Table 2.5. Model A2 Performance for Group A Data Sets. R.M.S. Trajectory Errors versus Beta.

Date		Beta = 0.75	0.80	0.85	0.90	0.95
Jan. 25	1138-1235	0.168	0.134	0.110	0.097	0.097
Apr. 1	0859-1005	0.085	0.098	0.119	0.143	0.167
July 12	1400-1440	0.153	0.120	0.097	0.085	0.086
July 20	1935-2026	0.107	0.070	0.048	0.050	0.069
July 21	1618-1658	0.153	0.159	0.171	0.187	0.205
July 21	1954-2040	0.063	0.084	0.112	0.139	0.165
July 25	1545-1628	0.269	0.226	0.189	0.158	0.133
Oct. 18	1602-1634	0.209	0.165	0.126	0.094	0.071
Oct. 19	1616-1700	0.102	0.085	0.085	0.099	0.118
Oct. 20	1538-1612	0.327	0.276	0.231	0.191	0.156
Oct. 24	0930-1002	0.097	0.098	0.110	0.130	0.151
Oct. 24	1046-1120	0.080	0.081	0.098	0.120	0.143
Average		0.151	0.133	0.125	0.125	0.130

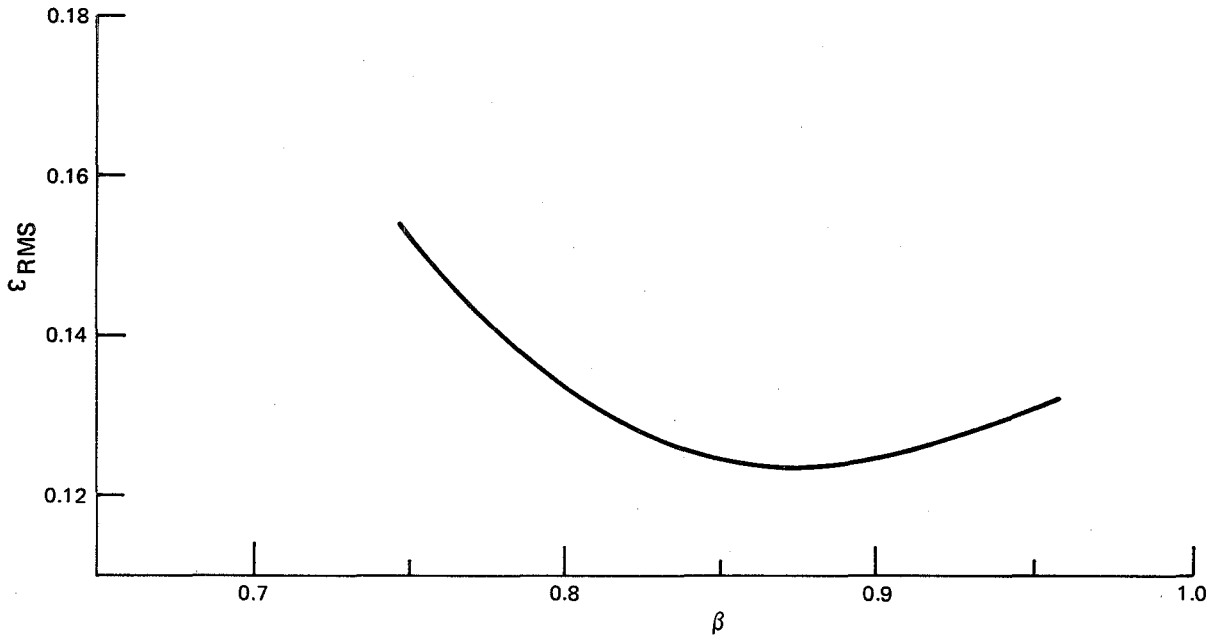

Figure 2.5. Model A2 average trajectory error for Group A data sets.

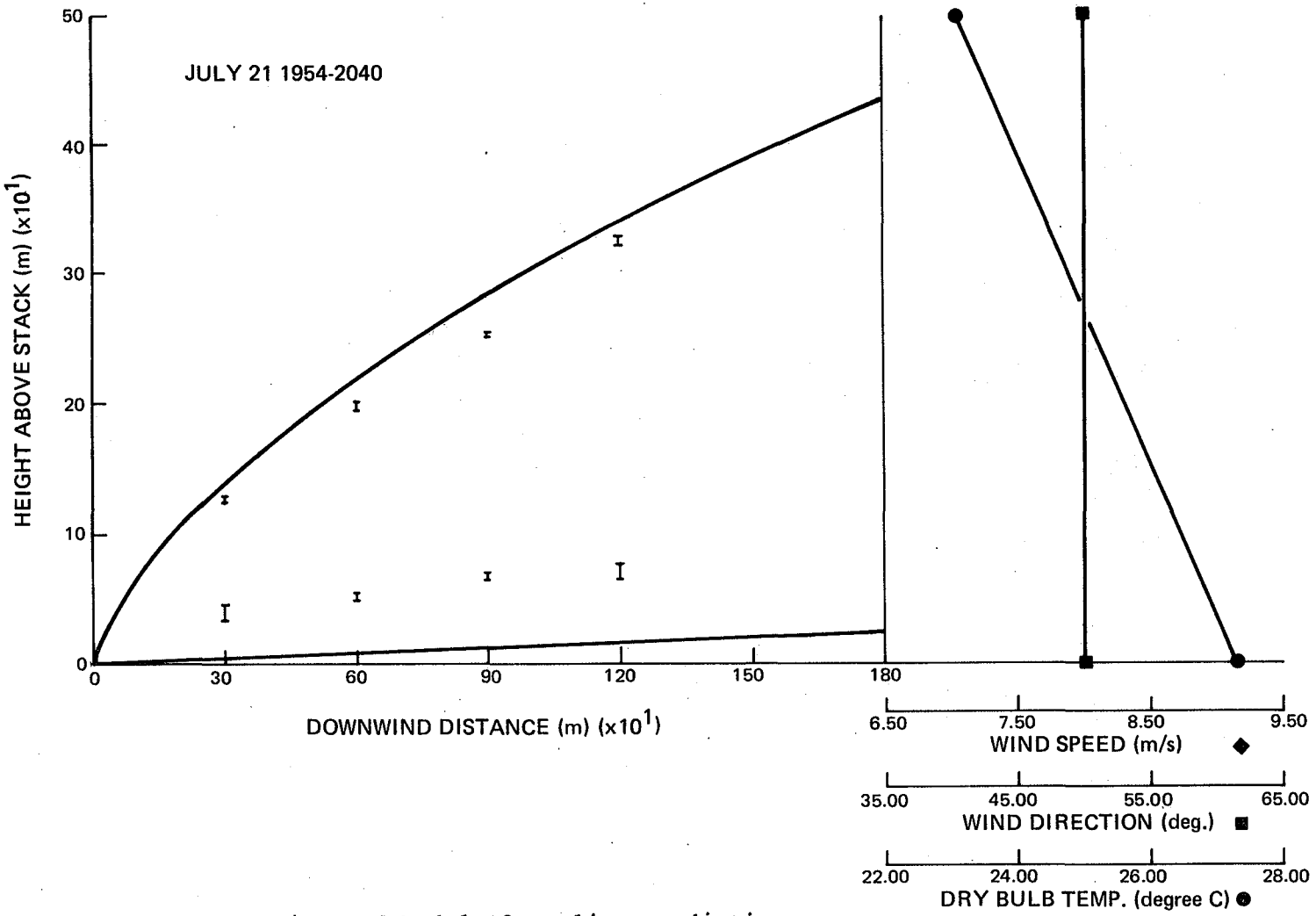

Figure 2.6. Comparison of Model A2 outline predictions (β = 0.88) with photographic data.

Table 2.6. Model A2 Performance for Group B Data Sets. R.M.S. Trajectory Errors for Beta = 0.88. Ambient Parameters: IT1 - Stack Top; IT2 - Average.

Date		Temp. Profile	IT1	IT2
Jan. 26	1138-1212	Inv. at 600 m	0.128	0.306
Jan. 26	1316-1407	Inv. at 600 m	0.041	0.034
Mar. 30	0840-0934	Linear	0.071	0.186
Mar. 30	0918-0954	Linear	0.243	0.247
Apr. 1	0659-0758	Inv. at 620 m	0.226	0.312
July 13	1524-1614	Kink at 700 m	0.080	0.103
July 23	2116-2202	Linear	0.160	0.187
Oct. 17	1548-1624	Linear	0.220	0.074
Oct. 17	1626-1700	Linear	0.226	0.192
Oct. 19	0920-1011	Inv. at 270 m	0.275	0.139
Oct. 19	1110-1144	Inv. at 470 m	0.595	0.071
Oct. 20	0956-1032	Linear	0.334	0.124
Oct. 25	0918-0956	Kink at 500 m	0.415	0.080
Oct. 25	0958-1030	Inv. at 460 m	0.476	0.159
Oct. 25	1056-1137	Inv. at 350 m	0.379	0.373
Oct. 25	1546-1640	Inv. at 620 m	0.400	0.192
Oct. 27	1516-1548	Linear	0.240	0.158
Average			0.265	0.173

Table 2.7. Model A2 Performance for Group C Data Sets. R.M.S. Trajectory Errors for Beta = 0.88. Ambient Parameters: IT1 - Stack Top; IT2 - Average.

Date		Temp. Profile	IT1	IT2
Jan. 25	1418-1455	Kink at 500 m	0.138	0.290
Jan. 25	1505-1545	Kink at 500 m	0.159	0.317
Mar. 28	1818-1852	Inv. at 320 m	0.446	0.420
July 15	0615-0700	Inv. at 210 m	0.342	0.310
July 15	1608-1652	Linear	0.268	0.258
July 18	0600-0623	Kink at 300 m	0.132	0.186
July 25	1630-1708	Linear	0.119	0.198
July 26	0615-0702	Inv. at 100 m	0.242	0.262
Average			0.231	0.280

model A2, as compared to its failure for model A1, is attributed to the correction of the initial fluxes. While model A2 iterates keeping fixed, correct initial fluxes, model A1 alters these fluxes when the wind speed is altered.

The iterative correction is not as effective, however, against Group C data sets. The average error is approximately 23% for iteration 1 and about 28% for iteration 2, with about half of these errors being underpredictions of rise and half overpredictions of rise. As for model A1, this deterioration in performance is attributed mainly to the failure of the bent-over plume assumption and entrainment hypothesis under low windspeed conditions.

2.4.3.5 Model A3 Derivation. Model A3, which follows the notation employed by Briggs, is derived by making two changes in model A2. The initial radius correction is ignored, so that R_o^* is replaced by R_o in equations such as (2.34) and (2.35), while the source buoyancy flux F_o^* is replaced by a flux defined in terms of a T_{p_o} divisor:

$$\mathcal{F}_o = R_o^2 w_o g \, (T_{p_o} - T_{a_o}) \, / \, T_{p_o} \qquad (2.38)$$

The source momentum flux remains defined as $R_o^2 w_o^2$. Note that, for the very hot GCOS plume, $\mathcal{F}_o \tilde{=} 1/2 \, F_o^*$, so that the redefinition of source buoyancy flux is a significant change.

2.4.3.6 Model A3 Performance.

Group A Data Sets. The performance of model A3 against Group A data sets is summarized in Table 2.8 and Figure 2.7. The minimum average ε_{RMS} of 13% occurs with $\beta = 0.66$. This value is in good agreement with Briggs recommendation of $\beta = 0.6$ for the simplified 2/3 law form of model A3:

$$z = \left(\frac{3\,\mathcal{F}_o}{2\beta^2 U^3}\right)^{1/3} x^{2/3} \qquad (2.39)$$

An increase to $\beta = 0.66$ is consistent with retaining initial radius and momentum terms in model A3.

A typical model A3 plume outline prediction is compared with measurements in Figure 2.8, where it is evident that both trajectory and rate of spread are well represented. While models A2 and A3 lead to comparable trajectory predictions, model A3 leads to superior predictions of rate of spread.

Group B and C Data Sets. In Tables 2.9 and 2.10, the tuned model A3 is tested against Group B and C data sets, again employing the iterative procedure outlined previously to account for windspeed shear, and nonlinear temperature profiles. The trajectory predictions of model A3 are comparable to those of model A2. For Group B cases,

Table 2.8. Model A3 Performance for Group A Data Sets. R.M.S. Trajectory Errors versus Beta.

Date	Beta = 0.50	0.55	0.60	0.65	0.70
Jan. 25 1138-1235	0.259	0.204	0.166	0.146	0.142
Apr. 1 0859-1005	0.080	0.061	0.085	0.121	0.157
July 12 1400-1440	0.244	0.179	0.126	0.086	0.065
July 20 1935-2026	0.207	0.142	0.091	0.061	0.064
July 21 1618-1658	0.174	0.156	0.157	0.172	0.194
July 21 1954-2040	0.075	0.043	0.067	0.106	0.144
July 25 1545-1628	0.367	0.292	0.228	0.175	0.131
Oct. 18 1602-1634	0.287	0.216	0.158	0.111	0.080
Oct. 19 1616-1700	0.140	0.089	0.067	0.081	0.111
Oct. 20 1538-1612	0.403	0.325	0.258	0.201	0.153
Oct. 24 0930-1002	0.120	0.115	0.133	0.160	0.189
Oct. 24 1046-1120	0.104	0.104	0.126	0.156	0.187
Average	0.205	0.161	0.139	0.131	0.135

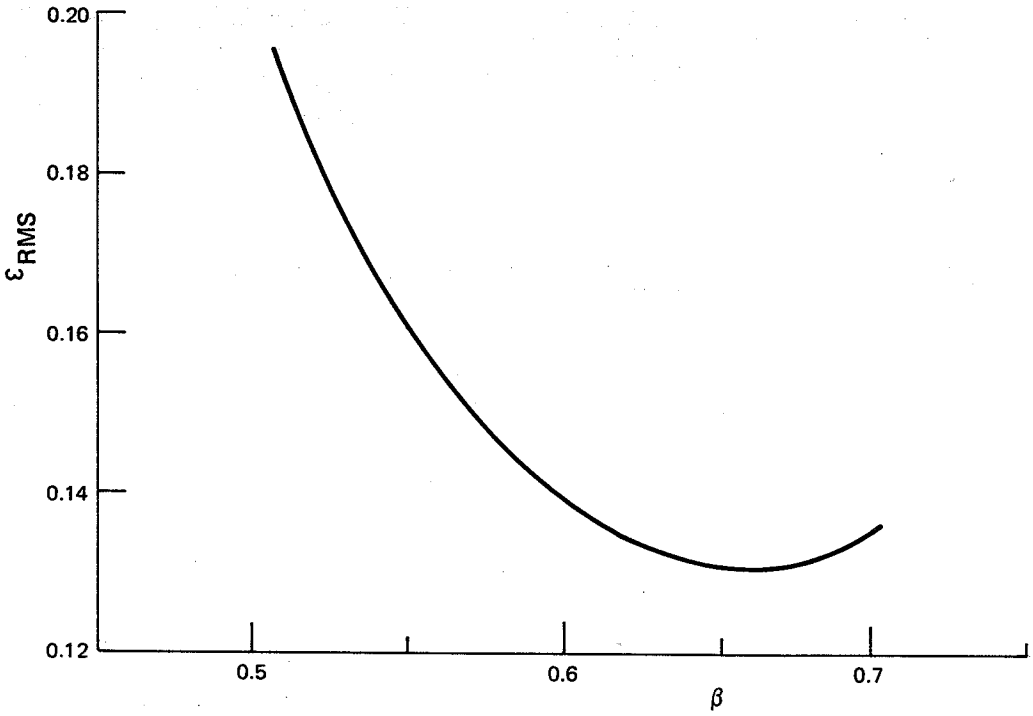

Figure 2.7. Model A3 average trajectory error for Group A data sets.

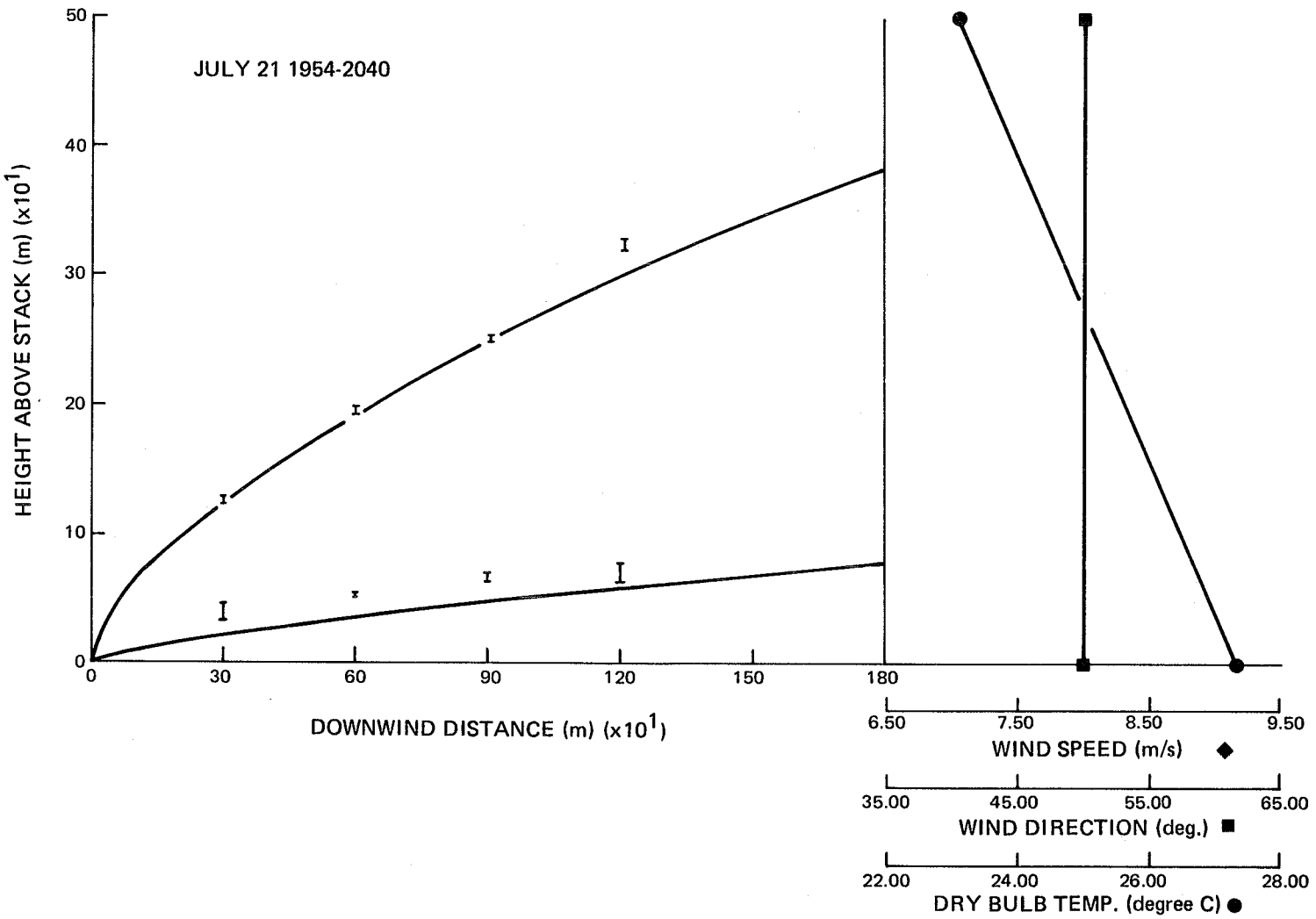

Figure 2.8. Comparison of Model A3 outline predictions (β = 0.66) with photographic data.

Table 2.9. Model A3 Performance for Group B Data Sets. R.M.S. Trajectory Errors for Beta = 0.66. Ambient Parameters: IT1 - Stack Top; IT2 - Average.

Date		Temp. Profile	IT1	IT2
Jan. 26	1138-1212	Inv. at 600 m	0.149	0.314
Jan. 26	1316-1407	Inv. at 600 m	0.034	0.034
Mar. 30	0840-0934	Linear	0.061	0.159
Mar. 30	0918-0954	Linear	0.228	0.209
Apr. 1	0659-0758	Inv. at 620 m	0.215	0.303
July 13	1524-1614	Kink at 700 m	0.110	0.105
July 23	2116-2202	Linear	0.182	0.167
Oct. 17	1548-1624	Linear	0.209	0.063
Oct. 17	1626-1700	Linear	0.204	0.171
Oct. 19	0920-1011	Inv. at 270 m	0.263	0.136
Oct. 19	1110-1144	Inv. at 470 m	0.575	0.076
Oct. 20	0956-1032	Linear	0.286	0.083
Oct. 25	0918-0956	Kink at 500 m	0.400	0.063
Oct. 25	0958-1030	Inv. at 460 m	0.456	0.158
Oct. 25	1056-1137	Inv. at 350 m	0.354	0.369
Oct. 25	1546-1640	Inv. at 620 m	0.347	0.154
Oct. 27	1516-1548	Linear	0.227	0.142
Average			0.253	0.159

Table 2.10. Model A3 Performance for Group C Data Sets. R.M.S. Trajectory Errors for Beta = 0.66. Ambient Parameters: IT1 - Stack Top; IT2 - Average.

Date		Temp. Profile	IT1	IT2
Jan. 25	1418-1455	Kink at 500 m	0.171	0.288
Jan. 25	1505-1545	Kink at 500 m	0.121	0.316
Mar. 28	1818-1852	Inv. at 320 m	0.413	0.427
July 15	0615-0700	Inv. at 210 m	0.323	0.303
July 15	1608-1652	Linear	0.253	0.274
July 18	0600-0623	Kink at 300 m	0.121	0.181
July 25	1630-1708	Linear	0.100	0.211
July 26	0615-0702	Inv. at 100 m	0.246	0.268
Average			0.219	0.283

the average root mean square error is about 25% for iteration 1, and about 16% for iteration 2. For Group C cases, the performance of the model deteriorates: the average error is about 22% for iteration 1, and about 28% for iteration 2. While the centerline trajectory performance of model A3 has the same strengths and weaknesses as model A2, it must be remembered that the tuned model A3 uses $\beta = 0.66$, which leads to better outline predictions. This point will be discussed further in section 2.5.

2.4.3.7 Model A4 Derivation. In a recent article, Djurfors and Netterville[40] have presented analytical solutions for plume rise and spread under wind speed shear conditions. If assumptions (i), (ii), (iv), and (v) of section 2.4.3.1 are retained, but assumption (iii), that U = constant with altitude, is relaxed, the conservation equations (2.1) to (2.4) may be reduced to

$$\frac{d}{dt}(R^2U) = 2RUv_e \tag{2.40}$$

$$\frac{dM}{dt} = F \tag{2.41}$$

$$\frac{dF}{dt} = -MN^2 \tag{2.42}$$

Introducing the entrainment hypothesis

$$v_e = \beta|w| \tag{2.43}$$

and, assuming that the wind profile can be described by

$$U = U_o(1 + z/z_o)^{\gamma} \tag{2.44}$$

leads to analytical solutions for R and z as functions of travel time t.

Under stable conditions ($N^2 > 0$) the solution becomes

$$R = R_o^* + \beta^* z \tag{2.45}$$

$$z = \left\{ \frac{(3+\gamma) z_o^{\gamma}}{U_o \beta^{*2}} \frac{F_o^*}{N^2} (1-\cos Nt + \frac{NM_o^*}{F_o^*} \sin Nt) + (\frac{R_o^*}{\beta^*})^{3+\gamma} \right\}^{\frac{1}{3+\gamma}} - \frac{R_o^*}{\beta^*} \tag{2.46}$$

where

$$\beta^* = \beta/(1+1/2\gamma) \tag{2.47}$$

$$z_o = R_o^*/\beta^* \tag{2.48}$$

Initial radius and momentum terms have been included in this solution, along with the source radius correction R_o^* of Hanna. Under neutral conditions ($N^2 = 0$), equation (2.46) becomes

$$z = \left\{ \frac{(3+\gamma) z_o^{\gamma} F_o^*}{2U_o \beta^{*2}} (t^2 + 2 \frac{M_o^*}{F_o^*} t) + (\frac{R_o^*}{\beta^*})^{3+\gamma} \right\}^{\frac{1}{3+\gamma}} - \frac{R_o^*}{\beta^*} \tag{2.49}$$

Although equations (2.45) to (2.49) represent an analytical solution in terms of t, a numerical integrating is required to relate downwind distance to travel time:

$$x = \int Udt = U_o \int \{ 1 + z(t)/z_o \}^{\gamma} dt \qquad (2.50)$$

2.4.3.8 Model A4 Performance.

Group A Data Set. For a uniform windfield, $\gamma = 0$ and model A4 becomes identical to model A2. Accordingly, the performance of model A4 against Group A data sets is the same as that of model A2: a minimum average error of 12.4% occurs with an entrainment constant $\beta = 0.88$ (see Table 2.5). Model A4, like model A2, therefore leads to reasonable centerline trajectory predictions, but leads to an overestimate in rates of spread. Improved outline predictions could be obtained from model A4, however, by introducing Briggs redefinition of source buoyancy flux, equation (2.38), into equations (2.45) to (2.49). Centerline predictions of model A4 would remain about the same, but the entrainment constant would be reduced to the model A3 value, $\beta = 0.66$.

Group B and C Data Sets. In Tables 2.11 and 2.12, the tuned model A4 with $\beta = 0.88$ is tested against Group B and C data sets. Under windspeed shear conditions, equation (2.44) was fitted to

Table 2.11. Model A4 Performance for Group B Data Sets. R.M.S. Trajectory Errors for Beta = 0.88.

Date		Temp. Profile	Error
Jan. 26	1138-1212	Inv. at 600 m	0.255
Jan. 26	1316-1407	Inv. at 600 m	0.136
Mar. 30	0840-0934	Linear	0.134
Mar. 30	0918-0954	Linear	0.120
Apr. 1	0659-0758	Inv. at 620 m	0.256
July 13	1524-1614	Kink at 700 m	0.093
July 23	2116-2202	Linear	0.067
Oct. 17	1548-1624	Linear	0.061
Oct. 17	1626-1700	Linear	0.199
Oct. 19	0920-1011	Inv. at 270 m	0.091
Oct. 19	1110-1144	Inv. at 470 m	0.114
Oct. 20	0956-1032	Linear	0.159
Oct. 25	0918-0956	Kink at 500 m	0.100
Oct. 25	0958-1030	Inv. at 460 m	0.072
Oct. 25	1056-1137	Inv. at 350 m	0.288
Oct. 25	1546-1640	Inv. at 620 m	0.135
Oct. 27	1516-1548	Linear	0.091
Average			0.139

Table 2.12. Model A4 Performance for Group C Data Sets. R.M.S. Trajectory Errors for Beta = 0.88.

Date		Temp. Profile	Error
Jan. 25	1418-1455	Kink at 500 m	0.385
Jan. 25	1505-1545	Kink at 500 m	0.299
Mar. 28	1818-1852	Inv. at 320 m	0.330
July 15	0615-0700	Inv. at 210 m	0.550
July 15	1608-1652	Linear	0.289
July 18	0600-0623	Kink at 300 m	0.129
July 25	1630-1708	Linear	0.118
July 26	0615-0702	Inv. at 100 m	0.374
Average			0.309

measured profiles by the method of least squares to find U_o and γ. An initial estimate of plume rise was necessary at this stage to fix the altitude range over which the least squares fit should be made. Just as for model A2, a first iteration was performed assuming uniform U and N^2 equal to stack-top values to provide the initial rise estimate. A least squares fit, such as that illustrated in Figure 2.9, can then be made, and model A4 applied in a second iteration.

A further complication in making the least squares fit is that of fixing the parameter z_o. This was done iteratively; that is, z_o was first estimated by assuming $\gamma = 0$ such that $\beta^* = \beta = 0.88$. Least squares equations were next applied to find U_o and γ:

$$U_o = \exp\left\{\frac{1}{D}\left\{\Sigma \ell n\ U_i\ \Sigma\left[\ell n(1+\frac{z_i}{z_o})\right]^2 - \Sigma \ell n(1+\frac{z_i}{z_o})\Sigma\left[\ell n\ U_i\ \ell n(1+\frac{z_i}{z_o})\right]\right\}\right\} \tag{2.51}$$

$$\gamma = \frac{1}{D}\left\{N\ \Sigma\left[\ell n\ U_i\ \ell n(1+\frac{z_i}{z_o})\right] - \Sigma \ell n\ U_i\ \Sigma \ell n\ (1+\frac{z_i}{z_o})\right\} \tag{2.52}$$

where $$D = N\ \Sigma\left[\ell n(1+\frac{z_i}{z_o}\right]^2 - \left[\Sigma \ell n(1+\frac{z_i}{z_o})\right]^2 \tag{2.53}$$

and the summations were carried out over N data points z_i, U_i. Using the new value of γ, β^* and z_o were recalculated, and the process was repeated until it converged. Two or three iterations were generally sufficient.

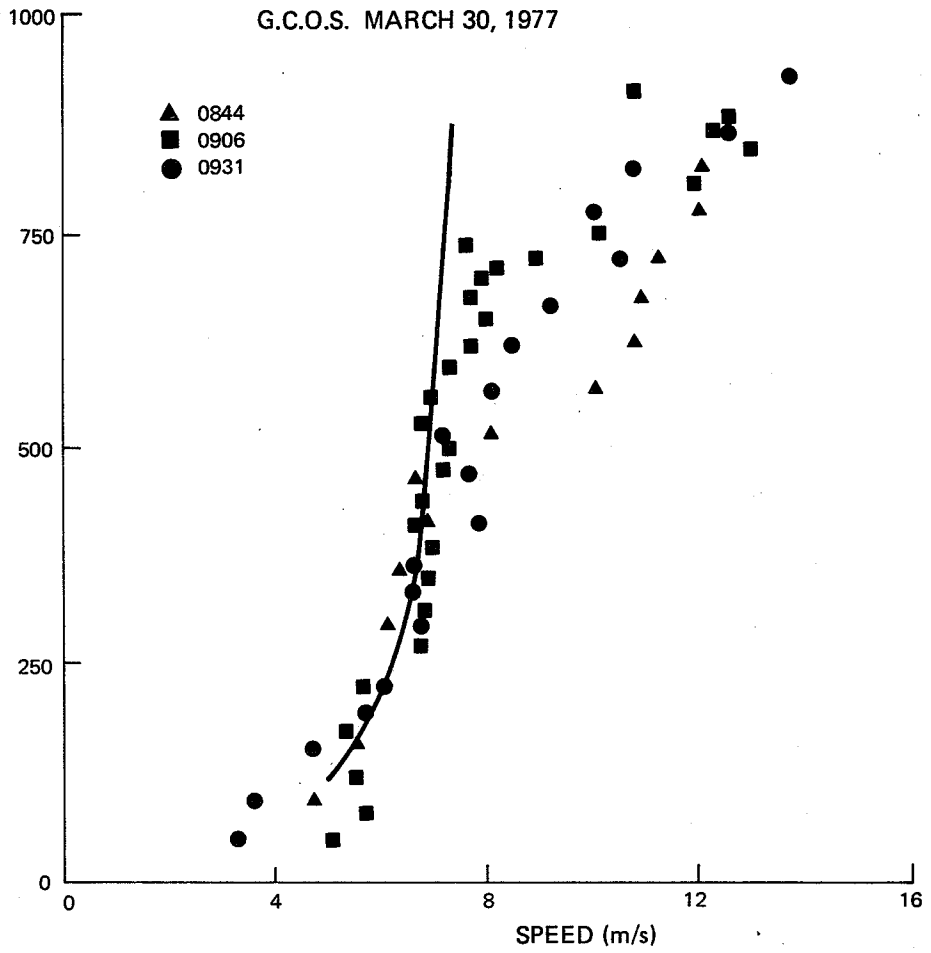

Figure 2.9. A least squares profile fit example for Model A4. ($U_{(z)} = 5.15\ (1 + z/6.24)^{0.072}$).

The average error in applying model A4 to Group B data sets (Table 2.11) following the steps outlined above, is 13.9%. Model A4 therefore leads to somewhat better predictions than models A1 to A3 under windspeed shear conditions. When model A4 is applied to Group C data sets (Table 2.12), however, its performance deteriorates in a similar manner as that of models A1 to A3. The average root mean square error for Group C cases increases to about 31%. The bent-over plume assumption becomes invalid for these low windspeed cases.

2.4.4 Numerical Models

2.4.4.1 Numerical Procedure. The simplifications required to obtain analytical models A1 and A4, which are listed in section 3.1, are no longer necessary if the conservation equations (2.1) to (2.9) are solved numerically. It therefore becomes possible to account in a precise way for wind speed shear U(z) and non-constant temperature lapse conditions (variable $N^2(z)$) in plume rise predictions. The Boussinesq approximation, whose validity might be questioned at least near the source for the very hot GCOS plume (T_{p_o} = 280°C), may also be relaxed, and various entrainment and drag hypotheses may be applied.

In this section of the report, several numerical models are evaluated. A fourth-order Runge-Kutta scheme, with automatic time step halving for error control, is used to perform the numerical integrations. Generally, the halving procedure finds that short time

steps are required near the source, while longer time steps are acceptable downwind. It is assumed that each atmospheric parameter is constant across a time step, and equal to the average value across the most recently calculated section of the plume, normal to its direction. An elevated inversion, for example, thus has an effect on the solution as soon as the upper plume boundary, as opposed to the plume centerline, reaches the inversion height.

2.4.4.2 Model N1 Derivation. Model N1 is based on equations (2.1) to (2.9) subject to the restrictions:

(i) $\rho_a = \rho_p$ = constant, except in density difference terms (Boussinesq approximation)

(ii) $v_x = U$, $w << V$ (bent-over plume assumption)

(iii) $v_e = \beta|w|$

The governing equations thereby reduce to six:

$$\frac{d}{dt}(R^2V) = 2RV\beta|w| \tag{2.54}$$

$$\frac{dM}{dt} = F - C_D R V V_R w \tag{2.55}$$

$$\frac{dF}{dt} = - MN^2 \tag{2.56}$$

$$\frac{dx}{dt} = U \tag{2.57}$$

$$\frac{dz}{dt} = w \tag{2.58}$$

$$V^2 = U^2 + w^2 \tag{2.59}$$

where $M = VR^2w$ and $F = VR^2g(T_p - T_a)/T_a$ are the vertical momentum and buoyancy fluxes respectively. These equations are solved numerically subject to the initial conditions

$$V(0) = w_o \tag{2.60}$$

$$R(0) = R_o \tag{2.61}$$

$$M(0) = R_o^2 w_o^2 \tag{2.62}$$

$$F(0) = R_o^2 w_o g(T_{p_o} - T_{a_o})/T_{a_o} \tag{2.63}$$

$$x(0) = z(0) = 0 \tag{2.64}$$

where zero subscripts refer to source values.

Model N1, which has been applied in previous studies by Slawson[15], represents an extension over analytical models in order to account for variable wind speeds U(z) and variable lapse rates $N^2(z)$. For Group A data sets, in which U and N^2 are constants, model N1 predictions with $C_D = 0$ should be comparable with the analytical solutions. This comparison is complicated, however, by the fact that model N1 contains some features of model A1 (the correct initial radius), and some features of model A2 (the correct initial fluxes).

2.4.4.3 Model N1 Performance. The behavior of ε_{RMS} when N1 with $C_D = 0$ is applied to all Group A data sets is summarized in Table 2.13 and Figure 2.10. The optimum entrainment constant is $\beta = 0.86$, which compares well with the A2 value, and the minimum average ε_{RMS} is 13.3%, which lies between the A1 and A2 minimum values.

The performance of model N1 for one Group A data set is illustrated in the outline plot of Figure 2.11. As is shown in the figure, model N1 predictions with $C_D = 0$ and $\beta = 0.86$ are almost identical to model A2 predictions. The two models only differ near the source, a discrepancy which is due to the R_o^* error introduced into model A2 to recover the correct initial fluxes. These results provide a check on the validity of the numerical procedure and computer calculations.

The tuned model N1, like A2, gives good trajectory predictions, but tends to overestimate the growth rate. On the basis of these results, it now becomes clear why a nonzero drag term is a useful addition to this model: a smaller entrainment constant can be used to reduce the rate of growth, while the drag term can be increased to reduce the rate of rise and maintain a good trajectory fit. The improved prediction of model N1 with $C_D = 0.5$, using the optimum entrainment constant for model A1, $\beta = 0.64$, are shown in the Figure 2.11 example.

Table 2.13. Model N1 Performance for Group A Data Sets. R.M.S. Trajectory Errors versus Beta.

Date	Beta =	0.70	0.75	0.80	0.85	0.90
Jan. 25	1138-1235	0.182	0.140	0.105	0.079	0.065
Apr. 1	0859-1005	0.113	0.119	0.134	0.154	0.175
July 12	1400-1440	0.169	0.135	0.109	0.096	0.095
July 20	1935-2026	0.120	0.082	0.057	0.054	0.070
July 21	1618-1658	0.153	0.154	0.163	0.178	0.195
July 21	1954-2040	0.070	0.081	0.103	0.130	0.156
July 25	1545-1628	0.252	0.212	0.180	0.155	0.137
Oct. 18	1602-1634	0.236	0.187	0.144	0.106	0.076
Oct. 19	1616-1700	0.156	0.138	0.133	0.136	0.150
Oct. 20	1538-1612	0.328	0.277	0.232	0.193	0.158
Oct. 24	0930-1002	0.163	0.156	0.160	0.171	0.185
Oct. 24	1046-1120	0.148	0.142	0.148	0.160	0.178
Average		0.174	0.152	0.139	0.134	0.137

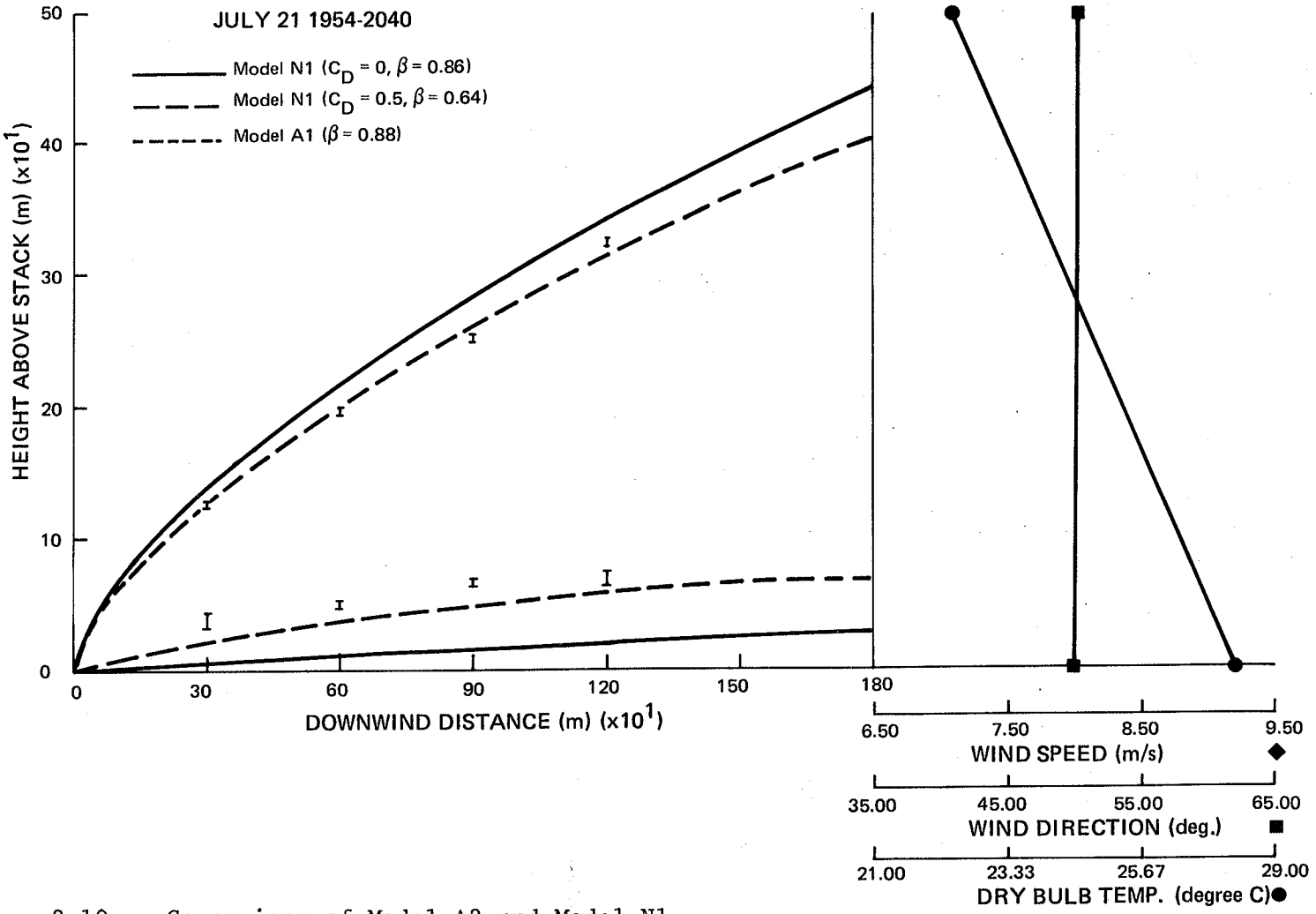

Figure 2.10. Comparison of Model A2 and Model N1 outline predictions with photographic data.

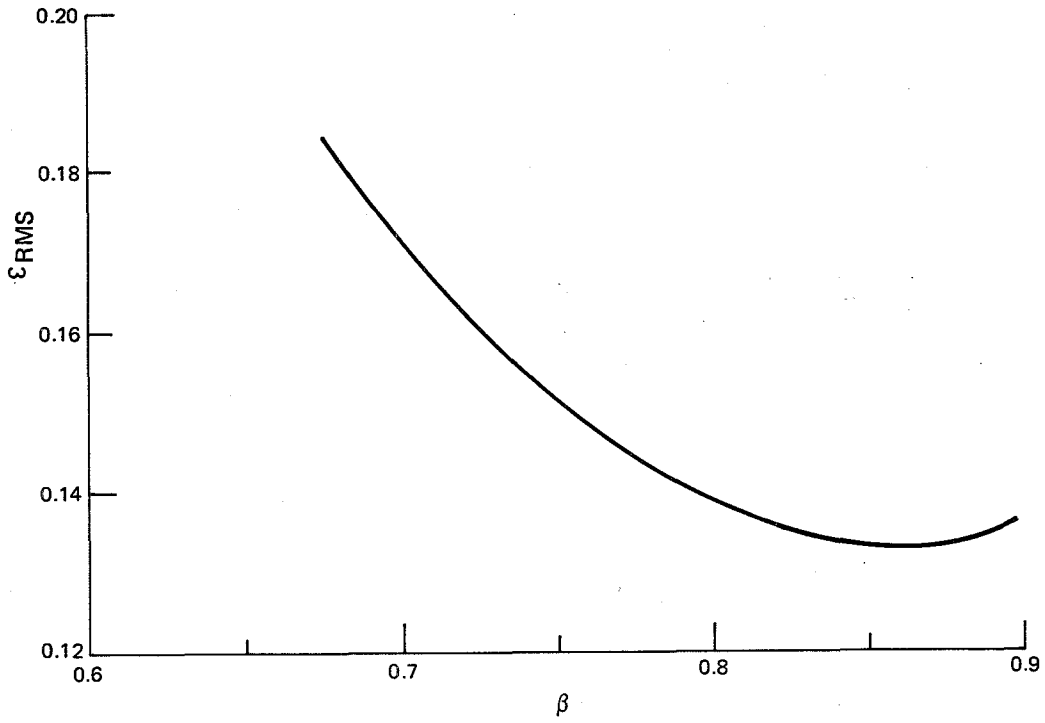

Figure 2.11. Model N1 average trajectory error for Group A data sets.

While it would be possible to optimize β and C_D for model N1 by seeking minimum ε_{RMS} for Group A plume outlines rather than centerlines, this procedure has not been carried out in detail (although a few trials have suggested that the optimum is near the $C_D = 0.5$, $\beta = 0.64$ values used above). The introduction of drag into model N1 is apparently necessary for good outline predictions, despite the arguments presented in section 2.4.1 that drag forces should not appear. It is suggested, however, that this drag force has no physical reality, but is necessary in the model only to compensate for the Boussinesq and bent-over plume assumptions. Models A1 and A3 compensate for these approximations by using incorrect, reduced initial fluxes; model N1 with $C_D = 0$ and models A2 and A4 have no mechanism for compensation, and so are able to predict the correct trajectory only at the expense of an overestimated growth rate; while model N1 with non-zero C_D compensates by introducing a fictitious drag force and without reducing the initial fluxes.

2.4.4.4 Model N2. Model N1 problems have been attributed to the bent-over plume and Boussinesq approximations. To gain insight into the relative importance of each of these assumptions for the G.C.O.S. data, model N2 retains the Boussinesq approximation and the $C_D = 0$ and $v_e = \beta|w|$ assumptions, but relaxes the bent-over plume restriction. The governing equations for model N2 thus becomes

$$\frac{d}{dt}(R^2V) = 2RV\beta|w| \qquad (2.65)$$

$$\frac{d}{dt}(R^2 V v_x) = 2RVU\beta|w| \tag{2.66}$$

$$\frac{d}{dt}(R^2 V w) = gR^2 V (T_p - T_a)/T_a \tag{2.67}$$

$$\frac{d}{dt}[gR^2 V (T_p - T_a)/T_a] = - N^2 R^2 V w \tag{2.68}$$

$$\frac{ds}{dt} = V \tag{2.69}$$

$$\frac{dz}{dt} = w \tag{2.70}$$

$$\frac{dx}{dt} = v_x \tag{2.71}$$

$$V^2 = v_x^2 + w^2 \tag{2.72}$$

These equations are solved numerically, subject to the initial conditions (2.60) to (2.64), and

$$v_x(0) = s(0) = 0 \tag{2.73}$$

The performance of model N2 for Group A data sets is summarized in Table 2.14 and Figure 2.12. The minimum average error ε_{RMS} of 12.8% occurs at $\beta = 0.89$. While the error figure indicates some improvement over model N1, the tuned model N2 still requires a large entrainment constant to match trajectories, and so overestimates the rate of spread. It is, therefore, concluded that the bent-over plume assumption has a relatively small effect, and that the Boussinesq approximation is the more important source of error in applying model N1 to G.C.O.S. data.

Table 2.14. Model N2 Performance for Group A Data Sets. R.M.S. Trajectory Errors versus Beta.

Date	Beta = 0.75	0.80	0.85	0.90	0.95
Jan. 25 1138-1235	0.159	0.122	0.091	0.070	0.070
Apr. 1 0859-1005	0.097	0.110	0.129	0.151	0.174
July 12 1400-1440	0.169	0.131	0.101	0.081	0.074
July 20 1935-2026	0.110	0.075	0.052	0.055	0.072
July 21 1618-1658	0.153	0.155	0.165	0.179	0.196
July 21 1954-2040	0.056	0.076	0.103	0.131	0.157
July 25 1545-1628	0.226	0.189	0.159	0.136	0.121
Oct. 18 1602-1634	0.214	0.169	0.131	0.099	0.076
Oct. 19 1616-1700	0.134	0.122	0.123	0.134	0.149
Oct. 20 1538-1612	0.306	0.258	0.216	0.179	0.147
Oct. 24 0930-1002	0.153	0.150	0.155	0.167	0.185
Oct. 24 1046-1120	0.141	0.139	0.145	0.157	0.173
Average	0.160	0.141	0.131	0.128	0.133

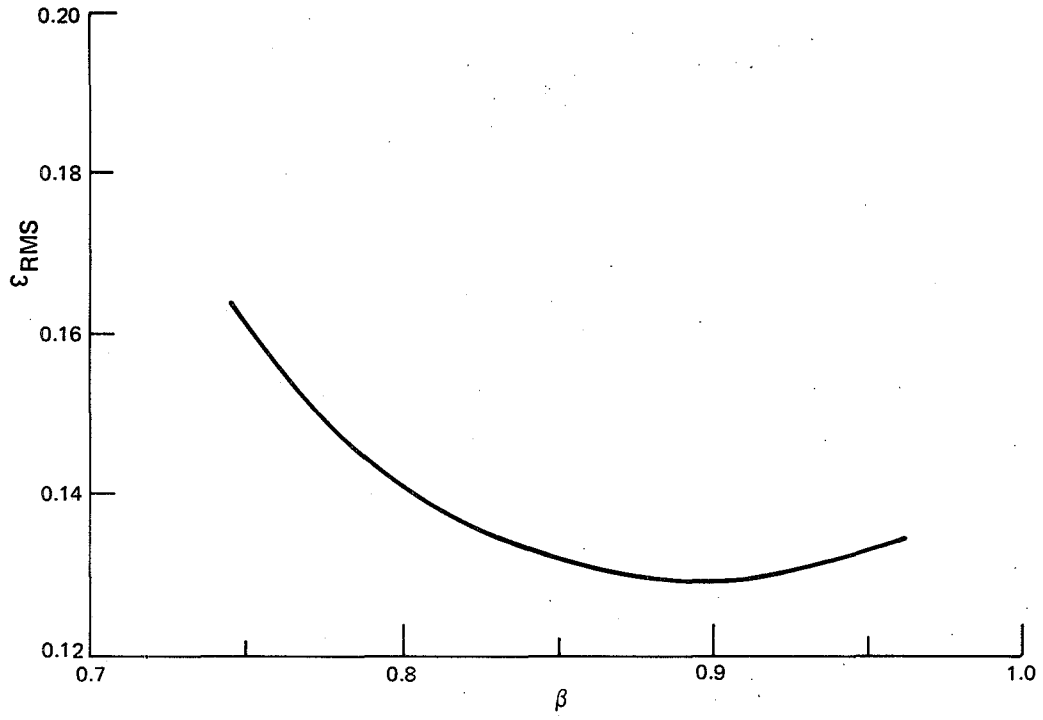

Figure 2.12. Model N2 average trajectory error for Group A data sets.

2.4.4.5 Model N3 Derivation. Model N3 consists of a numerical solution of the full set of conservation equations (2.1) to (2.9) without introducing either the Boussinesq or bent-over plume assumptions. With $C_D = 0$, the governing equations become

$$\frac{d}{dt}(\rho_p R^2 V) = 2\rho_a R V v_e \tag{2.74}$$

$$\frac{d}{dt}(\rho_p R^2 V v_x) = 2\rho_a R V v_e \tag{2.75}$$

$$\frac{d}{dt}(\rho_p R^2 V w) = g R^2 V (\rho_a - \rho_p) \tag{2.76}$$

$$\frac{d}{dt}[g R^2 V (\rho_a - \rho_p)] = -\rho_a N^2 R^2 V w \tag{2.77}$$

$$\frac{d}{dt}(\rho_p T_p) = -\frac{7}{2}\gamma_d \rho_a w \tag{2.78}$$

$$\frac{ds}{dt} = V \tag{2.79}$$

$$\frac{dz}{dt} = w \tag{2.80}$$

$$\frac{dx}{dt} = v_x \tag{2.81}$$

$$V^2 = v_x^2 + w^2 \tag{2.82}$$

which are solved numerically with the entrainment hypothesis

$$v_e = \beta |w|$$

and with the initial conditions (2.60) to (2.64) and (2.73).

An additional complication in this model is the requirement of specifying air density $\rho_a(z)$ from minisonde temperature profiles. Solution of the hydrostatic pressure law for an ideal gas layer exhibiting a linear temperature decrease with altitude, $\Gamma = -\frac{dT_a}{dz}$, yields:

$$\rho_a(z) = \rho_{a_o} \left(1 - \frac{\Gamma}{T_{a_o}} z\right)^{(g - R\Gamma)/R\Gamma} \tag{2.84}$$

where ρ_{a_o} and T_{a_o} are the density and temperature respectively at the bottom of the layer, and R is the ideal gas constant for air (R = 287J/kgK). Since the minisonde data gives Γ value appropriate to each layer, equation (2.84) can be applied layer by layer starting at the surface with

$$\rho_{a_o} = \frac{P_o}{RT_{a_o}} \tag{2.85}$$

Equation (2.85) suggests that surface pressure P_o must be known. In fact, it is easy to show that equations (2.74) to (2.82) are independent of P_o since the plume and atmosphere are assumed to be in pressure equilibrium throughout. Thus, standard surface pressure P_o = 101.325 KPa (or any other value) can be used in the numerical solution. While the actual magnitudes of $\rho_a(z)$ and $\rho_p(z)$ are in error, all other variables, which depend only on density ratios, remain unaffected.

2.4.4.6 Model N3 Performance.

Group A Data Sets. The performance of model N3 against Group A data sets is summarized in Table 2.15 and Figure 2.13. The minimum average ε_{RMS} of 12.9% occurs at $\beta = 0.62$, which is comparable with the performance of models A1 and A3. Model N3 with $\beta = 0.62$ predicts the trajectories of all twelve cases reasonably well, the worst error being about 19% for the October 20 case.

A typical plume outline plot from the tuned model N3 with $\beta = 0.62$ is compared with experimental data in Figure 2.14 where it is evident that both trajectory and rate of spread are well predicted. The claim made in section 2.4.4.3 that solutions of the full nine conservation equations with no further approximations, would lead to good results without the need for a fictitious drag term or an initial flux reduction, is supported by these results. Furthermore, by comparing models N2 and N3, the Boussinesq approximation can be identified as being more significant than the bent-over plume assumption for the G.C.O.S. plume.

Group B and C Data Sets. The performance of tuned model N3 against Group B and C data sets is summarizes in Tables 2.16 and 2.17. For Group B data sets, the average ε_{RMS} is about 17%, with the worst error being about 26% for the January 26 case. Model N3, therefore, handles wind speed shear and non-constant lapse conditions quite well,

Table 2.15. Model N3 Performance for Group A Data Sets. R.M.S. Trajectory Errors versus Beta.

Date	Beta = 0.50	0.55	0.60	0.65	0.70
Jan. 25	1138-1235	0.166	0.111	0.076	0.070	0.091
Apr. 1	0859-1005	0.106	0.121	0.150	0.181	0.212
July 12	1400-1440	0.200	0.144	0.103	0.083	0.088
July 20	1935-2026	0.146	0.088	0.053	0.057	0.088
July 21	1618-1658	0.160	0.152	0.163	0.184	0.208
July 21	1954-2040	0.069	0.067	0.098	0.135	0.170
July 25	1545-1628	0.259	0.204	0.161	0.133	0.120
Oct. 18	1602-1634	0.258	0.189	0.131	0.087	0.060
Oct. 19	1616-1700	0.158	0.129	0.129	0.143	0.167
Oct. 20	1538-1612	0.316	0.246	0.188	0.141	0.107
Oct. 24	0930-1002	0.163	0.150	0.159	0.179	0.203
Oct. 24	1046-1120	0.152	0.139	0.149	0.171	0.196
Average		0.179	0.145	0.130	0.133	0.143

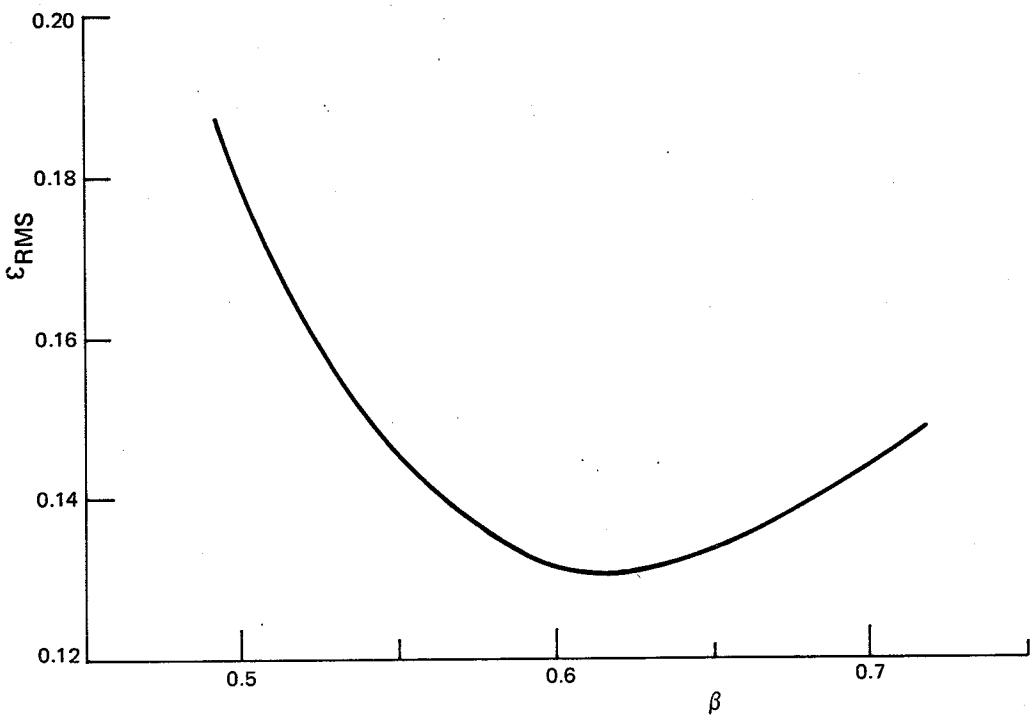

Figure 2.13. Model N3 average trajectory error for Group A data sets.

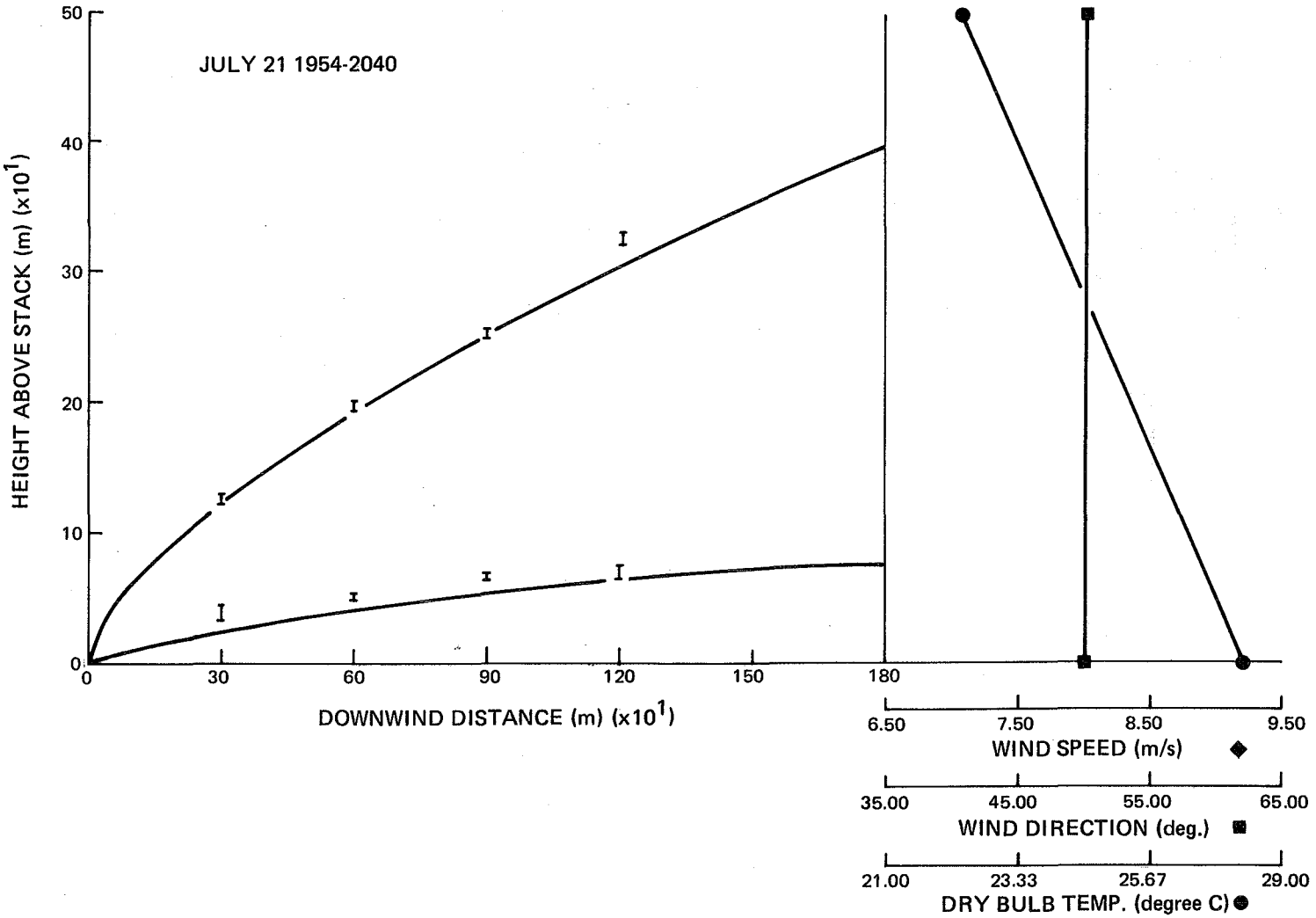

Figure 2.14. Comparison of Model N3 outline predictions (β = 0.62) with photographic data.

Table 2.16. Model N3 Performance for Group B Data Sets. R.M.S. Trajectory Errors for Beta = 0.62.

Date		Temp. Profile	Error
Jan. 26	1138-1212	Inv. at 600 m	0.264
Jan. 26	1316-1407	Inv. at 600 m	0.154
Mar. 30	0840-0934	Linear	0.121
Mar. 30	0918-0954	Linear	0.103
Apr. 1	0659-0758	Inv. at 620 m	0.252
July 13	1524-1614	Kink at 700 m	0.079
July 23	2116-2202	Linear	0.036
Oct. 17	1548-1624	Linear	0.151
Oct. 17	1626-1700	Linear	0.232
Oct. 19	0920-1011	Inv. at 270 m	0.088
Oct. 19	1110-1144	Inv. at 470 m	0.239
Oct. 20	0956-1032	Linear	0.226
Oct. 25	0918-0956	Kink at 500 m	0.175
Oct. 25	0958-1030	Inv. at 460 m	0.121
Oct. 25	1056-1137	Inv. at 350 m	0.196
Oct. 25	1546-1640	Inv. at 620 m	0.259
Oct. 27	1516-1548	Linear	0.177
Average			0.169

Table 2.17. Model N3 Performance for Group C Data Sets. R.M.S. Trajectory Errors for Beta = 0.62.

Date		Temp. Profile	Error
Jan. 25	1418-1455	Kink at 500 m	0.392
Jan. 25	1505-1545	Kink at 500 m	0.304
Mar. 28	1818-1852	Inv. at 320 m	0.349
July 15	0615-0700	Inv. at 210 m	0.452
July 15	1608-1652	Linear	0.321
July 18	0600-0623	Kink at 300 m	0.079
July 25	1630-1708	Linear	0.127
July 26	0615-0702	Inv. at 100 m	0.362
Average			0.298

performing only slightly worse for Group B data sets than for Group A data sets. Downwind rise predictions fall both above and below measured trajectories.

For Group C data sets, however, the performance of model N3 deterioriates. The average error increases to about 30%, with the worst case being about 45% for the July 15 case, and generally, downwind rise predictions fall below measured trajectories. These problems are attributed to the use of the bent-over plume entrainment hypothesis $v_e = \beta|w|$ for low windspeed conditions.

2.4.4.7 Model N4. Model N4 is identical to model N3 except that the entrainment hypothesis

$$v_e = \alpha\left|V - \frac{Uv_x}{V}\right| + \beta\left|\frac{Uw}{V}\right| \qquad (2.86)$$

is substituted into equations (2.74) to (2.82). Two entrainment constants α and β have to be fixed for this model. Morton and Taylor's work on jets with U = 0 suggest that $\alpha = 0.125$[9], while Briggs reports α values in the 0.08 to 0.155 range from previous studies, and recommends $\alpha = 0.10$ for a buoyant plume[2]. Guided by these results, the optimum β for model N4 will be sought by computing centerline trajectory errors for the four α values 0.05, 0.10, 0.15, and 0.20.

The performance of model N4 against Group A data sets is summarized in Table 2.18 a-d and Figures 2.15 a-d. For $\alpha = 0.05$, the minimum ε_{RMS} of 13.5% occurs with $\beta = 0.63$; for $\alpha = 0.10$, the minimum ε_{RMS} of 13.2% occurs with $\beta = 0.62$; for $\alpha = 0.15$, the minimum ε_{RMS} of 13.1% occurs with $\beta = 0.61$; and for $\alpha = 0.20$, the minimum ε_{RMS} of 13.0% occurs with $\beta = 0.60$. Model N4, therefore, predicts Group A trajectories about as well as model N3. While $\alpha = 0.20$ is slightly better than the smaller α values for Group A conditions, the model is insensitive to the actual value of α used within the range tested. Trajectories for all twelve Group A cases are predicted reasonably well, the worst error being of the order of 18%.

A typical tuned N4 outline prediction with $\alpha = 0.05$, $\beta = 0.63$ is compared with measurements in Figure 2.16, where it is evident that both trajectory and rate of spread are well represented.

Group B and C Data Sets. The performance of model N4 for Group B and C data sets is summarized in Tables 2.19 and 2.20. For Group B conditions, the average error of approximately 16% is essentially independent of α for the four optimum α,β combinations given above. For Group C conditions, however, the average error increases, and also becomes a function of α. The optimum ε_{RMS} is about 20% and occurs with the $\alpha = 0.05$, $\beta = 0.63$ combination, while the worst error is about 33% for the July 15 morning case. Model N4, with the v_e hypothesis of equation (2.86), accordingly gives the best low windspeed

Table 2.18A. Model N4 Performance for Group A Data Sets. R.M.S. Trajectory Errors versus Beta. Alpha = 0.05.

Date	Beta =	0.55	0.60	0.65	0.70	0.75
Jan. 25	1138-1235	0.146	0.099	0.071	0.073	0.096
Apr. 1	0859-1005	0.091	0.115	0.148	0.181	0.212
July 12	1400-1440	0.140	0.101	0.083	0.089	0.110
July 20	1935-2026	0.095	0.055	0.055	0.083	0.116
July 21	1618-1658	0.152	0.165	0.188	0.212	0.238
July 21	1954-2040	0.065	0.097	0.134	0.170	0.203
July 25	1545-1628	0.278	0.217	0.168	0.129	0.104
Oct. 18	1602-1634	0.186	0.129	0.084	0.059	0.064
Oct. 19	1616-1700	0.131	0.131	0.149	0.174	0.201
Oct. 20	1538-1612	0.267	0.206	0.155	0.116	0.092
Oct. 24	0930-1002	0.158	0.170	0.193	0.218	0.243
Oct. 24	1046-1120	0.148	0.166	0.191	0.218	0.244
Average		0.155	0.138	0.135	0.144	0.160

Table 2.18B. Model N4 Performance for Group A Data Sets. R.M.S. Trajectory Errors versus Beta. Alpha = 0.10.

Date		Beta = 0.55	0.60	0.65	0.70	0.75
Jan. 25	1138-1235	0.122	0.083	0.068	0.081	0.107
Apr. 1	0859-1005	0.105	0.133	0.164	0.196	0.225
July 12	1400-1440	0.130	0.096	0.084	0.094	0.116
July 20	1935-2026	0.081	0.051	0.061	0.092	0.124
July 21	1618-1658	0.154	0.168	0.190	0.216	0.241
July 21	1954-2040	0.073	0.106	0.142	0.177	0.209
July 25	1545-1628	0.237	0.186	0.145	0.116	0.102
Oct. 18	1602-1634	0.174	0.120	0.078	0.056	0.065
Oct. 19	1616-1700	0.131	0.133	0.152	0.177	0.201
Oct. 20	1538-1612	0.245	0.188	0.142	0.108	0.086
Oct. 24	0930-1002	0.157	0.172	0.195	0.220	0.245
Oct. 24	1046-1120	0.150	0.169	0.195	0.221	0.247
Average		0.147	0.134	0.135	0.146	0.164

Table 2.18C. Model N4 Performance for Group A Data Sets. R.M.S. Trajectory Errors versus Beta. Alpha = 0.15.

Date	Beta = 0.55	0.60	0.65	0.70	0.75
Jan. 25 1138-1235	0.103	0.073	0.070	0.090	0.117
Apr. 1 0859-1005	0.120	0.149	0.180	0.209	0.236
July 12 1400-1440	0.121	0.093	0.085	0.099	0.121
July 20 1935-2026	0.070	0.050	0.069	0.100	0.132
July 21 1618-1658	0.155	0.171	0.194	0.219	0.244
July 21 1954-2040	0.080	0.114	0.149	0.183	0.214
July 25 1545-1628	0.206	0.163	0.130	0.110	0.104
Oct. 18 1602-1634	0.163	0.111	0.072	0.055	0.068
Oct. 19 1616-1700	0.132	0.136	0.155	0.178	0.204
Oct. 20 1538-1812	0.226	0.173	0.131	0.100	0.085
Oct. 24 0930-1002	0.158	0.174	0.198	0.223	0.248
Oct. 24 1046-1120	0.153	0.170	0.198	0.225	0.251
Average	0.141	0.131	0.136	0.149	0.169

Table 2.18D. Model N4 Performance for Group A Data Sets. R.M.S. Trajectory Errors versus Beta. Alpha = 0.20.

Date	Beta =	0.55	0.60	0.65	0.70	0.75
Jan. 25	1138-1235	0.089	0.069	0.077	0.100	0.128
Apr. 1	0859-1005	0.135	0.163	0.193	0.221	0.247
July 12	1400-1440	0.114	0.090	0.088	0.103	0.126
July 20	1935-2026	0.062	0.049	0.076	0.108	0.139
July 21	1618-1658	0.157	0.174	0.197	0.221	0.246
July 21	1954-2040	0.087	0.121	0.156	0.189	0.219
July 25	1545-1628	0.181	0.146	0.121	0.109	0.110
Oct. 18	1602-1634	0.153	0.103	0.066	0.054	0.070
Oct. 19	1616-1700	0.130	0.138	0.158	0.180	0.207
Oct. 20	1538-1612	0.209	0.160	0.121	0.095	0.085
Oct. 24	0930-1002	0.159	0.177	0.200	0.225	0.250
Oct. 24	1046-1120	0.155	0.173	0.199	0.229	0.254
Average		0.136	0.130	0.138	0.153	0.173

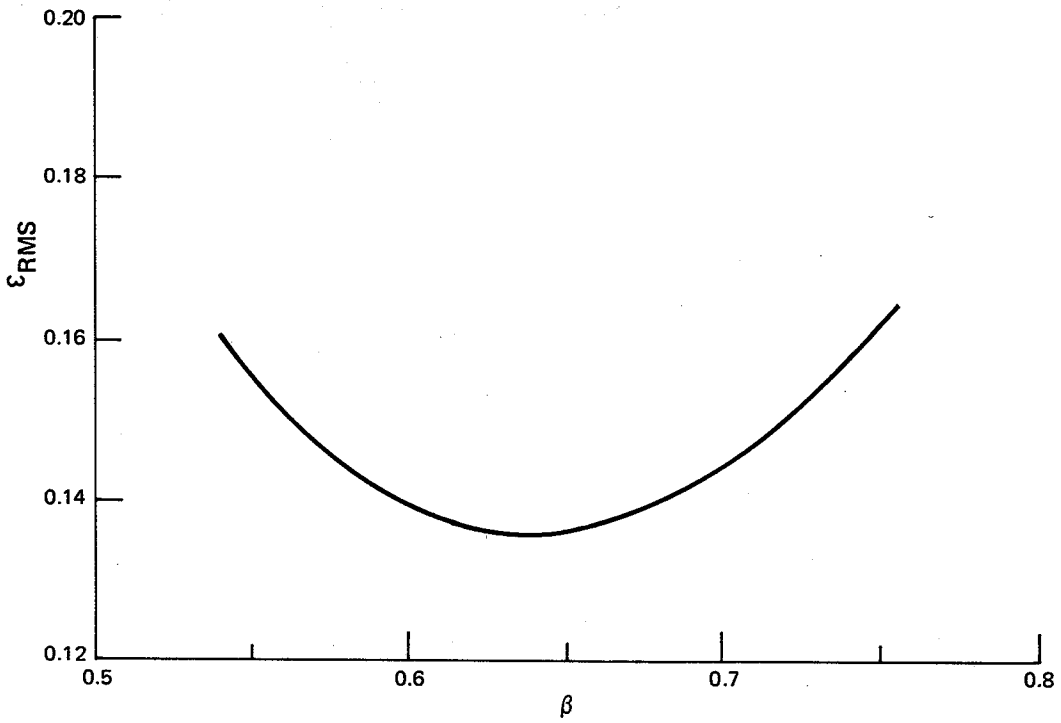

Figure 2.15a. Model N4 average trajectory error for Group A sets with α = 0.05.

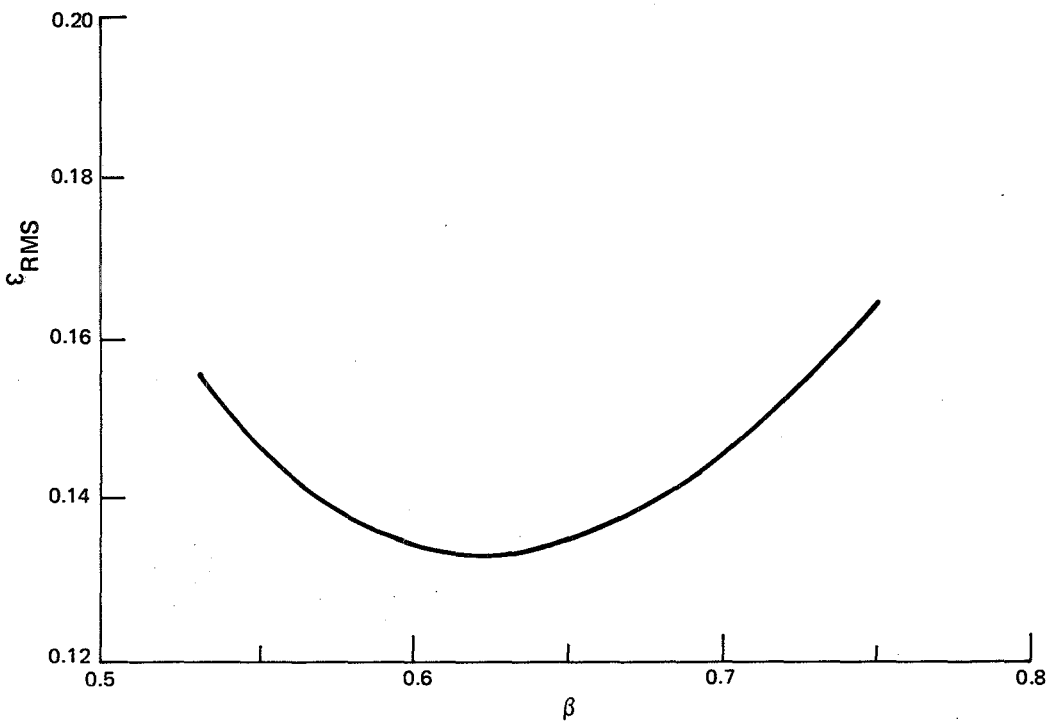

Figure 2.15b. Model N4 average trajectory error for Group A data sets with α = 0.10.

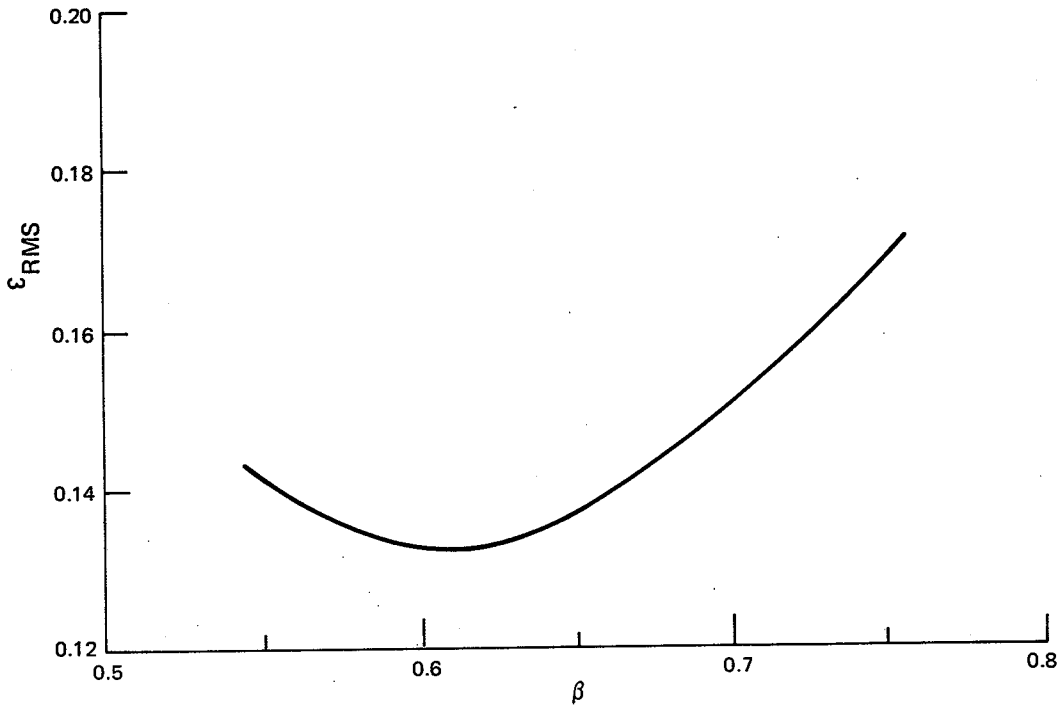

Figure 2.15c. Model N4 average trajectory error for Group A sets with $\alpha = 0.15$.

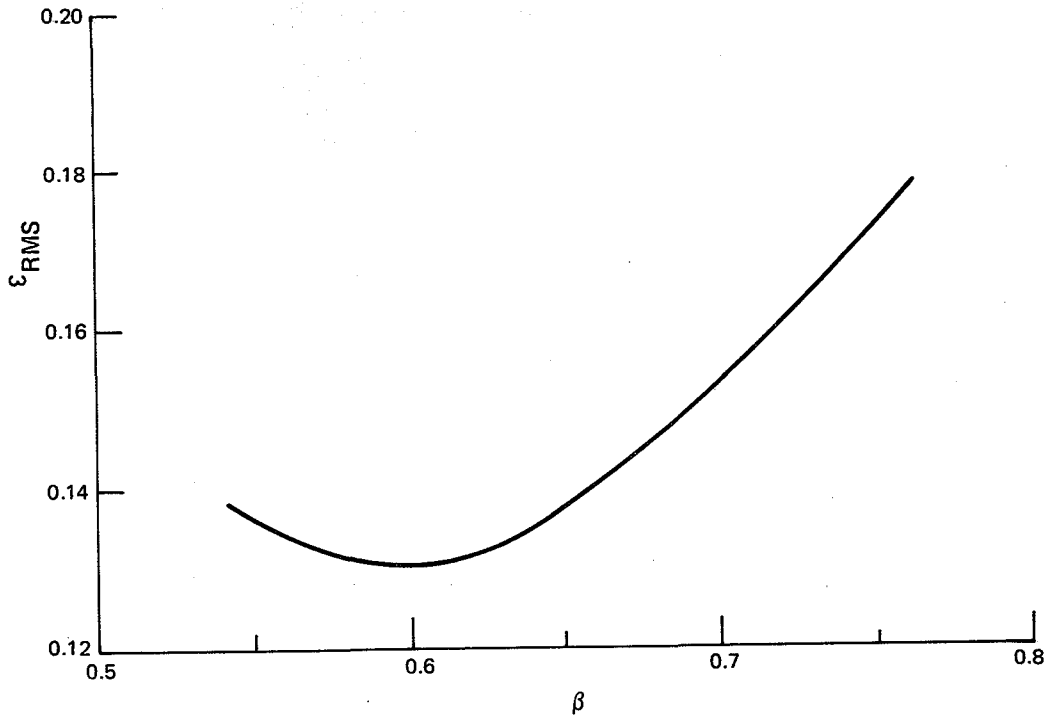

Figure 2.15d. Model N4 average trajectory error for Group A data sets with α = 0.20.

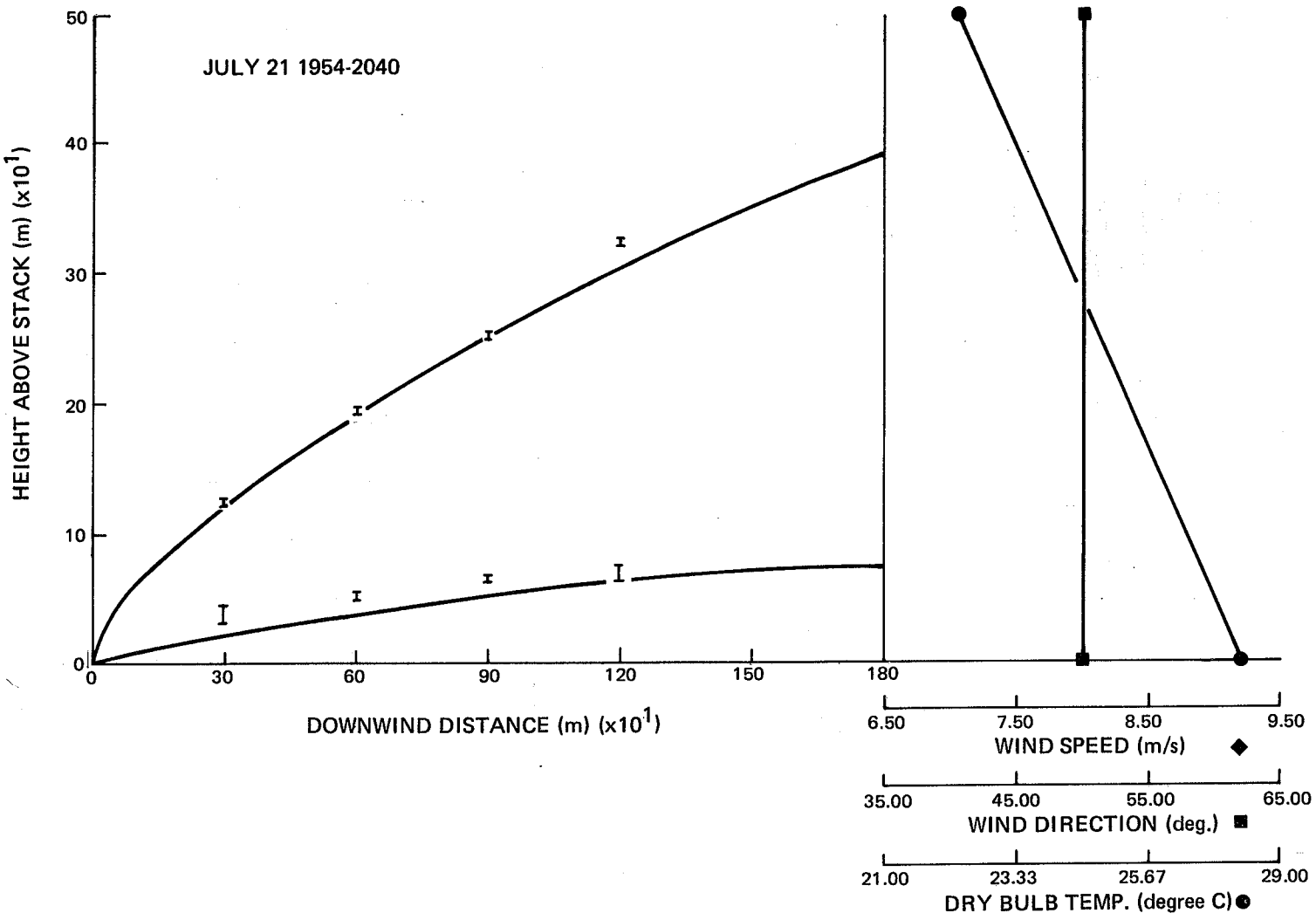

Figure 2.16. Comparison of Model N4 outline predictions (α = 0.05, β = 0.63) with photographic data.

Table 2.19. Model N4 Performance for Group B Data Sets. R.M.S. Trajectory Errors for Optimum Alpha,Beta Combinations.

Date		Temp. Profile	Alpha = 0.05 Beta = 0.63	0.10 0.62	0.15 0.61	0.20 0.60
Jan. 26	1138-1212	Inv. at 600 m	0.253	0.260	0.268	0.274
Jan. 26	1316-1407	Inv. at 600 m	0.127	0.133	0.140	0.152
Mar. 30	0840-0934	Linear	0.097	0.106	0.114	0.119
Mar. 30	0918-0954	Linear	0.077	0.085	0.092	0.097
Apr. 1	0659-0758	Inv. at 620 m	0.252	0.254	0.255	0.256
July 13	1524-1614	Kink at 700 m	0.093	0.086	0.083	0.083
July 23	2116-2202	Linear	0.078	0.062	0.048	0.037
Oct. 17	1548-1624	Linear	0.128	0.128	0.127	0.127
Oct. 17	1626-1700	Linear	0.210	0.217	0.225	0.234
Oct. 19	0920-1011	Inv. at 270 m	0.086	0.090	0.095	0.100
Oct. 19	1110-1144	Inv. at 470 m	0.244	0.229	0.220	0.211
Oct. 20	0956-1032	Linear	0.180	0.178	0.178	0.177
Oct. 25	0918-0956	Kink at 500 m	0.154	0.148	0.144	0.141
Oct. 25	0958-1030	Inv. at 460 m	0.131	0.110	0.110	0.111
Oct. 25	1056-1137	Inv. at 350 m	0.164	0.175	0.187	0.196
Oct. 25	1546-1640	Inv. at 620 m	0.227	0.226	0.226	0.224
Oct. 27	1516-1548	Linear	0.164	0.166	0.168	0.167
Average			0.156	0.156	0.158	0.159

Table 2.20. Model N4 Performance for Group C Data Sets. R.M.S. Trajectory Errors for Optimum Alpha,Beta Combinations.

Date		Temp. Profile	Alpha = 0.05 Beta = 0.63	0.10 0.62	0.15 0.61	0.20 0.60
Jan. 25	1418-1455	Kink at 500 m	0.221	0.261	0.297	0.324
Jan. 25	1505-1545	Kink at 500 m	0.131	0.153	0.176	0.201
Mar. 28	1818-1852	Inv. at 320 m	0.198	0.233	0.256	0.279
July 15	0615-0700	Inv. at 210 m	0.344	0.353	0.389	0.408
July 15	1608-1652	Linear	0.266	0.283	0.298	0.311
July 18	0600-0623	Kink at 300 m	0.074	0.080	0.086	0.092
July 25	1630-1708	Linear	0.070	0.076	0.090	0.107
July 26	0615-0702	Inv. at 100 m	0.309	0.320	0.332	0.344
Average			0.201	0.220	0.241	0.258

predictions of all models tested to this point in the report. This improvement can be attributed to the more complete physics contained in model N4; that is, in addition to including all conservation laws without further approximation, model N4 has an entrainment hypothesis which allows both jet-like and plume-like behavior to occur. As is illustrated in Figure 2.17, such an entrainment hypothesis leads to a more realistic plume prediction under low windspeed conditions.

A weighted average of Group A, B, and C results suggests that the $\alpha = 0.05$, $\beta = 0.63$ combination should be chosen to give best overall performance.

2.4.4.8 Model N5. Model N5 is similar to model N4 except that the two entrainment terms are added as a vector sum. Accordingly, this model is based on equations (2.74) to (2.82) with the entrainment hypothesis

$$v_e = \{\alpha^2 \left(V - U \frac{v_x}{V}\right)^2 + \beta^2 \left(\frac{Uw}{V}\right)^2\}^{1/2} \qquad (2.87)$$

The optimum β is sought by trajectory fits to Group A data for $\alpha = 0.05$, 0.10, 0.15, and 0.20.

The performance of model N5 against Group A data sets is summarized in Tables 2.21 a-d and Figures 2.18 a-d, where it is evident

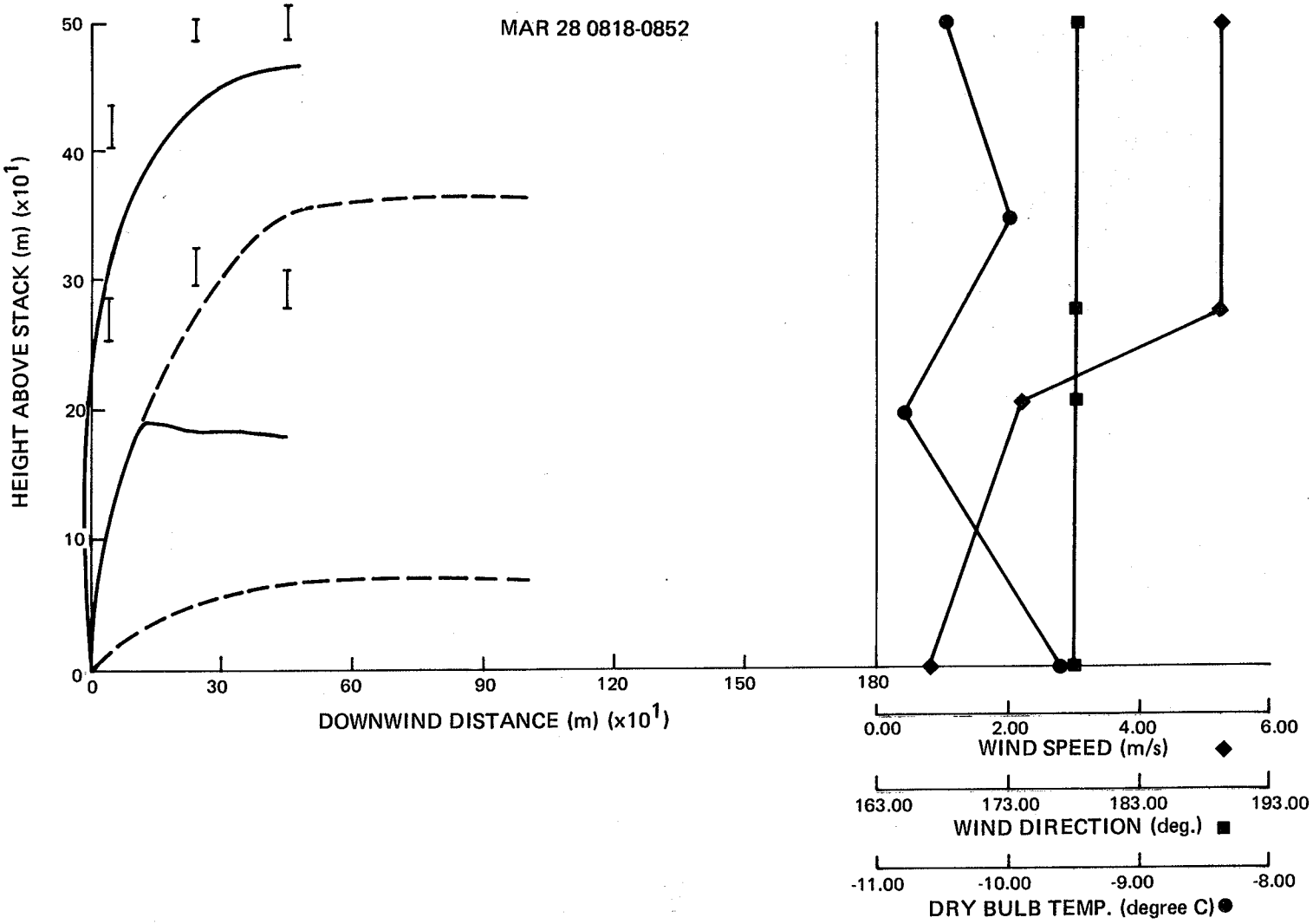

Figure 2.17. Comparison of low windspeed case outline predictions with photographic data.

Table 2.21A. Model N5 Performance for Group A Data Sets. R.M.S. Trajectory Errors versus Beta. Alpha = 0.05.

Date		Beta = 0.55	0.60	0.65	0.70	0.75
Jan. 25	1138-1235	0.177	0.120	0.081	0.070	0.086
Apr. 1	0859-1005	0.080	0.097	0.130	0.164	0.197
July 12	1400-1440	0.153	0.107	0.083	0.085	0.105
July 20	1935-2026	0.112	0.064	0.050	0.075	0.108
July 21	1618-1658	0.152	0.163	0.184	0.209	0.235
July 21	1954-2040	0.059	0.088	0.126	0.163	0.197
July 25	1545-1628	0.329	0.258	0.199	0.151	0.115
Oct. 18	1602-1634	0.199	0.140	0.092	0.062	0.062
Oct. 19	1616-1700	0.132	0.132	0.146	0.171	0.198
Oct. 20	1538-1612	0.292	0.225	0.171	0.126	0.096
Oct. 24	0930-1002	0.157	0.168	0.191	0.216	0.241
Oct. 24	1046-1120	0.146	0.163	0.188	0.214	0.240
Average		0.166	0.144	0.137	0.142	0.157

Table 2.21B. Model N5 Performance for Group A Data Sets. R.M.S. Trajectory Errors versus Beta. Alpha = 0.10.

Date	Beta = 0.55	0.60	0.65	0.70	0.75
Jan. 25 1138-1235	0.172	0.117	0.080	0.070	0.086
Apr. 1 0859-1005	0.082	0.099	0.132	0.166	0.199
July 12 1400-1440	0.152	0.107	0.083	0.085	0.105
July 20 1935-2026	0.110	0.063	0.050	0.075	0.109
July 21 1618-1658	0.152	0.163	0.184	0.209	0.235
July 21 1954-2040	0.060	0.088	0.127	0.164	0.197
July 25 1545-1628	0.319	0.251	0.194	0.148	0.113
Oct. 18 1602-1634	0.199	0.139	0.091	0.062	0.062
Oct. 19 1616-1700	0.132	0.132	0.146	0.171	0.198
Oct. 20 1538-1612	0.290	0.224	0.169	0.125	0.096
Oct. 24 0930-1002	0.157	0.168	0.191	0.216	0.241
Oct. 24 1046-1120	0.146	0.163	0.181	0.214	0.240
Average	0.164	0.143	0.136	0.142	0.157

Table 2.21C. Model N5 Performance for Group A Data Sets. R.M.S. Trajectory Errors versus Beta. Alpha = 0.15.

Date	Beta = 0.55	0.60	0.65	0.70	0.75
Jan. 25 1138-1235	0.166	0.113	0.077	0.070	0.088
Apr. 1 0859-1005	0.085	0.103	0.135	0.169	0.201
July 12 1400-1440	0.151	0.106	0.083	0.086	0.106
July 20 1935-2026	0.108	0.062	0.051	0.076	0.109
July 21 1618-1658	0.152	0.163	0.185	0.209	0.235
July 21 1954-2040	0.061	0.090	0.128	0.165	0.198
July 25 1545-1628	0.306	0.242	0.187	0.144	0.112
Oct. 18 1602-1634	0.197	0.138	0.091	0.062	0.062
Oct. 19 1616-1700	0.133	0.129	0.146	0.171	0.198
Oct. 20 1538-1612	0.286	0.221	0.168	0.124	0.095
Oct. 24 0930-1002	0.157	0.168	0.191	0.216	0.241
Oct. 24 1046-1120	0.146	0.163	0.188	0.215	0.241
Average	0.162	0.142	0.136	0.142	0.157

Table 2.21D. Model N5 Performance for Group A Data Sets. R.M.S. Trajectory Errors versus Beta. Alpha = 0.20.

Date		Beta = 0.55	0.60	0.65	0.70	0.75
Jan. 25	1138-1235	0.159	0.108	0.075	0.070	0.089
Apr. 1	0859-1005	0.088	0.108	0.140	0.172	0.204
July 12	1400-1440	0.149	0.105	0.083	0.086	0.106
July 20	1935-2026	0.106	0.060	0.051	0.077	0.111
July 21	1618-1658	0.152	0.163	0.185	0.210	0.235
July 21	1954-2040	0.062	0.091	0.129	0.165	0.198
July 25	1545-1628	0.292	0.231	0.181	0.140	0.110
Oct. 18	1602-1634	0.196	0.137	0.090	0.061	0.062
Oct. 19	1616-1700	0.133	0.129	0.147	0.172	0.198
Oct. 20	1538-1612	0.281	0.218	0.165	0.123	0.095
Oct. 24	0930-1002	0.157	0.168	0.191	0.216	0.241
Oct. 24	1046-1120	0.146	0.163	0.188	0.215	0.241
Average		0.160	0.140	0.135	0.142	0.158

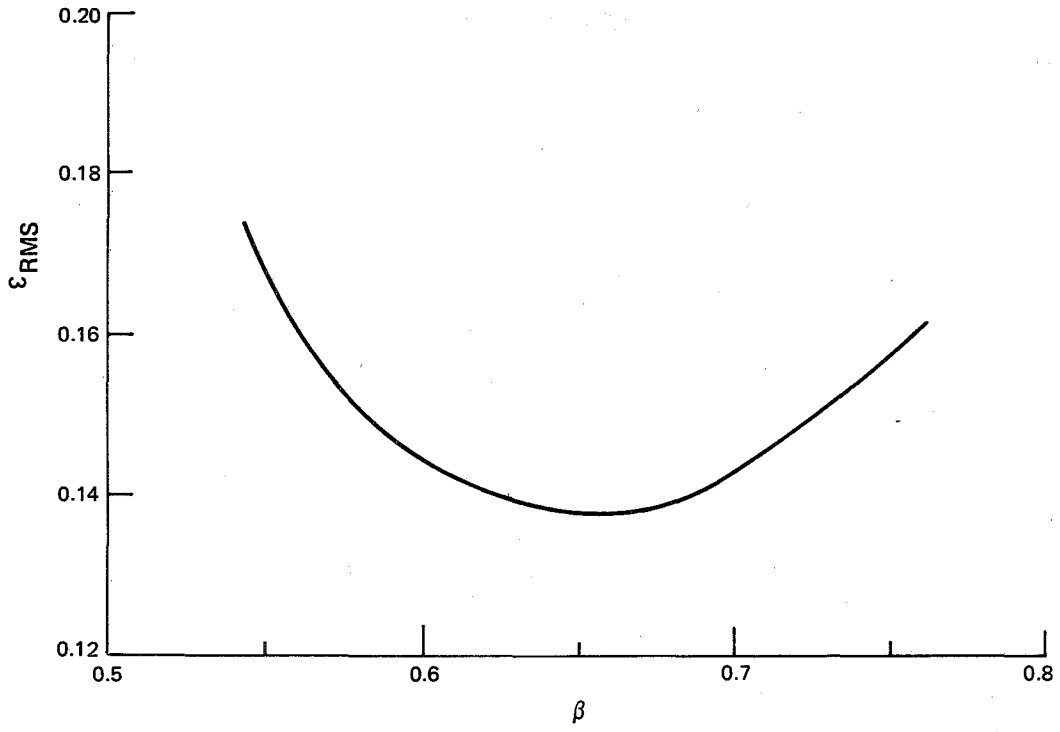

Figure 2.18a. Model N5 average trajectory error for Group A data sets with $\alpha = 0.05$.

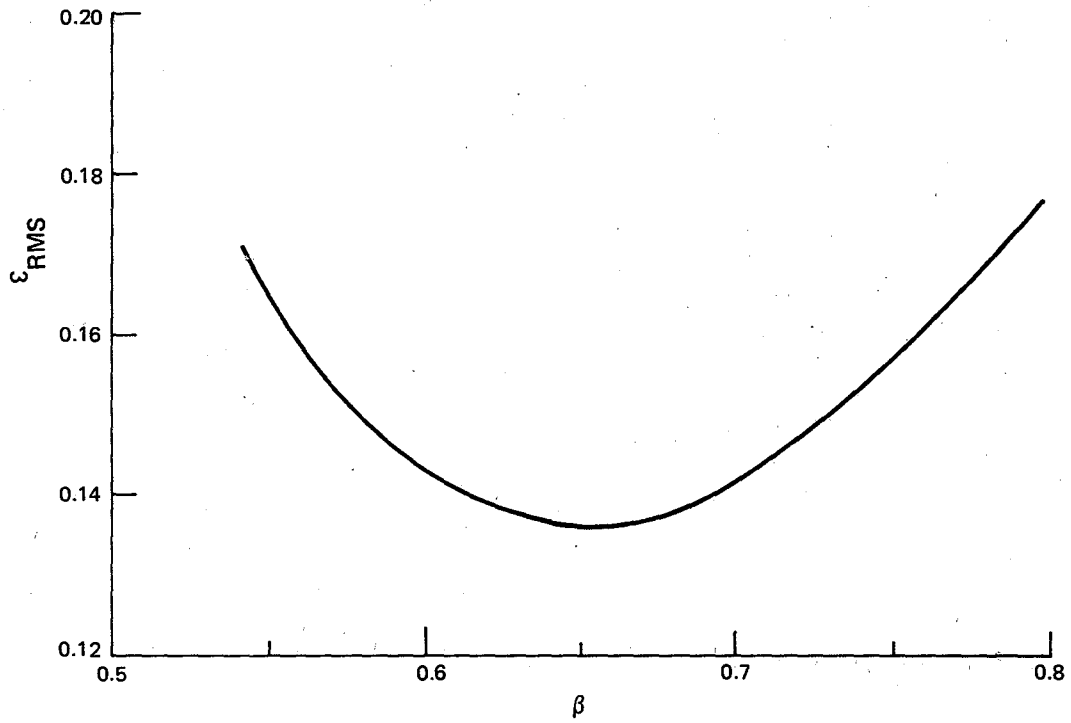

Figure 2.18b. Model N5 average trajectory error for Group A data sets with $\alpha = 0.10$.

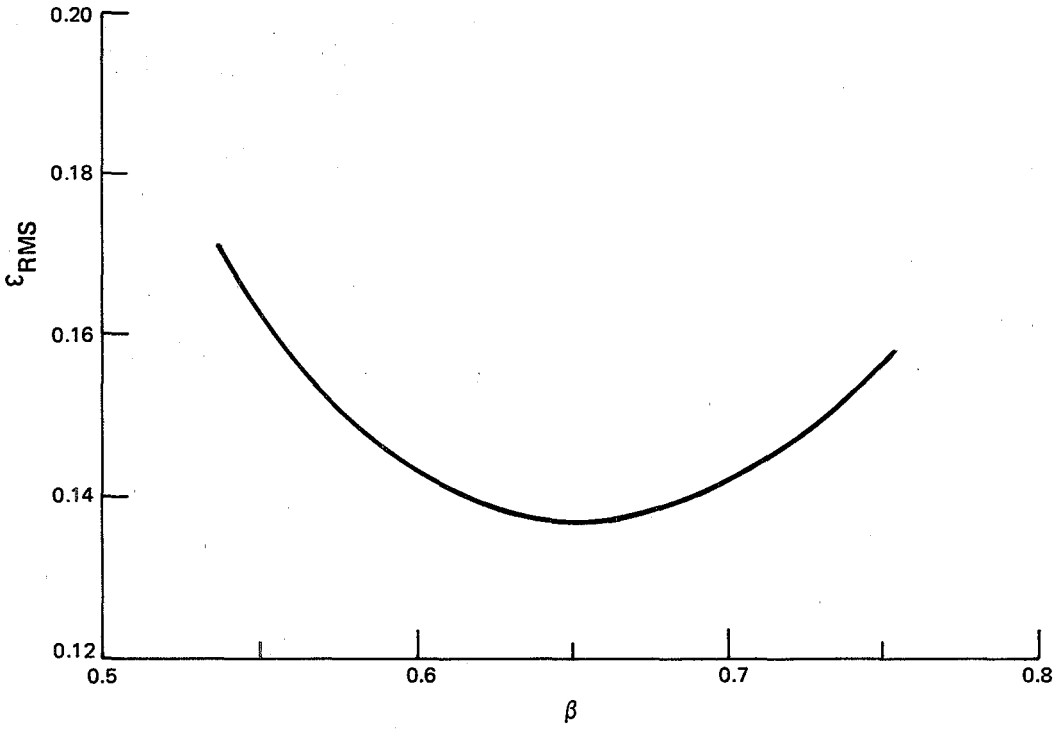

Figure 2.18c. Model N5 average trajectory error for Group A data sets with $\alpha = 0.15$.

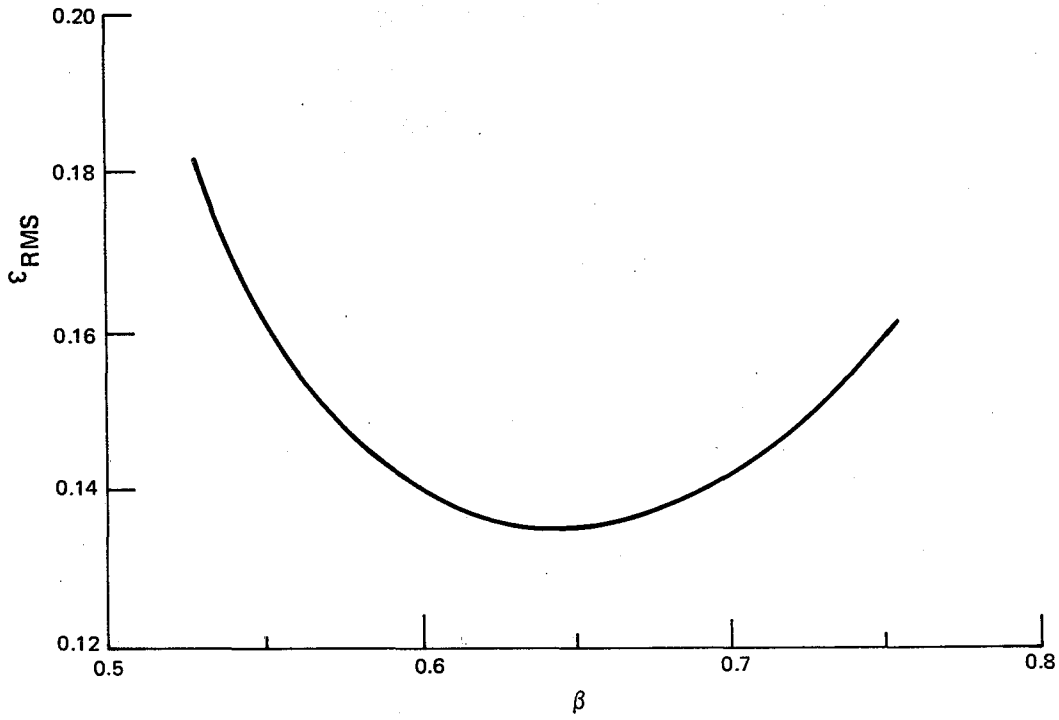

Figure 2.18d. Model NS average trajectory error for Group A data sets with α = 0.20.

that the minimum average error of about 14% occurs at $\beta = 0.65$ for all values of α tested. The trajectories of all twelve Group A cases are predicted quite well, the worst error being of the order of 20%.

Group B and C Data Sets. The performance of the tuned model N5 against Group B and C data sets for the four α,β combinations given above is summarizes in Tables 2.22 and 2.23. Group B results indicate that the average error of about 15% is nearly independent of α, while Group C results suggest that the $\alpha = 0.05$, $\beta = 0.65$ combination, which leads to an average ε_{RMS} of about 18%, is the best choice for the model. Model N5 leads to Group A predictions comparable to those of model N4, but gives slightly better Group B and C predictions. It is therefore concluded that the vector sum of equation (2.87) represents an improvement over the arithmetic sum of equation (2.86).

Based on a weighted average of Group A, B, and C performances, the optimum combination for model N5 is selected as $\alpha = 0.05$, $\beta = 0.65$.

2.4.4.9 Model N6. Model N6 follows from model N3 by introducing the entrainment hypothesis

$$v_e = \alpha \left| V - \frac{Uv_x}{V} \right| + \beta \frac{v_x}{V} \left| \frac{Uw}{V} \right| \qquad (2.88)$$

Table 2.22. Model N5 Performance for Group B Data Sets. R.M.S. Trajectory Errors for Optimum Alpha,Beta Combinations.

Date		Temp. Profile	Alpha = 0.05 Beta = 0.65	0.10 0.65	0.15 0.65	0.20 0.64
Jan. 26	1138-1212	Inv. at 600 m	0.250	0.250	0.253	0.253
Jan. 26	1316-1407	Inv. at 600 m	0.123	0.124	0.126	0.125
Mar. 30	0840-0934	Linear	0.096	0.098	0.098	0.097
Mar. 30	0918-0954	Linear	0.073	0.076	0.079	0.079
Apr. 1	0659-0758	Inv. at 620 m	0.256	0.257	0.258	0.253
July 13	1524-1614	Kink at 700 m	0.100	0.098	0.095	0.094
July 23	2116-2202	Linear	0.089	0.084	0.078	0.078
Oct. 17	1548-1624	Linear	0.120	0.119	0.118	0.126
Oct. 17	1626-1700	Linear	0.193	0.192	0.192	0.202
Oct. 19	0920-1011	Inv. at 270 m	0.087	0.087	0.084	0.084
Oct. 19	1110-1144	Inv. at 470 m	0.253	0.249	0.242	0.242
Oct. 20	0956-1032	Linear	0.174	0.173	0.172	0.179
Oct. 25	0918-0956	Kink at 500 m	0.157	0.155	0.152	0.154
Oct. 25	0958-1030	Inv. at 460 m	0.114	0.113	0.111	0.112
Oct. 25	1056-1137	Inv. at 350 m	0.158	0.156	0.161	0.162
Oct. 25	1546-1640	Inv. at 620 m	0.226	0.224	0.223	0.230
Oct. 27	1516-1548	Linear	0.161	0.161	0.161	0.163
Average			0.155	0.154	0.153	0.155

Table 2.23. Model N5 Performance for Group C Data Sets. R.M.S. Trajectory Errors for Optimum Alpha,Beta Combinations.

Date		Temp. Profile	Alpha = 0.05 Beta = 0.65	0.10 0.65	0.15 0.65	0.20 0.64
Jan. 25	1418-1455	Kink at 500 m	0.187	0.199	0.220	0.240
Jan. 25	1505-1545	Kink at 500 m	0.121	0.127	0.139	0.149
Mar. 28	1818-1852	Inv. at 320 m	0.165	0.190	0.212	0.226
July 15	0615-0700	Inv. at 210 m	0.187	0.307	0.332	0.344
July 15	1608-1652	Linear	0.252	0.257	0.264	0.265
July 18	0600-0623	Kink at 300 m	0.073	0.074	0.074	0.075
July 25	1630-1708	Linear	0.075	0.073	0.071	0.074
July 26	0615-0702	Inv. at 100 m	0.294	0.299	0.308	0.304
Average			0.182	0.191	0.202	0.210

into equations (2.74) to (2.82) to force only jet-like entrainment to occur near the source. Similar to model N4, the optimum β is sought by trajectory fits to Group A data for α = 0.05, 0.10, 0.15, and 0.20.

The performance of model N6 against Group A data sets is summarized in Tables 2.24 a-d, and Figures 2.19 a-d. For α = 0.05, the minimum average ε_{RMS} of 16.4% occurs with β = 0.78; for α = 0.10, the minimum ε_{RMS} of 14.6% occurs with β = 0.73; for α = 0.15, the minimum ε_{RMS} of 13.8% occurs with β = 0.68; and for α = 0.20, the minimum ε_{RMS} of 13.3% occurs with β = 0.66. The trajectories of all twelve Group A data sets are predicted reasonably well; for example, for the α = 0.1, β = 0.73 combination, the worst error is about 21%.

A typical tuned N6 outline prediction using α = 0.1, β = 0.73 is compared with measurements in Figure 2.20. Both trajectory and rate of spread are predicted reasonably well by this model.

Group B and C Data Sets. The performance of the tuned model N6 for Group B and C data sets using the four α,β combinations given above is summarized in Tables 2.25 and 2.26. For Group B conditions, the minimum ε_{RMS} of about 16% occurs approximately for $0.1 \leq \alpha \leq 0.2$, while, for Group C conditions, the minimum ε_{RMS} of about 16% occurs with the α = 0.1, β = 0.73 combination. A weighted average of Group A, B, and C results suggests that the α = 0.15, β = 0.68 combination is the best choice for overall optimum performance.

Table 2.24A. Model N6 Performance for Group A Data Sets. R.M.S. Trajectory Errors versus Beta. Alpha = 0.05.

Date	Beta =	0.65	0.70	0.75	0.80	0.85
Jan. 25	1138-1235	0.258	0.210	0.172	0.149	0.135
Apr. 1	0859-1005	0.089	0.066	0.072	0.097	0.126
July 12	1400-1440	0.196	0.144	0.098	0.062	0.042
July 20	1935-2026	0.169	0.132	0.103	0.099	0.109
July 21	1618-1658	0.162	0.170	0.185	0.205	0.226
July 21	1954-2040	0.029	0.070	0.109	0.144	0.176
July 25	1545-1628	0.510	0.437	0.372	0.315	0.263
Oct. 18	1602-1634	0.180	0.139	0.111	0.100	0.104
Oct. 19	1616-1700	0.108	0.121	0.148	0.176	0.202
Oct. 20	1538-1612	0.331	0.273	0.223	0.182	0.148
Oct. 24	0930-1002	0.158	0.180	0.204	0.231	0.254
Oct. 24	1046-1120	0.158	0.182	0.208	0.232	0.259
Average		0.196	0.177	0.167	0.166	0.170

Table 2.24B. Model N6 Performance for Group A Data Sets. R.M.S. Trajectory Errors versus Beta. A = 0.10.

Date	Beta = 0.55	0.60	0.65	0.70	0.75
Jan. 25	1138-1235	0.264	0.207	0.161	0.127	0.107
Apr. 1	0859-1005	0.096	0.059	0.057	0.083	0.115
July 12	1400-1440	0.246	0.185	0.133	0.090	0.058
July 20	1935-2026	0.196	0.145	0.104	0.081	0.080
July 21	1618-1658	0.167	0.157	0.163	0.179	0.199
July 21	1954-2040	0.049	0.032	0.067	0.106	0.142
July 25	1545-1628	0.468	0.397	0.334	0.277	0.226
Oct. 18	1602-1634	0.250	0.191	0.143	0.108	0.089
Oct. 19	1616-1700	0.127	0.111	0.116	0.139	0.165
Oct. 20	1538-1612	0.377	0.310	0.251	0.201	0.159
Oct. 24	0930-1002	0.151	0.151	0.168	0.191	0.216
Oct. 24	1046-1120	0.139	0.144	0.165	0.194	0.219
Average		0.211	0.174	0.155	0.148	0.148

Table 2.24C. Model N6 Performance for Group A Data Sets. R.M.S. Trajectory Errors versus Beta. Alpha = 0.15.

Date	Beta = 0.55	0.60	0.65	0.70	0.75
Jan. 25 1138-1235	0.201	0.152	0.114	0.092	0.088
Apr. 1 0859-1005	0.066	0.064	0.088	0.119	0.150
July 12 1400-1440	0.204	0.149	0.104	0.070	0.055
July 20 1935-2026	0.154	0.106	0.075	0.067	0.083
July 21 1618-1658	0.158	0.156	0.168	0.186	0.208
July 21 1954-2040	0.039	0.053	0.090	0.127	0.161
July 25 1545-1628	0.361	0.302	0.248	0.201	0.159
Oct. 18 1602-1634	0.223	0.167	0.123	0.092	0.079
Oct. 19 1616-1700	0.124	0.116	0.126	0.148	0.174
Oct. 20 1538-1612	0.323	0.161	0.209	0.165	0.128
Oct. 24 0930-1002	0.148	0.155	0.174	0.198	0.223
Oct. 24 1046-1120	0.137	0.150	0.173	0.198	0.227
Average	0.178	0.153	0.141	0.139	0.145

Table 2.24D. Model N6 Performance for Group A Data Sets. R.M.S. Trajectory Errors versus Beta. Alpha = 0.20.

Date	Beta = 0.55	0.60	0.65	0.70	0.75
Jan. 25 1138-1235	0.159	0.116	0.088	0.078	0.088
Apr. 1 0859-1005	0.071	0.088	0.117	0.147	0.176
July 12 1400-1440	0.176	0.126	0.088	0.063	0.063
July 20 1935-2026	0.125	0.081	0.060	0.068	0.092
July 21 1618-1658	0.155	0.158	0.173	0.193	0.215
July 21 1954-2040	0.044	0.070	0.106	0.141	0.174
July 25 1545-1628	0.294	0.242	0.196	0.155	0.121
Oct. 18 1602-1634	0.203	0.150	0.109	0.082	0.075
Oct. 19 1616-1700	0.123	0.117	0.132	0.155	0.181
Oct. 20 1538-1612	0.282	0.229	0.181	0.141	0.109
Oct. 24 0930-1002	0.148	0.159	0.179	0.203	0.229
Oct. 24 1046-1120	0.140	0.155	0.179	0.204	0.233
Average	0.160	0.141	0.134	0.136	0.146

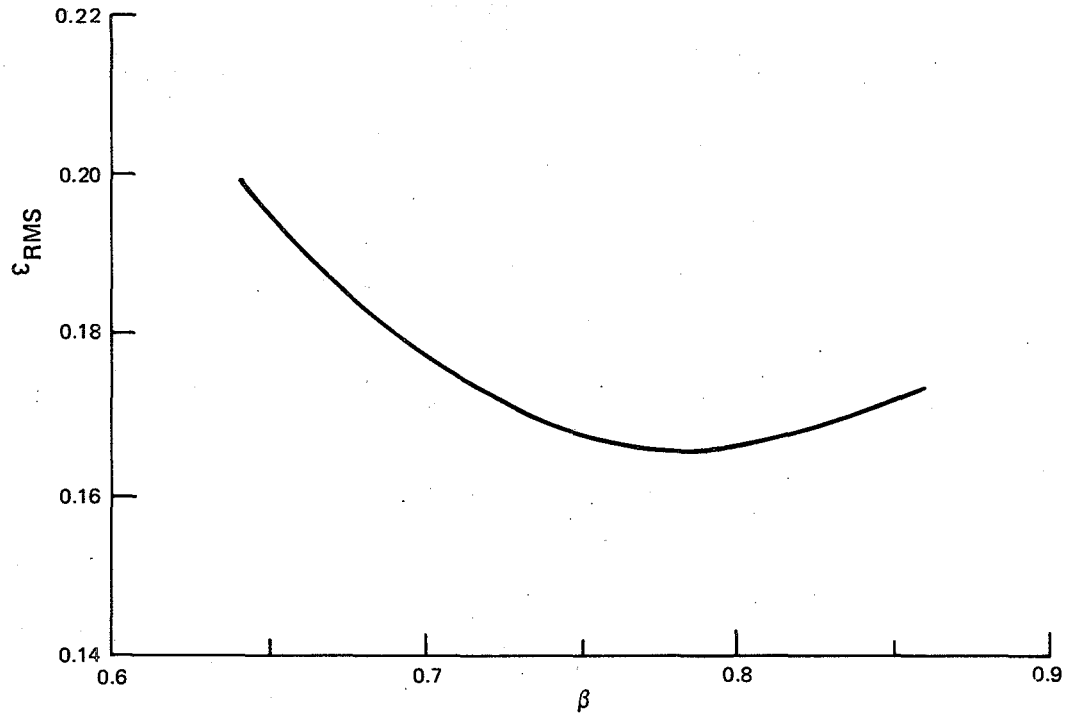

Figure 2.19a. Model N6 average trajectory error for Group A data sets with $\alpha = 0.05$.

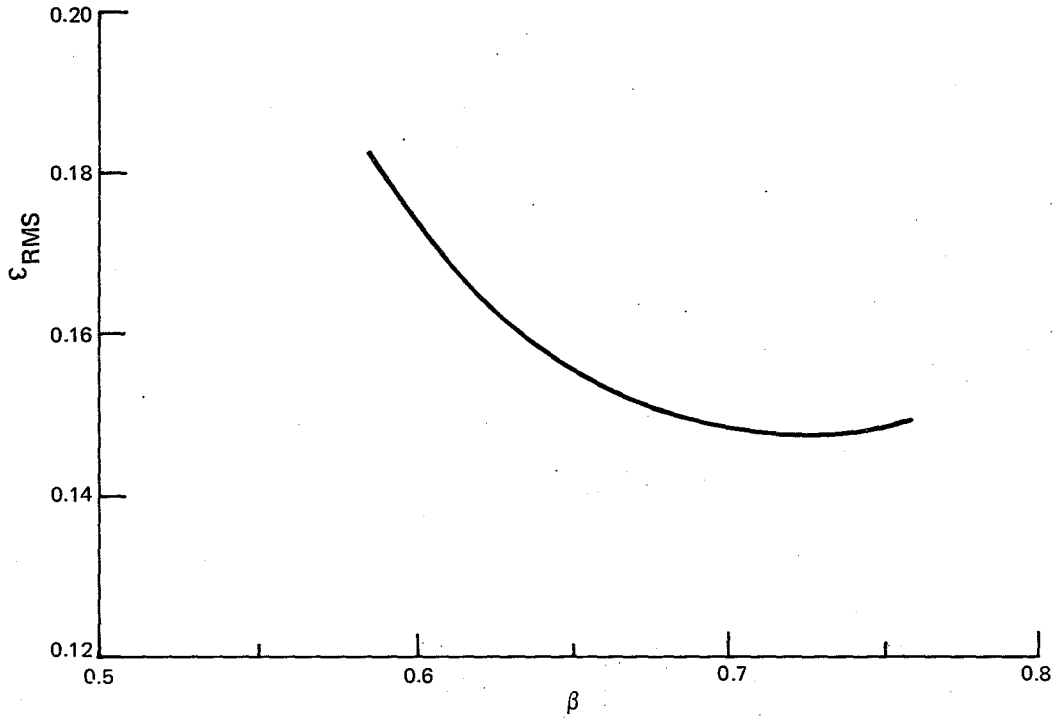

Figure 2.19b. Model N6 average trajectory error for Group A data sets with $\alpha = 0.10$.

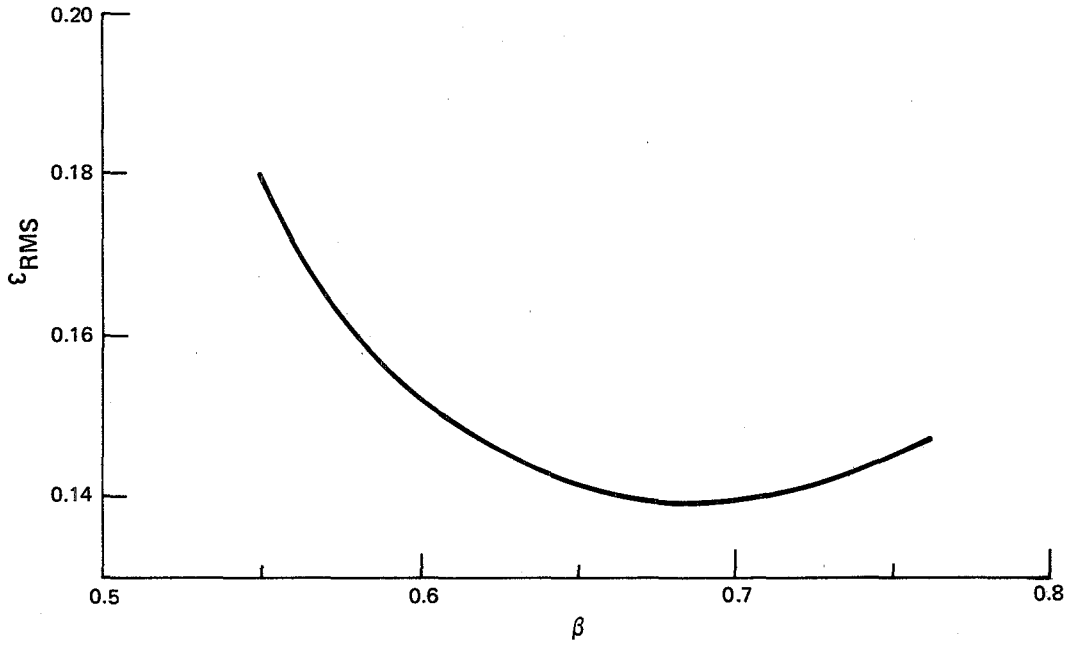

Figure 2.19c. Model N6 average trajectory error for Group A data sets with α = 0.15.

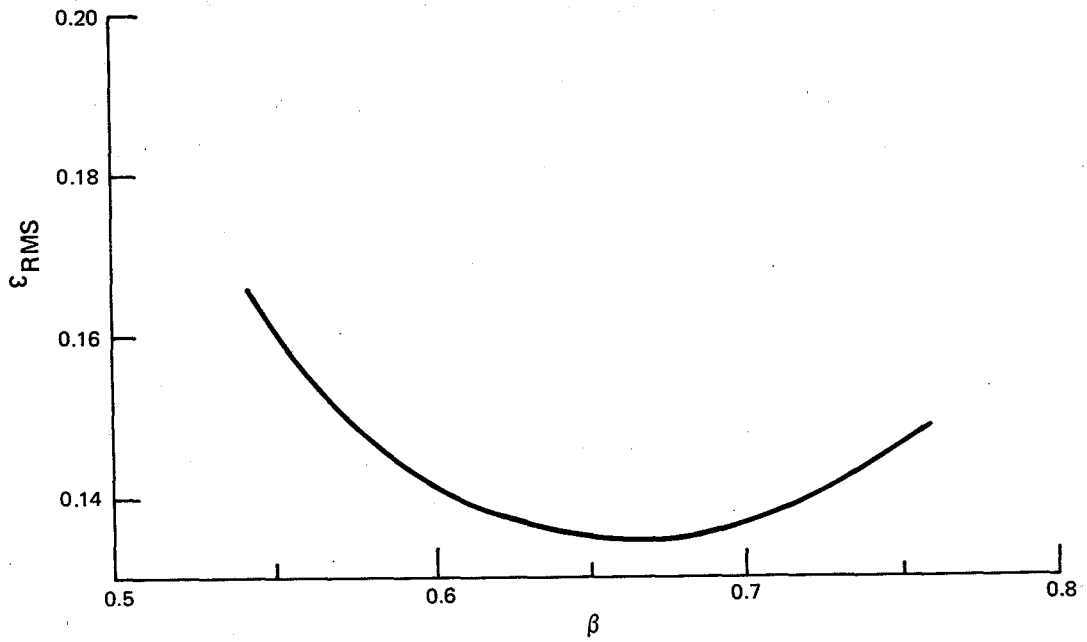

Figure 2.19d. Model N6 average trajectory error for Group A data sets with $\alpha = 0.20$.

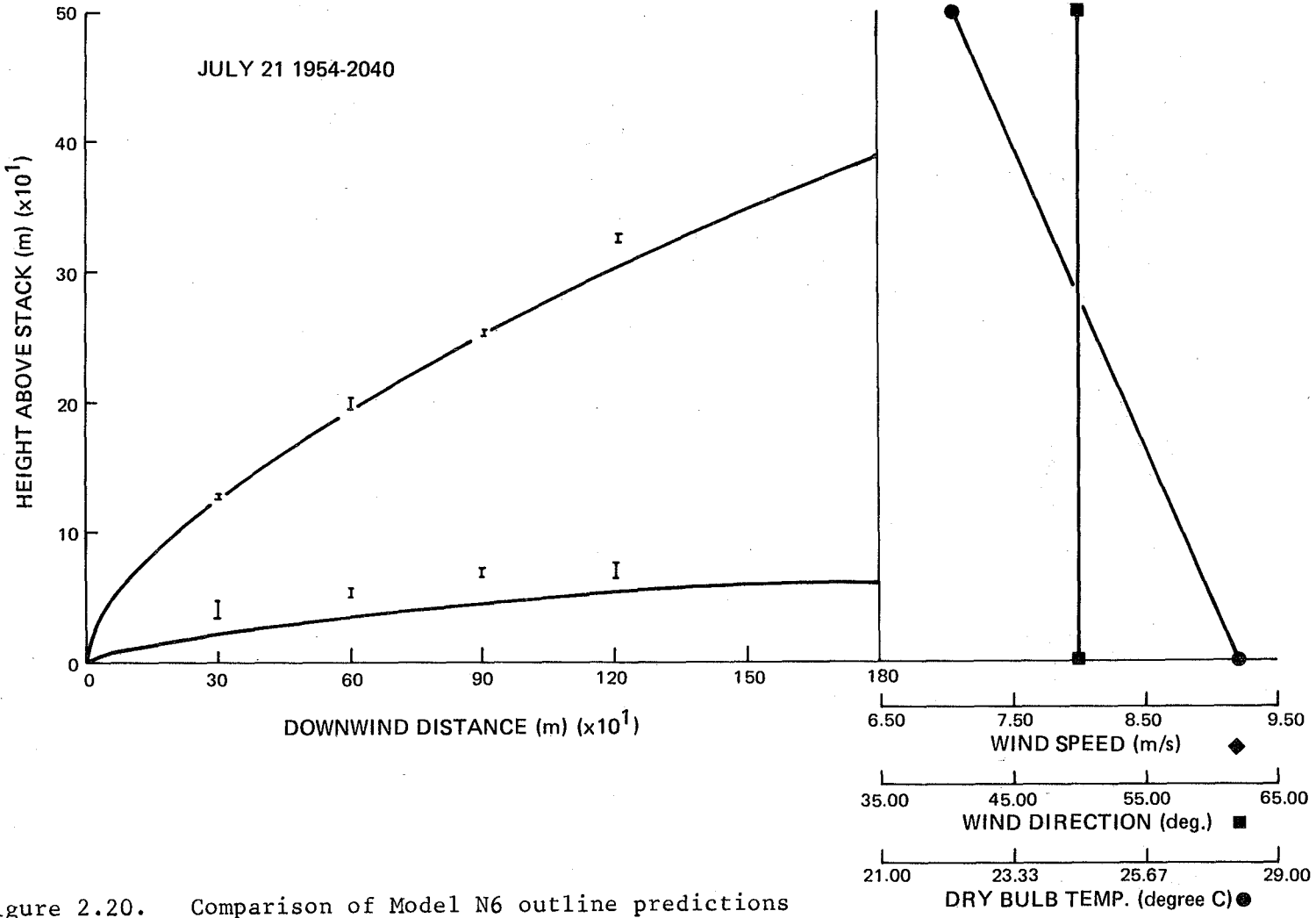

Figure 2.20. Comparison of Model N6 outline predictions (α = 0.15, β = 0.68) with photographic data.

Table 2.25. Model N6 Performance for Group B Data Sets. R.M.S. Trajectory Errors for Optimum Alpha,Beta Combinations.

Date		Temp. Profile	Alpha = 0.05 Beta = 0.78	0.10 0.73	0.15 0.68	0.20 0.66
Jan. 26	1138-1212	Inv. at 600 m	0.230	0.245	0.244	0.254
Jan. 26	1316-1407	Inv. at 600 m	0.136	0.123	0.120	0.123
Mar. 30	0840-0934	Linear	0.083	0.081	0.078	0.087
Mar. 30	0918-0954	Linear	0.057	0.056	0.056	0.065
Apr. 1	0659-0758	Inv. at 620 m	0.231	0.232	0.236	0.240
July 13	1524-1614	Kink at 700 m	0.262	0.187	0.158	0.132
July 23	2116-2202	Linear	0.249	0.172	0.144	0.112
Oct. 17	1548-1624	Linear	0.104	0.102	0.120	0.120
Oct. 17	1626-1700	Linear	0.118	0.146	0.183	0.197
Oct. 19	0920-1011	Inv. at 270 m	0.102	0.096	0.095	0.100
Oct. 19	1110-1144	Inv. at 470 m	0.326	0.286	0.274	0.255
Oct. 20	0956-1032	Linear	0.115	0.132	0.152	0.154
Oct. 25	0918-0956	Kink at 500 m	0.178	0.159	0.160	0.152
Oct. 25	0958-1030	Inv. at 460 m	0.156	0.137	0.131	0.125
Oct. 25	1056-1137	Inv. at 350 m	0.168	0.149	0.151	0.156
Oct. 25	1546-1640	Inv. at 620 m	0.170	0.183	0.198	0.202
Oct. 27	1516-1548	Linear	0.145	0.148	0.159	0.159
Average			0.166	0.155	0.157	0.155

Table 2.26. Model N6 Performance for Group C Data Sets. R.M.S. Trajectory Errors for Optimum Alpha,Beta Combinations.

Date		Temp. Profile	Alpha = 0.05 Beta = 0.78	0.10 0.73	0.15 0.68	0.20 0.66
Jan. 25	1418-1455	Kink at 500 m	0.231	0.171	0.173	0.204
Jan. 25	1505-1545	Kink at 500 m	0.202	0.142	0.121	0.126
Mar. 28	1818-1852	Inv. at 320 m	0.168	0.138	0.156	0.188
July 15	0615-0700	Inv. at 210 m	0.162	0.195	0.280	0.329
July 15	1608-1652	Linear	0.166	0.207	0.227	0.252
July 18	0600-0623	Kink at 300 m	0.035	0.052	0.055	0.064
July 25	1630-1708	Linear	0.242	0.114	0.071	0.044
July 26	0615-0702	Inv. at 100 m	0.179	0.235	0.253	0.282
Average			0.173	0.157	0.168	0.187

2.4.4.10 Model N7. Model N7 is identical to model N6 except that the two entrainment terms are added as a vector sum to yield the entrainment hypothesis

$$v_e = \{\alpha^2 (V - U \frac{v_x}{V})^2 + \beta^2 (\frac{v_x}{V} \frac{Uw}{V})^2\}^{\frac{1}{2}} \quad (2.89)$$

A few trials indicated that larger α values were necessary for this model; accordingly optimum β was sought by fitting trajectories for α values between 0.1 and 0.3.

The performance of model N7 for Group A data sets is summarized in Tables 2.27 a-e and Figures 2.21 a-e. For $\alpha = 0.10$, the minimum average error of 16.5% occurs with $\beta = 0.79$; for $\alpha = 0.15$, the minimum ε_{RMS} of 15.4% occurs with $\beta = 0.76$; for $\alpha = 0.20$; the minimum ε_{RMS} of 14.9% occurs with $\beta = 0.75$; for $\alpha = 0.25$, the minimum ε_{RMS} of 14.9% occurs with $\beta = 0.73$; and $\alpha = 0.30$, the minimum ε_{RMS} of 15.3% occurs with $\beta = 0.71$.

Group B and C Data Sets. The performance of model N7 with the above optimum α,β combinations against Group B and C data sets is summarized in Tables 2.28 and 2.29. Group B results show a weak α dependence, the minimum error of about 15% occurring for $0.15 \leq \alpha \leq 0.30$. Group C results show a minimum ε_{RMS} of about 15% with the $\alpha = 0.15$, $\beta = 0.76$ combination. Comparing the minima with those of model N6 suggests that the vector sum approach does improve low windspeed predictions slightly, although at the expense of a deterioration of Group A predictions.

Table 2.27A. Model N7 Performance for Group A Data Sets. R.M.S. Trajectory Errors versus Beta. Alpha = 0.10

Date	Beta = 0.65	0.70	0.75	0.80	0.85
Jan. 25 1138-1235	0.268	0.215	0.176	0.148	0.132
Apr. 1 0859-1005	0.094	0.063	0.066	0.092	0.122
July 12 1400-1440	0.198	0.145	0.098	0.061	0.042
July 20 1935-2026	0.171	0.128	0.103	0.097	0.106
July 21 1618-1658	0.161	0.169	0.185	0.205	0.226
July 21 1954-2040	0.027	0.068	0.107	0.143	0.176
July 25 1545-1628	0.529	0.452	0.385	0.324	0.269
Oct. 18 1602-1634	0.184	0.141	0.112	0.099	0.102
Oct. 19 1616-1700	0.104	0.122	0.148	0.175	0.202
Oct. 20 1538-1612	0.341	0.279	0.229	0.184	0.149
Oct. 24 0930-1002	0.158	0.180	0.204	0.231	0.254
Oct. 24 1046-1120	0.157	0.181	0.206	0.231	0.258
Average	0.199	0.179	0.168	0.166	0.170

Table 2.27B. Model N7 Performance for Group A Data Sets. R.M.S. Trajectory Errors versus Beta. Alpha = 0.15.

Date		Beta = 0.65	0.70	0.75	0.80	0.85
Jan. 25	1138-1235	0.214	0.167	0.135	0.116	0.112
Apr. 1	0859-1005	0.058	0.056	0.083	0.116	0.148
July 12	1400-1440	0.163	0.113	0.073	0.048	0.051
July 20	1935-2026	0.132	0.096	0.082	0.090	0.109
July 21	1618-1658	0.160	0.173	0.192	0.214	0.236
July 21	1954-2040	0.046	0.087	0.125	0.160	0.191
July 25	1545-1628	0.428	0.361	0.301	0.248	0.200
Oct. 18	1602-1634	0.165	0.124	0.098	0.090	0.099
Oct. 19	1616-1700	0.113	0.129	0.157	0.184	0.210
Oct. 20	1538-1612	0.299	0.241	0.194	0.153	0.123
Oct. 24	0930-1002	0.164	0.185	0.210	0.233	0.260
Oct. 24	1046-1120	0.163	0.186	0.211	0.236	0.262
Average		0.175	0.160	0.155	0.157	0.167

Table 2.27C. Model N7 Performance for Group A Data Sets. R.M.S. Trajectory Errors versus Beta. Alpha = 0.20.

Date	Beta = 0.60	0.65	0.70	0.75	0.80
Jan. 25 1138-1235	0.231	0.178	0.138	0.110	0.100
Apr. 1 0859-1005	0.072	0.051	0.070	0.102	0.135
July 12 1400-1440	0.196	0.141	0.096	0.062	0.051
July 20 1935-2026	0.157	0.109	0.080	0.075	0.091
July 21 1618-1658	0.157	0.162	0.177	0.198	0.219
July 21 1954-2040	0.030	0.059	0.099	0.136	0.170
July 25 1545-1628	0.432	0.365	0.305	0.251	0.202
Oct. 18 1602-1634	0.204	0.153	0.113	0.090	0.086
Oct. 19 1616-1700	0.112	0.118	0.135	0.161	0.188
Oct. 20 1538-1612	0.335	0.272	0.218	0.172	0.135
Oct. 24 0930-1002	0.153	0.167	0.190	0.214	0.238
Oct. 24 1046-1120	0.146	0.166	0.191	0.216	0.239
Average	0.185	0.162	0.151	0.149	0.150

Table 2.27D. Model N7 Performance for Group A Data Sets. R.M.S. Trajectory Errors versus Beta. Alpha = 0.25.

Date		Beta = 0.60	0.65	0.70	0.75
Jan. 25	1138-1235	0.202	0.154	0.117	0.095
Apr. 1	0859-1005	0.062	0.060	0.087	0.119
July 12	1400-1440	0.170	0.127	0.085	0.058
July 20	1935-2026	0.137	0.093	0.070	0.073
July 21	1618-1658	0.155	0.163	0.180	0.202
July 21	1954-2040	0.037	0.070	0.109	0.145
July 25	1545-1628	0.382	0.321	0.266	0.217
Oct. 18	1602-1634	0.195	0.144	0.106	0.085
Oct. 19	1616-1700	0.114	0.118	0.140	0.167
Oct. 20	1538-1612	0.383	0.314	0.252	0.201
Oct. 24	0930-1002	0.155	0.170	0.193	0.218
Oct. 24	1046-1120	0.143	0.164	0.193	0.219
Average		0.179	0.158	0.150	0.151

Table 2.27E. Model N7 Performance for Group A Data Sets. R.M.S. Trajectory Errors versus Beta. Alpha = 0.30.

Date	Beta = 0.60	0.65	0.70	0.75
Jan. 25 1138-1235	0.181	0.135	0.102	0.085
Apr. 1 0859-1005	0.063	0.072	0.101	0.133
July 12 1400-1440	0.166	0.117	0.079	0.058
July 20 1935-2026	0.122	0.081	0.064	0.074
July 21 1618-1658	0.155	0.165	0.183	0.205
July 21 1954-2040	0.044	0.078	0.116	0.152
July 25 1545-1628	0.343	0.287	0.236	0.191
Oct. 18 1602-1634	0.187	0.137	0.100	0.080
Oct. 19 1616-1700	0.116	0.121	0.144	0.171
Oct. 20 1538-1612	0.296	0.238	0.187	0.145
Oct. 24 0930-1002	0.156	0.171	0.195	0.220
Oct. 24 1046-1120	0.147	0.168	0.196	0.221
Average	0.165	0.148	0.142	0.146

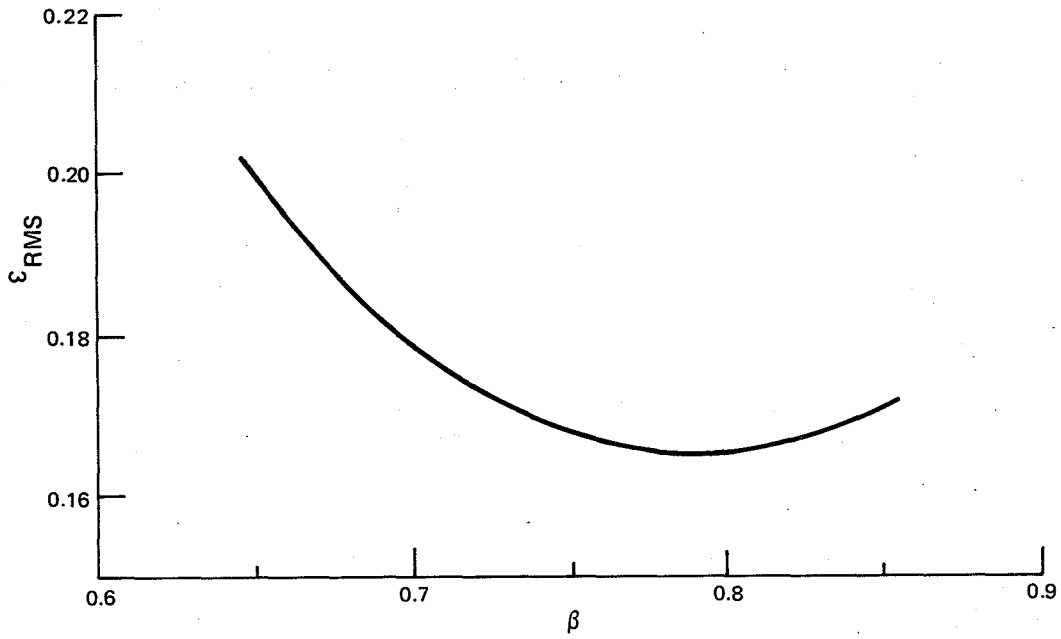

Figure 2.21a. Model N7 average trajectory error for Group A data sets with α = 0.10.

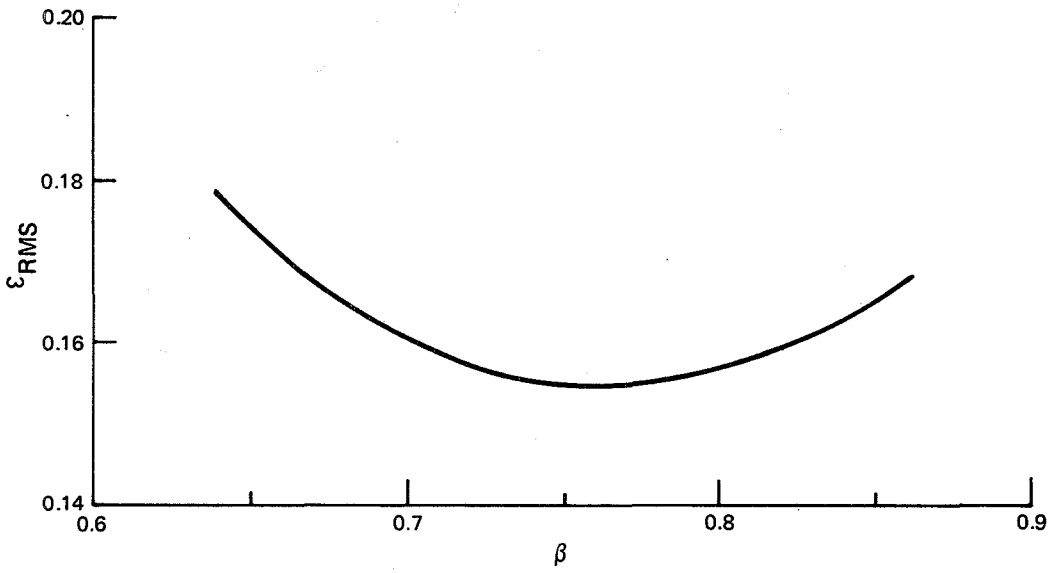

Figure 2.21b. Model N7 average trajectory error for Group A data sets with α = 0.15.

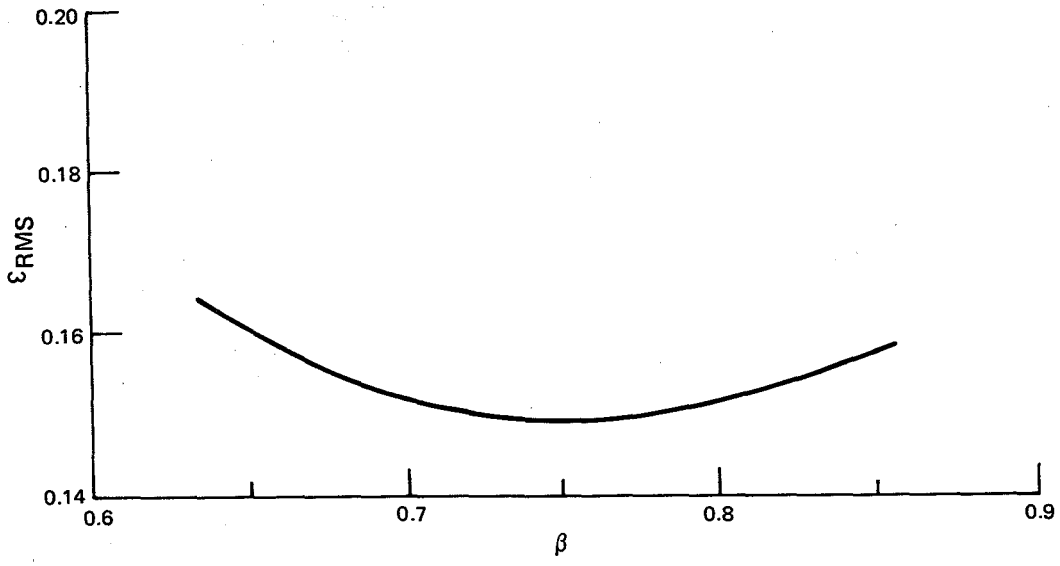

Figure 2.21c. Model N7 average trajectory error for Group A data sets with α = 0.20.

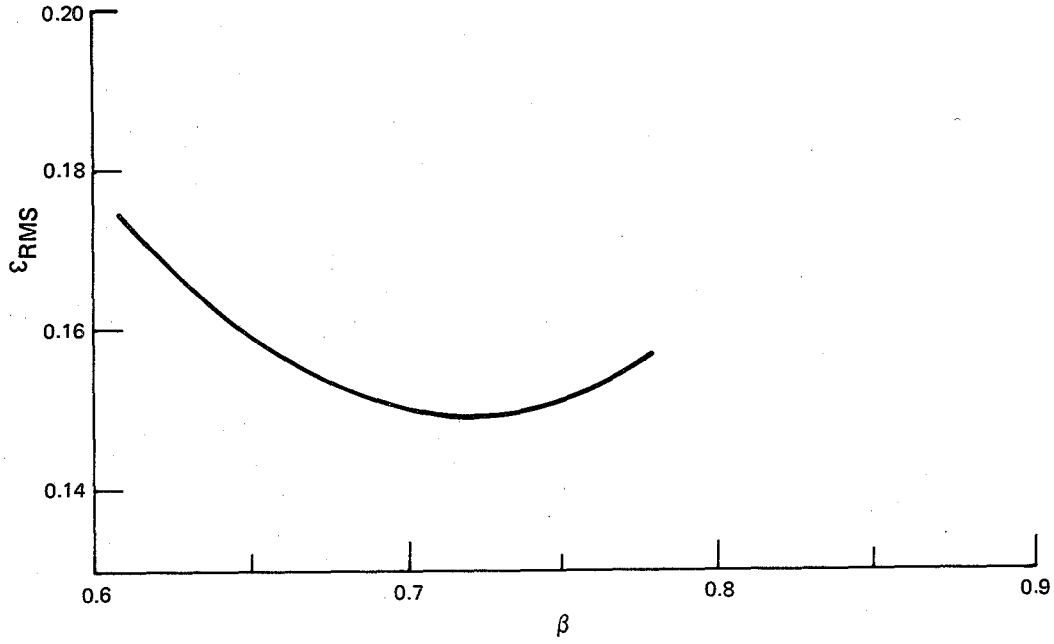

Figure 2.21d. Model N7 average trajectory error for Group A data sets with α = 0.25.

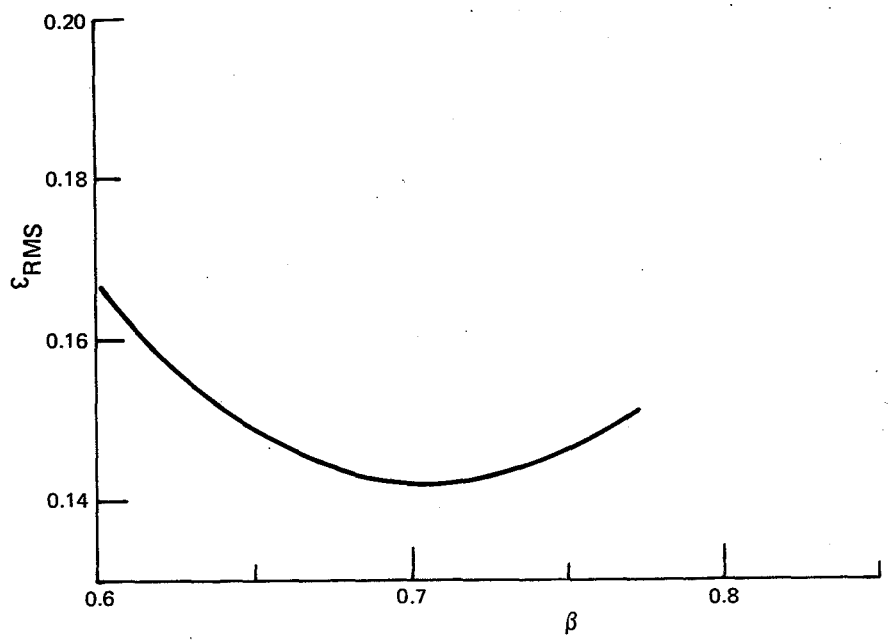

Figure 2.21e. Model N7 average trajectory error for Group A data sets with α = 0.30.

Table 2.28. Model N7 Performance for Group B Data Sets. R.M.S. Trajectory Errors for Optimum Alpha,Beta Combinations.

Date		Temp. Profile	Alpha = 0.10 Beta = 0.79	0.15 0.76	0.20 0.75	0.25 0.73	0.30 0.71
Jan. 26	1138-1212	Inv. at 600 m	0.229	0.234	0.244	0.245	0.244
Jan. 26	1316-1407	Inv. at 600 m	0.138	0.125	0.121	0.120	0.119
Mar. 30	0840-0934	Linear	0.083	0.078	0.084	0.085	0.082
Mar. 30	0918-0954	Linear	0.057	0.055	0.061	0.062	0.062
Apr. 1	0659-0758	Inv. at 620 m	0.232	0.236	0.247	0.244	0.241
July 13	1524-1614	Kink at 700 m	0.253	0.213	0.179	0.161	0.149
July 23	2116-2202	Linear	0.240	0.198	0.162	0.144	0.131
Oct. 17	1548-1624	Linear	0.098	0.100	0.094	0.100	0.110
Oct. 17	1626-1700	Linear	0.111	0.127	0.132	0.145	0.159
Oct. 19	0920-1011	Inv. at 270 m	0.099	0.095	0.094	0.093	0.092
Oct. 19	1110-1144	Inv. at 470 m	0.326	0.306	0.285	0.276	0.270
Oct. 20	0956-1032	Linear	0.113	0.130	0.128	0.138	0.147
Oct. 25	0918-0956	Kink at 500 m	0.176	0.167	0.160	0.158	0.158
Oct. 25	0958-1030	Inv. at 460 m	0.153	0.145	0.132	0.128	0.127
Oct. 25	1056-1137	Inv. at 350 m	0.165	0.149	0.151	0.149	0.150
Oct. 25	1546-1640	Inv. at 620 m	0.171	0.182	0.186	0.193	0.200
Oct. 27	1516-1548	Linear	0.143	0.147	0.147	0.150	0.157
Average			0.164	0.158	0.153	0.152	0.153

Table 2.29. Model N7 Performance for Group C Data Sets. R.M.S. Trajectory Errors for Optimum Alpha,Beta Combinations.

Date		Temp. Profile	Alpha = 0.10 Beta = 0.79	0.15 0.76	0.20 0.75	0.25 0.73	0.30 0.71
Jan. 25	1418-1455	Kink at 500 m	0.206	0.169	0.159	0.176	0.198
Jan. 25	1505-1545	Kink at 500 m	0.178	0.141	0.123	0.125	0.137
Mar. 28	1818-1852	Inv. at 320 m	0.139	0.136	0.151	0.175	0.200
July 15	0615-0700	Inv. at 210 m	0.139	0.145	0.219	0.274	0.309
July 15	1608-1652	Linear	0.163	0.181	0.203	0.215	0.225
July 18	0600-0623	Kink at 300 m	0.038	0.046	0.056	0.058	0.061
July 25	1630-1708	Linear	0.245	0.178	0.125	0.101	0.087
July 26	0615-0702	Inv. at 100 m	0.184	0.209	0.234	0.249	0.262
Average			0.161	0.151	0.160	0.172	0.185

On the basis of a weighted average of Group A, B, and C results, the $\alpha = 0.20$, $\beta = 0.75$ combination is selected for model N7 as giving the best overall performance.

2.5 CONCLUSIONS AND RECOMMENDATIONS ON PLUME RISE

In the preceding sections, four analytical models and seven numerical models have been tuned for, and tested against plume rise data from the G.C.O.S. plume.

2.5.1 Analytical Model Summary

Optimum entrainment constants for the four analytical models, and tuned model performances against Group A, B, and C data sets are summarized in Table 2.30, from which it is evident that the performance of models A2, A3, and A4 are comparable while that of model A1 is the poorest. Each of models A2, A3, and A4 predict Group A trajectories reasonably well, while each leads to less accurate predictions under the low windspeed conditions of Group C, where the bent-over plume assumption becomes invalid. Model A4 leads to slightly better trajectory predictions under the windspeed shear and nonlinear temperature profile conditions of Group B, but the computationally simpler averaging method employed in models A2 and A3 gives results that are only slightly worse.

Table 2.30. Analytical Model Performance Summary.

Average R.M.S. Trajectory Errors for Group A,B,C Data Sets				
	Model A1	Model A2	Model A3	Model A4
	(β = 0.64)	(β = 0.88)	(β = 0.66)	(β = 0.88)
Group A	0.135	0.124	0.130	0.124
Group B	0.262	0.173	0.159	0.139
Group C	0.397	0.280	0.283	0.309
Weighted Average*	0.250	0.180	0.176	0.171

*Average weighed by size of data set:
Weighted Average = (12A + 17B + 8C)/37

Model A3, which employs Briggs definition of source buoyancy flux has $\beta = 0.66$, which leads to the most realistic rate of spread predictions, while models A2 and A4 with $\beta = 0.88$ tend to overestimate rates of spread. The paradox in this result is that model A3 performs better when outlines are considered even though Briggs buoyancy flux definition appears to be less exact. Numerical models N1, N2, and N3 show that the Boussinesq approximation is the source of this paradox. Models N1 and N2, which contain the Boussinesq approximation, also require large entrainment constants to give good trajectory predictions, while relaxation of the bent-over plume assumption in model N2 has no effect on predicted rates of spread. Model N3, on the other hand, which makes neither the Boussinesq nor the bent-over plume assumption, leads to both good trajectory and outline predictions with the smaller entrainment constant, $\beta = 0.62$. It can thus be concluded that models A2 and A4 compensate for the Boussinesq assumption $\rho_p = \rho_a$, which significantly overestimates the source mass flux, by requiring a large entrainment constant to pull predicted trajectories down to measured levels. Model A3 compensates, however, by reducing the source buoyancy flux by a T_{a_o}/T_{p_o} factor, such that realistic trajectories can be predicted along with realistic rates of spread.

In addition to the above results, model N1 also leads to clarification of the role of a drag force in integral plume rise formulations. It is concluded that a drag force, while questionable both on physical and mathematical grounds, can be introduced into a numerical

model as another method of compensating for the Boussinesq approximation; that is, model N1 gives comparable trajectory predictions either with $C_D = 0$, $\beta = 0.88$ or with $C_D = 0.5$, $\beta = 0.64$. The latter combination leads to superior rate of spread predictions. Model N3, however, is able to give both good trajectory and rate of spread predictions by relaxing the Boussinesq approximation rather than by introducing a drag force into the governing equations.

On the basis of Table 2.30 and the above arguments, model A3 with $\beta = 0.66$ is selected as the best analytical model. While model A4 does handle shear conditions better than model A3, the additional computational effort required to apply model A4 is not justified by the improvements in performance. It is more fruitful to apply a computational effort of about the same magnitude required by model A4 to a full numerical model.

2.5.2 Numerical Model Summary

Optimum entrainment constants for the seven numerical models considered, and tuned model performances in terms of average trajectory errors for Group A, B, and C data sets are summarized in Table 2.31. As was discussed above, models which contain the Boussinesq approximation, models N1 and N2, require relatively large entrainment constants for good trajectory predictions, and so tend to overestimate rates of spread. Models which do not make the Boussinesq

Table 2.31. Numerical Model Performance Study.

	Average R.M.S. Trajectory Errors for Group A,B,C Data Sets						
	Model N1	Model N2	Model N3	Model N4	Model N5	Model N6	Model N7
	(β=0.86)	(β=0.89)	(β=0.62)	(α=0.05)	(α=0.05)	(α=0.15)	(α=0.20)
				(β=0.63)	(β=0,65)	(β=0.68)	(β=0.75)
Group A	0.134	0.128	0.129	0.135	0.137	0.138	0.149
Group B	0.155	0.169	0.169	0.156	0.155	0.157	0.153
Group C	0.305	0.299	0.298	0.201	0.182	0.168	0.160
Weighted Average	0.181	0.184	0.184	0.159	0.155	0.153	0.153

approximation, models N3 to N7, require smaller entrainment constants for good trajectory predictions, and so predict more realistic rates of spread.

The performance of models N3 to N7 is comparable for Group A and B data sets, with an average root mean square error of the order of 14 to 15 percent. However, for Group C data sets, the bent-over plume entrainment hypothesis of model N3 leads to the poorest results, with an average error of about 30%, while the entrainment hypothesis of model N7 leads to the best results, with an average error of about 16%. The performance of each of models N5 to N7 is similar for Group A, B, and C conditions, which indicates that these models contain sufficient physical information to describe plume trajectory and spread under most atmospheric conditions.

2.5.3 Final Rise Comparisons and Model Recommendations

The most important single parameter that a plume rise model must provide for atmospheric dispersion calculations is probably the final rise height of the plume. Tables 2.32 and 2.33 compare measurements of final rise above stack-top during stable conditions with the predictions of models A3 and N4 to N7 respectively. Measured final rises were taken to be the geometrical center of the plume cross-section isopleths charted by an aircraft as described in chapter 3. Predicted final rises were related to the altitude at which the plume

Table 2.32. Final Rise Measurements and Predictions of Model A3.

Date	Data Group	Measured Altitude (m)	A3 Peak Height (m)	A3 Peak Error (%)	A3 Equilibrium Height (m)	A3 Equilibrium Error (%)
July 25 1545	A	575	576	+0.2	484	-15.9
Oct. 18 1602	A	325	336	+3.4	282	-13.2
Oct. 19 1616	A	325	322	+0.9	270	-16.8
Oct. 20 1548	A	450	356	-20.9	299	-33.6
Jan. 26 1138	B	400	317	-20.8	266	-33.4
Jan. 26 1316	B	425	418	-1.7	351	-17.4
Apr. 1 0659	B	325	401	+23.4	337	+3.6
July 23 2116	B	250	228	-8.8	192	-23.4
Oct. 17 1548	B	300	311	+3.7	261	-12.9
Oct. 19 0920	B	150	139	-7.3	117	-22.2
Oct. 20 0956	B	225	172	-23.6	144	-35.8
Oct. 25 0958	B	225	239	+6.2	201	-10.8
Oct. 25 1546	B	350	264	-24.6	222	-36.6
Oct. 27 1516	B	300	322	+7.3	270	-9.8
Jan. 25 1418	C	425	364	-14.4	306	-28.1
Mar. 28 0818	C	275	217	-21.1	182	-33.7
July 25 1630	C	625	649	+3.8	545	-12.8
July 26 0615	C	150	114	-24.0	96	-36.2
Average r.m.s. error				15.0		24.4

Table 2.33. Final Rise Measurements and Predictions of Models N4 to N7.

Date	Data Group	Measured Altitude (m)	N4 Peak		N5 Peak		N6 Peak		N7 Peak	
			Height (m)	Error (%)	Height (m)	Error (%)	Height (m)	Error (%)	Height (m)	Error (%)
July 23 1545	A	575	594	+3.3	592	+3.0	575	0	564	-1.9
Oct. 18 1602	A	325	345	+6.2	340	+4.6	330	+1.5	315	-3.1
Oct. 19 1616	A	325	330	+1.5	325	0	316	-2.8	300	-7.7
Oct. 20 1548	A	450	379	-15.8	374	-16.9	362	-19.6	348	-22.9
Jan. 26 1138	B	400	322	-19.5	322	-19.5	312	-22.0	311	-22.3
Jan. 26 1316	B	425	349	-17.9	349	-17.9	343	-19.3	340	-20.0
Apr. 1 0659	B	325	352	+8.3	352	+8.3	335	+3.1	332	+1.9
July 23 2116	B	250	235	-6.0	237	-5.2	228	-8.8	228	-8.8
Oct. 17 1548	B	300	314	+4.7	317	+5.7	292	-2.7	292	-2.7
Oct. 19 0920	B	150	148	-1.3	150	0	144	-4.0	145	-3.3
Oct. 20 0956	B	225	173	-23.1	174	-22.7	162	-28.0	161	-28.4
Oct. 25 0958	B	350	244	+8.4	248	+10.2	236	+4.9	239	+6.2
Oct. 25 1546	B	300	332	+10.7	334	+11.3	317	+5.7	317	+5.7
Jan. 25 1418	C	425	426	+0.2	450	+5.9	458	+7.8	473	+11.3
Mar. 28 0818	C	275	273	-0.7	314	+14.2	316	+14.9	270	-1.8
July 25 1630	C	625	672	+7.5	682	+9.1	640	+2.4	658	+5.3
July 26 0615	C	150	123	-18.0	125	-16.7	133	-11.3	136	-9.3
Average r.m.s. error				11.5		12.2		12.1		12.4

vertical velocity first reaches zero and the centerline trajectory reaches its maximum value. Eighteen cases, consisting of 4 Group A, 10 Group B, and 4 Group C data sets, were available for comparison.

In Table 2.32, measurements are compared with (i) the peak centerline altitude predictions of model A3, and (ii) the final equilibrium, centerline altitude prediction of model A3. This latter equilibrium altitude has been shown to be 16% below the peak altitude[10]. Two conclusions can be drawn from the table. First, peak altitude predictions correlate better with measured final rises, with an average root-mean-square error of about 15%, than do final equilibrium altitude predictions, which are generally too low, with an average root-mean-square error of about 24%. Secondly, final rise predictions of model A3 are on average better than detailed trajectory predictions. This result is not unexpected, since the analytical models should contain sufficient physics to predict final rise altitudes reasonably well. They will be unable, however, to accurately predict the downwind location where the final rise altitude first occurs, particularly under Group C conditions.

In Table 2.33, model N4 to N7 predictions are compared with aircraft data. Numerical model predictions are similar, with model N4 having the least average error (11.5%), and model N7 having the largest average error (12.4%). All numerical models show a small improvement over the analytical model A3. In view of the measurement

uncertainties inherent in both plume rise and aircraft data, these final rise comparisons are quite good.

From the trajectory performance summary, Table 2.31, and the final rise performance summary, Table 2.33, it is evident that models N4 to N7 lead to comparable results when average errors are considered. As well as good average results, however, model N6 also gives separately good Group A, Group B, and Group C trajectory predictions and good final rise predictions. In view of this fact, and in view of the physical content of the model, model N6 with $\alpha = 0.15$, $\beta = 0.68$ is recommended for use in the Syncrude dispersion model. A computer listing of model N6 is contained in Appendix B1.

3. PLUME SPREAD

3.1 INTRODUCTION

The rate of plume spread or growth as a function of downwind distance may (as outlined earlier) be considered to occur in two phases. In the first phase or buoyancy dominated phase the turbulence responsible for the relative diffusion about the center of mass of the plume cross-sectional element is considered to originate from the buoyant forces within the plume and the relative motion between the plume and its surroundings. This buoyancy dominated phase subsequently gives way to the second phase where atmospheric turbulence in the appropriate length scale range assumes the dominant role for diffusion of the plume. Further details on buoyant plume rise and growth are given in chapter 2 of this report and the references cited there.

Our attention in this chapter is directed toward the atmospheric turbulence phase of plume spread or growth. However, any plume dispersion model must somehow account for both the buoyant phase as well as the atmospheric phase of plume spread and thus some comments on the rate of plume spread in the buoyant phase will be made.

A great deal of research has been directed toward understanding the atmospheric diffusion of industrial plumes. Researchers have attempted to describe the atmospheric diffusion of plumes by (a)

direct solution of the convective diffusion equation (b) Gaussian plume dispersion (a special case of (a)), and employing statistical theories of diffusion or some combination of the above. Direct solution of the convective diffusion equation requires specification of eddy diffusivities (K-theory) as a means of parameterizing the appropriate turbulence length and velocity scales. Also, the mean wind field must be specified. Most workers using this approach have opted for the empirical specification of eddy diffusivities or K's as a function of space and generally assume steady state conditions. Often, however, the K distributions specified are parameterizations of atmospheric turbulence in the planetary boundary layer and are used in the solution of the convective diffusion equation without due consideration given to the appropriate turbulence scale dependence which requires some knowledge of turbulence spectra. Higher order closure methods have also been attempted as a means of describing the turbulence responsible for diffusion. These models generally use finite difference procedures for numerically solving the governing equations for diffusion and are thus complicated and expensive.

The closed form Gaussian plume model results from the solution of the convective diffusion equation assuming a constant eddy diffusivity and a uniform wind field. This model has been and continues to be very popular due to its simplicity. Here, the appropriate turbulence responsible for the relative diffusion of the plume is parameterized through the specification of the standard deviations of the

Gaussian distributions. Thus, a great deal of effort has been devoted to the specification of these empirical, so-called sigma curves. The Pasquill-Gifford sigma curves are probably the most notable of the various sigma curve typing schemes presently available. Some form of the Gaussian plume model is used by legislative bodies responsible for air quality (at least those for which the authors are familiar). Since sigma curves are generated from field measurement programs they tend to be site specific in nature and suffer from the measurement errors associated with the various field studies. Also, the Pasquill-Gifford curves have been extrapolated to distances far beyond the original data base of some 800 meters, and used for tall stack (300 m) diffusion when most of the data was based on surface layer measurements. Nevertheless, some sigma curve typing scheme based on a given site data base and used in a Gaussian plume model is a very attractive way to develop a site-specific operational plume dispersion model as considerable success has been achieved in the past.

The statistical approach to atmospheric relative diffusion based on the work of G.I. Taylor has received more recent attention by some researchers. The work of Pasquill[21] (1976) and Draxler[22] (1975) for example, may be noted. The statistical theory offers additional insight into the physics of diffusion. The standard deviations of particle displacement are shown to be functions of the appropriate turbulence length and velocity scales. Strict application of the statistical theory requires as input, at least, measurements of

appropriate turbulence r.m.s. velocity (or intensity of turbulence) and a Lagrangian time or length scale. These measurements or those of parameters from which they can be determined are seldom available at the altitudes of industrial plume diffusion. Also, the statistical theory assumes homogeneous and stationary turbulence, which except under certain limiting conditions seldom occurs over the range of plume dispersion of interest. Thus, in recent work researchers have attempted to compensate for the limitations of the statistical theory (as is done in other approaches) by resorting to some form of empirical input. The principal author feels that this approach to a sigma typing scheme has a great potential and perhaps may lead itself to greater generality of application. However, the present data base for use in this report, does not have sufficient turbulence measurements to pursue the statistical approach. Some reliance on statistical theory is used however, to classify the time dependent behaviour of some of the measured sigma data.

Complicating the classification or typing of sigma curves are such effects as: plume buoyancy, terrain (including roughness), multiple sources, non-homogeneity of the wind field, inversion lids, wind speed and direction shear, and errors associated with measurement techniques.

The sigma's produced from aerial transect data in the report by Slawson et al[12] (1978) were calculated using three techniques: a

statistically defined sigma, an edge method where the observed width of the transect was assumed equal to 4.3 standard deviations and an area matching technique performed on each individual transect. The sigmas resulting from all three of the above techniques produced considerable scatter when plotted on the graphs of some currently used sigma typing schemes. Thus a fourth technique was tried for the present report. The method used here is an equivalent area method whereby the area within a concentration isopleth of a given plume cross-section is set equal to an elliptical area having major and minor axis in the same ratio as the observed width and depth of the plume cross-section isopleth. It was hoped that this method might further filter errors associated with individual transects and, where two successive cross-sections were available, produce at least a better estimate of the correct rate of growth of the plume cross-sectional area. Further details are given below.

3.2 GENERAL SCOPE OF WORK ON PLUME SPREAD

The scope of work on plume spread for this report focuses on a re-analysis of the aerial plume cross-section data given in the report by Slawson et al[12] (1978) to try and reduce scatter in the sigma data and subsequently produce a more consistent data set for comparison with some of the currently used sigma typing schemes. Thus, for this work at least, a Gaussian plume model for the atmospheric phase of plume growth is presumed. In the subsequent analysis of the resulting

sigma data, consideration was given to the following: (i) the effect of sampling time on the data, (ii) the effect of source height, (iii) the effect of surface roughness, (iv) the effect of complex terrain, (v) the effect of wind shear (speed and direction), (vi) the effect of plume buoyancy, (vii) the effect of ambient stability, and (viii) multiple source effects. Also, if the data allowed, the intent was to examine the dispersion data under limited mixing conditions.

3.3 SIGMAS FROM A REDUCED DATA SET

According to the Gaussian plume model, the steady-state concentration distribution C(x,y,z) downwind of a stack, ignoring ground effects, is given by[1]

$$C_{(x,y,z)} = C_{max}(x) \exp\left(-\frac{1}{2}\left(\left(\frac{y}{\sigma_y}\right)^2 + \left(\frac{z - H}{\sigma_z}\right)^2\right)\right) \qquad (3.1)$$

where x is downwind distance, y is cross-wind distance, z is vertical distance, and H is the constant effective stack height (actual stack height plus buoyant rise). The peak concentration of the double Gaussian distribution described by equation 3.1 decreases with x according to

$$C_{max}(x) = \frac{Q}{2\pi\sigma_y(x)\,\sigma_z(x)\,\bar{U}} \qquad (3.2)$$

where Q is the pollutant mass flow from the source, $\bar{U}$ is the mean wind speed, and σ_y and σ_z are the standard deviations of the distribution in the cross-wind and vertical directions respectively. These sigma parameters are the empirical measure of atmospheric turbulence which controls the rate of plume spread; they therefore depend on such factors as atmospheric stability and surface roughness. The accurate specification of the sigma functions is crucial to the success of a Gaussian plume model of dispersion.

Several schemes for sigma specification as a function of atmospheric parameters appear in the literature. Four of these schemes, the Pasquill-Gifford (PG) curves, Briggs' curves, the Tennessee Valley Authority (TVA) curves, and the Brookhaven National Laboratory (BNL) curves, will be referred to. These different schemes are compared in Fig. 3.1(a) and Fig. 3.1(b) and Table 3.1, where it is evident that the four sets of curves are quite similar. Note that the TVA curves are only specified for neutral to very stable conditions, while the other curves are specified for very unstable to very stable conditions. Background information on these and other sigma specification schemes may be found for example in Reference 24.

In a previous Syncrude report,[12] an aircraft measurement program to obtain sigma data was described in detail. Sulfur dioxide concentrations were measured at various altitudes and downwind distances from the GCOS powerhouse stack, and sigmas were generated in

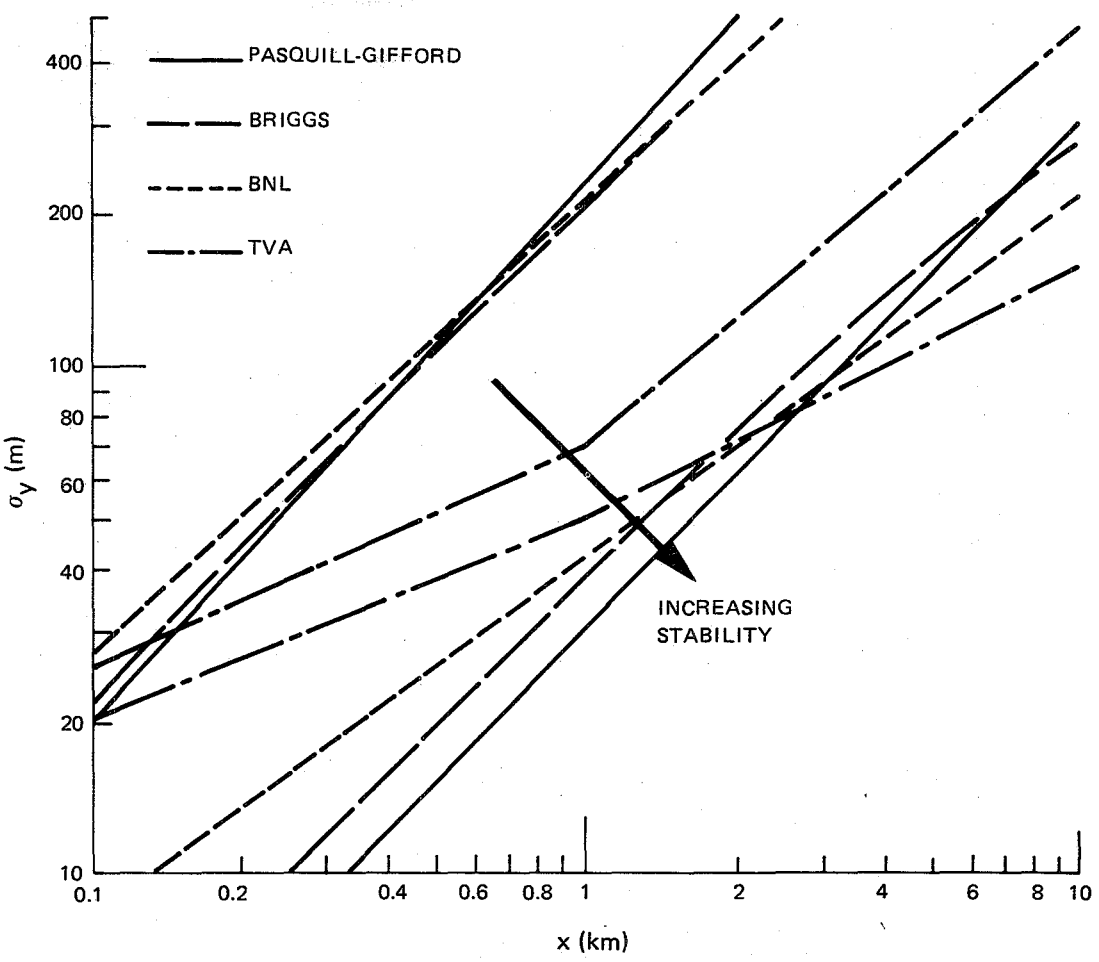

Figure 3.1a. A comparison of σ_y versus x typing schemes.

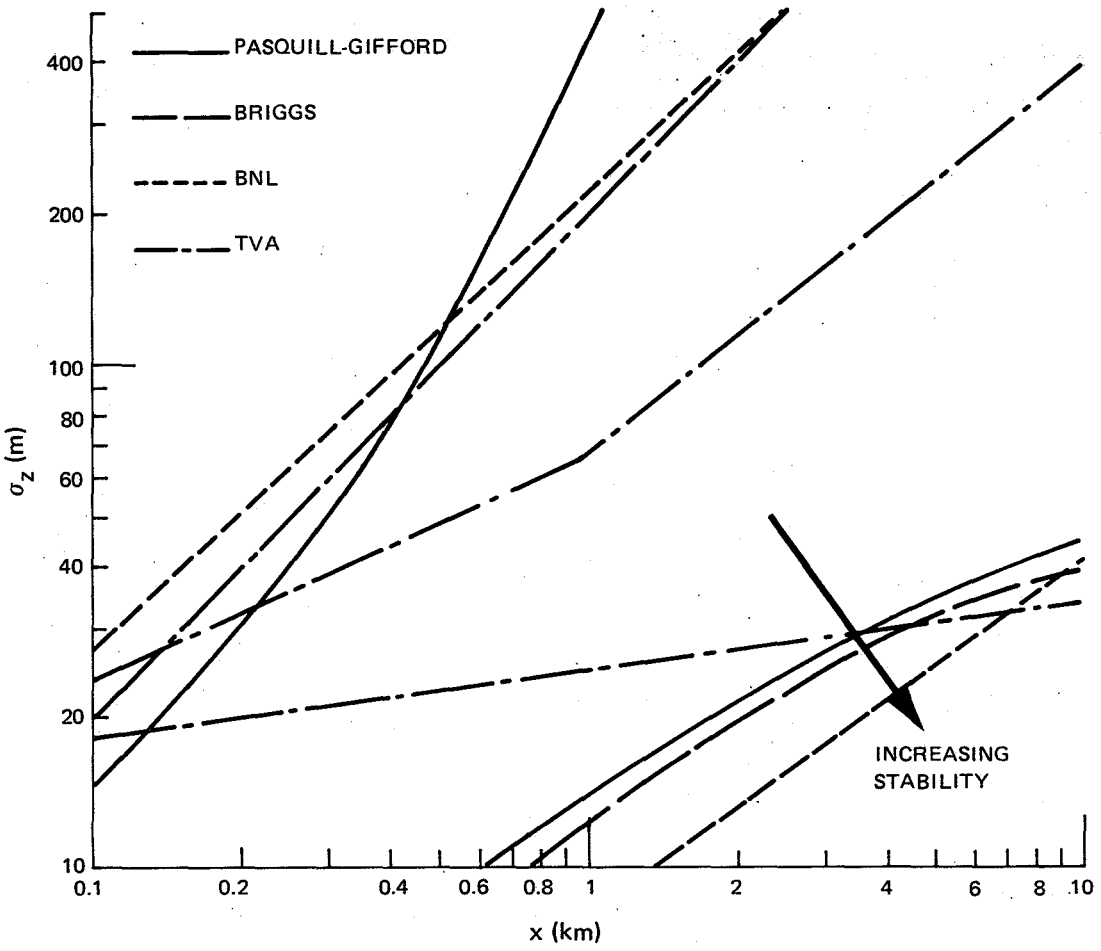

Figure 3.1b. A comparison of σ_z versus x typing schemes.

Table 3.1. Empirical Sigma Curves.

(i) Pasquill-Gifford and Briggs (USAEC classifications)

Stability Class	ΔT per 100 m (°C)
A (very unstable)	<-1.9
B	-1.9 to -1.7
C	-1.7 to -1.5
D (neutral)	-1.5 to -0.5
E	-0.5 to 1.5
F (very stable)	1.5 to 4.0
G	>4.0

Pasquill-Gifford: σ_y and σ_z from empirical curves

Briggs correlations: σ_y =	σ_z =
0.22 x c	0.20 x
0.16 x c	0.12 x
0.11 x c	$0.08\ x(1+0.0002x)^{-0.5}$
0.08 x c	$0.06\ x(1+0.0015x)^{-0.5}$
0.06 x c	$0.03\ x(1+0.0003)^{-1}$
0.04 x c	$0.016x(1+0.0003x)^{-1}$

where $c=(1+0.0001x)^{-0.5}$ and x is in meters

(ii) Tennessee Valley Authority

Stability Class	Δ_θ per 100 m (°C)
A (neutral)	0.00
B	0.27
C (stable)	0.64
D (isothermal)	1.00
E	1.36
F (strong inversion)	1.73

σ_y and σ_z from empirical curves

(iii) Brookhaven National Laboratories (classes often overlap)

Stability Class	ΔT per 123 m (°C)	Windspeed at 108 m	σ_y (m)	σ_z (m)
A (very unstable)	-1.25 ± 7	1.8 ± 7	$-$	$-$
B_2	-2.1 to -1.1	2.0 to 5.6	$0.40x^{0.91}$	$0.41x^{0.91}$
B_1	-1.85 to -0.65	3.9 to 10.1	$0.36x^{0.86}$	$0.33x^{0.86}$
C (neutral)	-1.16 to -0.12	7.3 to 13.5	$0.32x^{0.78}$	$0.22x^{0.78}$
D	-0.6 to +4.6	3.8 to 9.0	$0.31x^{0.71}$	$0.06x^{0.71}$

where x is in meters

three different ways from the concentration distributions. Preliminary attempts to correlate these sigmas with atmospheric stability were also made in the previous study, but scatter in the data made it difficult to draw any definite conclusions. Other field studies have encountered similar problems.[26]

The aim of this section of the report is to continue the analysis started in the previous study. It was anticipated that a more detailed examination of the aircraft data, combined with an improved method of extracting the sigma values, would permit more definite conclusions and recommendations regarding appropriate sigma parameters for use in a Syncrude dispersion model.

3.4 SIGMA DATA ABSTRACTION

In the previous study, sigmas were obtained essentially by examining the concentration distribution from each plume transect at a fixed downwind distance and fixed altitude. From equation (3.1), a Gaussian distribution of the form

$$C(y) = C'_{max} \exp \left(- \frac{1}{2} \left(\frac{y}{\sigma_y} \right)^2 \right) \qquad (3.3)$$

had to be fitted to the measured distributions. Different σ_y values could be derived, however, depending on the method of analysis. Both

the statistical method of finding σ_y and a Gaussian fit through the plume edges (defined as the points where $C(y) = 0.1\ C'_{max}$) were sensitive to the shape of the tails of the distribution, where measurement errors were relatively higher. It was therefore concluded that an area matching method was likely to give the most reliable σ_y value. The area matching method also gave consistently the smallest sigma; that is, abstracted σ_y values followed a correlation[12]

$$\sigma_{y_{AREA}} = 0.72\sigma_{y_{STAT}} = 0.77\sigma_{y_{EDGE}} \tag{3.4}$$

For a given plume cross-section at a fixed downwind distance, several aircraft transects were made at different altitudes, with at least two repeated transects at a given altitude, and a σ_y was found for each transect. Since each transect represented one realization of a randomly fluctuating concentration distribution, these σ_y values were then averaged over the cross-section. A vertical standard deviation σ_z was also found by fitting a Gaussian distribution to the measured peak concentration at different altitudes. These σ_z values exhibited considerably more scatter when compared against the P.G. curves for example, than the σ_y values since the resolution in the vertical was quite coarse, consisting of typically about six points at different altitudes.

The method employed to determine σ_y and σ_z in this report follows from equation (3.1). It is straight-forward to show that the

isopleth of concentration $C(y,z) = \frac{1}{n} C_{max}$ at a fixed downwind distance is given by

$$\frac{y^2}{(\sqrt{2 \ln n}\, \sigma_y)^2} + \frac{z^2}{(\sqrt{2 \ln n}\, \sigma_z)^2} = 1 \qquad (3.5)$$

which is the equation of an ellipse with semi-major and semi-minor axes related to the horizontal and vertical sigmas. Note that, for an elliptical contour, the isopleth concentration is defined as a fraction of the peak concentration for the entire cross-section, and not for an individual transect.

A typical plume outline derived from aircraft measurements and subsequently used for sigma analysis is illustrated with a greatly expanded vertical scale in Figure 3.2(a). Two isopleths were drawn for each case, the 0.1 C_{max} isopleth and the 0.25C_{max} isopleth, although only the 0.1C_{max} isopleth was used in data abstraction. As is evident from the figure, contours were usually distorted from an elliptical shape, due in part to random fluctuations, to uncertainties in aircraft position, to plume meander between consecutive transects, and to cross-wind shear effects.* To simplify sigma abstraction, raw contours were smoothed by applying a moving average for horizontal

---

*It is assumed here that cross-wind shear distorts the plume cross-sectional shape producing a tilted axis while at the same time increasing the cross-sectional area of the plume due to enhanced vertical diffusion. Further discussion of cross-wind shear effects are given later in this report.

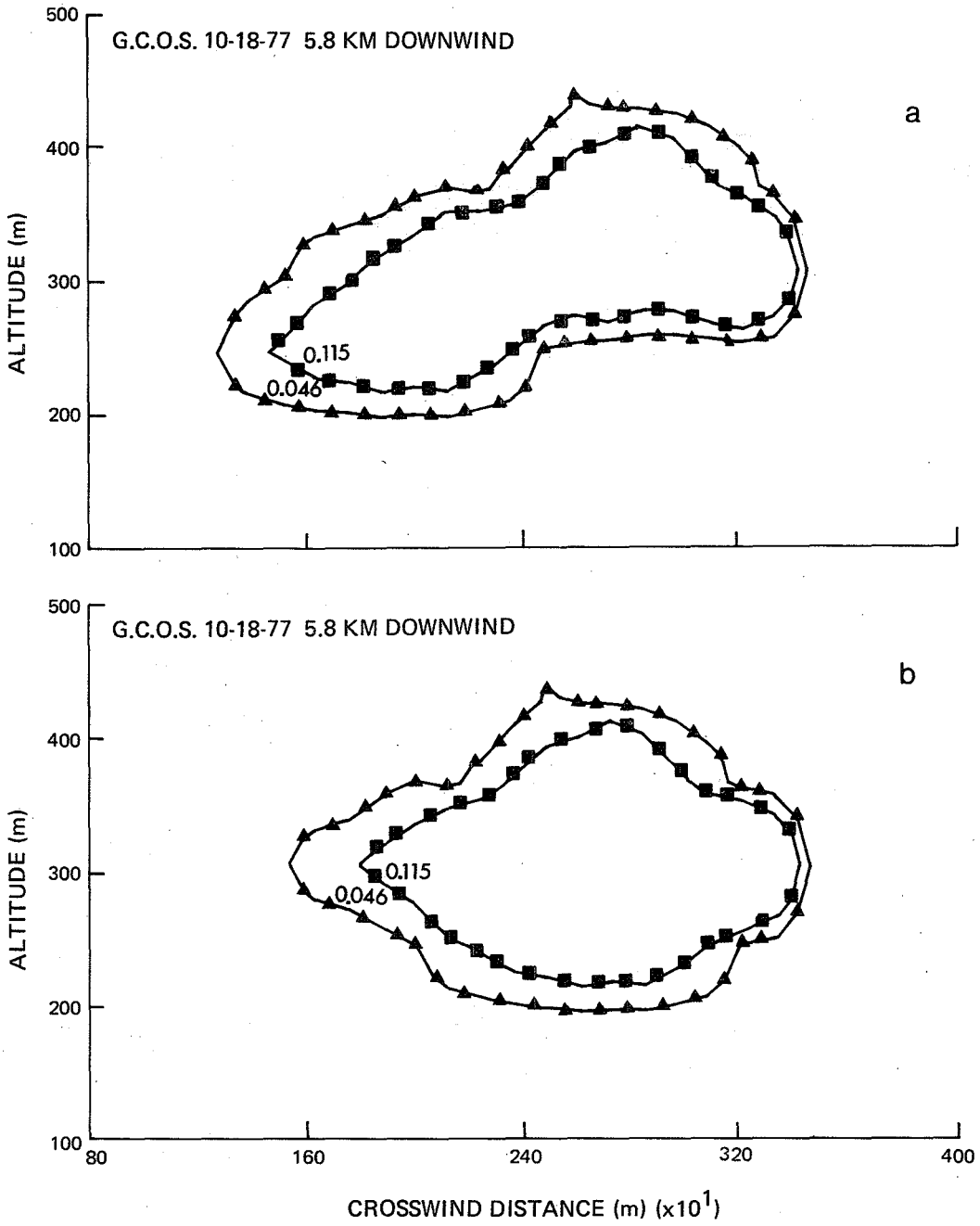

Figure 3.2. Plume contour plots without (top) and with (bottom) alignment of transect center of gravities.

distributions, and by lining up the centers of gravity of distributions obtained at different altitudes. The re-alignment of each transect on a single vertical line through corresponding centers of gravity of the individual transects better approximates the equivalent elliptical shape which the Gaussian plume model would produce and eliminates to a great extent the effect of plume distortion while retaining any enhanced diffusion effects due to cross-wind shear. It also removes errors associated with the relative positioning of the transects in space due to aircraft positioning error. However, if the positioning errors are in fact small the re-alignment can result in a distorted view of the true cross-sectional plume shape. Appendix E.2 contains the plume cross-section prior to re-alignment. In any subsequent model development where both cross-wind shear enhanced diffusion and distortion are quantitatively included, one would want to use for comparison the plume cross-section without the re-alignment.

An example of a contour with and without re-alignment is shown in Figures 3.2(a), 3.2(b). Sigmas were obtained by estimating the major and minor axes of an ellipse matched to the $0.1C_{max}$ contour to fix the ratio $r = \sigma_y/\sigma_z$. The area A within the $0.1C_{max}$ contour was then measured and an ellipse with this area and with semi-axes in the ratio r was fitted to yield

$$\sigma_z = \frac{1}{2.15}\left(\frac{A}{\pi r}\right)^{\frac{1}{2}} \tag{3.6}$$

$$\sigma_y = r\sigma_z \tag{3.7}$$

This approach has the advantage of simultaneously employing and averaging the full range of aircraft data. It also conserves cross-sectional area, an important parameter in atmospheric dispersion calculations, while abstracting the appropriate sigmas to fit the elliptical contour for a Gaussian plume model.

The main advantage in employing the contour method is that it gives a clear pictorial representation of a plume cross-section, so that the data can be "filtered". It, therefore, becomes possible to select only integral cross-sections for sigma abstraction, (such as Figure 3.2), and to eliminate any disjointed or broken plumes (see examples in Appendix E2), where problems would arise with a Gaussian model. Thus, the approximately 120 cross-sections considered in the previous report were reduced to a set of 54 integral cross-sections, from which it was felt more reliable sigma information could be obtained.

It should also be noted that the contour method clarifies the importance of multiple source effects in our analysis of G.C.O.S. data. Figures 3.3(a) and 3.3(b) illustrate predicted and measured contours due to the two major sources, the power house stack and the incinerator stack. Since the incinerator source strength is about 10% that of the powerhouse, its contribution to the total cross-sectional area is small. This small additional area can appear in the aircraft data either in the form of a small, separate plume, as is visible in

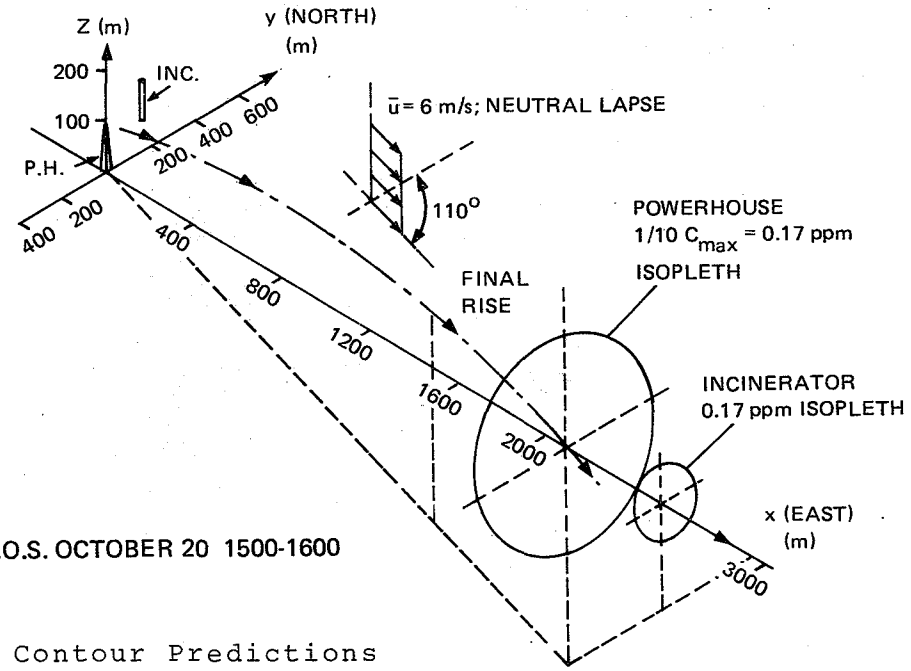

3.3a Contour Predictions

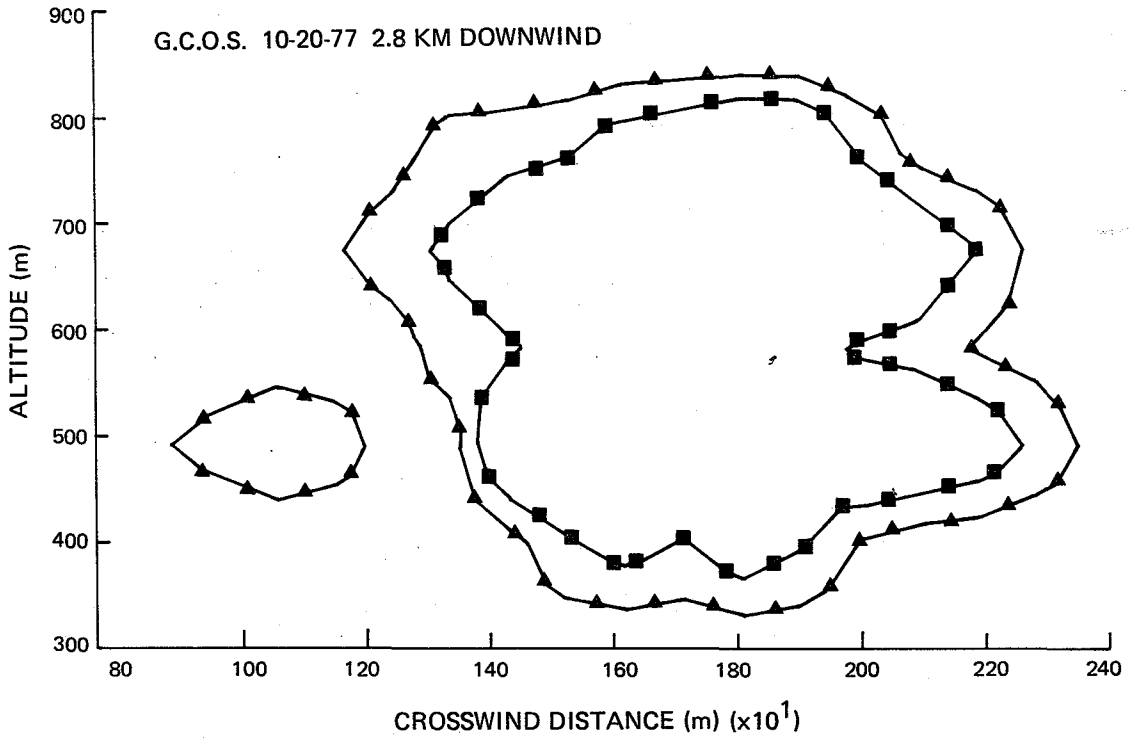

Figure 3.3b. Contour Measurements (Looking Downwind).

Figure 3.3a,b. Contours from Powerhouse and Incinerator Sources.

the raw data contours of Figure 3.3(b), or in the form of a small distortion of the powerhouse plume, as is visible in the smoothed data contours of Appendix E. Whether or not this additional area is included in the data reduction process has little effect on abstracted sigma values.

Figures 3.4 to 3.6 compare typical sigmas obtained from contour measurements with those calculated in the previous study. Contour sigmas are considerably different, and, to within ±15 to 20 percent accuracy, follow the correlations

$$\sigma_{y_{CONTOUR}} = 1.61\sigma_{y_{AREA}} = 1.30\sigma_{y_{EDGE}} = 1.18\sigma_{y_{STAT}} \tag{3.8}$$

Therefore, $\sigma_{y_{STAT}}$ from a transect distribution is the best estimate of $\sigma_{y_{CONTOUR}}$. However, as was mentioned before, $\sigma_{y_{STAT}}$ is sensitive to errors in the tails of the distribution, and is subject to large amounts of scatter.

In this report, the contour method of calculating sigmas is applied to 54 plume cross-sections measured in the 1977 study during periods of nearly constant lapse rate in the plume mixing layer. Among the 54 cases are several days where two consecutive cross-sections were completed by aircraft. Contour plots and abstracted

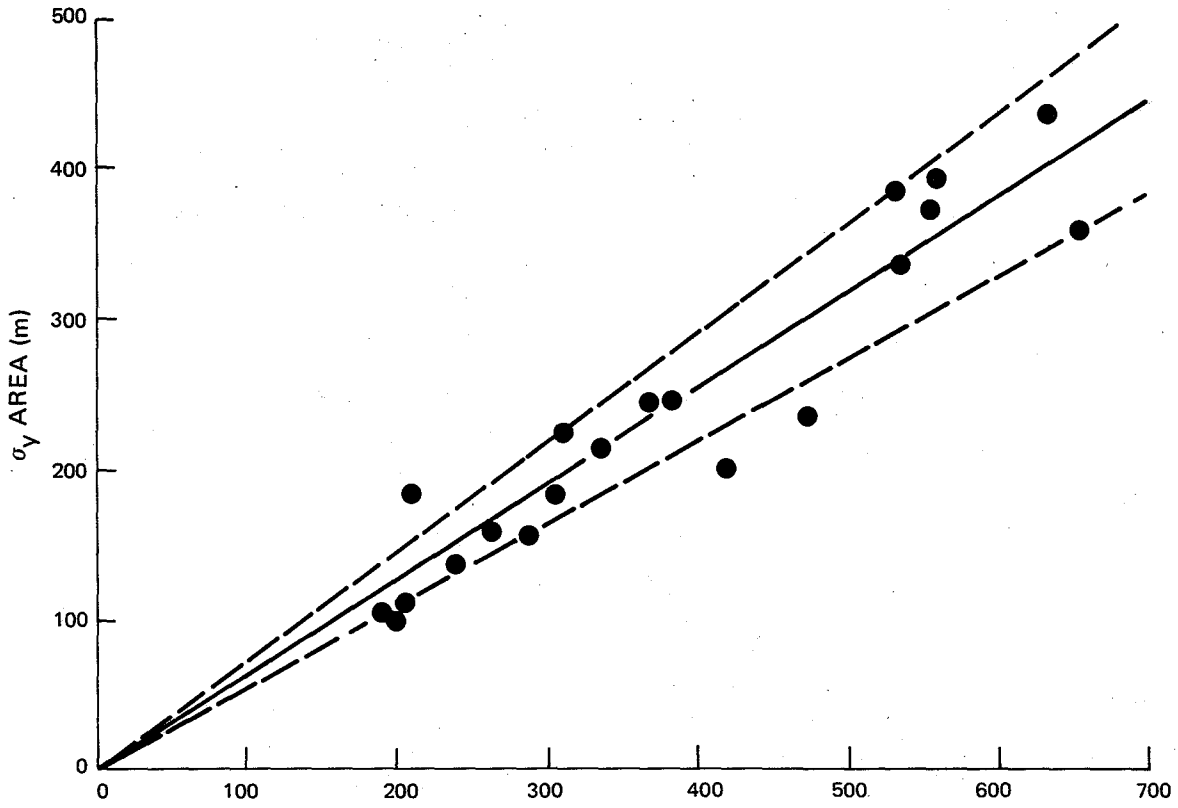

Figure 3.4. σ_{yAREA} versus $\sigma_{yCONTOUR}$. The solid line is equation (3.8), while the dotted lines indicate the root mean square error of $\pm$ 14% of the data about the line.

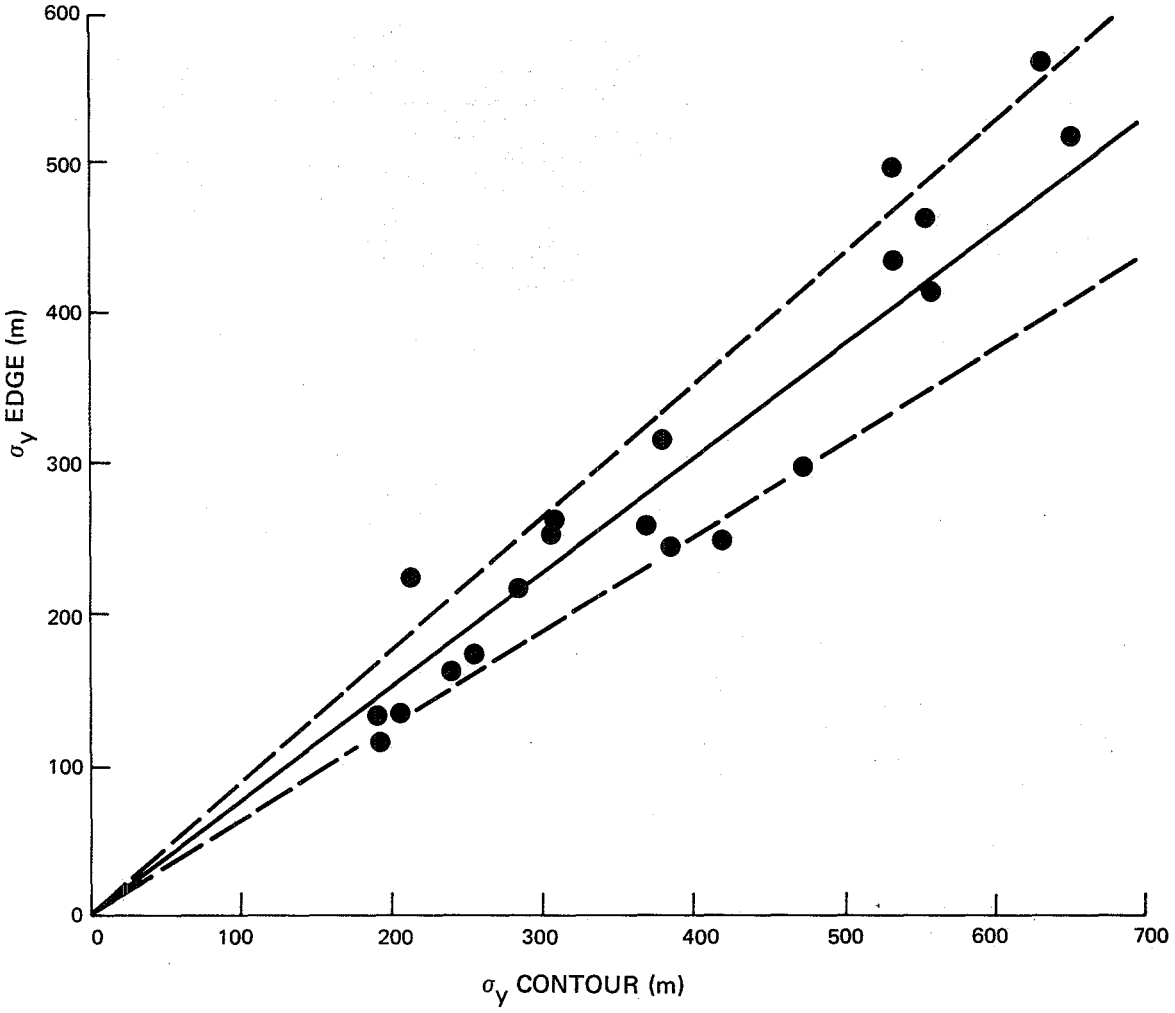

Figure 3.5. σ_{yEDGE} versus $\sigma_{yCONTOUR}$. The solid line is equation (3.8), while the dotted lines indicate the root mean square error of $\pm$ 17% of the data about the line.

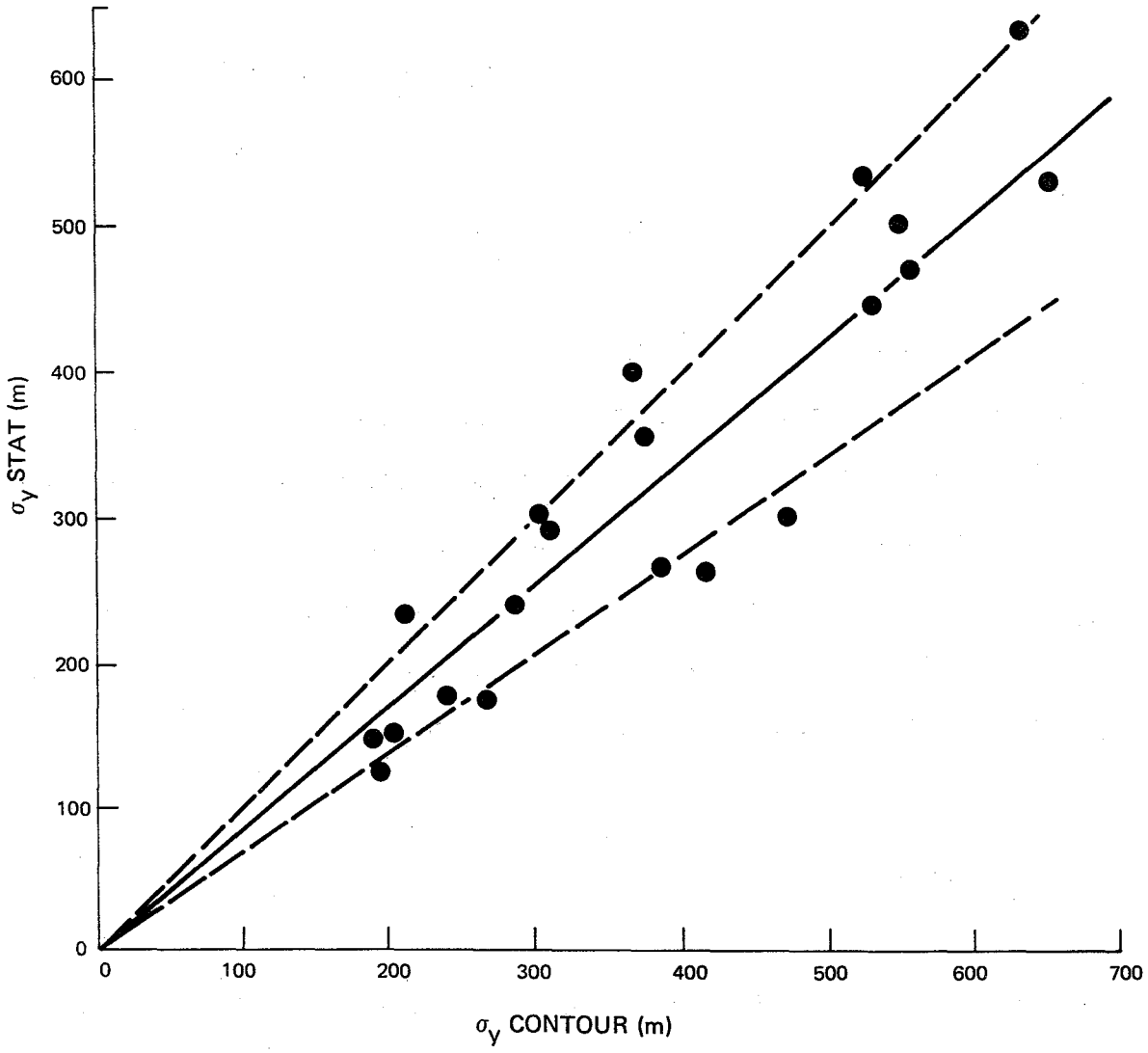

Figure 3.6. σ_{ySTAT} versus $\sigma_{yCONTOUR}$. The solid line is equation (3.8), while the dotted lines indicate the root mean square error of $\pm$ 19% of the data about the line.

data for the 54 selected plumes are summarized in Appendix E1. The remaining plume cross-sectional contours are given in Appendix E2.

3.5 ANALYSIS OF SIGMA MEASUREMENTS FROM CONSECUTIVE CROSS-SECTIONS

3.5.1 Analysis of Consecutive σ_z Data

In Figures 3.7 to 3.17, σ_z is shown versus downwind distance x for 11 cases where two consecutive aircraft cross-sections were completed. Additional information for these plots has been obtained from photographic records of the plume during the period when aircraft measurements were being made. Assuming that plume edges on the photographs correspond to the points where the concentration is 10 percent of that at the centerline, leads to

$$\sigma_{z_{PHOTO}} = D/4.3 \tag{3.19}$$

where D is the plume diameter. Both $\sigma_{z_{PHOTO}}$ and $\sigma_{z_{CONTOUR}}$ are plotted in the figures, along with the appropriate neutral or stable PG, TVA, BNL, and Briggs curves for comparison.

Recognizing the poor quality of the σ_z data compared to what one would expect for σ_y, several conclusions can be drawn from these plots:

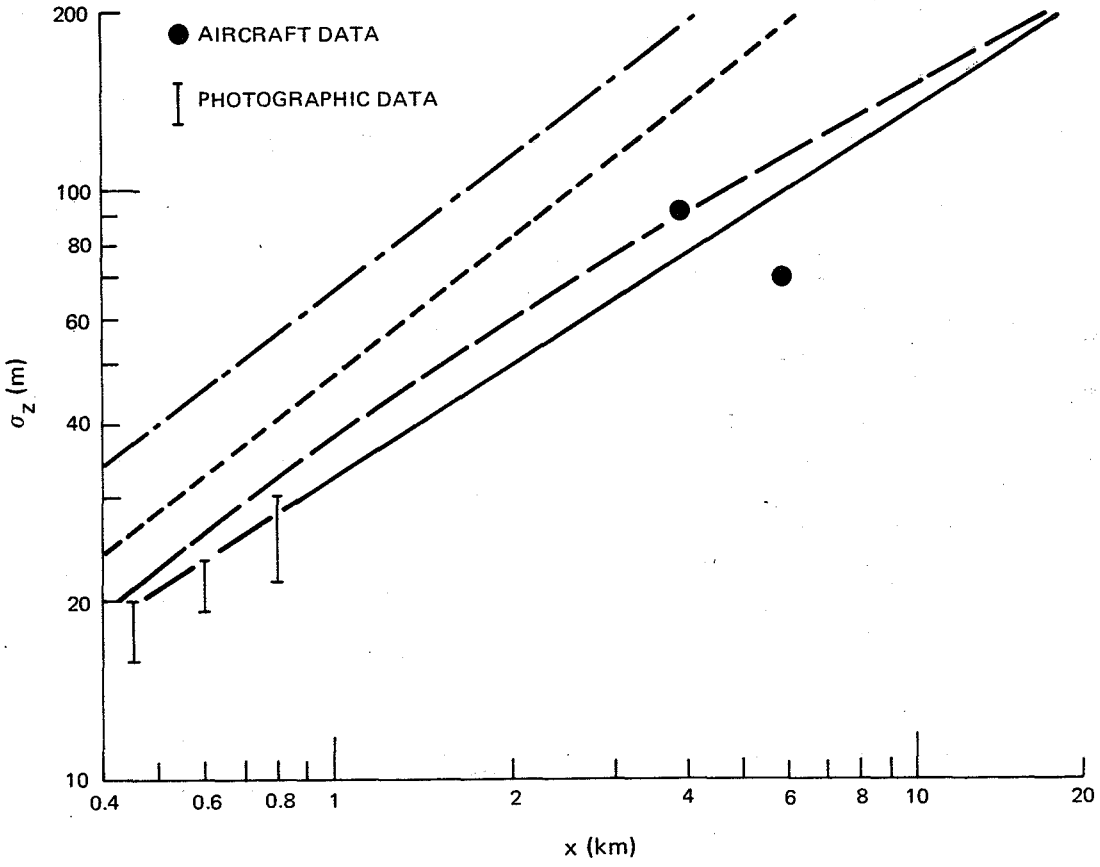

Figure 3.7. σ_z measurements for July 19, 0625-0800 under neutral lapse conditions with significant cross-wind shear. From top to bottom, curves show respectively TVA class A, BNL class C, Briggs class D, and Pasquill-Gifford class D.

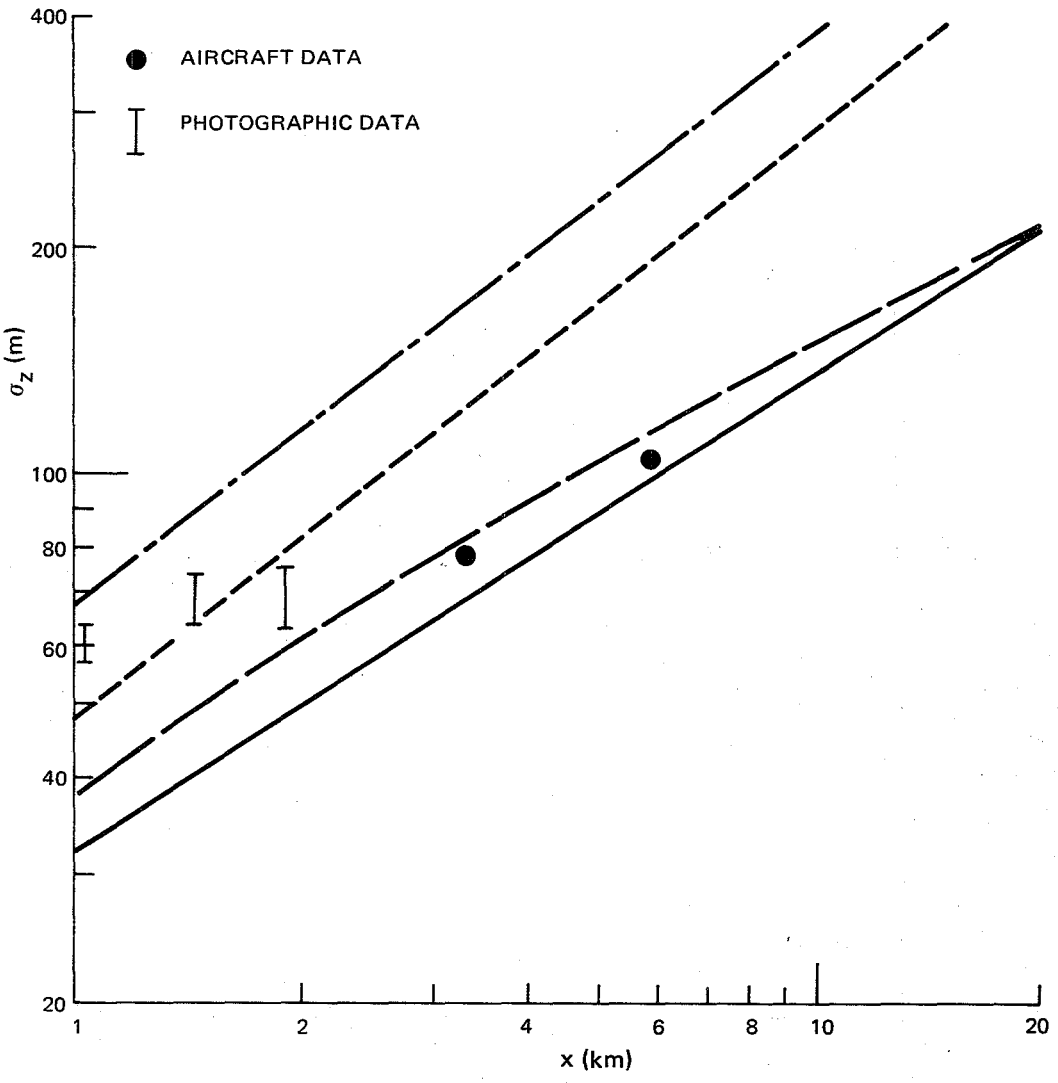

Figure 3.8. σ_z measurements for Oct. 19, 1537-1650 under neutral lapse conditions with negligible cross-wind shear. Curves as in Figure 3.7.

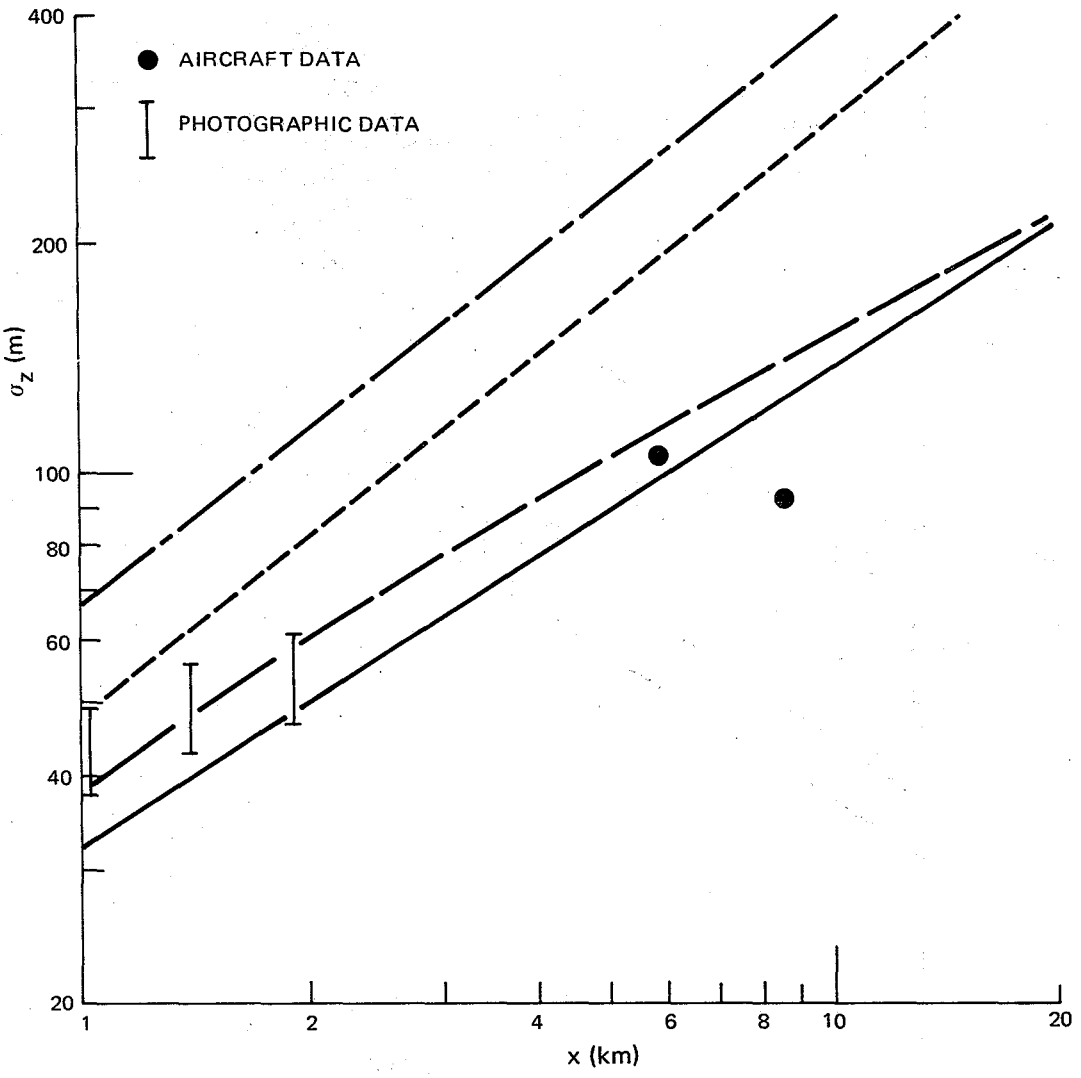

Figure 3.9. σ_z measurements for Oct. 20, 0900-1104 under neutral lapse conditions with significant cross-wind shear. Curves as in Figure 3.7.

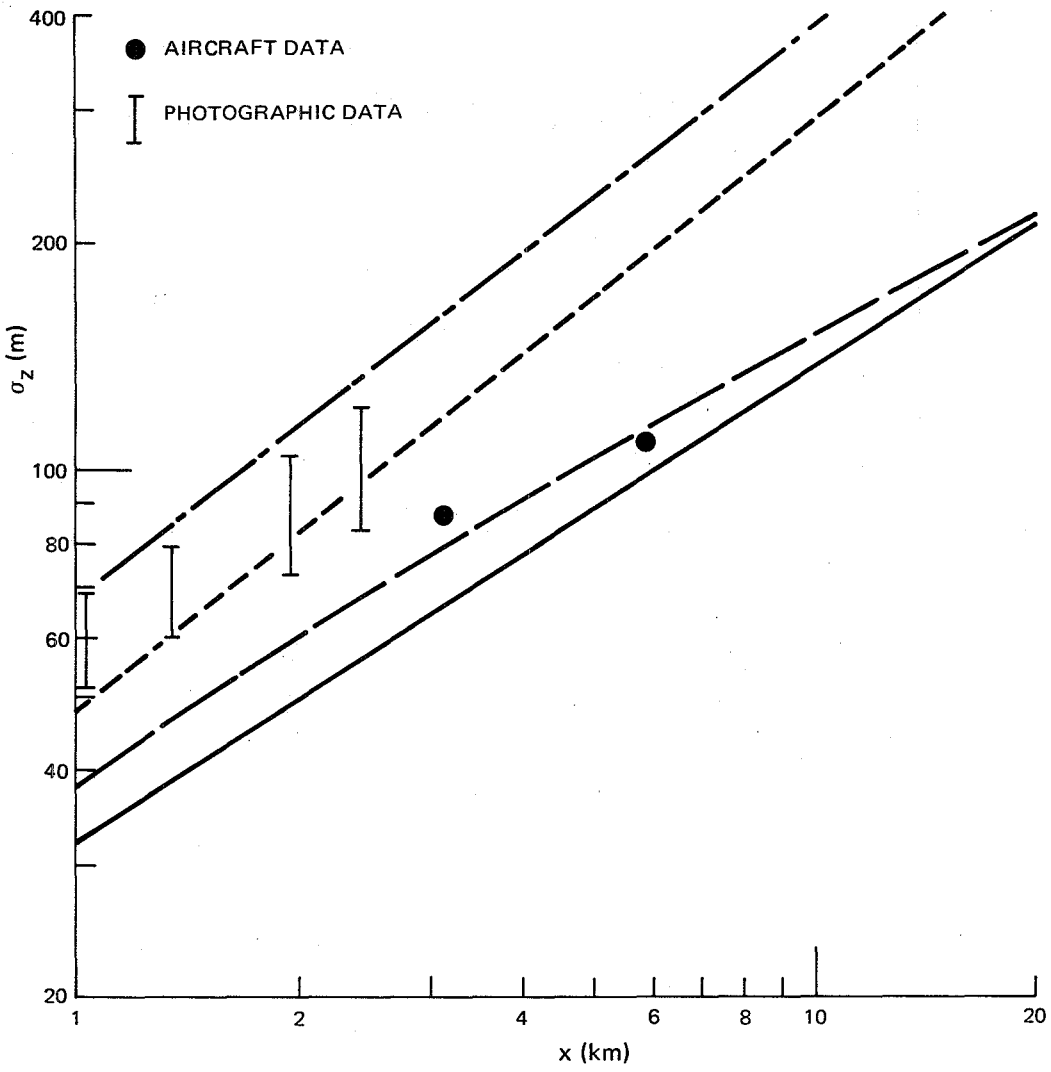

Figure 3.10. σ_z measurements for Oct. 24, 0912-1037 under neutral lapse conditions with negligible cross-wind shear. Curves as in Figure 3.7.

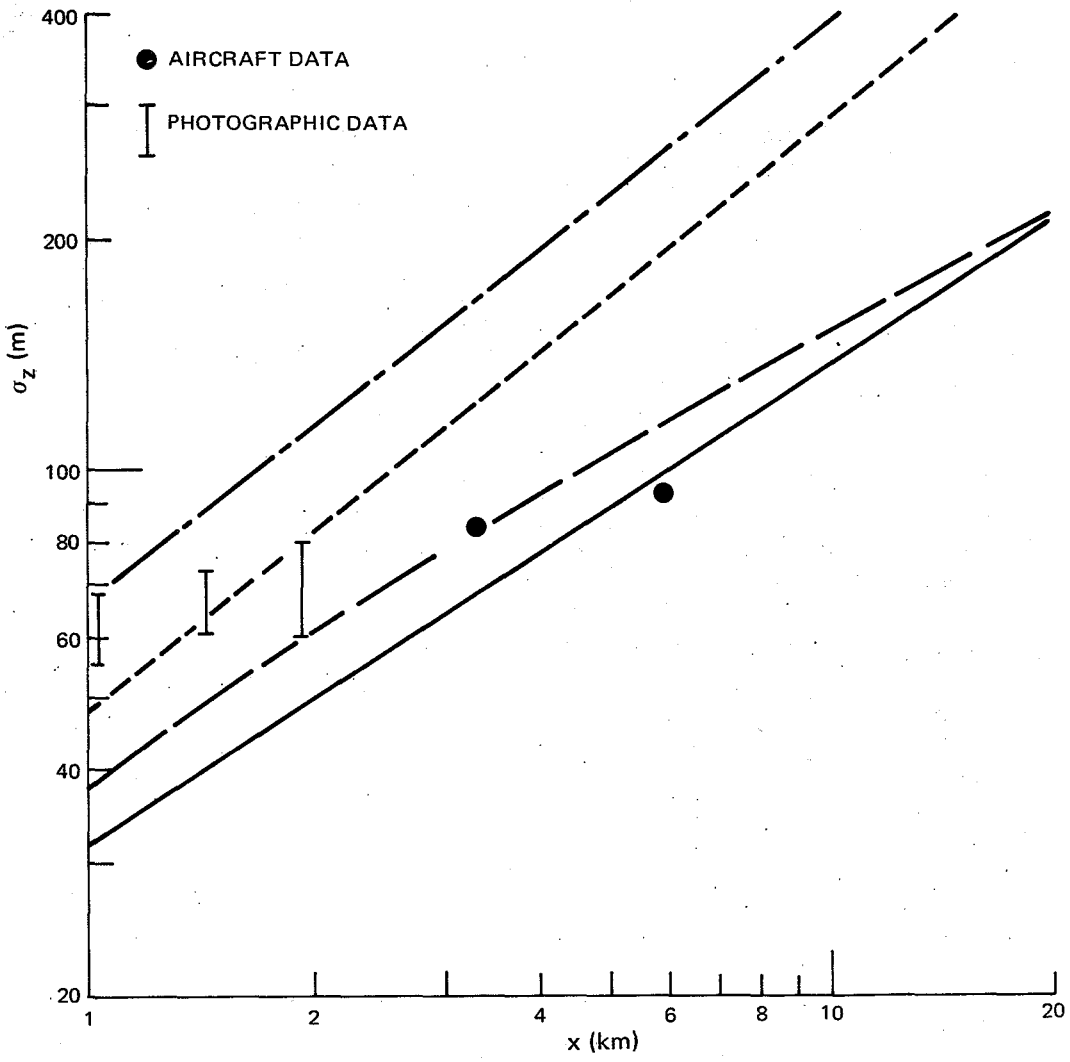

Figure 3.11. σ_z measurements for Oct. 25, 0915-1050 under neutral lapse conditions with significant cross-wind shear. Curves as in Figure 3.7.

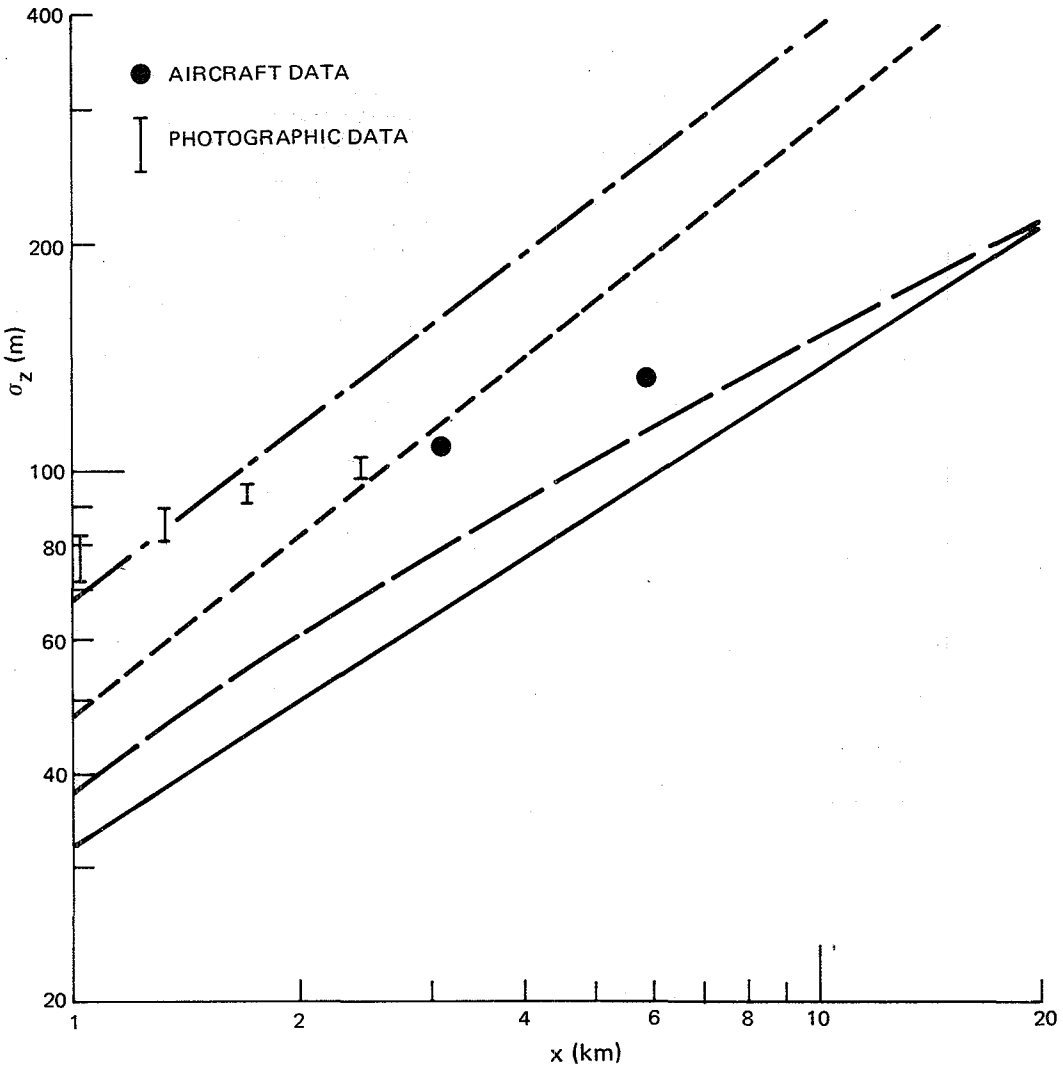

Figure 3.12. σ_z measurements for Oct. 25, 1525-1651 under neutral lapse conditions with significant cross-wind shear. Curves as in Figure 3.7.

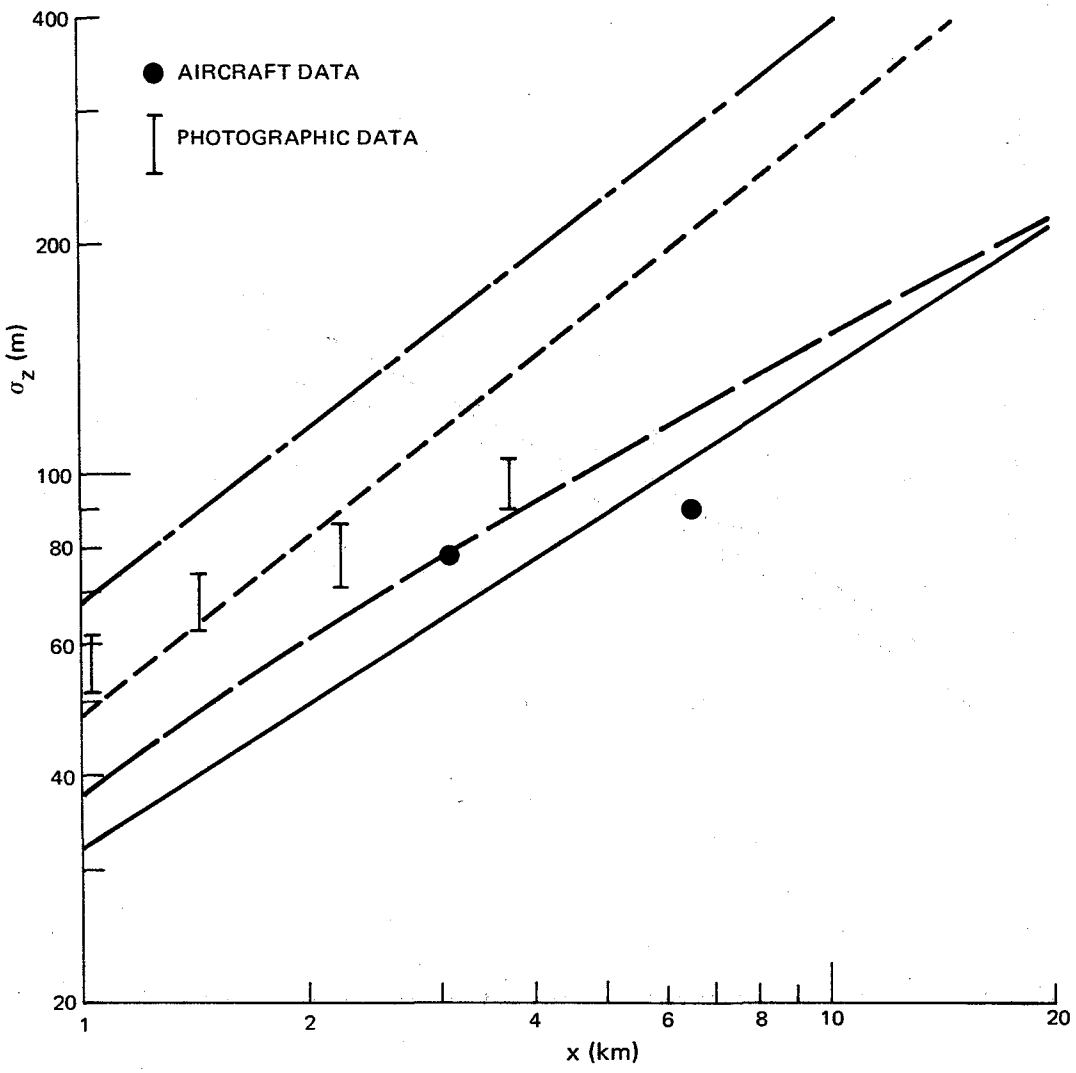

Figure 3.13. σ_z measurements for Oct. 26, 0926-1042 under neutral lapse conditions with significant cross-wind shear. Curves as in Figure 3.7.

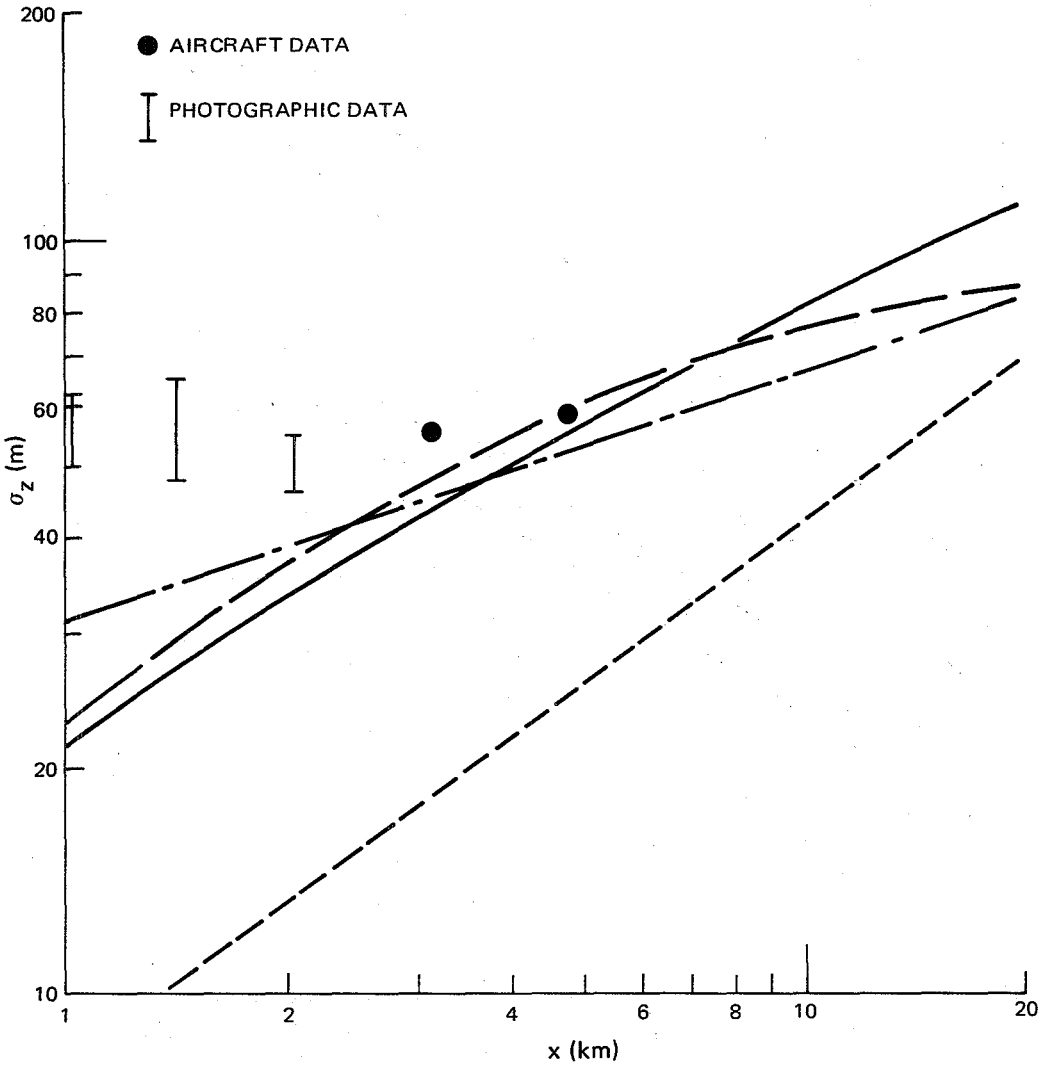

Figure 3.14. σ_z measurements for Mar. 28, 0725-0839 under stable conditions with significant cross-wind shear. From top to bottom on the right, curves show respectively, Pasquill-Gifford, class E, Briggs class E, TVA class C, and BNL class D.

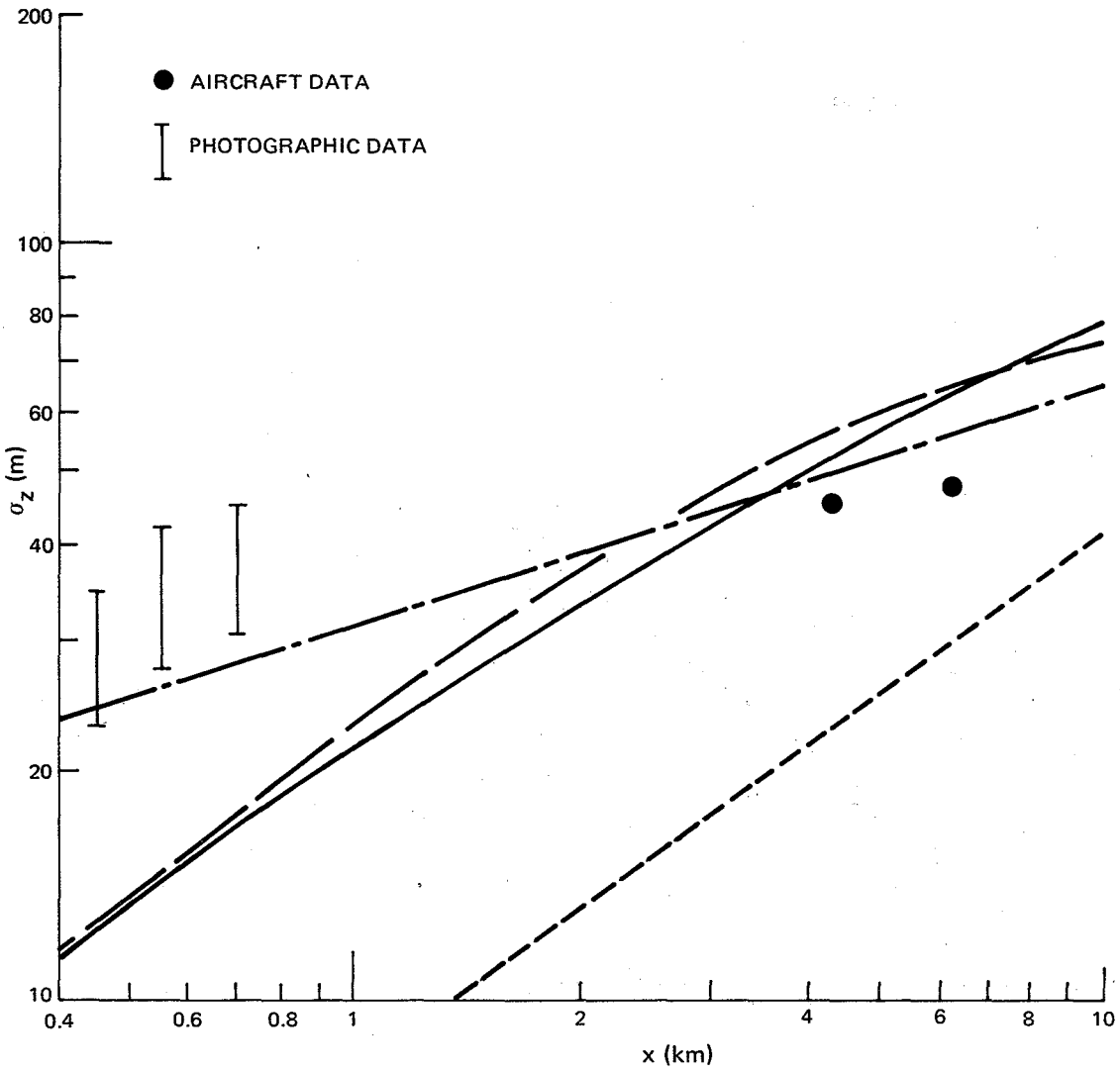

Figure 3.15. σ_z measurements for July 26, 0650-0752 under stable conditions with significant cross-wind shear. Curves as in Figure 3.14.

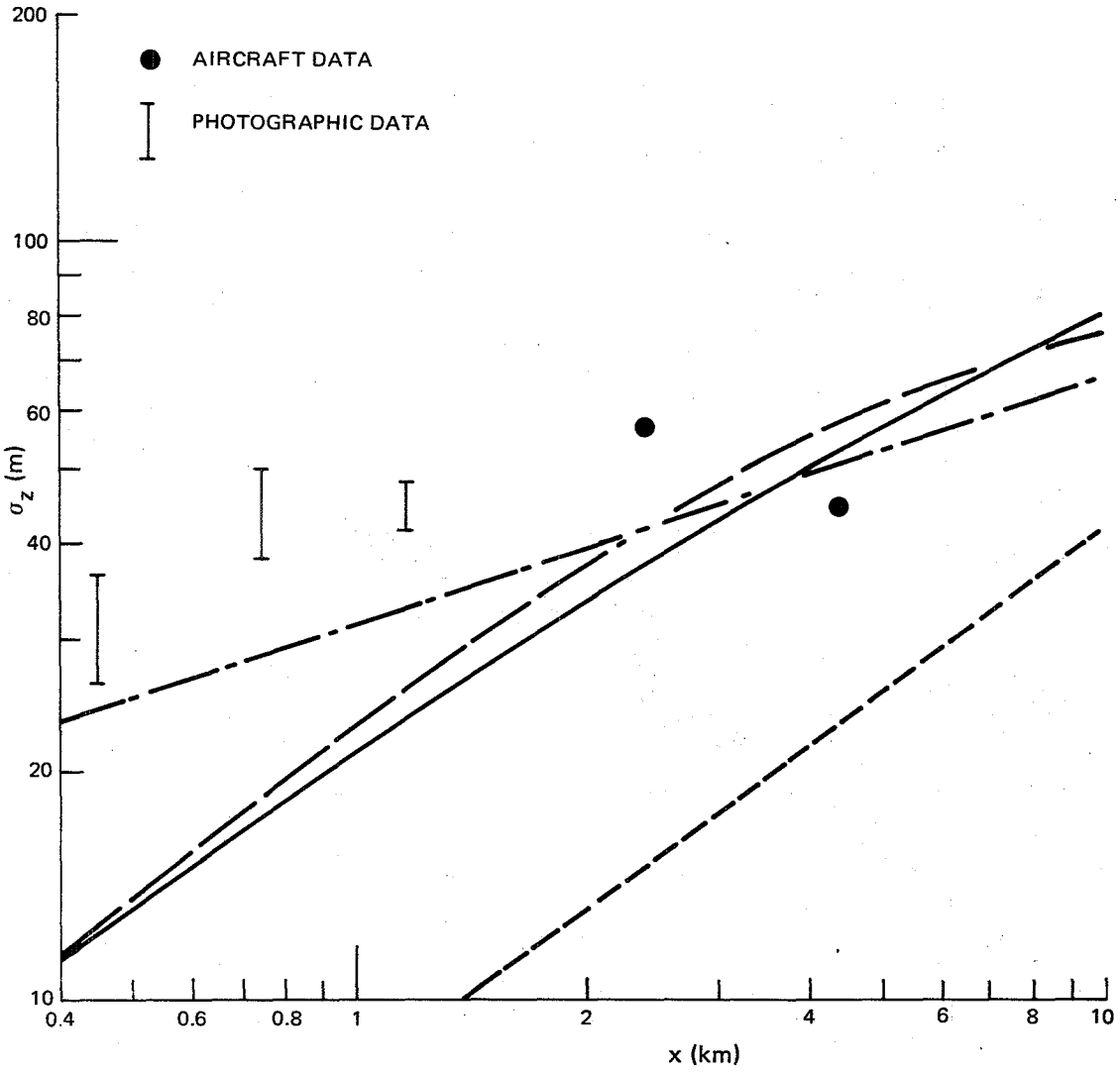

Figure 3.16. σ_z measurements for Oct. 15, 1410-1455 under stable conditions with significant cross-wind shear. Curves as in Figure 3.14.

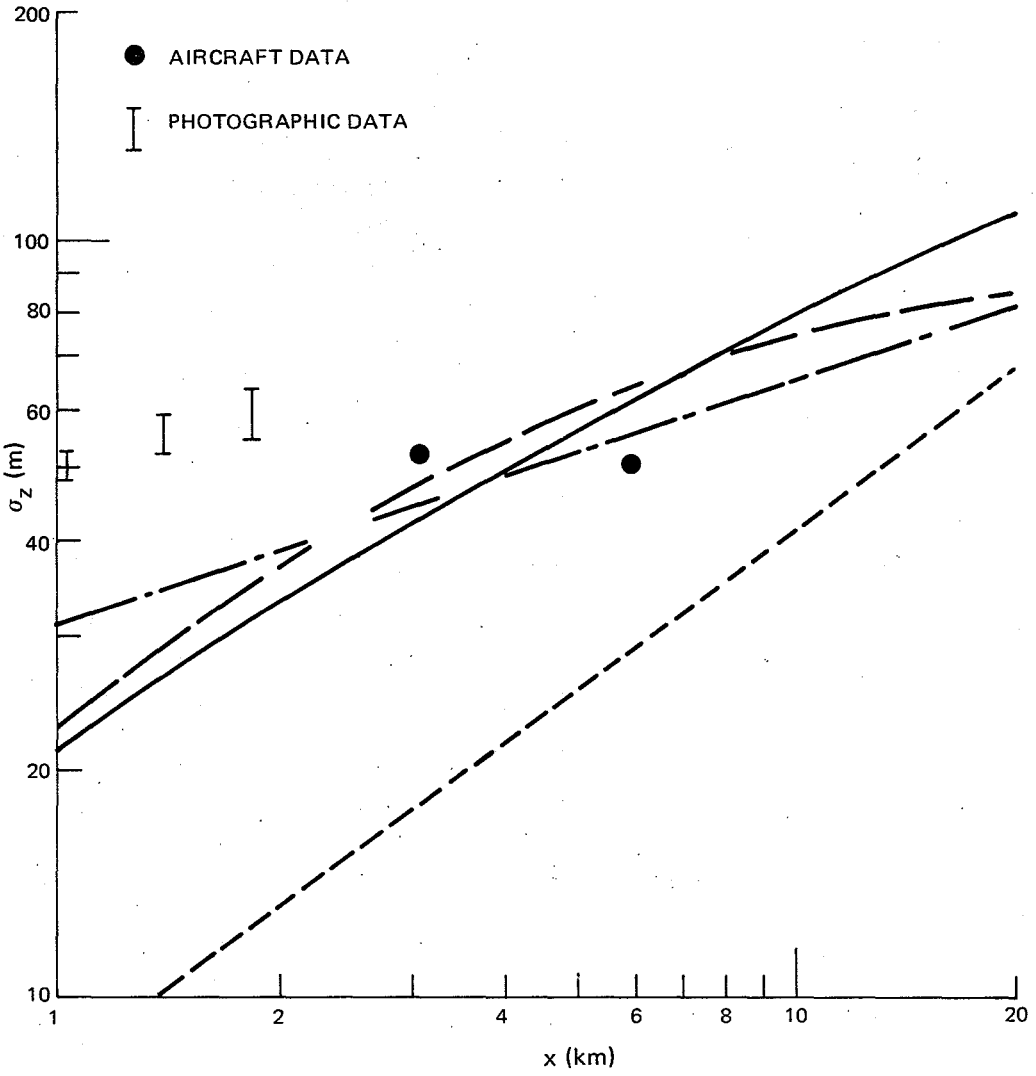

Figure 3.17. σ_z measurements for Oct. 18, 0905-1020 under stable conditions with significant cross-wind shear. Curves as in Figure 3.14.

(i) Photographic and contour σ_z values are generally consistent, although in some plots (Figs. 3.10, 3.13), it does appear the photographic values are slightly higher. This difference can be attributed to errors of perspective and to errors associated with equating the visible plume edges with the 10 percent concentration levels. The photographic sigmas would be smaller if the visible plume edges actually extend out to perhaps the 2 percent concentration levels.

(ii) During the period of one to two hours required for the aircraft to complete two consecutive cross-sections, photographic σ_z values vary over a range of ±5% approximately for the best case (Fig. 3.12) to a range of ±20% approximately for the worst case (Fig. 3.15). This variation gives an indication of the uncertainty in a contour σ_z which results from changes in conditions during the finite sampling time. For some runs, stability changes during the measurement period are sufficient to produce σ_z values which appear to decrease with increasing x (Figs. 3.7, 3.9, 3.16).

(iii) During neutral to weakly stable lapse conditions (Figs. 3.7 to 3.13), Briggs' D curve appears to best represent the magnitude and rate of growth of σ_z beyond about 2 km from the source. Near the source, however, measured σ_z values appear to be higher than Briggs' predictions, and closer to TVA A curve and BNL C curve predictions. The presence of wind directional shear (Figs. 3.7, 3.9, 3.11, to 3.13)

appears to have no significant effect on the no shear σ_z behaviour (Figs. 3.8, 3.10).

(iv) During stable conditions (Figs. 3.14 to 3.17), Briggs' E curve again represents σ_z versus x behaviour beyond about 2 km from the source, while the higher TVA C curve predictions are more accurate closer to the source. In this case, however, the TVA C curve also predicts measured values reasonably well over the entire range of measurement. For all these stable measurements, wind directional shear was present.

3.5.2 Analysis of Consecutive σ_y Data

In Figures 3.18 to 3.20, σ_y is shown versus downwind distance x for the same 11 cases presented in the previous section where two consecutive aircraft cross-section were completed. For all sets of measurements, σ_y increases as downwind distance x increases. The influence of atmospheric stability and wind directional shear can be seen in the aircraft data:

(i) The effect of wind shear during neutral to weakly stable lapse conditions may be seen by comparing Figures 3.18 and 3.19. When no shear is present, measured σ_y values are in good agreement with both the PG and Briggs D curve (Figure 3.18). However, measured σ_y values are larger than the D curve predictions when directional shear

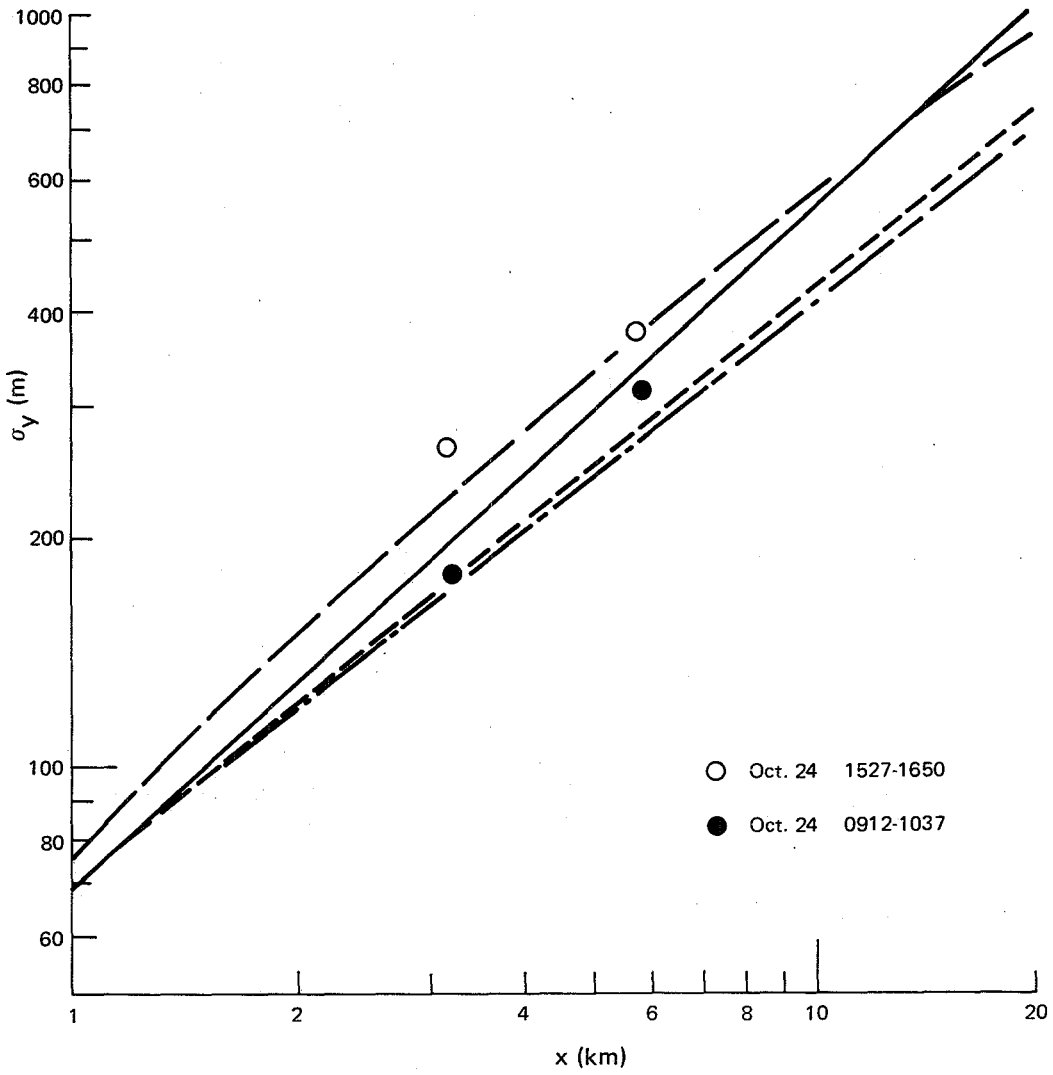

Figure 3.18. σ_y measurements from consecutive aircraft cross-sections under neutral conditions with negligible cross-wind shear. From top to bottom, curves show respectively Briggs class D, Pasquill-Gifford class D, BNL class C, and TVA class A.

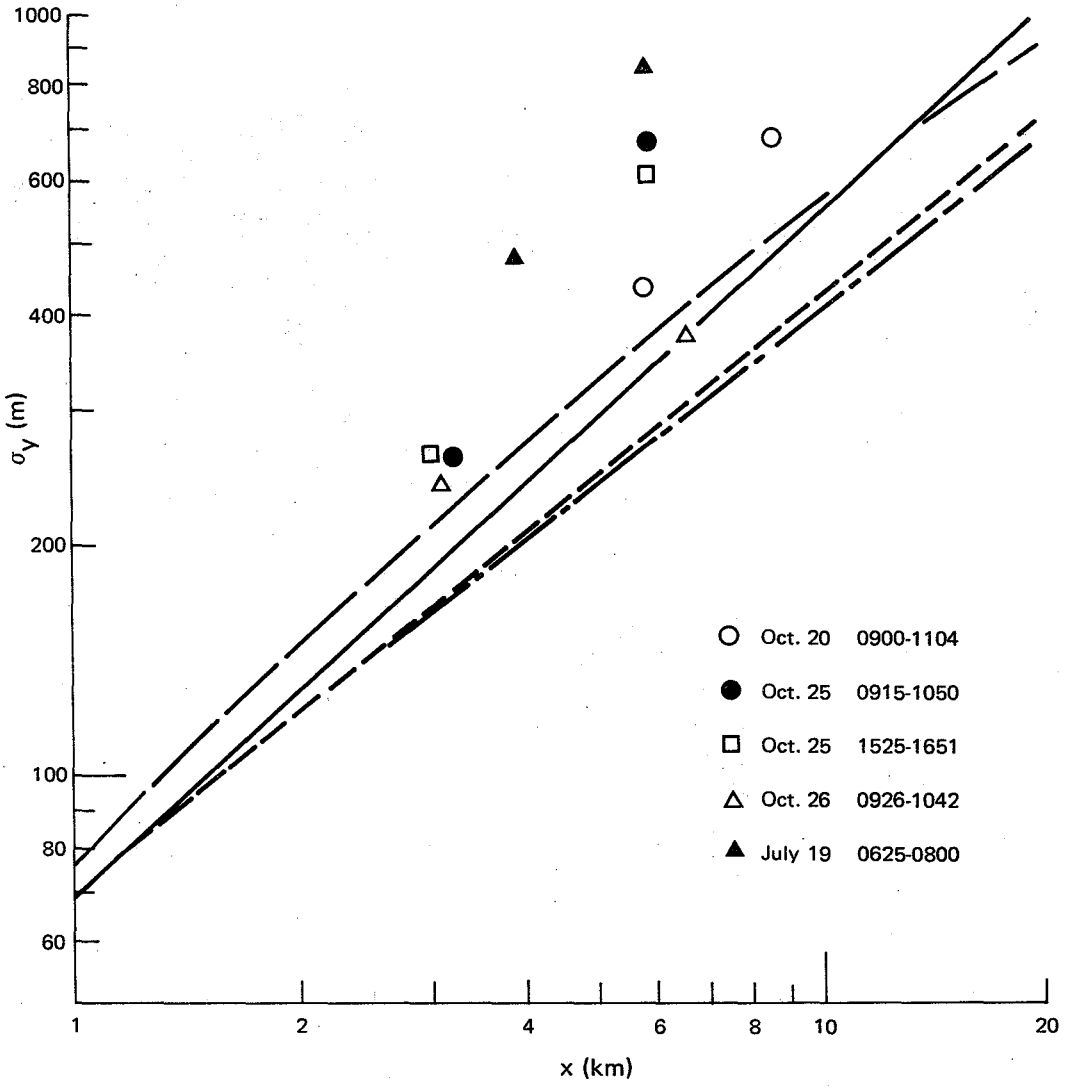

Figure 3.19. σ_y measurements from consecutive aircraft cross-sections under neutral conditions with significant cross-wind shear. Curves as in Figure 3.18.

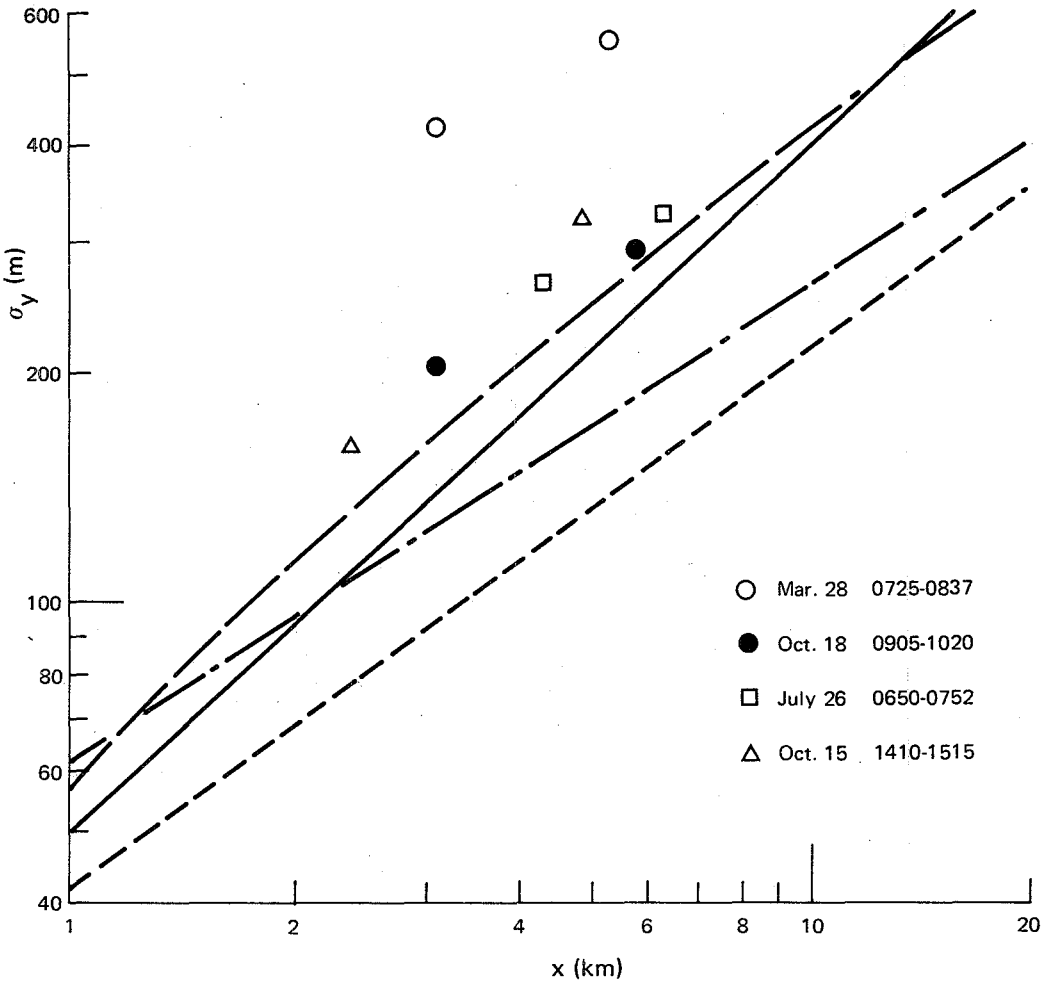

Figure 3.20. σ_y measurements from consecutive aircraft cross-sections under stable conditions with significant directional shear. From top to bottom on the right, curves show respectively Pasquill-Gifford class E, Briggs class E, TVA class C and BNL class D.

is present (Figure 3.19). Quantitative information on the dependence of σ_y on shear is difficult to establish from this data since both stability and shear parameters vary from case to case, and since consecutive pibal runs sometimes give different directional shear information. Directional shear effects will be considered further in a later section; however, Figure 3.19 shows that the effect is significant and equivalent to a change in stability from Pasquill-Gifford D class to perhaps C or B class.

(ii) The effect of atmospheric stability on σ_y can be seen by comparing Figure 3.19 and 3.20, in which stability changes from near-neutral to stable. Wind directional shear is present in both plots. As discussed above, the PG D curve underpredicts σ_y during neutral conditions when wind shear is significant (Fig. 3.19). Similarly, the PG E curve underpredicts σ_y during stable conditions when wind shear is present (Fig. 3.20). The trend to lower σ_y with increasing stability is clear, however.

3.6 ANALYSIS OF ALL SIGMA DATA FOR CONSTANT LAPSE CONDITIONS

3.6.1 Near Neutral, No Directional Shear Cases

Figures 3.21 and 3.22 show the behaviour of σ_y and σ_z with x for 15 cross-sections obtained by the aircraft during near-neutral lapse conditions when the wind field exhibited negligible directional

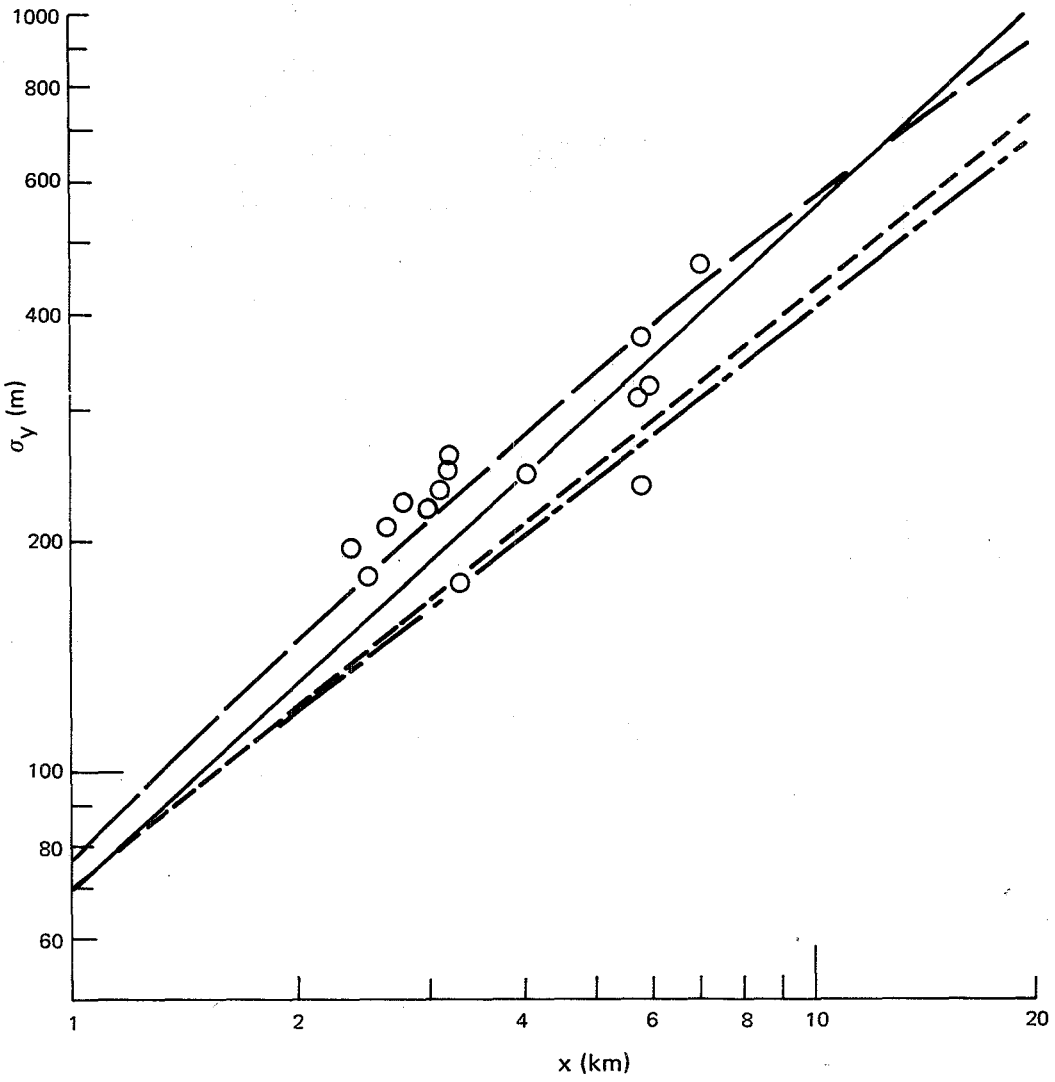

Figure 3.21. σ_y measurements under neutral conditions with negligible cross-wind shear. Curves as in Figure 3.18.

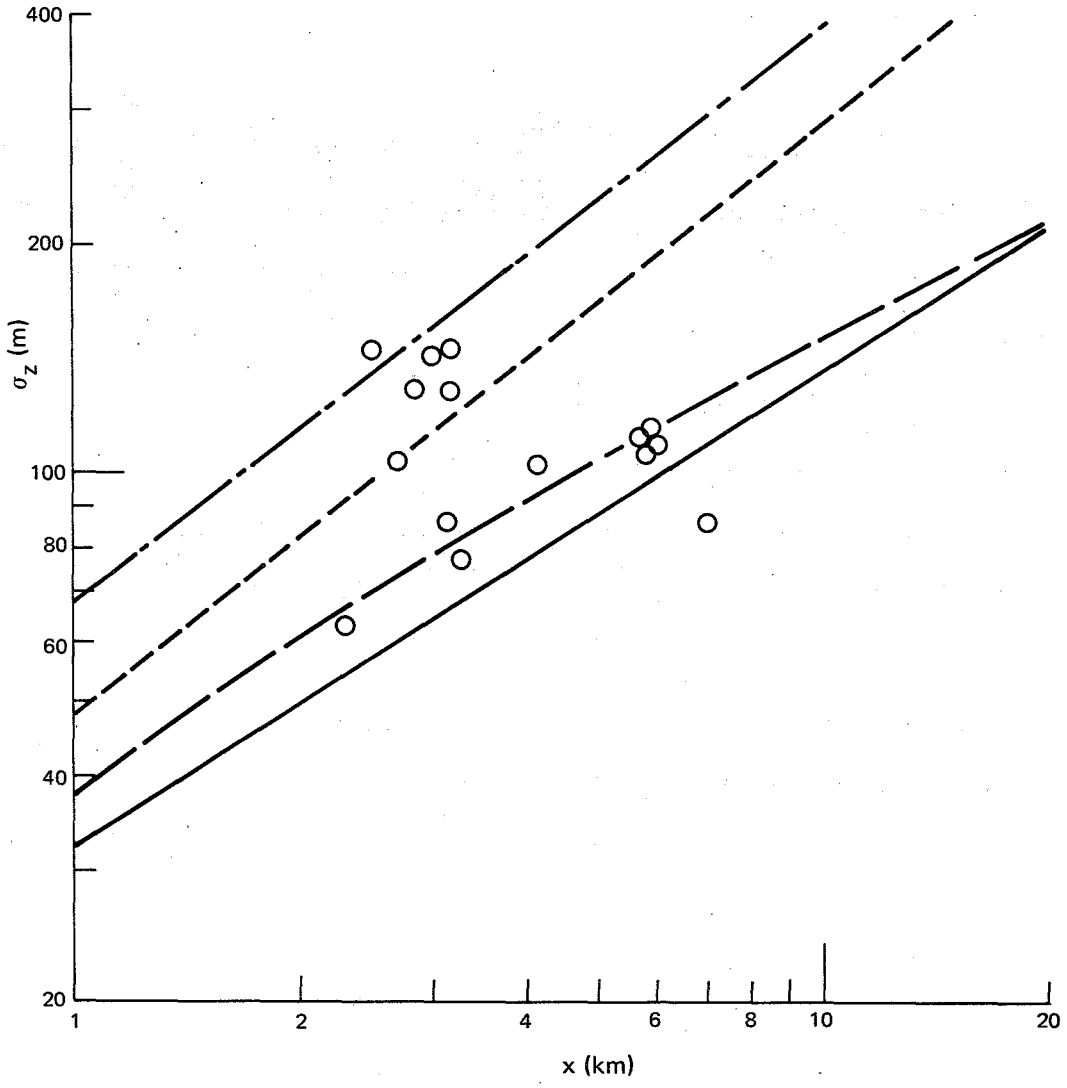

Figure 3.22. σ_z measurements under neutral conditions with negligible cross-wind shear. Curves as in Figure 3.7.

shear. Applicable consecutive cross-section results from the previous section are included in these plots, along with single cross-sections measured at different times during the study.

Values of σ_y correlate well with the PG and Briggs' D curve, and, compared with previous results[24,26], scatter in the data is relatively small. Some scatter does remain, however, in the σ_z plot, although nine data points still correlate well with the Briggs' D curve. Considering the sensitivity of σ_z to stability changes, the experimental uncertainty of up to ±20% suggested by the photographic data, and the relatively coarse resolution of measurements in the vertical, it seems that some scatter in σ_z is unavoidable.

An attempt was made to reduce σ_z scatter by reclassifying data according to the stability ratio of the air layer near the ground:

$$SR = g \frac{\partial \theta}{\partial z} \frac{H_s^2}{T_o U_o^2}$$

where g is gravitational acceleration, $\frac{\partial \theta}{\partial z}$ is potential temperature gradient, H_s is stack height, T_o is air temperature at stack top, and U_o is windspeed at stack top. The stability ratio parameter is one form of the Richardson number. Figure 3.23 shows that those data points which follow Briggs' D curve are those points with the smaller stability ratio (SR < 0.005). Scatter remains, however, for these data points with SR > 0.005 and no clear trend can be identified.

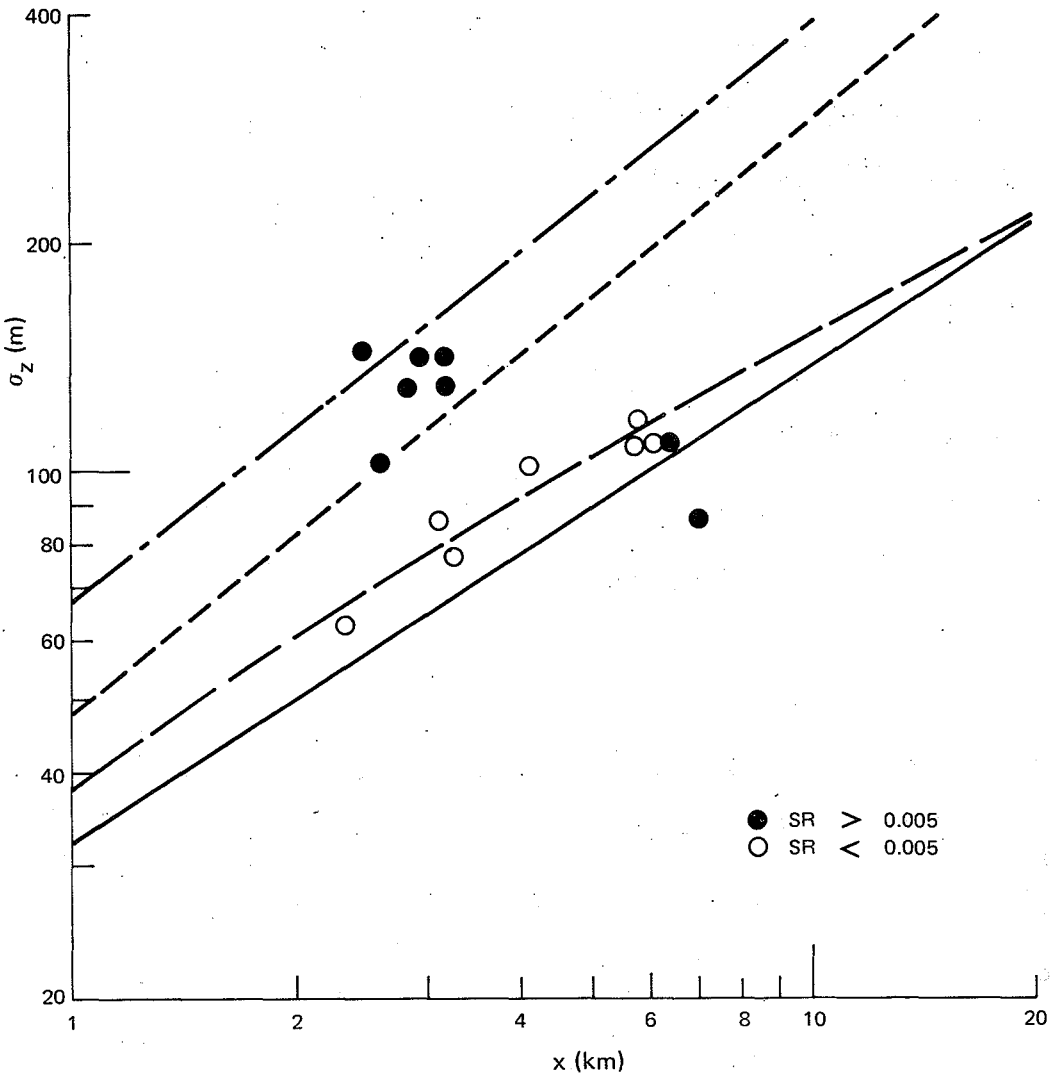

Figure 3.23. A replot of Figure 3.22, considering the stability ratio parameter.

3.6.2 Near Neutral-Weakly Stable Cases with Directional Shear

Figures 3.24 and 3.25 show the variation of σ_y and σ_z with x for 21 cross-sections obtained by the aircraft when lapse conditions were in the near neutral to weakly stable range, and when appreciable directional shear was evident in the wind field. Directional shear leads to an increase in σ_y of up to a factor of about 3 over no shear conditions, while σ_z values are not significantly changed. The large scatter in σ_y data which appears in Figure 3.24 and in other studies is therefore due in part to variable amounts of cross-wind shear.

3.6.3 Stable with Directional Shear

Figures 3.26 and 3.27 show the variation of σ_y and σ_z with x for 17 cross-sections obtained by the aircraft when lapse conditions were stable and when the wind field exhibited directional shear. Once again, it appears that directional shear leads both to scatter in the data and a general increase in σ_y over predictions for the no shear case.

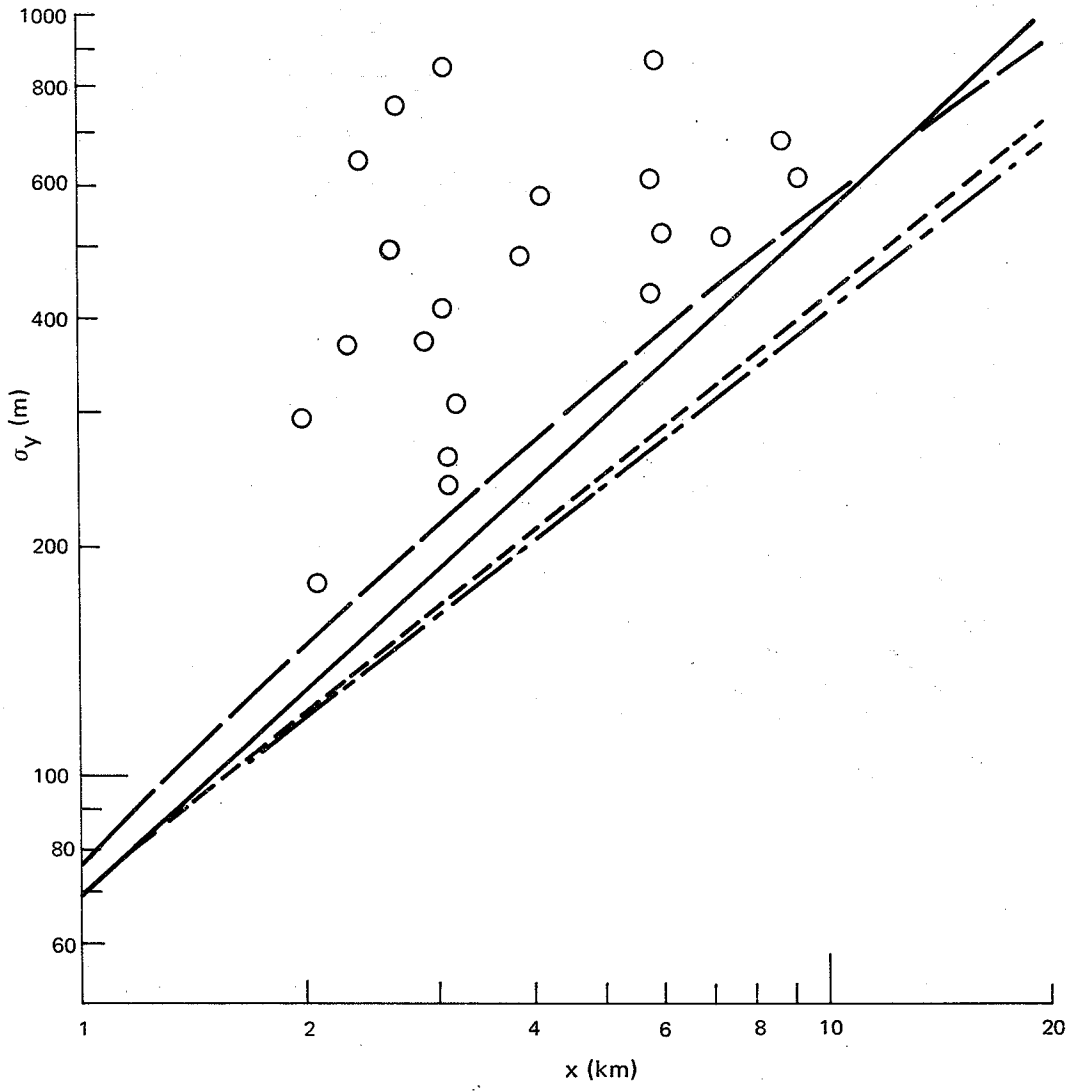

Figure 3.24. σ_y measurements under neutral to weakly stable conditions with significant cross-wind shear. Curves as in Figure 3.18.

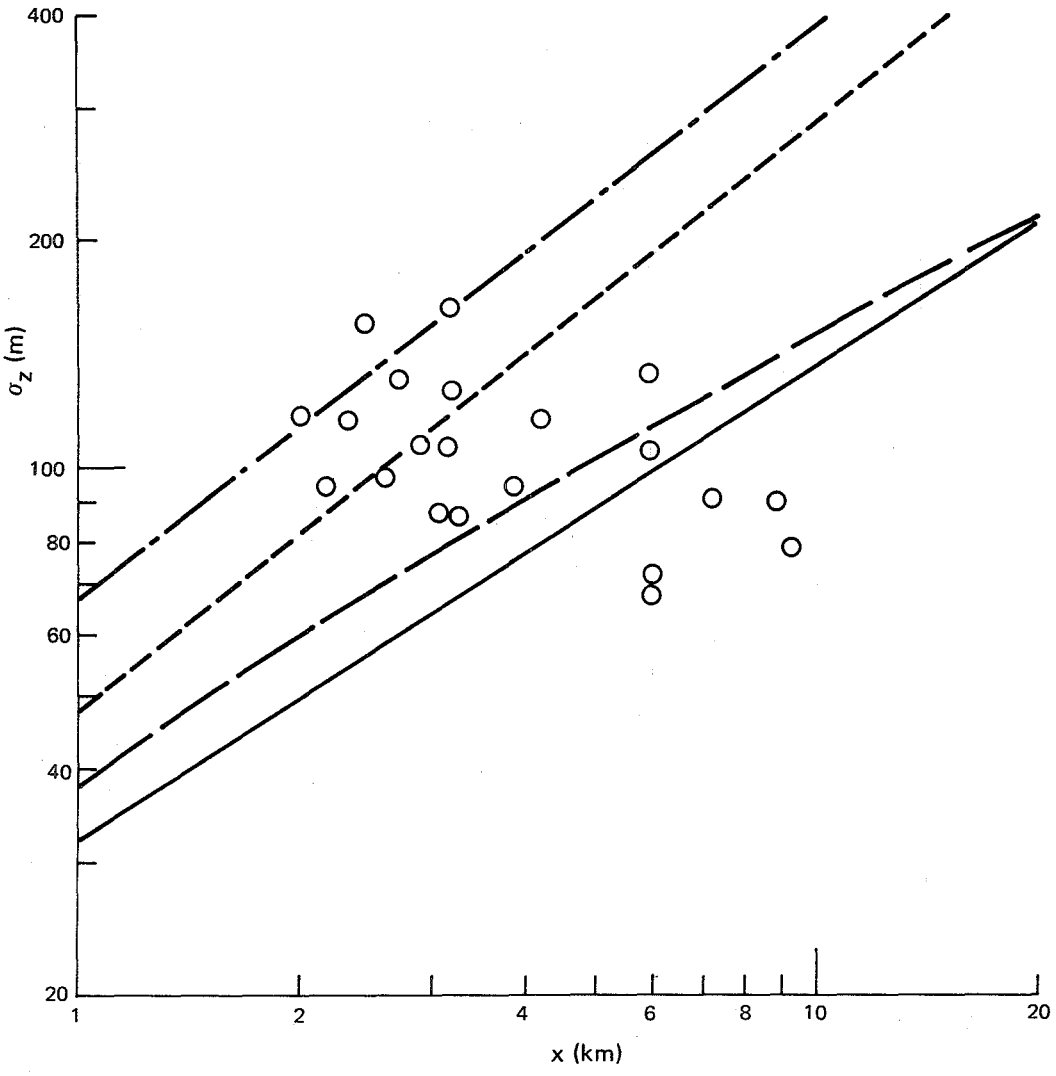

Figure 3.25. σ_z measurements under neutral to weakly stable conditions with significant cross-wind shear. Curves as in Figure 3.7.

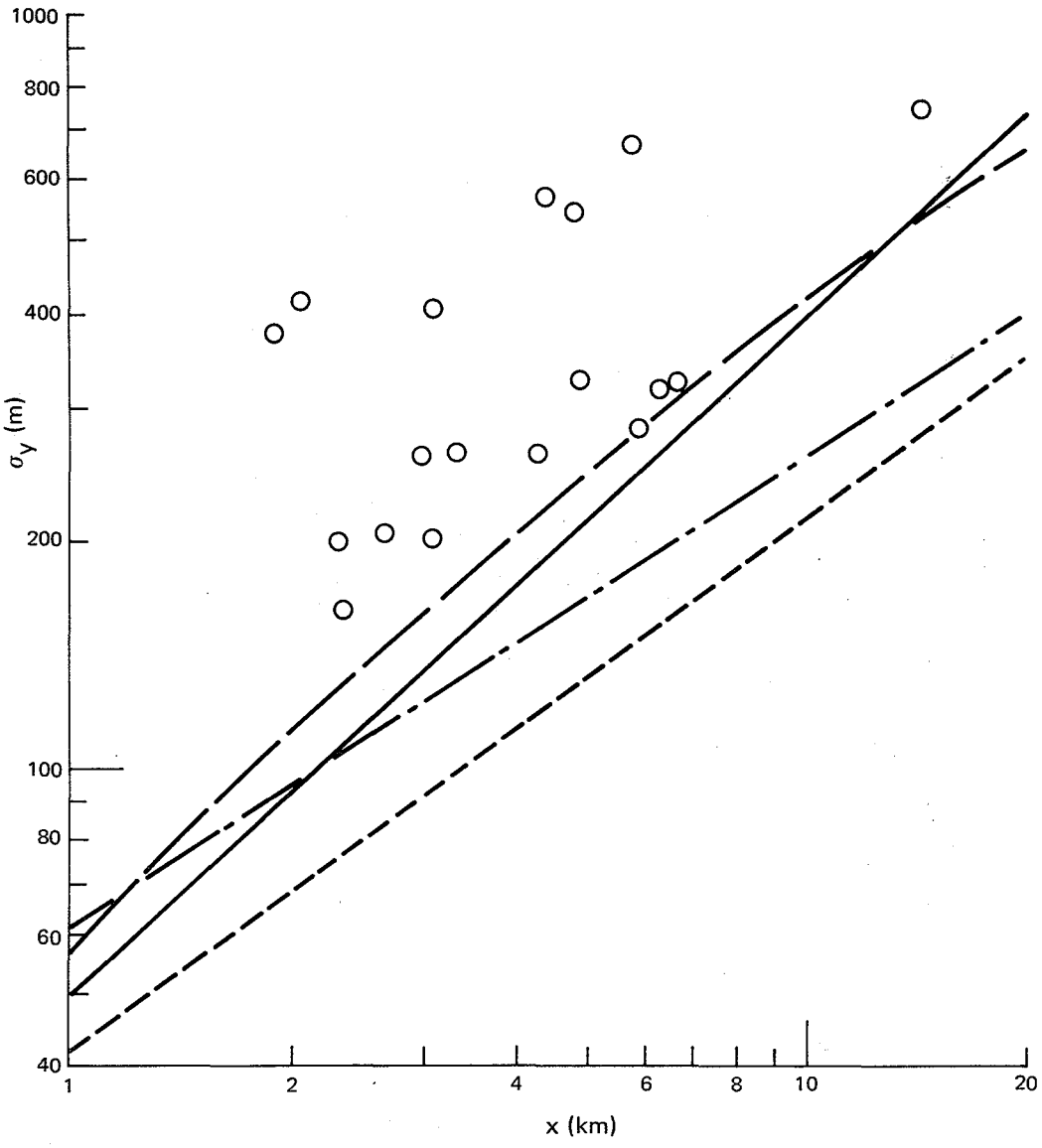

Figure 3.26. σ_y measurements under stable conditions with significant directional shear. Curves as in Figure 3.20.

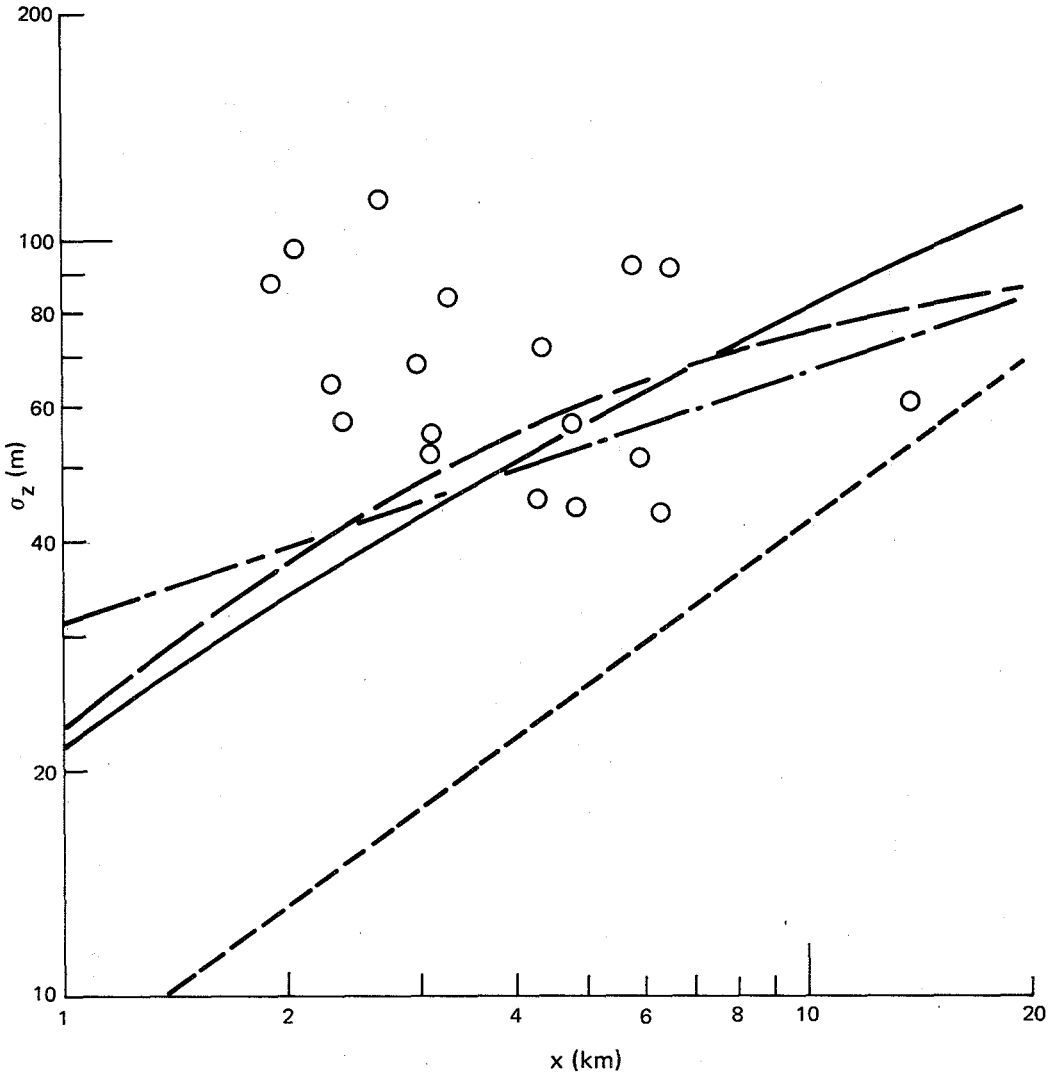

Figure 3.27. σ_z measurements under stable conditions with significant cross-wind shear. Curves as in Figure 3.14.

3.7 ANALYSIS OF SOME SIGMA PARAMETERS

3.7.1 Multiple Source and Terrain Effects

Multiple source and irregular terrain effects on the σ_y and σ_z data may possibly be identified from the dependence of the sigma measurements on wind direction, if other factors such as stability and wind shear are approximately constant. The neutral, no shear data of Figures 3.21 and 3.22 are, therefore, the best choice for an evaluation of wind direction effects.

To try and identify such effects, the percentage deviation between each measured sigma and the corresponding Briggs' D curve prediction at a measurement point is evaluated. Figure 3.28 and 3.29 show how the percentage deviation,

$$\varepsilon = 100 \times \frac{\sigma(\text{measured}) - \sigma(\text{Briggs D})}{\sigma(\text{measured})} \qquad (3.10)$$

depends on wind direction. Within the accuracy of this data, there appears to be no significant correlation. Any multiple source and irregular terrain effects are therefore hidden within the scatter of the sigma data collected during this study. It should also be recalled that the 10% isopleth method for extracting sigmas has already indicated that multiple source effects will be small.

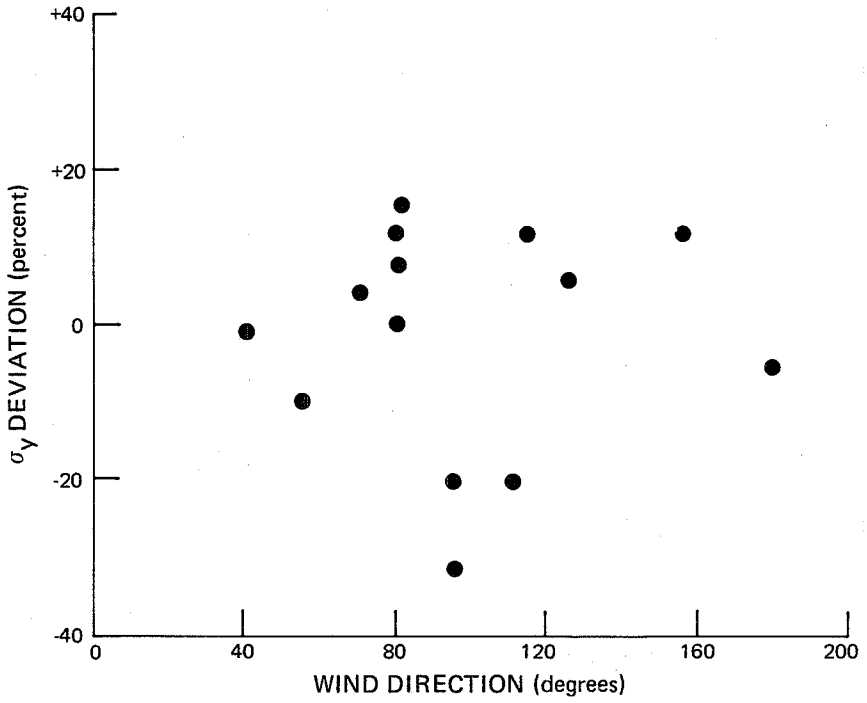

Figure 3.28. σ_y deviation from Brigg's curves versus wind direction (clockwise from north, blowing to).

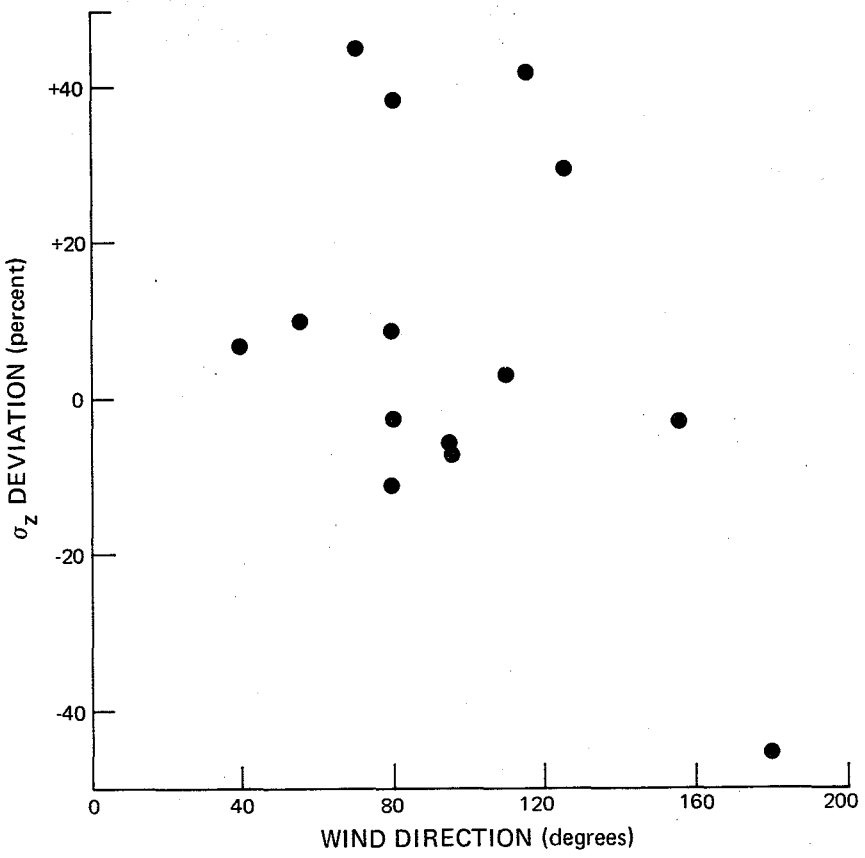

Figure 3.29. σ_z deviation from Briggs' curves versus wind direction (clockwise from north, blowing to).

3.7.2 Wind Directional Shear Effects

Qualitatively, it has been shown that wind directional shear leads to a significant increase in σ_y while having no measureable effect on σ_z. As noted earlier this is accomplished through both plume distortion and an enhanced diffusion. In this section, a preliminary attempt to quantify the enhanced diffusion through a simple empirical formula is presented.

Due to a wind directional shear of ϕ degrees per 100m, there will be an enhanced diffusion $\Delta\sigma_y$ which can be expected to depend on the amount of shear present and the vertical diameter D of the plume:

$$\Delta\sigma_y \propto f_1 (D,\phi) \tag{3.11}$$

Substituting $D = 4.3\ \sigma_z$ suggests that

$$\Delta\sigma_y = f_2 (\sigma_z,\phi) \tag{3.12}$$

Equation (3.12) indicates that attempts to correlate $\Delta\sigma_y$ with x will be subject to the same scatter noted in σ_z measurements, along with additional scatter due to uncertainties in ϕ. These uncertainties often make it difficult to assign one definite ϕ value for a particular cross-section. Successive pibal releases, for example, can give different directional shear information. Also, in data collected for

this study[3], directional shear appears in different forms across a plume section: well-defined, near-linear shear occurs in some cases, oscillatory shear about either a constant or varying direction occurs in other cases, while a relatively sudden change from one wind direction to another has also been observed. Another problem is that a correlation of measurements with equation (3.12) must assume that shear is constant throughout the dispersion history of the plume. A region of strong shear which might cause a large $\Delta\sigma_y$ during the initial rise phase, for example, would complicate the analysis further. One appealing factor of equation (3.12), on the other hand, is that it suggests stability effects and downwind distance variations are inpart absorbed into the σ_z factor. Accordingly, a dimensionless correlation:

$$\frac{\Delta\sigma_y}{\sigma_z} = f_3(\phi) \tag{3.13}$$

should be less dependent on stability and on x than either σ_y or σ_z alone.

Despite the uncertainties discussed above, Figure 3.30 illustrates that equation (3.13) correlates reasonably well with the measured σ_y's (with the distortion effect removed) collected during this study during both neutral and stable lapse conditions. The shear enhanced diffusion increment $\Delta\sigma_y$ has been evaluated for each data point using

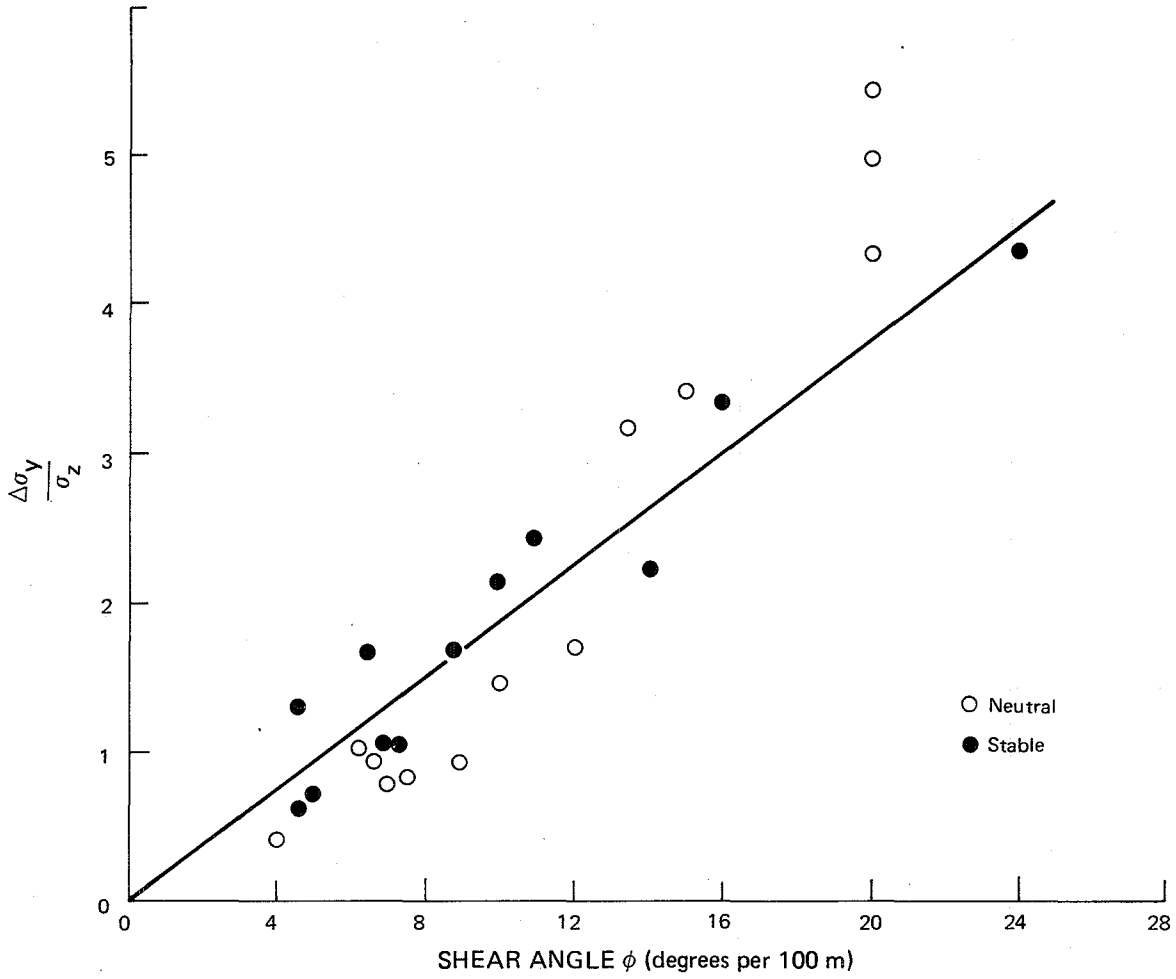

Figure 3.30. The correlation of equation (3.14) for cross-wind shear enhancement of σ_y.

$$\Delta\sigma_y = \sigma_y \text{ (measured)} - \sigma_y \text{ (Briggs)} \qquad (3.14)$$

where the Briggs' D curve prediction was employed for neutral no-shear conditions, and Briggs' E curve prediction for stable no shear conditions and assumes that the shear influences on σ_y Briggs' is small. A straight line fit to the data of Figure 3.30 yields an empirical relation for shear enhanced diffusion of the form

$$\Delta\sigma_y = 0.19\ \sigma_z\phi \qquad (3.15)$$

3.7.3 Buoyancy Effects on Sigmas

We intuitively do not expect buoyancy effects on plume spread to play an important role in determining the ground level concentrations from elevated releases such as large industrial stacks, the reason being that at those distances downwind where the maximum ground level concentration is expected to occur (of order 10 km) any enhanced growth in the buoyancy phase has long been forgotten by the plume. The same argument could be applied to some cases of multiple sources. Both buoyancy and multiple source stacks contribute to the initial size of the source as far as Gaussian plume modelling is concerned. Providing this initial size is not large compared to the plume dimension at the point of concern for the concentration field, its effect is small. In other words, the effect of buoyancy and multiple sources on plume spread is to locate the virtual origin of release at a point

different from the real source and, if this distance to a virtual origin is small compared to the distance of maximum ground level concentration, then the effect can be ignored (as most legislative plume dispersion models now do). However, the effect of buoyancy on the spread of the G.C.O.S. plume will be investigated in this section in order to provide a better understanding of the relative diffusion process.

In order to determine the rate of plume spread in the vertical and horizontal during the buoyant phase of plume rise and spread, one would require good measurements of plume cross-sections during that phase. Given these measurements along with an equivalent set of plume cross-sectional measurements from a passive point source release during the same time-interval, one could then sort out the effects of plume buoyancy on the rate of spread and hence the equivalent Gaussian sigmas. The only truly buoyant phase data on plume spread available from Slawson et al[12] (1978) is contained in the time-mean plume photographic data. Thus we have some measured of the buoyancy induced spread in the vertical (σ_z) only. However, we also have access to buoyant phase plume spread from LIDAR measurements taken at the Nanticoke G.S. during a study conceived and initiated by S. Djurfors and in which the senior author and a graduate student (Edwards) participated. This data is available in a report by A.C. McMillan, Ontario Hydro[17] (1977), and in the MA Sc thesis of Edwards[18] (1977).

If the buoyancy dominated phase plume spread data were of good quality one could simply plot the sigmas versus distance or time and compare the values or rates of spread with that in the passive phase of diffusion. The passive phase occurs in the atmospheric phase where all plume excess buoyancy is lost or is insignificant. Figure 3.31 illustrates the observed time dependent behaviour of the ratio σ_y/σ_z both in the buoyant phase of the Nanticoke plume and the atmospheric phase of the G.C.O.S. plume. A linear regression analysis on the buoyant phase data results in the best fit empirical equation (3.16) with a correlation coefficient of 0.7

$$\frac{\sigma_y}{\sigma_z} = 1.36 + 0.00836t \qquad (3.16)$$

and a standard error of estimate of 0.3. The G.C.O.S. plume data consists of observations taken in near-neutral atmospheric conditions or Class D on the Pasquill-Gifford curves or Brigg's curves. Also little or no wind directional shear was present. For a single stack release one would expect σ_y/σ_z at t = 0 to be equal to unity. However, two stacks were operating during the Nanticoke observations. Scatter in the buoyant phase data can be attributed to wind direction relative to stack alignment and errors in measurement. Edwards[18] (1977) shows that both the σ_z obtained from photographs of the plume and those from the LIDAR data agree fairly well and that σ_z varies as the 2/3 power of x in the buoyant phase. It is of interest to note that the ratio

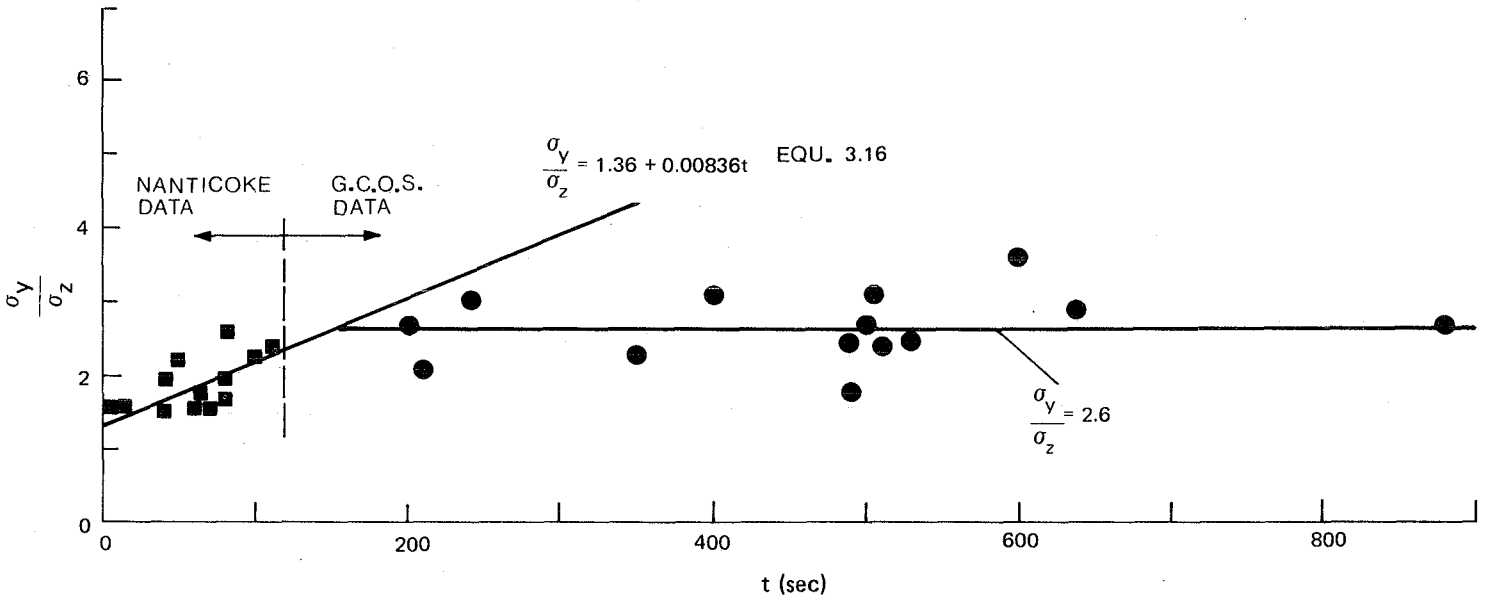

Figure 3.31. Observed ratio σ_y/σ_z versus time, buoyant and passive phase.

σ_y/σ_z is fairly constant beyond t = 150 secs and equal to about 2.6. This would indicate that both σ_y and σ_z are varying with time in the same fashion. In the report by McMillan[17] (1977) $\sigma_z \propto t^{\frac{1}{2}}$. Thus, if this were the correct time variation for σ_z then one would expect $\sigma_y \propto t^{\frac{1}{2}}$ which is the time dependent variation given by the statistical theory (homogeneous turbulence) for long diffusion times. Further discussion on the time dependent behaviour of the observed sigmas will be given later.

Since the σ_y data from the G.C.O.S. plume observations is considered to be of better quality than σ_z, its time dependence is illustrated in Figure 3.32. Here the Nanticoke LIDAR observations of σ_y are shown with the G.C.O.S. σ_y's on the same graph. Since σ_z was observed to be proportional to $x^{2/3}$ in the buoyant phase (as neutral plume rise in uniform winds predicts) then $\sigma_z = At^{2/3}$ also, where A is weakly dependent on initial buoyancy flux and wind speed. This functional dependence of σ_z on time can be derived from the governing equations for buoyant plume rise in a neutral atmosphere. Substitution of this relationship into the empirical relation for σ_y, equation (3.16) results in

$$\frac{\sigma_y}{A} = (1.36\ t^{2/3} + 0.00836\ t^{5/3}) \qquad (3.17)$$

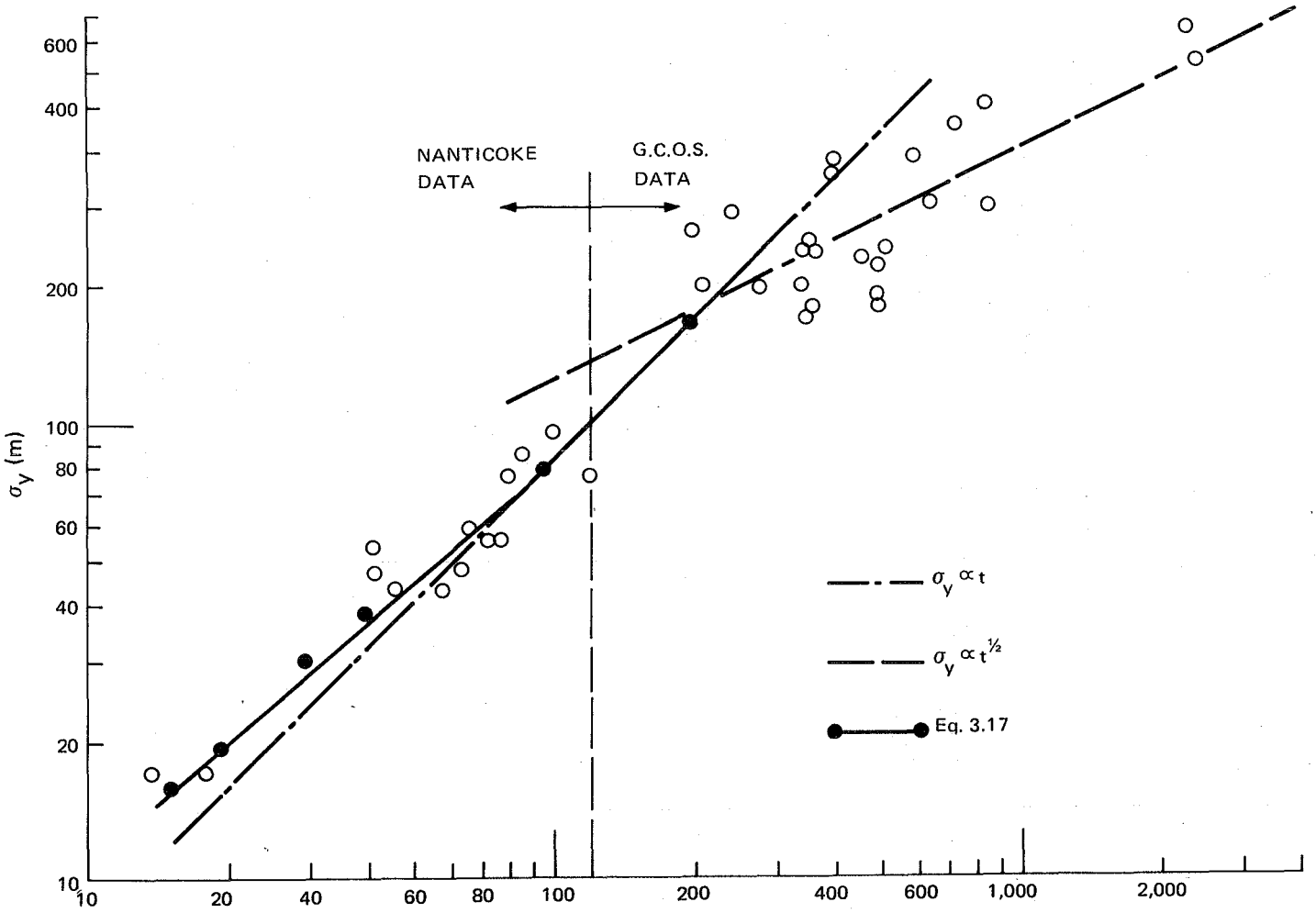

Figure 3.32. σ_y versus time, buoyant and passive phases.

which is shown in Figure 3.32. Thus, 3.17 suggests for very short times, $\sigma_y \propto t^{2/3}$ while $\sigma_y \propto t$ represents equation 3.17 fairly well over the range $25 < t < 250$ and also correlates well with the observations. Thus one might conclude from this limited data that the effect of buoyancy is to have σ_y and σ_z varying with $t^{2/3}$ initially, then a region where $\sigma_y \propto t$ while $\sigma_z \propto t^{2/3}$ still holds out to the distance where atmospheric turbulence dominates plume dispersion. This means that there is little measureable effect of plume buoyancy on σ_y as it behaves just as the statistical theory predicts for small diffusion times for passive releases.

3.7.4 Time Dependence of Observed Sigmas

From the above discussion it seems appropriate to discuss further the time dependent behaviour of the observed sigmas. We have already seen above (Figure 3.31) that the ratio σ_y/σ_z is approximately constant out to $t = 900$ secs beyond the buoyant phase within the scatter of the neutral no-shear data. Since the areas under the curves of atmospheric turbulent kinetic energy spectra for the lateral and vertical components are substantially different then there should be a region (time interval) where $\sigma_z \propto t^{\frac{1}{2}}$ while $\sigma_y \propto t$, provided the statistical theory of diffusion adequately represents diffusion at the elevations of the observation. McMillan[17] (1977) reports $\sigma_y \propto t$, and $\sigma_z \propto t^{\frac{1}{2}}$ in the Nanticoke observations. In Figure 3.32 we have plotted the observed σ_y's (neutral no shear) against time out to 2400 secs.

down wind. This is much further in time than the Nanticoke observations. However, only two σ_y values were observed at that time. From Figures 3.32 one can see that even within the large scatter $\sigma_y \propto t$ does not correlate well with the observations beyond approximately t = 250 to 300 secs. However, $\sigma_y \propto t^{\frac{1}{2}}$ does fit the data reasonably well from t = 250 to 2500 secs. Thus, our observations would indicate that both σ_y and σ_z vary as $t^{\frac{1}{2}}$ beyond $t \simeq 300$ secs. Again, if the statistical theory holds for our neutral no-shear observations, then one expects a $t^{\frac{1}{2}}$ behaviour in the sigmas beyond $t > 3t_L$[30] where t_L is the Lagrangian time scale of turbulence for the appropriate component. Thus this data suggests a t_L of approximately 100 secs. for the lateral component of turbulence, which is not an unrealistic value.

3.7.5 The Effects of Averaging Time on Observed Sigmas

The work by Davison and Leavitt[24] (1978), with the references cited there, adequately describes possible effects of averaging time on the magnitude of the sigmas. The sigma data in this report and the previous one by Slawson et al[12] (1978) represent ensemble averages of relative dispersion about the centre of mass. The total or absolute dispersion of the plume at any point downwind can be described by the sum of the absolute (Eulerian) and relative (Lagrangian) variances provided that the corresponding Eulerian and Lagrangian turbulence scales are sufficiently different. When one considers the time involved in constructing a complete plume cross-section from

individual realizations (transects) taken at different points in time, and the errors associated with the measurement techniques, it becomes difficult to justify any attempt to correct for averaging time within the context of the data base at hand. If a strong correlation between measured standard deviations of mass and that of the corresponding variances of the turbulent wind components (say from a fixed tower) could be established as functions of averaging time then an empirical correction may be possible.

Davison and Leavitt[24] found that differences between averaged (30 minutes) relative and Eulerian σ_y values were not large based on an analysis of some limited COSPEC data for downwind distances between 3.6 and 4 km. The σ_y's presented in this report represent an average for each plume cross-section which was constructed from measurements taken over a period of approximately 30 to 60 minutes. Thus, if Davison and Leavitt's findings are reasonable for the G.C.O.S. site, one might expect the σ_y's (averaged relative to the plume center of mass) presented in this report to be close to the Eulerian dispersion values for the same time period. If one then applies a correction for averaging time say from 30 minutes to 60 minutes using the formula given in Gifford[37] (1975) we find that the 30 minute σ_y values should be increased by approximately 15%. Also, one might also note that corresponding corrections to the measured σ_z values (particularly in stably stratified atmospheric conditions) are expected to be small (see De Bower et al[38] (1979) for example).

In view of the above we feel at this time, that there is not sufficient justification nor a well established method for correcting the elevated plume sigmas for averaging time (note that any such correction would probably result in larger sigma values than those presented). Hanna[39] (1978) concludes that the best way to estimate σ_y is to obtain good measurements of turbulent wind direction fluctuations, sampled and averaged over times corresponding to the sampling and averaging times of diffusion.

3.7.6 Effects of Release Height on Observed Sigmas

Since the intensity of atmospheric turbulence (gustiness components) and the Lagrangian length scales vary as functions of height and stability within the planetary boundary layer, one would also expect the resulting standard deviations of mass (sigmas) for the plume to vary with height above the ground. Thus, the dispersion of a plume is dependent on the height of release above ground level. Or more simply, the rate of spread of a given plume elemental cross-section is a function of the height above ground as well as stability, surface roughness, terrain anomalies, stratification, wind shear etc. While in the buoyant phase of plume rise, the plume element is least affected by the spatial variation of atmospheric turbulence and the characteristic dimension of the element is usually small compared with the height above ground. However, in the atmospheric phase of relative diffusion the plume element will grow to vertical and horizontal

dimensions where significant variation of the turbulence responsible for diffusion occurs over these dimensions (particularly the vertical extent of the plume element). If one could measure or otherwise calculate the planetary boundary layer turbulence field (turbulent intensity and length scales), then a dispersion model that employed the numerical solution of the convective diffusion equation might be suitable to account for the effects of release height and or plume elemental position on the dispersion of that plume element. However, our concern here is with ultimately developing sigmas for a Gaussian plume model and as such, a simple correction scheme to the input sigmas would have to be used. Here again, we feel at this time that the scatter in the sigma data base of this report is too large to extract such an empirical correction.

The experimental observations of Doran et al[34] (1978) on the variation of the lateral and vertical dispersion characteristics with source height illustrate the kinds of changes in the sigmas that can be expected. Their analysis is, however, confined to the short distance from the respective sources of 400 m or less and to source heights of 56 m above ground. They conclude that in neutral and stable stratified conditions, σ_z generally increases with height and that the difference between ground level and elevated σ_z's increases with stability. The latter result probably arises due to the vertical variation in the character of turbulence (mechanical to thermal) in a stably stratified atmosphere. The measurements for σ_y and σ_z were

taken at or near ground level. However, no correction formula for release height is given for the sigmas.

Some analytical work on this problem is given in a paper by Lamb[35] (1979) for dispersion in a convective planetary boundary layer capped by an inversion lid. Lamb's work is very interesting in that he suggests modifications to the Gaussian plume model in order to incorporate his findings. However, this work focuses on a particular meteorological condition and comparison with real data is lacking.

In summary, the importance of release height on the effective sigmas one would use for ground level concentration calculations with a simple Gaussian model would have to be demonstrated through a model validation program.

3.8 MODELLING PLUME DISTORTION DUE TO CROSS-WIND SHEAR

Previously in Section 3.7.2 an empirical relation was developed from the σ_y data base to account for only the cross-wind shear enhanced diffusion on the values of σ_y. Ultimately, one would like a dispersion model that accounted for both shear enhanced diffusion as well as plume cross-sectional distortion, while providing the correct plume trajectory over the ground plane in the presence of a turning wind vector with height above ground.

In this section a simple and preliminary Gaussian plume dispersion model is developed that accounts for the change in plume direction as well as the effect of distortion on the plume cross-section due to crosswind shear. The predicted plume cross-section isopleths are then compared with a few of those observed. It is assumed here that the rate of growth of the plume cross-section with downwind distance can be adequately described by the P.G. or Briggs sigma typing schemes. The P.G. curves are used in the model described below. The main purpose of the comparison between model predictions and observations is to test the validity of some of the assumptions employed in developing the model. If such simple models for plume distortion prove adequate, then one may simply replace the P.G. curves employed in them with a suitably modified set that incorporates shear enhanced diffusion in order to account for both effects in the same model.

The model in its present form consists of a plume rise and buoyant diffusion phase coupled to an atmospheric diffusion phase. The plume rise phase of the model is obtained by numerically integrating the integral equations governing buoyant plume rise. During this phase the change in direction of the plume in the presence of wind shear is accounted for, but any distortion of the plume cross-section is assumed small. Thus numerical plume rise models, such as those presented earlier that account for variable winds with height above ground, may be used in place of the one given here. If the change in direction of the plume is unimportant, an analytical plume

rise model may be used. Thus, the details of the particular plume rise model used are not given here.

During the atmospheric non-buoyant phase (assuming flat terrain, and linear cross-wind shear) the centerline of the plume will remain constant in direction and height above ground. However, as described earlier the wind directional shear is expected to cause (1) distortion of the shape of the plume (tilted axis) and (2) some enhanced diffusion.

3.8.1 The Atmospheric Phase

The plume, after reaching maximum height, is assumed to diffuse by atmospheric turbulence. At the beginning of this stage, the circular plume cross-section from the one-dimensional buoyant phase is changed to an equivalent elliptical one keeping the area of cross-section constant. For this elliptical cross-section σ_z and σ_y (from Pasquill's curves) and a virtual origin of the plume are found. Here again, one could use some other suitable sigma typing scheme in place of the P.G. curves.

The effect of a changing wind direction with height is applied to the elliptical plume cross-section obtained above. The result, for an ideal case of linear cross-wind shear, is schematically represented in Figure 3.33. In this Figure, GLNMC represents the plume cross-

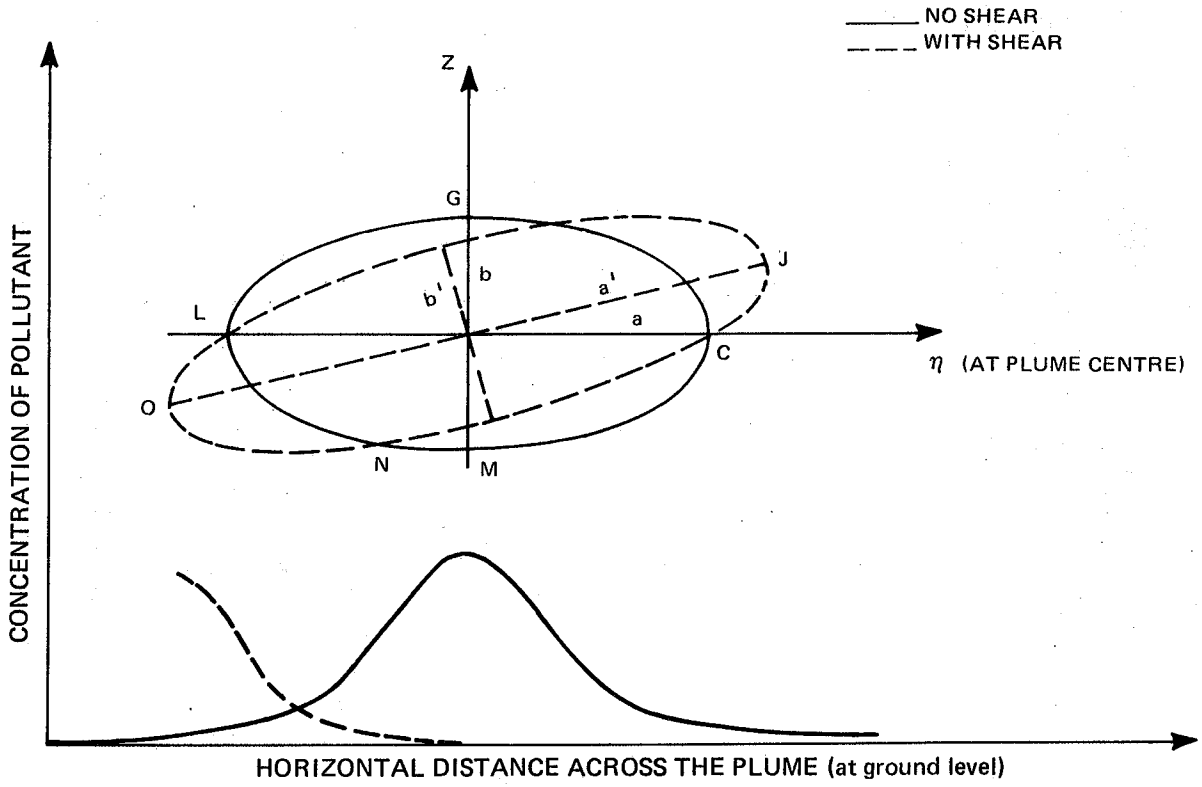

Figure 3.33. Schematic representation (not to scale) of cross-wind shear effects on a plume cross-section and resulting ground level concentration distributions.

section in the absence of wind shear. LONGJ represents the cross-section of the plume after the application of the effect of linear cross-wind shear.

Note that the major axis of the new ellipse is longer than that of the old one, and it is tilted from the horizontal. Also, note that the minor axis of the new ellipse is smaller than that of the old one. The major and minor axes of the new elliptical cross-section of the plume and the angle of the major axis to the horizontal are computed as described below.

Let 'a' be the major axis and 'b' the minor axis of the ellipse before the effect of shear is introduced. Also, it may be noted that the major axis of this ellipse is parallel to the horizontal (see Fig. 3.34).

Referring to Figure 3.34, let z be the vertical axis and η be the horizontal axis normal to the trajectory of the plume. Let GDC represent a section of the elliptical plume cross-section before the distorting effects of cross-wind shear are introduced. Let G move to H because of the cross-wind component. The point A remains at the same place, since no cross-wind component exists at this point (see Figure 3.34). Let the plume before the introduction of the distortion effect be designated the old plume.

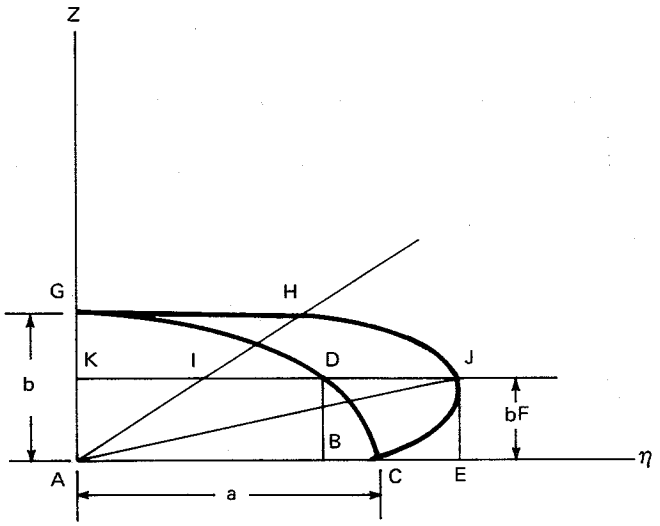

Figure 3.34. Schematic representation (not to scale) of the effect of the cross-wind shear on the plume cross-section.

Now, assuming linear cross-wind shear, point K moves to I and D moves to J (see Figure 3.34) therefore KI = DJ. We assume that J is the vertex of the new ellipse (i.e. HJC). Let AE be the projection of AJ on the horizontal axis.

It is required to find AJ and EAJ. Alternatively, we have to find AE (= KJ) and JE (= TE = DB). Now, from the equation of an ellipse, we may write for the old ellipse,

$$\eta = \frac{a}{b} (b^2 - z^2)^{\frac{1}{2}} \tag{3.18}$$

If we let F be a fraction between 0 and 1 we can write

$$z = bF \tag{3.19}$$

Therefore, 3.17 may be written as

$$\eta = \frac{a}{b} (b^2 (1 - F^2))^{\frac{1}{2}} = a (1 - F^2)^{\frac{1}{2}} \tag{3.20}$$

Now, if ΔV_r is the relative velocity of the top of the plume with respect to the centre, and t is the time step, the top point (G) of the old ellipse would move along the horizontal to the point H at a distance equal to $\Delta V_r \times \Delta t$ (= GH). But, the point DC assuming a linear variation of the lateral wind component would move to J at a distance of $F \times V_r \times \Delta t$. Therefore, using (3.20) we can write

$$\eta_J = a\,(1 - F^2) + F \times \Delta V_r \times \Delta t \qquad (3.21)$$

when η_J is the η coordinate of the point J. Now, if η_J has to be a maximum,

$$\frac{d\eta_J}{dF} = 0.$$

Therefore,

$$\frac{d\eta_J}{dF} = -\,a\,(1 - F^2)^{-\frac{1}{2}} + GH = 0 \qquad (3.22)$$

Therefore,

$$F = \frac{GH}{(a^2 + GH^2)^{\frac{1}{2}}} \qquad (3.23)$$

This value is substituted in 3.20 to get η_J. AJ is found by the relation

$$AJ^2 = b^2F^2 + \eta_J{}^2 \qquad (3.24)$$

The minor axis of the new ellipse is found by keeping the area of the new ellipse the same as the old ellipse. This procedure of

assuming the growth of the plume by diffusion given by Pasquill's σ's and then applying the effect of shear is repeated at every 100 m interval downstream.

For computing the ground level pollutant concentrations, a Gaussian plume equation, which is a solution to the simplified conservation of mass equation assuming nonzero constant wind speed and constant eddy diffusivities along the principal axes of the new (i.e. tilted) ellipse, is used. The assumption of a normal distribution of pollutant concentrations along the axes of the new (slanted) plume is, of course, questionable. However, this appears to be a plausible assumption, in light of the recent observational data (see the Appendices for sample cross-sections of the plume). Its validity may be checked by solving the convective-diffusion equation with the help of a finite-difference scheme (i.e. a grid model) or by a further detailed measurement program. Therefore, in interpreting the conclusions of this study in a quantitative way one has to exercise caution, bearing in mind the assumptions of linear cross-wind shear and of Gaussian distributions of pollutant concentrations along the principal axes of the tilted plume. One may also note that the actual time averaged plume cross-section is probably seldom elliptical in shape. However, by neglecting any enhanced diffusion due to the presence of cross-wind shear (i.e. using Pasquill's sigma for plume growth) and using the above assumptions which are no more restrictive than the no-shear Gaussian plume model, one can illustrate the effect on GLCs of

plume distortion due to cross-wind shear as compared with that predicted in the absence of cross-wind shear.

3.8.2 Results and Discussion

The data* obtained on October 22, 1977 and July 19, 1977 were chosen here to test the model. The results are discussed below.

October 22, 1977. The wind and temperature data input to the model are shown in Figures 3.35 and 3.36. From these figures one can notice that shear exists in both wind speed and direction up to a height of 500 m above the ground, and that the atmosphere is very stably stratified. The plume cross-sections predicted by the model, together with the observed cross-sections at downwind distances of 2.3, 8.1 and 13.3 km, are presented in Figures 3.37, 3.38 and 3.39 respectively. From Figure 3.37 it can be seen that at the downwind distance of 2.3 km the observed plume cross-section is considerably larger than the predicted plume cross-section. Also, the predicted plume height is somewhat higher. The direction of the predicted plume centre (β, measured anti-clockwise from the East-West axis) differs by about 20^{o} from that of the observed plume. One reason for this is the difference between the observed plume height and that predicted by the plume rise part of the model. Of course, errors in observations also contribute to this.

---

*Original data (i.e. before the removal of the distortion effect) are used.

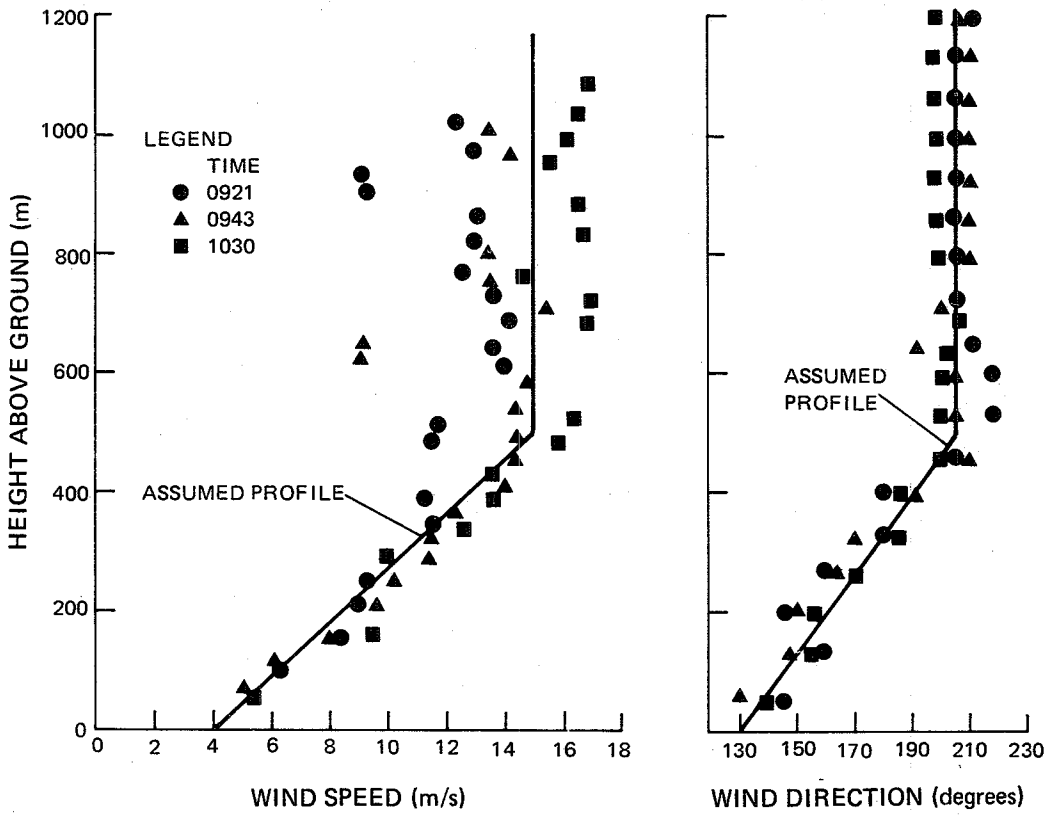

Figure 3.35. Observed and assumed wind profiles for the SHEAR model (October 22, 1977).

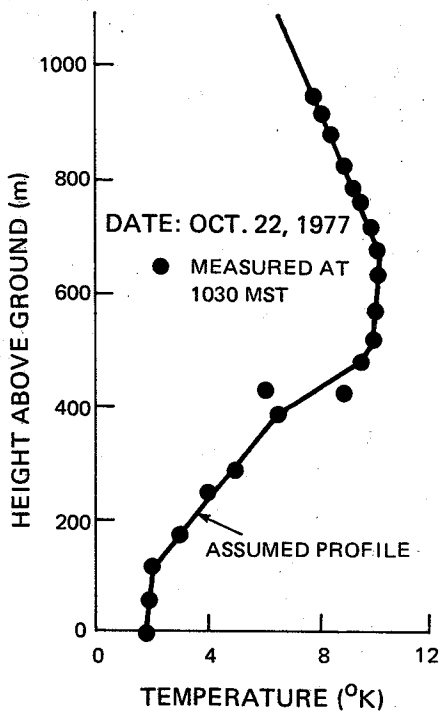

Figure 3.36. Observed and assumed temperature profiles used in the SHEAR model.

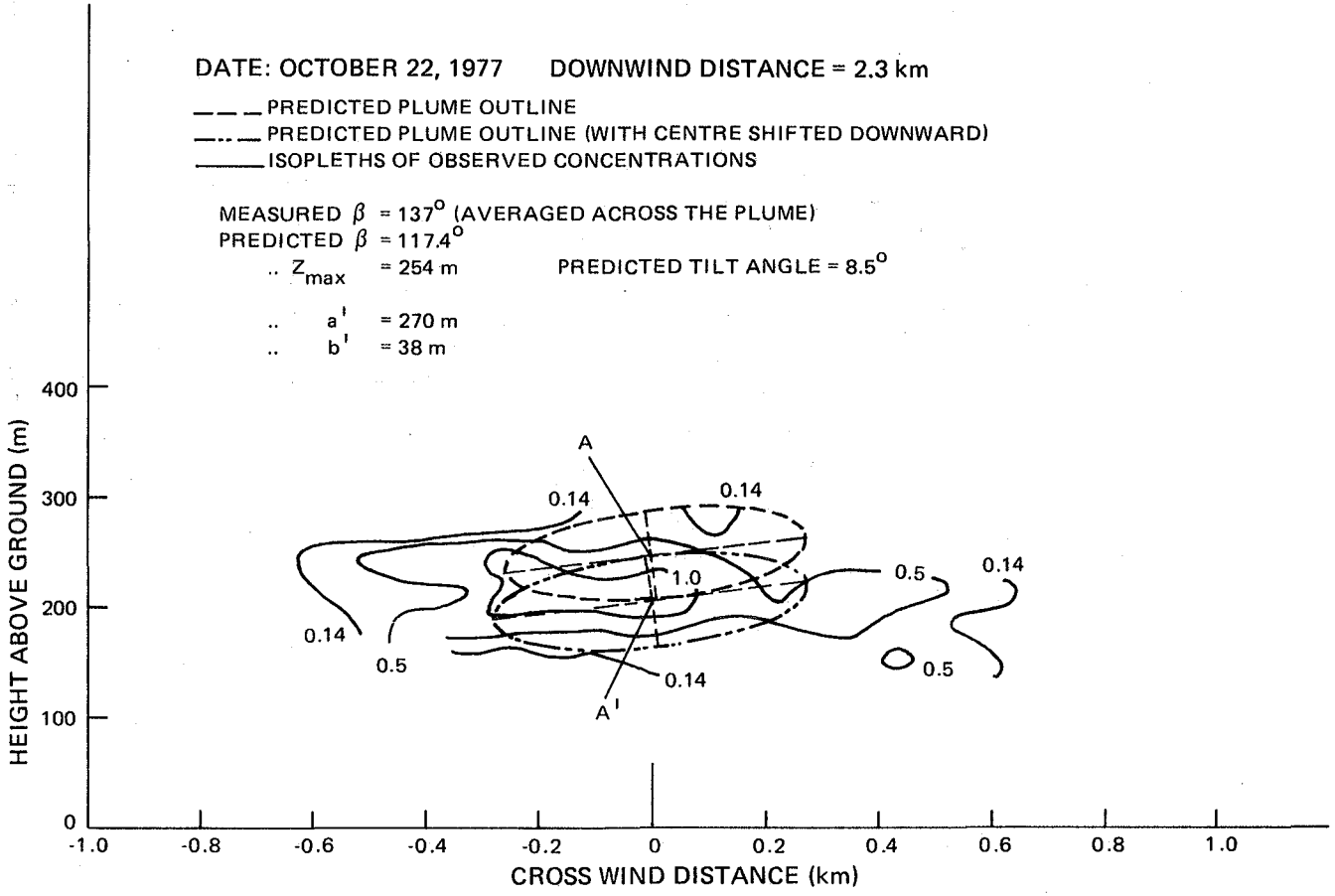

Figure 3.37. Observed and predicted plume cross-sections (October 22, 1977).

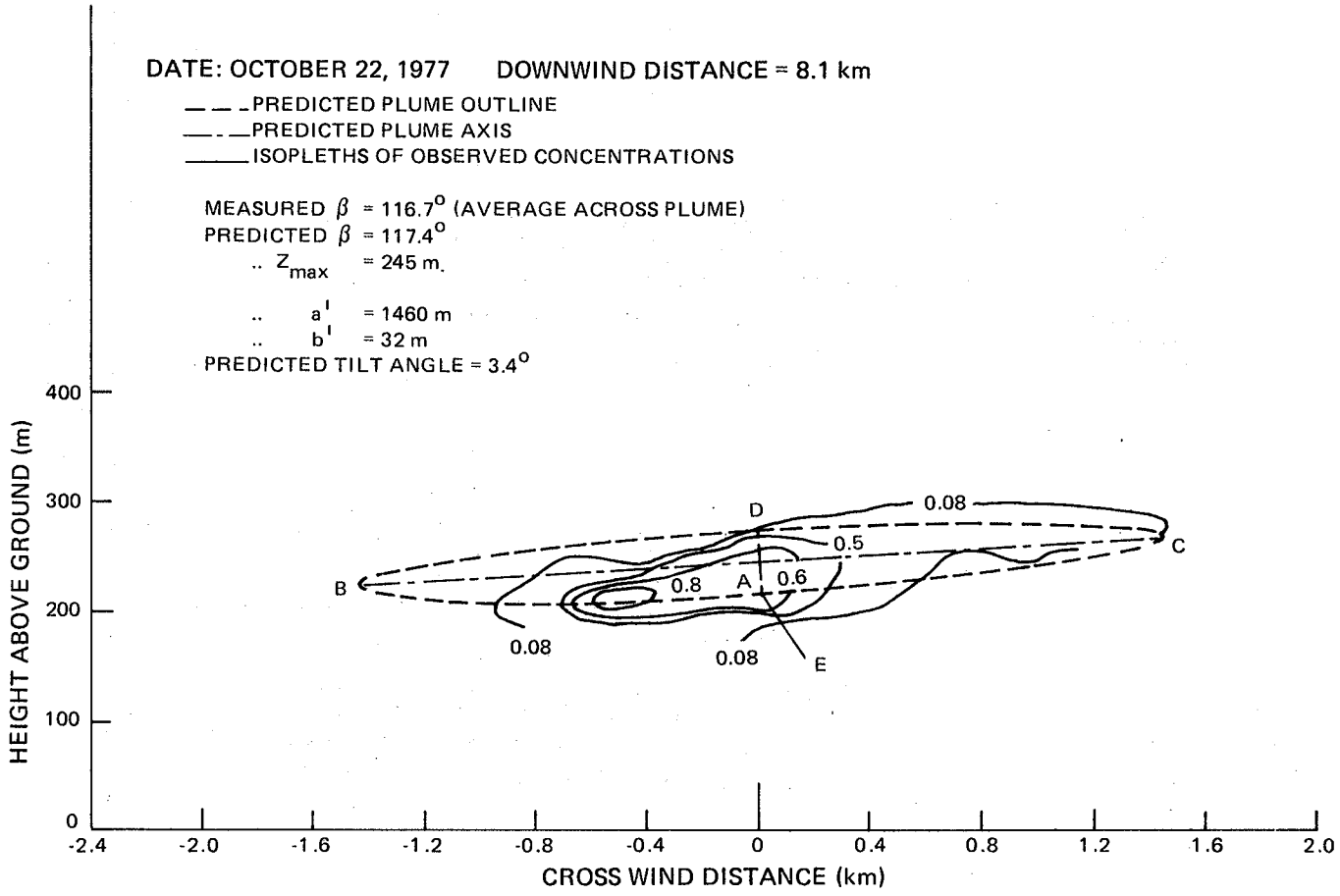

Figure 3.38. Observed and predicted plume cross-sections (October 22, 1977).

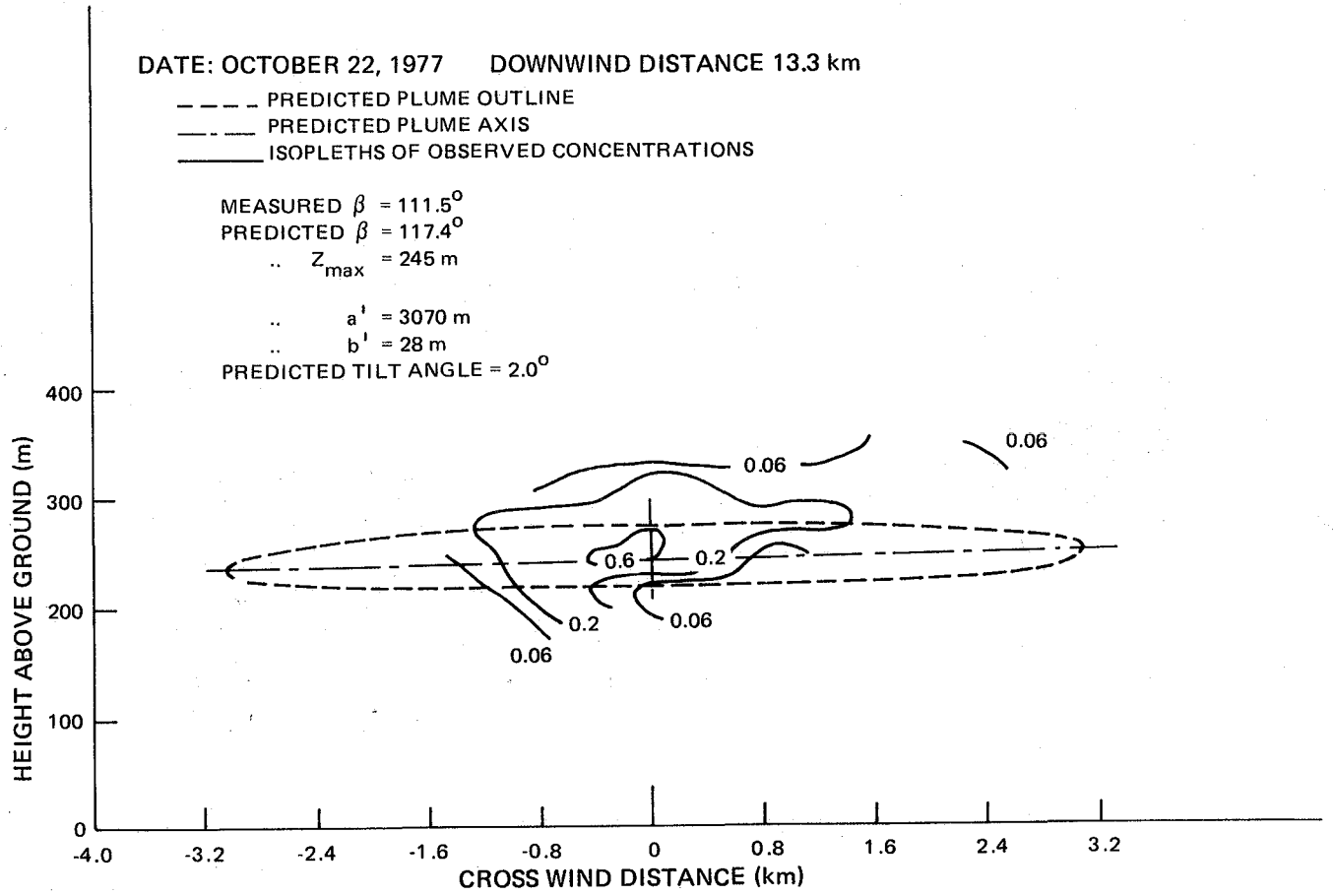

Figure 3.39. Observed and predicted plume cross-sections (October 22, 1977).

At 8.1 km downwind (see Figure 3.38) the observed plume rises higher than that at 2.3 km and almost matches with the predicted one. The tilt angle of the major axis of the observed plume appears to be somewhat larger than that of the predicted one. Because the centres of the plume nearly match, the directions (β) also match very closely. The agreement between the outline of the predicted plume and that of the observed one is also good. At still further downwind, however, (Fig. 3.39) the predicted plume overestimates the horizontal axis while the vertical is under-estimated. Once again, the error is at least partly due to the underestimation of plume radius by the plume rise part of the model. Also, shear enhanced diffusion can be expected to increase as the plume moves downwind.

Therefore, in order to make a fairer comparison of the performance of the atmospheric phase part of the model with observations, the buoyant phase part of the model is decoupled in the next test discussed below.

July 19, 1977. The maximum plume rise (z_{max}), the downwind distance at which the maximum rise occurs (x_{max}), and the radius (R_{max}) of the plume at this point are needed as input to the atmospheric phase part of the model (in addition to, of course, the wind and temperature profile data). The maximum rise (z_{max}) was specified using the observed cross-section at 3.8 km downwind distance. R_{max} and x_{max} were specified, by trial and error, such that the computed

plume cross-section had approximately the same area as that of the observed one at 3.8 km. The input wind and temperature profiles are shown in Figures 3.40 and 3.41.

The observed and predicted cross-sections at 3.8 km and 5.9 km downwind are presented in Figures 3.42 and 3.43 respectively. From these Figures one can note that the agreement between the observed and predicted plume cross-sections are quite good.

3.8.3 Concluding Remarks on Plume Distortion Model

A preliminary plume diffusion and dispersion model that accounts for plume distortion due to cross-wind shear has been described. The model was tested against plume cross-sectional data observed at the G.C.O.S. plant site. It was found that errors in the predictions of the buoyant plume rise phase can contribute to errors in the predictions of the plume cross-sectional distortion within the atmospheric phase, where the effect of distortion due to cross-wind shear is introduced. However, if the buoyant plume rise model is decoupled, and z_{max} and R_{max} are specified based on experimental data, the predictions of the atmospheric phase part of the model are quite good. However, the model should be tested more extensively against observed plume cross-sections before incorporating it into a more general dispersion model. On inspection of some of the observed plume cross-sections it would appear that the assumption of Gaussian

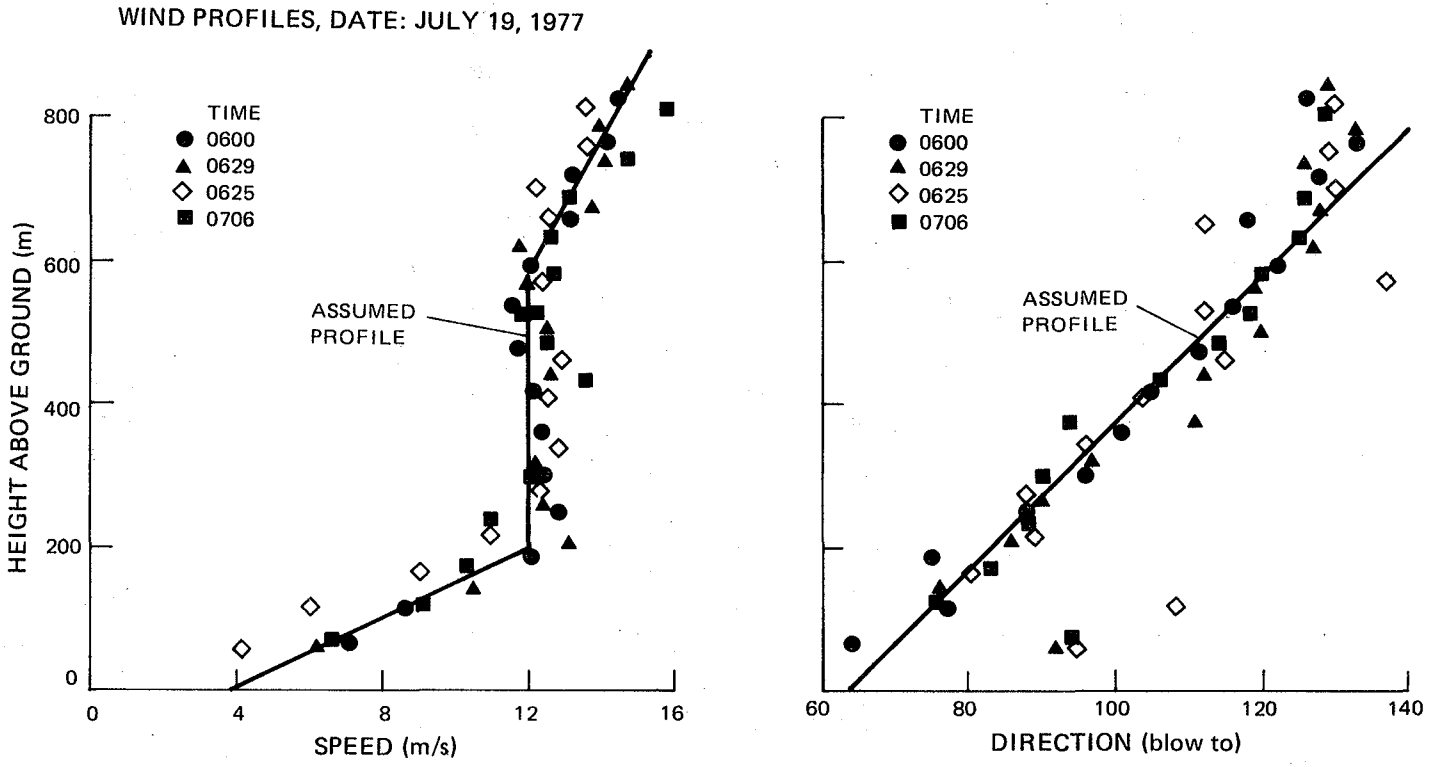

Figure 3.40. Observed and assumed wind profiles used in the SHEAR model (July 19, 1977).

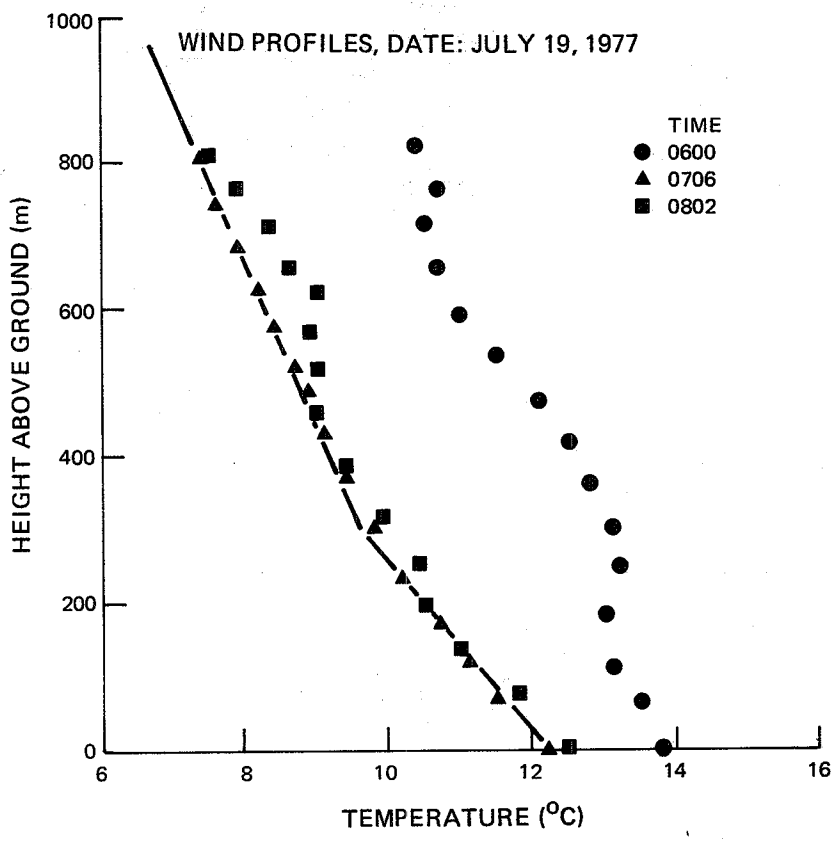

Figure 3.41. Observed and assumed temperature profiles used in the SHEAR model (July 19, 1977).

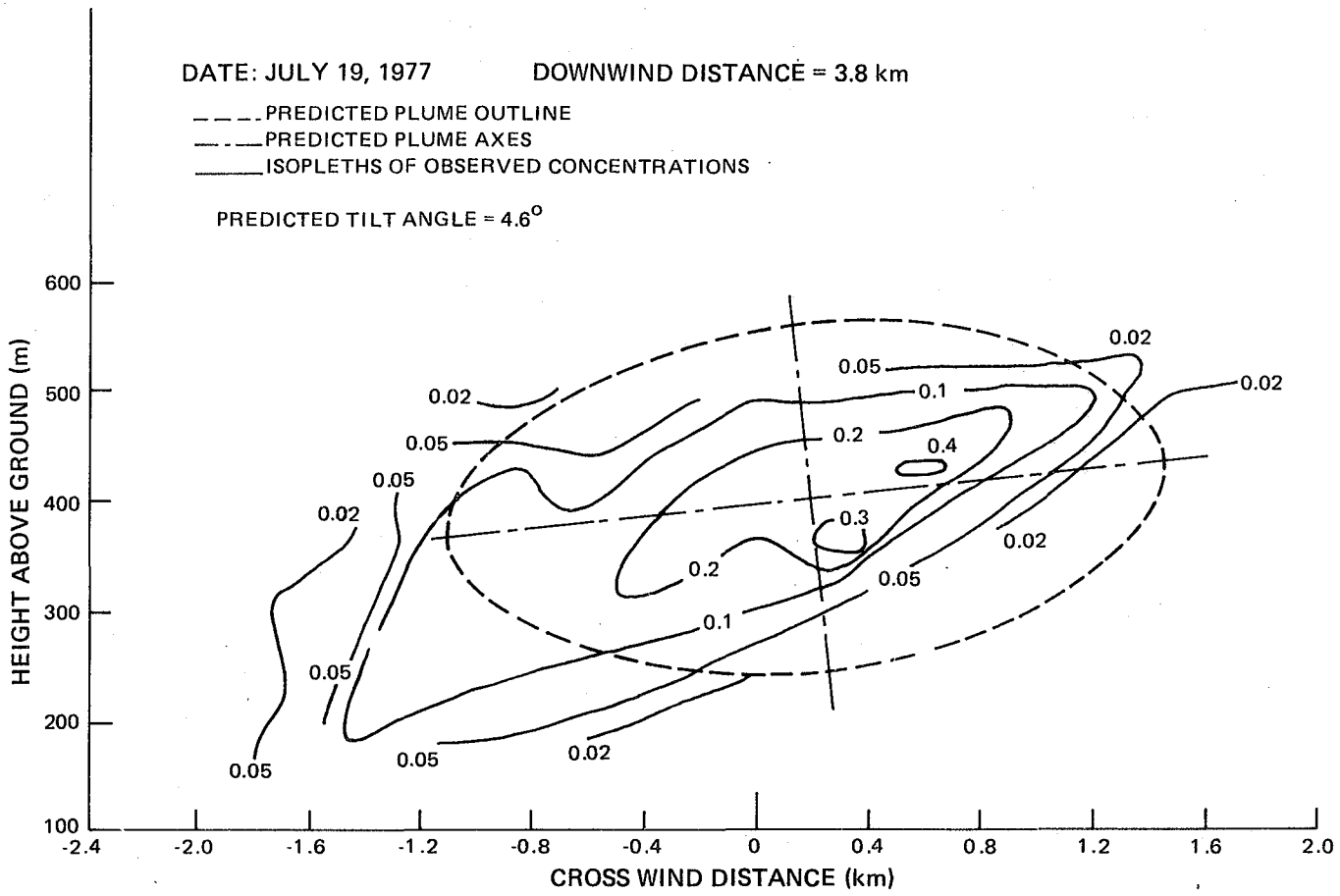

Figure 3.42. Observed and predicted plume cross-sections (July 19, 1977).

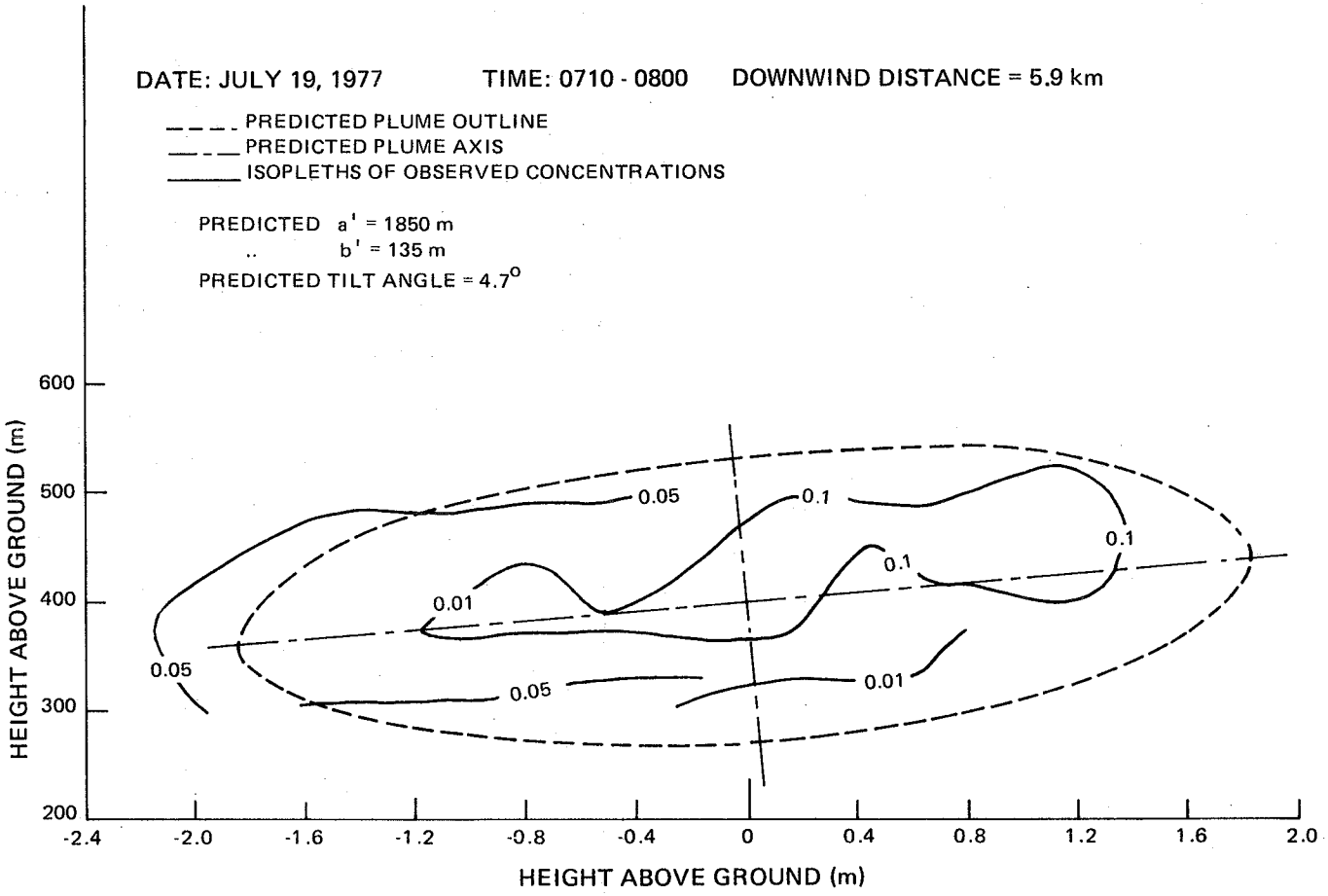

Figure 3.43. Observed and predicted plume cross-sections (July 19, 1977).

distributions along and across the tilted plume cross-sectional axis are reasonable. Thus this model may ultimately be used to calculate both axial and cross-wind ground level concentrations in the presence of linear wind directional shear.

3.9 CONCLUDING REMARKS ON PLUME SPREAD

Our primary effort in re-analyzing the sigma data focused on attempting to further filter errors associated with measurement. Also, since our main interest was to determine the rate of growth of the plume cross-sectional area, a new set of sigmas based on equating an elliptical area to the area inside a given concentration isopleth was used to back out appropriate equivalent Gaussian plume sigmas. This method appeared to reduce scatter in the data and thus allowed better comparison with some currently used sigma typing schemes than that found in Slawson et al[12] (1978).

The following conclusions based on our measured sigmas can be given:

(i) The measured sigmas (equivalent Gaussian) follow the Brigg's class D typing scheme fairly well under near-neutral no wind shear conditions.

(ii) The corresponding correct trends are evident in the data so far as the effects of atmospheric stability are concerned. However, satisfactory quantitative specification is lost in the scatter of the data using the stability classification schemes outlined in this and the previous report by Slawson et al[12] (1978).

(iii) The buoyant plume phase results in σ_z being more affected by buoyancy than σ_y. Limited data are given to illustrate this. In addition the photographically produced σ_z's compare favourably with those produced by the near field aircraft measurements.

(iv) The time rate of change of σ_y appears to have a buoyancy dominated phase followed by a far field behaviour representative of that given by the statistical theory of diffusion, at least for near-neutral no shear atmospheric conditions.

(v) Wind directional shear greatly affects the magnitude of the σ_y's but appears to have little effect on the σ_z's. The magnitude of the wind directional shear effect appears to be represented by moving as much as two stability classes on the unstable side on the P-G curves at the distances of the observations. One would expect this

effect to increase with increasing distances from the source.

(vi) A tentative empirical formula to quantify the effects of shear enhanced diffusion on σ_y was found to correlate reasonably well with the observations.

(vii) A rather simple and preliminary computer model was developed to attempt to account for the quantitative effects of plume distortion due to cross-wind shear on the observed plume cross-section. Although the comparisons of theory with observation are limited, the model appears to offer some promise. However, one should note that wind speed and direction profiles are required as input to the model.

The plume cross-section concentration isopleths and tables of the extracted sigmas may be found in Appendix E. Appendix E.1 contains the observed cross-sections where the transects have been aligned on a vertical line through their centres of gravity. Appendix E.2 contains the plume cross-sections as observed in space based on the aircraft sampling location. Although only some 54 cross-sections were used for sigma analysis, all of the observed cross-sections are contained in Appendix E.2, for reference and possible future analysis for such things as inversion penetration cases. On perusal of the plume cross-section data base one can easily notice the de-coupling of

plume behaviour through inversions and the degree of non-homogeneity present in some of the data.

Additional work on this data base for the classification of sigmas is recommended. Perhaps one could further classify the sigma data according to the type of wind shear present, i.e. linear directional shear, oscillating (degree of meander) etc. If suitable bivane data is available for the corresponding time periods a more effective classification scheme may be established.

4. DISPERSION MODEL DEVELOPMENT

4.1 MODEL DESCRIPTION

In this section of the report, a Gaussian dispersion model based on the results of the preceding chapters is formulated. Preliminary tests of the model against ground plane data collected during the 1977 study are also presented and discussed.

The object here is to construct a computer code for a Gaussian plume dispersion model consistent with the modular design described earlier and in Slawson et al (1978). The dispersion model consists of a buoyant plume rise and growth phase followed by an atmospheric dispersion phase. At this stage of the model development we are primarily interested in predicting ground level centre-line concentrations. The model presented here uses a one-dimensional numerical integration model for plume rise and growth matched to a Gaussian plume spread model for the atmospheric phase. The standard deviations of mass are obtained from empirical curves with modification for the effects of shear enhanced diffusion due to crosswind shear. The point of buoyant and atmospheric phase matching is assumed to occur at a predicted final plume rise height for both stable, neutral and slightly unstable atmospheric conditions. A tentative empirical formulation for the final rise in near neutral atmospheres based on the data of Slawson et al (1978) has been used. At present, provision for plume distortion

due to cross-wind shear, multiple sources, and non flat terrain have not been included in the model. If one wishes to include the effects of plume distortion on ground level concentrations then the model outlined in Section 3.8 (or a similar model) may be incorporated into the atmospheric phase. Multiple source and terrain effects can also be added if the actual Syncrude source and site warrant their inclusion.

While a complete computer listing is contained in Appendix B.1, the major features of the dispersion calculations are outlined in the following sections.

4.1.1 Model Input

The model requires ambient wind and temperature data, and source data, all expressed in SI units. Wind speed and direction (measured in degrees clockwise from north, blowing to) are specified at any chosen number of altitude points starting from ground level. Air temperatures (in ^{o}C) are specified at any chosen altitude points in the same way. Linear profiles are assumed between specified points. Stack exit temperature (in ^{o}C), exit velocity and sulphur dioxide flowrate (in kg/s) must also be given.

4.1.2 Plume Rise Phase

The initial plume rise calculations are based on model N6 of section 2, (although one may replace this by some other plume rise model if so desired). A fourth-order Runge-Kutta scheme with time-step halving for error control is used to solve the set of one-dimensional plume conservation equations. The Boussinesq assumption is not made in these equations, and no drag forces are included in the horizontal and vertical momentum balances, and the entrainment hypothesis

$$v_e = \alpha \left| V - U \frac{V_x}{V} \right| + \beta \frac{UV_x}{V^2} |W| \qquad (4.1)$$

is employed with $\alpha = 0.15$, $\beta = 0.68$.

At each step in the calculation, ambient parameters are averaged across the vertical extent of the plume to establish a one-dimensional value. Similarly, one value of each plume variable is found, consistent with the assumed top-hat profile approach. The following variables are outputted as the calculation proceeds: the diffusion time, the distance the plume centerline has moved downwind, the co-ordinates of the plume centerline, the plume radius, velocity components, temperatures, and density, the wind speed and direction, the air temperature, density, lapse rate, and the value of the Brunt-

Vaisala frequency. The plume centerline co-ordinates are specified in a co-ordinate system with source at the origin, where the positive x-axis is east, the positive y-axis is north, and the positive z-axis is vertically upwards, measured from stack top.

4.1.3 Plume Rise Cutoff

Plume rise is allowed to continue until one of the following criteria is met:

(i) In those situations when the plume cross-section is contained within a stable layer, the plume vertical velocity 'w' eventually becomes negative. The plume rise phase is assumed to end as soon as 'w' reaches a zero value.

(ii) When the plume cross-section is contained within a neutral or unstable layer, however, the vertical velocity remains positive. For these cases, plume rise is assumed to end when one of the following empirical correlations is satisfied. When $U_o \leq 5$ m/s, the 2/3 law plume rise of equation (2.39) ends at a downwind distance x given by Briggs as

$$x = 119\, F_o^{0.4} \qquad (4.2)$$

where $_o$ is the initial buoyancy flux defined by equation (2.38). When $U_o \leq 5$ m/s, a correlation developed during this study is applied (see section 4.1.4). Plume rise ends at a final rise height Z_f of

$$Z_f = \ell_B \ (46.2U_o - 181.) \tag{4.3}$$

where $\ell_B = F_o/U_o^3$ is the buoyancy length scale and U_o is the windspeed at stack top.

4.1.4 Final Plume Rise in Near-Neutral Atmospheric Conditions

As mentioned above, a final plume rise (Z_f) for neutral and slightly unstable atmospheres is required in order to match the buoyant plume rise phase to the atmospheric dispersion phase of plume spread. A comparison of Briggs final rise formulation with the observations of Slawson et al (1978) indicated that Brigg's formulation (equ. 4.2) underestimated the observed final rise from aircraft transects in the majority of plume rise cases in near neutral atmospheric conditions (see Figure 4.1). Thus an attempt was made to find an empirical formulation for Z_f that at least for the observations of this study improved on 4.2. In subsequently arriving at 4.3 atmospheric turbulence was assumed to be primarily responsible for limiting the rise in neutral and slightly unstable atmospheres. The 2/3 law for plume rise was also assumed for plume trajectory. In order to

eliminate or reduce the effects of differing source heat fluxes and average wind speeds over the plume rise region from subsequent correlations the normalized observed final rise Z_f/ℓ_B was calculated. Here ℓ_B is the buoyant length scale as defined by Briggs. Since terrain (surface roughness and albedo) effects the levels of atmospheric turbulence an attempt was made to correlate Z_f/ℓ_B with wind direction. No such correlation was found in the data indicating no discernable effect of terrain on normalized plume rise. Thus one might then assume that the contribution of terrain at the G.C.O.S. site to turbulence levels in the atmosphere at plume heights is homogeneous in space and at least as far as Z_f/ℓ_B is concerned can be considered to be represented by a single constant surface roughness and friction velocity. In neutral atmospheric conditions the surface friction velocity (U_*) may represent a characteristic turbulence velocity scale and thus the intensity of atmospheric turbulence may be considered to be proportional to the ratio of friction velocity to wind speed. One might then expect a relationship of the form

$$Z_f/\ell_B = G\left(\frac{U_*}{U}\right) \tag{4.4}$$

Equations similar to 4.4 were used in early plume rise work but were of the form

$$Z_f = C\ell_B^{\,n} \tag{4.5}$$

where C and n were empirically determined constants. We see that the constant C in 4.5 would have to be a function of atmospheric turbulence level and n equal to unity in order for 4.4 and 4.5 to be identical. Many different equations of the form 4.5 exist in the literature and tend to be site specific and data base specific in nature indicating both failure to incorporate all the necessary physics explicitly in a given equation and differences in observational methods and data.

Since we are interested here in the G.C.O.S. site only, and it appears that a single representative U_* may be used as a turbulence velocity scale for atmospheric turbulence at plume heights then 4.4 can be written as

$$Z_f/\ell_B = G_i \left(\frac{1}{U} \right) \tag{4.6}$$

and the only variable upon which Z_f/ℓ_B depends becomes the wind speed. One might then expect an inverse relationship between Z_f/ℓ_B and intensity of atmospheric turbulence which would lead to a direct dependence of Z_f/ℓ_B on wind speed. Such a relationship was found (equ. 4.3) with a resulting correlation coefficient of 0.88 and a standard error of estimate of 101. From Figure 4.1, one can see that few final plume rise observazions in neutral atmospheric conditions, existed for wind speeds much below 4 m/s, and thus equation 4.2 is used there.

It should be emphasized here that equation 4.3 is very tentative; it simply happens to best fit the available observations. If it turns out that an equation of the form of 4.6 is valid, then additional final rise observations in neutral conditions at wind speeds less than 4 m/s are required. One might also note that the length scale ℓ_B as defined here is strictly valid only for bent-over plumes (i.e. above some threshold wind speed). Thus equation 4.3 suffers at least the same limitations in application as does the 2/3 law for plume trajectory.

4.1.5 Atmospheric Dispersion Phase

Once the final rise height has been attained, subsequent downwind dispersion is calculated according to the Gaussian plume model for either unlimited or limited mixing situations. The main variable of interest in this section of the program is the pollutant concentration C under the plume centerline at some specified altitude z and downwind distance x. For unlimited mixing cases, this concentration is given by

$$C\ (x,z) = \frac{Q}{2\pi \bar{U} \sigma_y \sigma_z} \left(\exp\ \left(-\tfrac{1}{2}\ \left(\frac{Z - H}{\sigma_z}\right)^2 + \exp\ \left(-\tfrac{1}{2}\ \left(\frac{Z + H}{\sigma_z}\right)^2\right)\right)\right) \tag{4.7}$$

where Q is the rate of pollutant release, $\bar{U}$ is the mean windspeed across the plume, $\sigma_y(x)$ and $\sigma_z(x)$ are the empirical measures of plume spread, and H is the effective height of the source (stack height plus plume rise). During limited mixing situations, a series correction is added to equation (4.7). These equations are given in Turner (1970).

The solution (4.7) is obtained by solving the diffusion equation assuming a uniform wind and a constant eddy diffusivity above a flat plane at z = 0 assuming complete reflection occurs at the plane. To apply this solution to the sloping terrain around the G.C.O.S. site, a fictitious ground plane was assumed to exist at the mean terrain elevation, in the region of ground plane measurements and the effective source height was measured from this mean plane. While more sophisticated methods could be used to account for sloping terrain, it was felt that the additional sophistication was not warranted here because of the nature of the aircraft ground plane data. Further, the ultimate aim of this work is to develop a model for the Syncrude site, and a detailed consideration of the terrain around the G.C.O.S. plant would not significantly advance this aim at this time.

Based on the results of Section 3, Briggs' sigma curves were used to specify $\sigma_y(x)$ and $\sigma_z(x)$. The enhancement in σ_y due to cross-wind shear was also calculated, using the correlation

$$\Delta\sigma_y = 0.19\ \sigma_z\phi \qquad (4.8)$$

where ϕ is the angle of shear across the plume vertical diameter, expressed in degrees per hundred meters and the constant absorbs the necessary dimensions.

Atmospheric dispersion calculations begin with the specification of zhe height of stack top above the average ground plane and the height at which aircraft ground plane measurements were made. At each step in the calculation, the following variables are found: the diffusion time, downwind distance, the plan-view coordinates of the plume centerline, the sigmas, the shear correction to σ_y, the average wind speed and direction across the vertical plume diameter, and the centerline concentration at the specified altitude of aircraft measurements. Steps in the numerical procedure are summarized as follows:

(i) At the final rise point, the atmospheric lapse rate is averaged from pibal ground level to plume top. This average lapse rate is used to establish the appropriate stability class following the U.S.A.E.C. recommendations of Table 3.1.

(ii) A decision is made whether to use the unlimited or limited mixing solution by checking the input temperature profile.

(iii) The plume cross-section is initially assumed to be round such that

$$\sigma_y = \sigma_z = R/2.15 \qquad (4.9)$$

where R is the plume radius, taken to be the 10% peak concentration isopleth. Briggs' sigma curves are entered to find the appropriate x origin for σ_y and for σ_z.

(iv) For each increment in downwind distance, the corresponding distances for Briggs' σ_y and σ_z curves are calculated from these origins, and the two sigmas are found. The average shear angle across the last-calculated vertical plume diameter is used to find $\Delta\sigma_y$.

(v) Windspeed and direction are averaged across the last-calculated vertical plume diameter. With this average windspeed and the empirical sigma values, the centerline concentration at the specified measurement altitude can be found. The position of the plume centerline is also calculated, assuming that the plume moves with this average wind.

4.2 COMPARISON WITH GROUND PLANE DATA

4.2.1 Peak Concentration Versus Downwind Distance

During the 1977 study, eight ground plane measurement sets were completed, covering periods when overlapping pibal and source data were available. The aircraft was flown at a constant altitude of 1400 feet or 1500 feet ASL while it traversed under the plume and moved downwind, continuously monitoring the sulphur dioxide level. Source and ambient data for these eight cases are listed in Appendix B.2.

Figures 4.2 to 4.9 compare aircraft measurements of peak concentration versus downwind distance from the source with the predictions of the dispersion model. These predictions were obtained for two assumed ground plane elevations which bracket the terrain variation over the measurement area. The higher prediction assumed a ground elevation of 1200 feet ASL. Since the top of the G.C.O.S. stack has an elevation also approximately equal to 1200 feet ASL, this prediction was made for a zero stack height (above ground level) and an aircraft altitude of about 75 meters AGL. The lower prediction assumed a ground elevation of 875 feet ASL, which implied a stack height of about 100 meters AGL and an aircraft altitude of about 175 meters AGL. The data points shown in the figures represent the peak concentration of the cross-wind concentration distribution obtained by the aircraft at each downwind position.

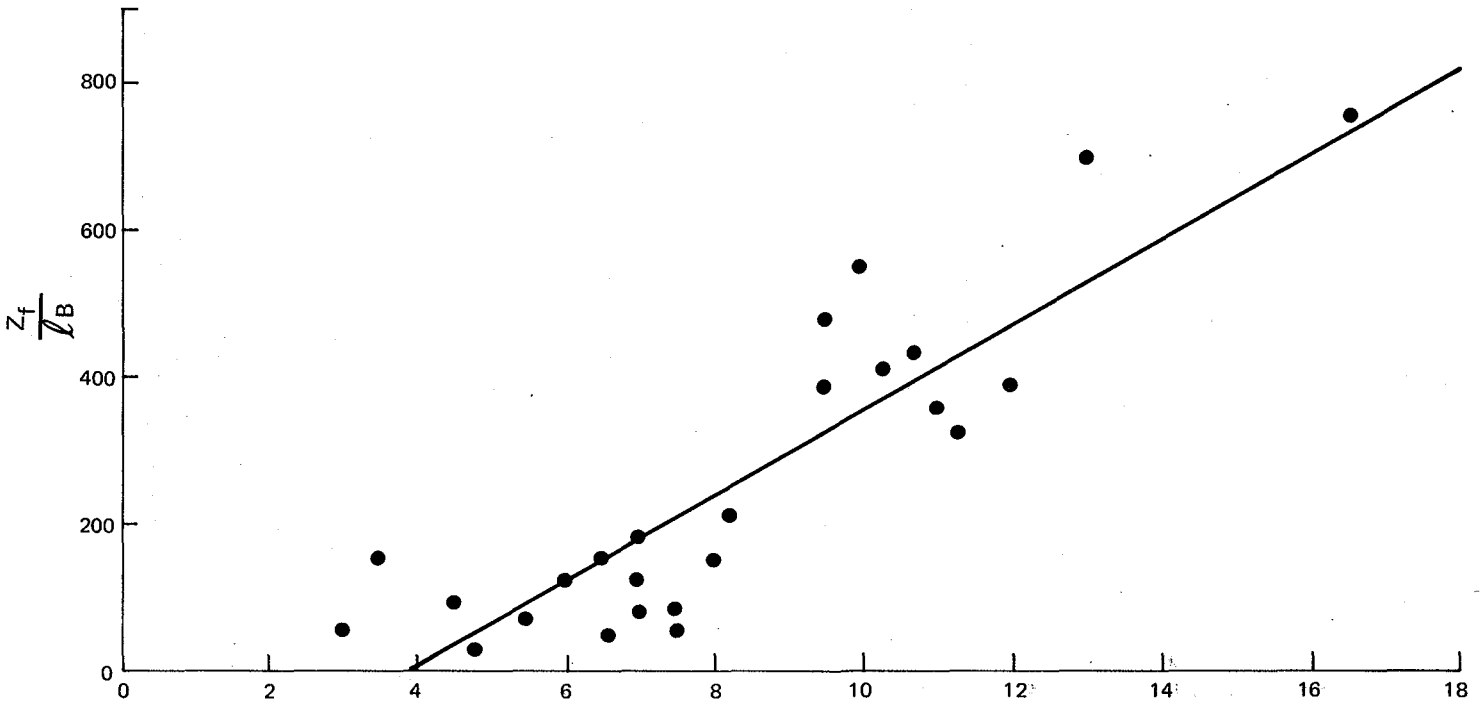

Figure 4.1. Final plume rise observations in near neutral atmospheric conditions, and the correlation of equation 4.3 (solid line).

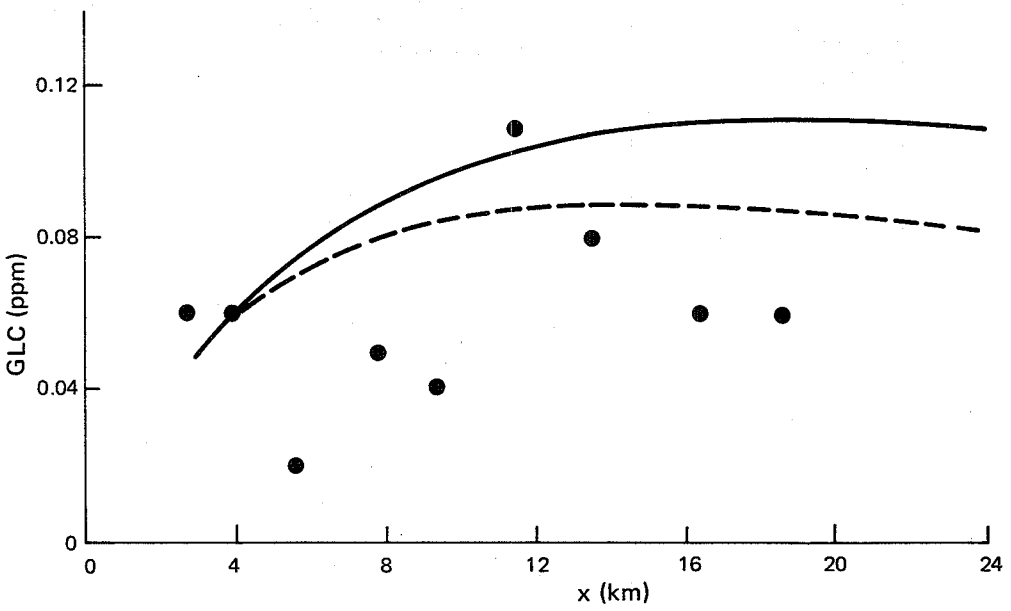

Figure 4.2. Peak GLC (ppm) versus downwind distance x(km) for Jan. 25 1130. Lines show model predictions using Z_f/ℓ_B final rise correlation, under D stability without cross-wind shear enhancement, and with plume trapping at 645 meters above stack exit.

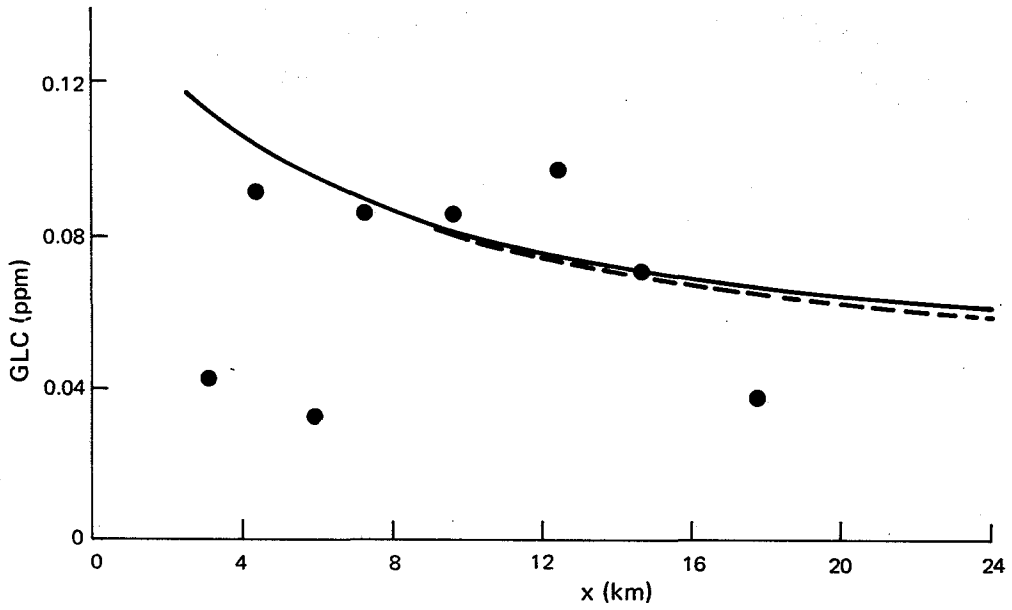

Figure 4.3. Peak GLC (ppm) versus downwind distance x(km) for Jan. 28 1315. Lines show model predictions using the negative w plume rise cutoff, under E stability with cross-wind shear enhancement, and with no plume trapping.

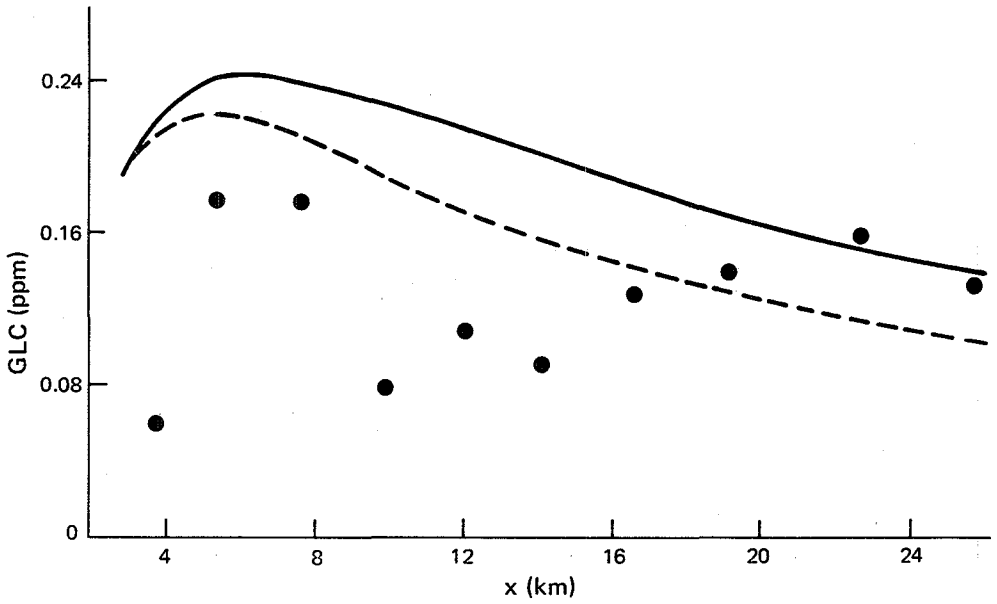

Figure 4.4. Peak GLC (ppm) versus downwind distance x(km) for Jan. 31 1455. Lines show model predictions using the negative w plume rise cutoff, under D stability with cross-wind shear enhancement, and with no plume trapping.

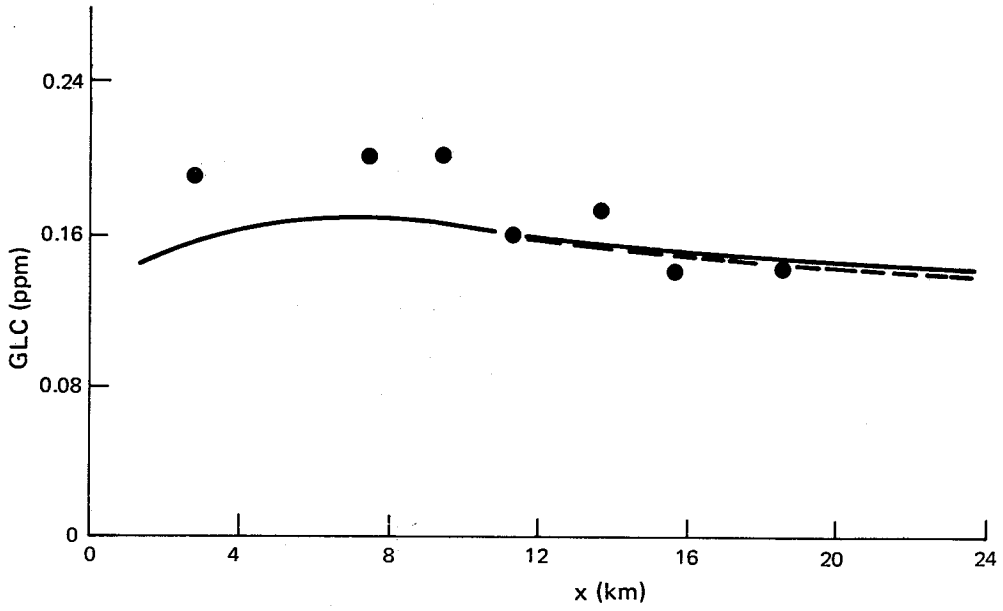

Figure 4.5. Peak GLC (ppm) versus downwind distance x(km) for Mar. 25 1020. Lines show model predictions using the negative w plume rise cutoff, under E stability with cross-wind shear enhancement, and with no plume trapping.

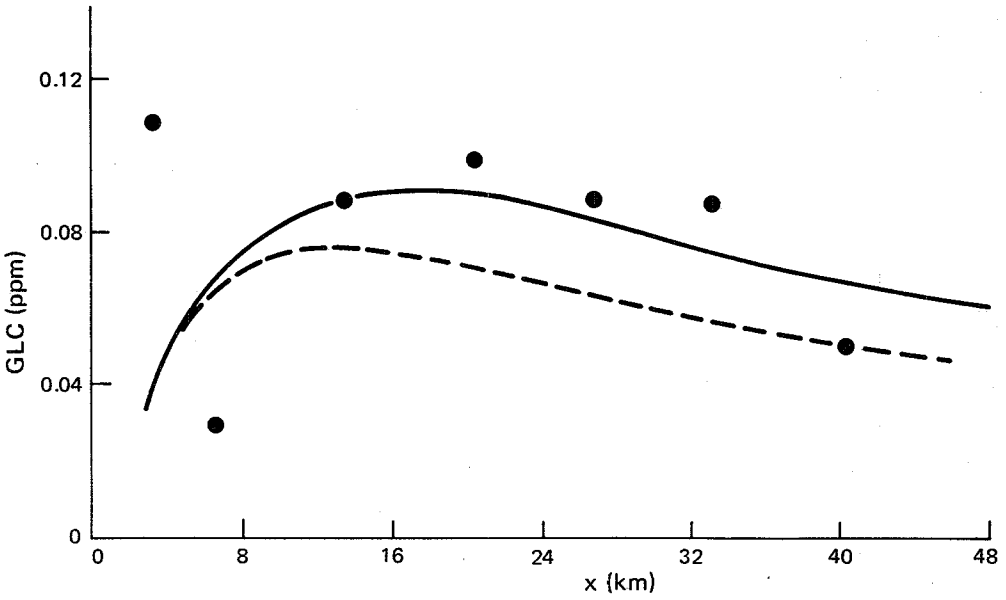

Figure 4.6. Peak GLC (ppm) versus downwind distance x(km) for Mar. 30 0955. Lines show model predictions using Briggs' final rise correlation, under D stability with shear enhancement and with no plume trapping.

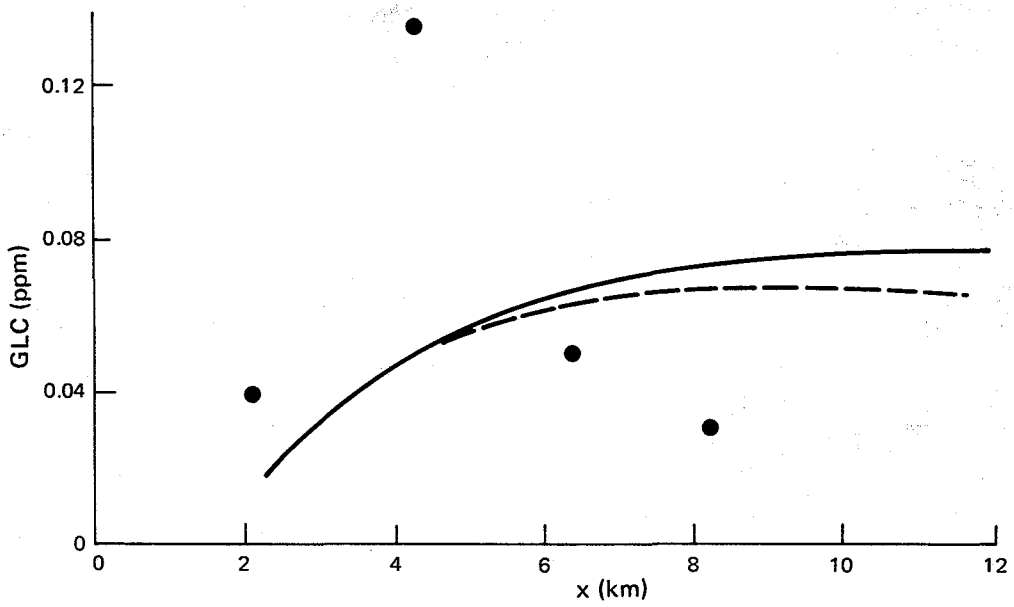

Figure 4.7. Peak GLC (ppm) versus downwind distance x(km) for Oct. 17 1125. Lines show model predictions using Briggs' final rise cutoff, under D stability with shear enhancement, and with no plume trapping.

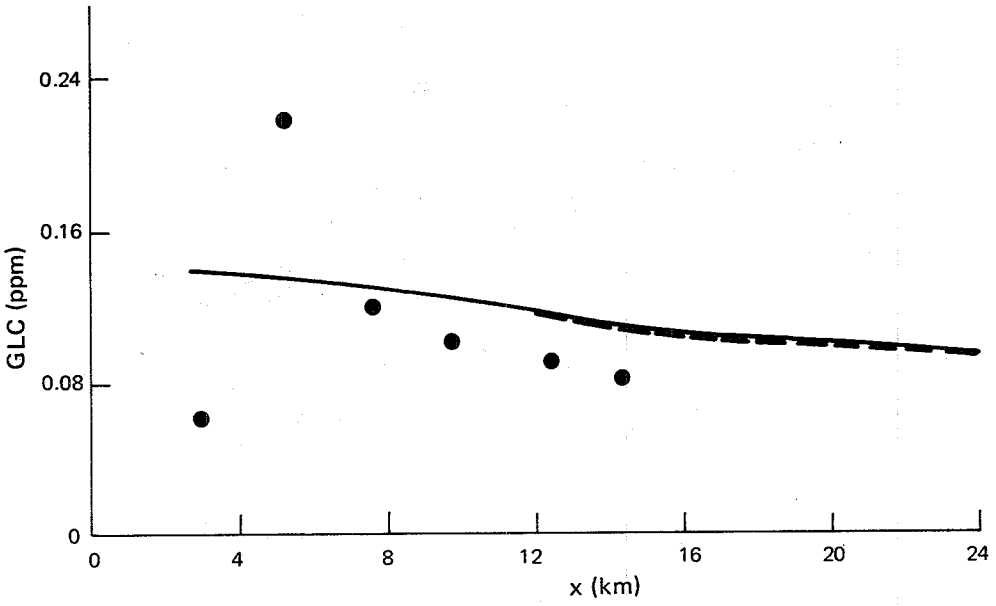

Figure 4.8. Peak GLC (ppm) versus downwind distance x(km) for Oct. 19 1055. Lines show model predictions using the negative w plume rise cutoff, under E stability with shear enhancement, and with no plume trapping.

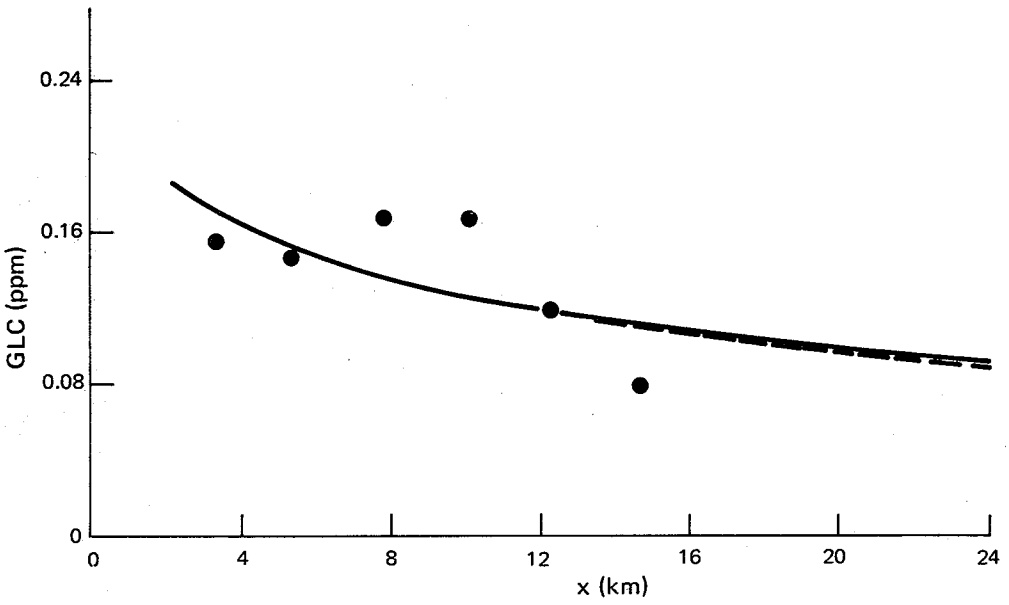

Figure 4.9. Peak GLC (ppm) versus downwind distance x(km) for Oct. 25 1100. Lines indicate model predictions using the negative w plume rise cutoff, under E stability with no shear enhancement, and with no plume trapping.

Despite the experimental scatter (which is inevitable in a single measurement of each randomly fluctuating concentration distribution), agreement between predictions and measurements is good over the wide range of ambient conditions encountered. Plume rise in both stable and neutral lapse situations had been modelled, and each of the $W < 0$, z_f correlation, and Briggs' correlation has been used to end the plume rise phase. Downwind dispersion has been modelled successfully using Briggs sigma curve for D and E stability classes both with and without σ_y enhancement due to cross-wind shear. Finally, both unlimited and limited mixing cases have been treated. Considering the uncertainties in input data, the kind of ground plane data available for comparison, and the simplified description of terrain around the G.C.O.S. site, this preliminary test of the dispersion model is very encouraging.

4.2.2 Cross-Wind Spread Versus Downwind Distance

A second test using aircraft ground plane data involves a comparison of measured and predicted cross-wind spread of the plume versus downwind distance from the source. In Figures 4.10 to 4.17, predicted σ_y variation with downwind distance is compared with the equivalent area $\sigma_{y_{AREA}}$ measurement abstracted from ground plane, cross-wind sulphur dioxide distributions.

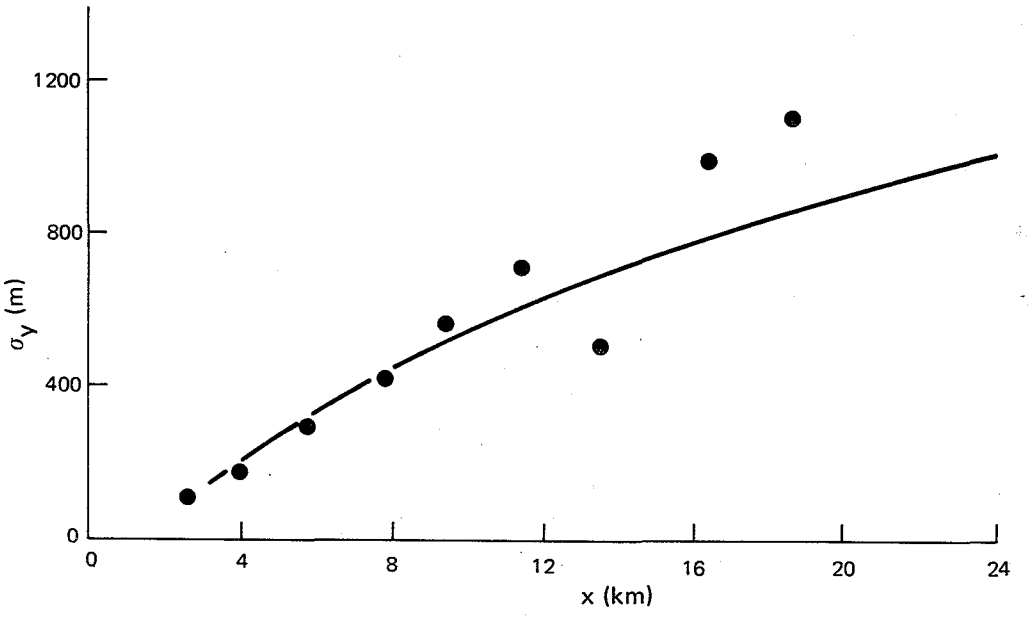

Figure 4.10. Comparison of measured and predicted plume spread σ_y(m) versus downwind distance x(km) for the ground plane traverses of Jan. 25 1130. Conditions as in Figure 4.2.

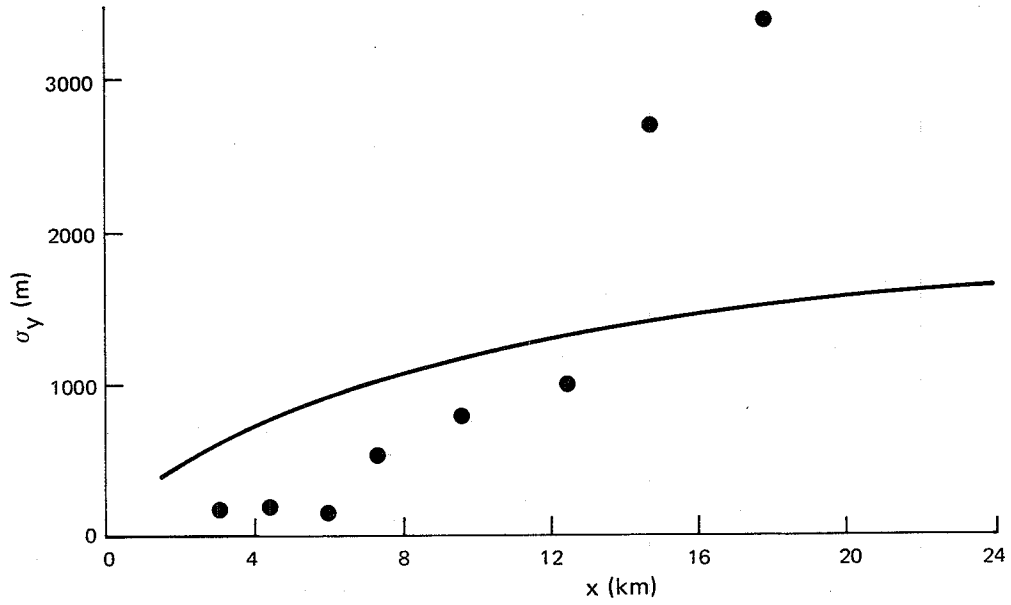

Figure 4.11. Comparison of measured and predicted plume spread σ_y(m) versus downwind distances x(km) for the ground plane traverse of Jan. 28 1315. Conditions are in Figure 4.3.

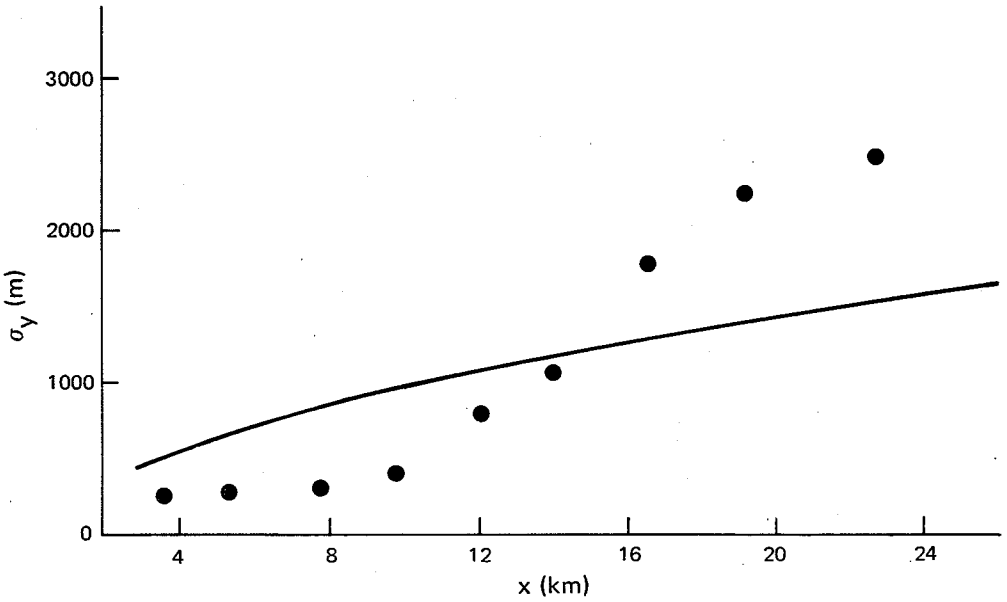

Figure 4.12. Comparison of measured and predicted plume spread σ_y(m) versus downwind distance x(km) for the ground plane traverse of Jan. 31 1455. Conditions as in Figure 4.4.

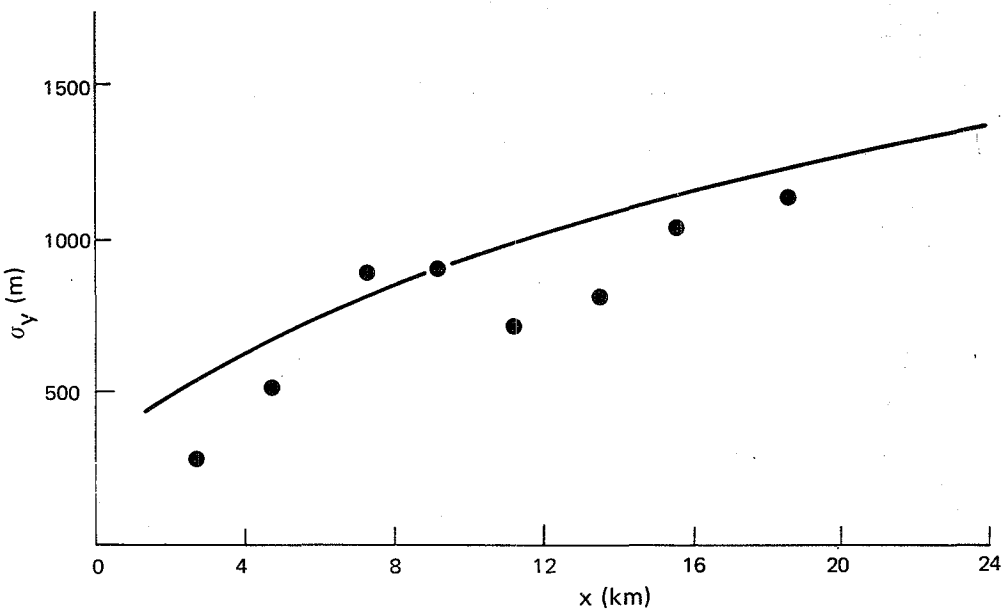

Figure 4.13. Comparison of measured and predicted plume spread σ_y(m) versus downwind distance x(km) for the ground plane traverses of Mar. 25 1020. Conditions as in Figure 4.5.

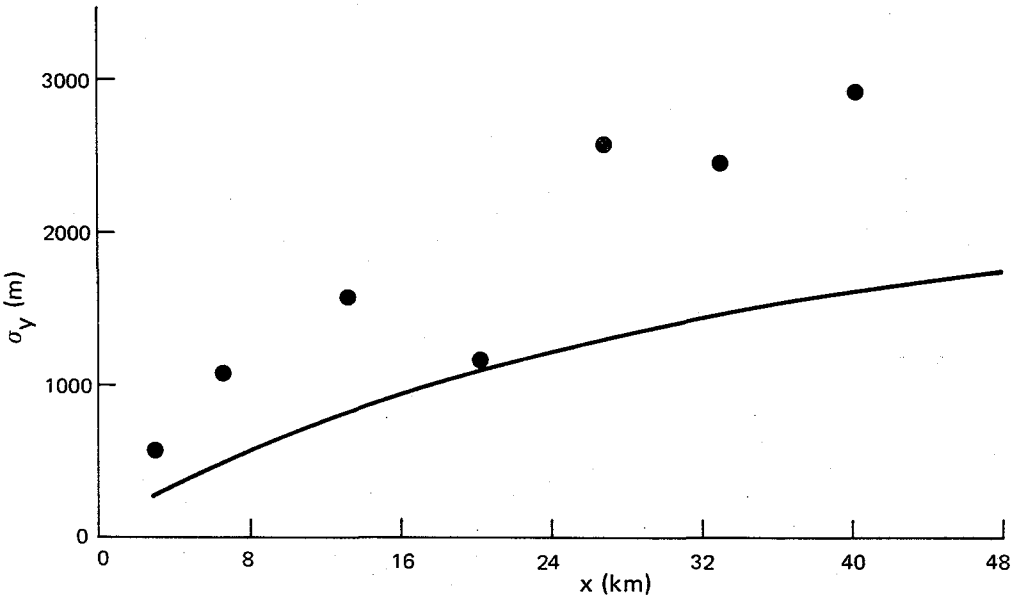

Figure 4.14. Comparison of measured and predicted plume spread σ_y(m) versus downwind distance x(km) for the ground plane traverses of Mar. 30 0955. Conditions as in Figure 4.6.

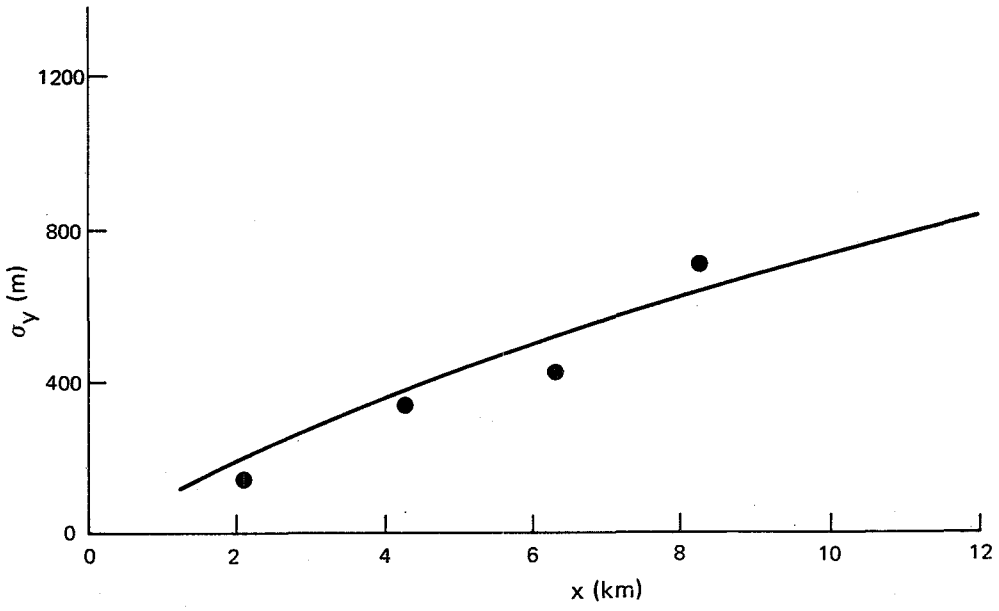

Figure 4.15. Comparison of measured and predicted plume spread σ_y(m) versus downwind distance x(km) for the ground plane traverses of Oct. 17 1125. Conditions as in Figure 4.7.

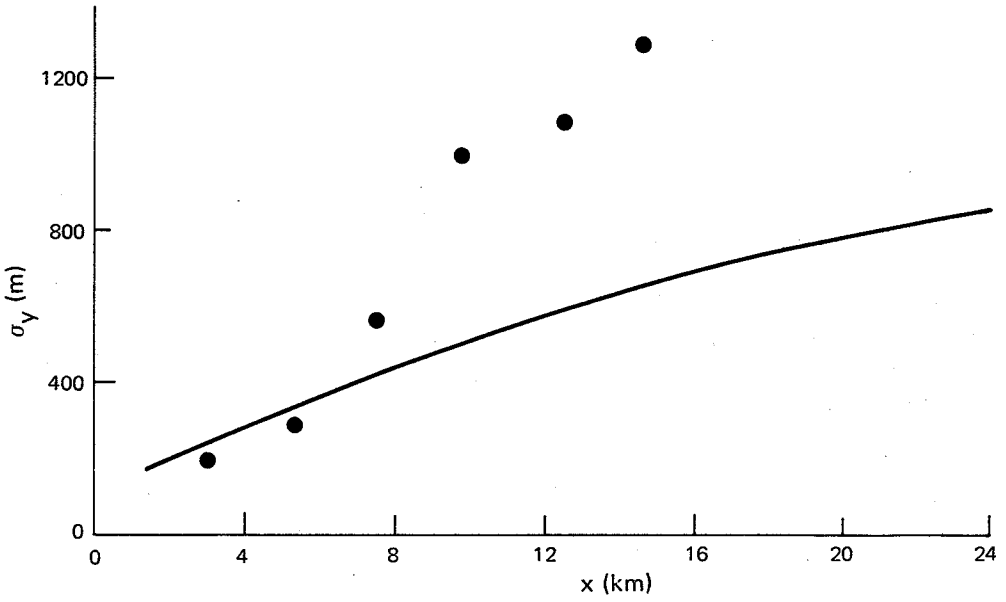

Figure 4.16. Comparison of measured and predicted plume spread σ_y(m) versus downwind distance x(km) for the ground plane traverses of Oct. 19 1055. Conditions as in Figure 4.8.

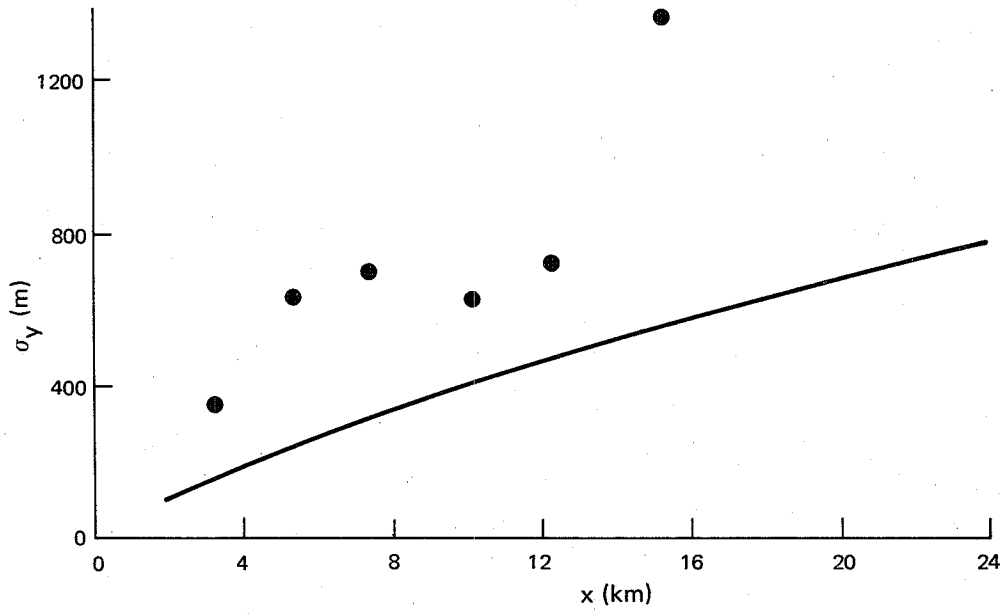

Figure 4.17. Comparison of measured and predicted plume spread σ_y(m) versus downwind distance x(km) for the ground plane traverses of Oct. 25 1100. Conditions as in Figure 4.9.

Agreement between measured and predicted values is less satisfactory than in the previous section. However, this disagreement is not unexpected, and can be attributed to two main causes. First, according to the discussion in Section 3, $\sigma_{y_{AREA}}$ from a single aircraft transect usually tends to underestimate actual plume spread, as might be measured, for example, by $\sigma_{y_{CONTOUR}}$ (see equation 3.8). Secondly, multiple sources become important when an attempt is made to map out the edges of the plume on the ground. From our measurements, the major contributor to the peak ground level SO_2 concentration will be the G.C.O.S. powerhouse stack, with other sources having only a small influence. All sources can contribute significantly, however, to the lower SO_2 levels near the plume edges, and modelling the powerhouse stack by itself will not be sufficient to predict the extent of these lower levels.

4.3 SENSITIVITY ANALYSIS

To evaluate the sensitivity of model predictions to uncertainties in source and ambient input data, the model was run using the values listed in Tables 4.1 and 4.2, which are representative of conditions for the G.C.O.S. powerhouse stack. A stack height of 100 m AGL was assumed, and peak ground level concentrations downwind were calculated on a flat ground plane at z = 0. Each of the various input parameters was independently altered by +20% and -20% while the others were held constant, and the model run was repeated.

Table 4.1. Sensitivity Test Data for Stable Conditions.

Input Parameters			
Source data:	W_o = 19 m/s	T_{p_o} = 290°C	Q = 2.5 kg/s
Wind data:	altitude (m)	z = 0	900
	speed (m/s)	u = 8.0	8.0
Temperature data:	altitude (m)	z = 0	900
	temperature (°C)	T = 15.0	14.0
	lapse rate	Γ = 0.00111°C/m	
Entrainment constants	α = 0.15	β = 0.68	

Output predictions

Final rise downwind distance = 1438 m
Effective stack height = 260 m
Peak GLC downwind distance = 32 km
Magnitude = 0.0147 ppm

Table 4.2. Sensitivity Test Data for Neutral Conditions.

Input Parameters

As in Table 4.1 except for temperature profile.

altitude (m)	z = 0	900
temperature (^{o}C)	T = 15.0	6.0
lapse rate	Γ = 0.01 ^{o}C/m	

(a) Output predictions using z_f/ℓ_B correlation

Final rise downwind distance = 2,071 m

Effective stack height = 384 m

Peak GLC downwind distance = 25,070 m

Magnitude = 0.0856 ppm

(b) Output prediction using Briggs' correlation

Final rise downwind distance = 1,438 m

Effective stack height = 326 m

Peak GLC downwind distance = 18,440 m

Magnitude = 0.123 ppm

A sensitivity analysis was performed for three basic situations: a stable lapse condition in the atmosphere employing the negative w plume rise cutoff; a neutral lapse condition in the atmosphere employing the z_f/ℓ_B correlation for plume rise cutoff; and a neutral lapse condition in the atmosphere employing Briggs correlation for plume rise cutoff. For all cases, only unlimited mixing was considered since it was felt that this situation would be most sensitive to variations in the input parameters.

The results of these calculations are presented in Tables 4.3, 4.4, and 4.5. The first line of Table 4.3 indicates, for example, that a +20% change in w_o (from 15 m/s to 18 m/s) leads to a -0.2% change in the downwind position of the final rise point (from 1438 m to 1435 m), and a +3.8% change in the effective stack height (from 260 m to 270 m). Further, this +20% w_o change leads to a +9.4% change in downwind distance to peak ground level concentration (from 32 km to 35 km) and a -27.9% change in the magnitude of the peak (from 0.0147 ppm to 0.0106 ppm). In reading these tables, it must be realized that only a few indicators of the model performance are being compared. There will be changes, for instance, in the overall shape of centerline GLC curve as well as in the position and magnitude of the peak, and it may be artificial to vary Q and w_o independently. Our aim here, however, is only to compare the relative importance of errors in various input parameters rather than to consider the actual predictions of the model in detail.

Table 4.3. Model Sensitivity During Stable Conditions.

Input Parameters		Output Parameters			
		Final Rise Change (%)		Peak GLC Change (%)	
Parameter	Change (%)	Distance	Height	Distance	Magnitude
w_o	+20	-0.2	+3.8	+9.4	-27.9
	-20	+0.2	-4.6	-9.4	+43.5
T_{p_o}	+20	+0.2	+1.9	+3.0	-15.6
	-20	-0.3	-2.7	-6.7	+24.5
u	+20	+20	-3.8	-7.2	+12.9
	-20	-20	+5.4	+9.8	-19.0
T	+20	+1.8	+0.3	+1.4	-3.4
	-20	-1.8	-0.8	-1.8	+3.4
Γ	+20	+1.3	+0.3	+1.4	-4.8
	-20	-1.3	-0.8	-1.8	+4.8
β	+20	+0.1	-6.9	-20.8	+76.2
	-20	-0.1	+9.6	+32.5	-56.5
Q	+20	nc	nc	nc	+20
	-20	nc	nc	nc	-20

Table 4.4. Model Sensitivity During Neutral Conditions.

Using the z_f/ℓ_B Final Rise Correlation

Input Parameters		Output Parameters			
		Final Rise Change (%)		Peak GLC Change (%)	
Parameter	Change (%)	Distance	Height	Distance	Magnitude
w_o	+20	+17.7	+14.8	+33.4	-26.3
	-20	-19.1	-14.8	-25.5	+43.2
T_{p_o}	+20	+7.4	+7.3	+16.6	-14.4
	-20	-14.4	-8.9	-15.4	+22.5
u	+20	-4.9	-14.3	-24.3	+18.0
	-20	-9.7	+13.8	+28.8	-6.3
T	+20	-15.0	-0.8	+0.9	+2.4
	-20	+52.4	-2.3	+2.1	+4.2
Γ	+20	-15.5	nc	+0.9	-0.5
	-20	+53.2	-2.3	+2.1	+5.3
β	+20	+17.6	nc	-4.7	+2.5
	-20	-21.0	nc	+6.1	-2.1
Q	+20	nc	nc	nc	+20
	-20	nc	nc	nc	-20

Table 4.5. Model Sensitivity During Neutral Conditions.

Input Parameters		Output Parameters			
		Final Rise Change (%)		Peak GLC Change (%)	
Parameter	Change (%)	Distance	Height	Distance	Magnitude
w_o	+20	+10.6	+7.4	+14.4	-15.4
	-20	-6.3	-8.6	-16.8	+23.6
T_{p_o}	+20	+5.8	+4.0	+5.8	-8.1
	-20	-4.7	-4.9	-11.2	+13.0
u	+20	+3.6	-11.3	-21.4	+10.6
	-20	+0.3	+17.5	+32.3	-12.2
T	+20	-6.7	-0.3	-0.5	+2.4
	-20	+18.8	+0.6	+1.5	-1.6
Γ	+20	-7.3	nc	-0.6	nc
	-20	+11.7	nc	+0.9	nc
β	+20	+23.9	nc	-6.2	+3.3
	-20	-17.5	nc	+4.1	-1.6
Q	+20	nc	nc	nc	+20
	-20	nc	nc	nc	-20

With this approach in mind, the sensitivity of peak GLC to change in effective stack height is evident in the tables.

The model is apparently very sensitive to variations in those input parameters which change the effective stack height. Of the source parameters, w_o has the strongest effect, while the effort of T_{po} is somewhat less, and variations in Q are linearly related to variations in peak GLC. Of the ambient parameters, wind speed is the most important, while variations in air temperature and lapse rate are of minor importance. Model sensitivity to changes in windspeed is reduced, however, by competing effects. An increase in u during stable conditions, for example, leads to a decrease in effective stack height which tends to increase peak GLC. On the other hand peak GLC according to the Gaussian plume model is inversely proportional to u (see equation 4.7), so that an increase in u tends to decrease peak GLC.

Differences in sensitivity between stable and neutral lapse conditions arise from the method of ending plume rise. During stable conditions, plume rise ends when $w < 0$, and the downwind position and altitude of this point depends on several input parameters and on β. During neutral conditions, however, plume rise ends at a predetermined altitude fixed either by the z_f/ℓ_B correlation or by Briggs' correlation. Briggs' correlation for final rise, for example, depends only on buoyancy length, which contains the parameters w_o, T_{p_o}, T_o, and u.

Note also that the z_f/ℓ_B correlation leads to a higher final rise prediction than does Briggs' correlation, in agreement with our observations.

5. A ONE DIMENSIONAL PLANETARY BOUNDARY LAYER MODEL

5.1 INTRODUCTION

In this chapter a one-dimensional* planetary boundary layer (PBL) model was developed and tested using the observed meteorological data from Slawson et al (1978). The model was developed by modifying an existing version of a two-dimensional planetary boundary layer model developed by Maddukuri (1977) which was subsequently applied by Maddukuri et al (1978) to the Nanticoke region on the North shore of Lake Erie.

The model assumes horizontal homogeneity in the x and y directions. The model in its present form consists of a constant flux layer near the surface and a transition layer above the constant flux layer. The original model (Maddukuri, 1977) consisted of a soil layer also. However, in the present case this layer is not included as no sub-surface temperature measurements were available for the present application.

---

*Only a one dimensional model is used here as the Syncrude data are obtained at only one location.

5.2 THE GOVERNING EQUATIONS

5.2.1 The Transition Layer

In writing the planetary boundary layer equations the vertical coordinate z is replaced by a new vertical coordinate (ϕ) by the following relation:*

$$\phi = \frac{z - h}{H}$$

Here, z is the vertical coordinate in the Cartesian coordinate system, h is the elevation of the surface, H (a constant) is the distance between the local surface and the top of the model. Hence z = h corresponds to ϕ = 0 and z = H + h corresponds to ϕ = 1. According to this definition the distance between any two surfaces of constant ϕ remains unaltered along the horizontal.

In order to avoid non-uniform grid spacing, a further coordinate transformation in the vertical to a new independent variable is made. In the present study the following transformation is used:

$$\zeta = \ell n \frac{(H\phi + 0.01)}{0.01} + \frac{H\phi}{30}$$

---

*This is not necessary for the present case of a one-dimensional model. However, since in the original two-dimensional model this relation was used to take topography into account, it is left unchanged.

The present model extends up to H above the local surface (i.e. H + h from a reference surface). This log-linear transformation is chosen arbitrarily but it gives good resolution (as given in Table 5.1) throughout the model's vertical extent. With this transformation, the governing equations for a one-dimensional planetary boundary layer model can be written as:

$$\frac{\partial u}{\partial t} = fv - c_p\theta \frac{\partial P}{\partial x} + \frac{1}{H^2} \frac{\partial \zeta}{\partial \phi} \frac{\partial}{\partial \zeta} \left(K \frac{\partial u}{\partial \zeta} \frac{\partial \zeta}{\partial \phi}\right), \tag{5.1}$$

$$\frac{\partial v}{\partial t} = - fu - c_p\theta \frac{\partial P}{\partial y} + \frac{1}{H^2} \frac{\partial \zeta}{\partial \phi} \frac{\partial}{\partial \zeta} \left(K \frac{\partial v}{\partial \zeta} \frac{\partial \zeta}{\partial \phi}\right), \tag{5.2}$$

and

$$\frac{\partial \theta}{\partial t} = \frac{1}{H^2} \frac{\partial \zeta}{\partial \phi} \frac{\partial}{\partial \zeta} \left(K \frac{\partial \theta}{\partial \zeta} \frac{\partial \zeta}{\partial \phi}\right) \tag{5.3}$$

In the above equations, x and y are the two horizontal axes while t is time. The eastward (x-) and northward (y-) components of the wind velocity are represented by u and v respectively. The Coriolis parameter is denoted by f, while K is the eddy exchange coefficient for momentum and heat along the vertical. The variables θ and P are the potential temperature and the pressure respectively. Further,

$$P \equiv (p/p_o)^{R/c_p},$$

Table 5.1. Heights above the local surface corresponding to the vertical grid levels used in the model.

Vertical grid number	Height in metres
1	0.00
2	0.21
3	4.24
4	34.34
5	96.33
6	171.84
7	253.10
8	337.35
9	423.42
10	510.66
11	598.80
12	687.53
13	776.73
14	866.35
15	956.25
16	1046.15
17	1136.82
18	1227.39
19	1318.13
20	1409.00
21	1500.00

where R is the gas constant, p_o is the standard pressure and c_p is the specific heat of air at constant pressure.

The first two equations are the equations of motion, the third one is the equation for potential temperature. Since horizontal homogeneity is assumed along x and y directions, the pressure gradients in (5.1) and (5.2) are computed using the geostrophic relations, namely:

$$fu_g + c_p\theta \frac{\partial P}{\partial y} = 0, \text{ and} \tag{5.4}$$

$$fv_g - c_p\theta \frac{\partial P}{\partial x} = 0. \tag{5.5}$$

Here, u_g and v_g are the eastward and northward components of geostrophic wind velocity respectively.

To solve the system of equations (5.1) through (5.3), the eddy exchange coefficient, K must be specified. The parameterized expressions for the vertical eddy exchange coefficient are different in the constant flux layer and the transition layer. The expressions used in the transition layer are given below:

$$K = K(z) = \begin{cases} \ell^2 S_w (1 + \alpha R_i), & \text{for } 0 > R_i \quad (5.6a) \\ \ell^2 S_w (1 - \alpha R_i)^{-1}, & \text{for } R_i > 0 \quad (5.6b) \end{cases}$$

where $$S_w \equiv \left\{ \left(\frac{\partial u}{\partial z} \right)^2 + \left(\frac{\partial v}{\partial a} \right)^2 \right\}^{\frac{1}{2}},$$

ℓ is the mixing length, R_i is the Richardson number, and α is a constant (-3). The above expressions were suggested by Estoque and Bhumralkar (1970).

The mixing length, ℓ, is specified by using the empirical expression, as given by Blackadar (1962),

$$\ell = \frac{k_o (z + z_o)}{1 + k_o (z + z_o)/\lambda}$$

where $\lambda = 0.0004\ U_g f^{-1}$ as suggested by Taylor (1969). Here U_g is the geostrophic wind speed, k_o is von Karman constant and z_o is the roughness length.

In the present study z_o was set equal to 0.1 m. In order to prevent K(z) becoming too small in the region of negligible wind shear, S_w in (5.6) is replaced by 0.001 if S_w falls below this limit and R_i in (5.6b) is replaced by 0.2 if R_i exceeds this limit. However, if the value of K(z) so computed still falls below a limiting value of 1 m^2/s, this limiting value is used for K(z).

5.2.2 The Constant Flux Layer

The constant flux layer used here extends up to about 35 m above the local surface. In this layer the parameterized expressions for the vertical eddy exchange coefficient are given below:

$$\Gamma\ (z + z_o)^2\ (\frac{g}{\theta})^{\frac{1}{2}} \left|\frac{\partial\theta}{\partial z}\right|^{\frac{1}{2}}, \text{ for } R_i \leq -0.048 \qquad (5.7a)$$

$$\ell^2 S_w\ (1 + \alpha R_i)^2, \text{ for } 0 \geq R_i > 0.048 \qquad (5.7b)$$

$$K_{mz} = K_{\theta z} = K(z) =$$

$$\ell^2 S_w\ (1 - \alpha R_i)^{-2}, \text{ for } R_i > 0 \qquad (5.7c)$$

where Γ is a constant (0.9) and all other symbols have the same meaning as before. The expression (9a) was suggested by Priestly (1959). The other two expressions were used by Estoque and Bhumralkar (1970).

Using the above expressions for K(z) in conjunction with the assumption of constant fluxes of momentum and heat, the following profile equations are derived.

$$V = U_* \left\{ \frac{1}{k_o} \ell n \frac{(z + z_o)}{z_o} + \frac{z}{\lambda} - \alpha \frac{g}{\theta_o} \frac{\theta_*}{U_*^2} z \right\}, \qquad (5.8)$$

and

$$\theta - \theta_o = \theta_* \left\{ \frac{1}{k_o} \ell n \frac{(z + z_o)}{z_o} + \frac{z}{\lambda} - \frac{\alpha g}{\theta_o} \frac{\theta_*}{U_*^2} z \right\} \text{ for } R_i \geq -.048 \qquad (5.9)$$

For $R_i < -0.048$

$$V = -3\Gamma^{-2/3} U_*^{5/3} \left(\frac{g}{\theta_o}\right)^{-1/3} \theta_*^{-1/3} \{(z + z_o)^{-1/3} - z_o^{-1/3}\} \tag{5.10}$$

and

$$(\theta - \theta_o) = -3\Gamma^{-2/3} U_*^{2/3} \theta_*^{2/3} \left(\frac{g}{\theta_o}\right)^{-1/3} \{(z + z_o)^{-1/3} - z_o^{-1/3}\} \tag{5.11}$$

In the above equations U_* and θ_* are friction velocity and friction potential temperature respectively, while V is the wind speed and θ_o is the potential temperature at the surface.

5.2.3 The Finite Difference Scheme

Forward differences are adopted in time. The independent variables ζ, and t are rendered discrete by the transformations $\zeta = (k - 1)\,\Delta\zeta$ and $t = (n - 1)\,\Delta t$, where k, and n are integers, $\Delta\zeta$ is a space interval in the ζ direction and Δt is the time interval.

For the diffusion term implicit centered differencing (Laasonen, 1949) was used. Using this scheme, (5.2) may be re-written (as an example) in the following way:

$$V_k^{n+1} - \frac{\Delta t}{H^2} \left(\frac{\partial \zeta}{\partial \phi}\right)_k \left[K_{k+\frac{1}{2}}^n \left(\frac{\partial \zeta}{\partial \phi}\right)_{k+\frac{1}{2}} (v_{k+1}^{n+1} - v_k^{n+1})\right.$$

$$- K^{n}_{k-\frac{1}{2}} \left(\frac{\partial \zeta}{\partial \phi} \right)_{k-\frac{1}{2}} (v^{n+1}_{k} - v^{n+1}_{k-1})]/\Delta\zeta^{2} = E_{c} \Delta t + v^{n}_{k} \qquad (I)$$

where $E_c = f(u_g - u^n_k)$. It may be noted that the vertical eddy exchange coefficient in (I) is explicit. At any time step, n, E_c is constant. Then the coefficients of the variables v^{n+1}_{k+1}, v^{n+1}_{k}, v^{n+1}_{k-1} form the elements of a tridiagonal matrix. The variables can then be obtained easily by using a simple subroutine such as that described by Roache (1972) to solve the tridiagonal matrix.

5.2.4 Boundary Conditions

(A) At the top boundary, $\zeta = \zeta_1$:

$$u\ (\zeta_1) = u_g,\ v\ (\zeta_1) = v_g,\ \theta\ (\zeta_1) = \theta_1$$

(B) At the surface boundary, $\zeta = \zeta_o$:

$$u = 0,\ v = 0,\ \theta = \theta\ (\zeta_o, t)$$

The value $\theta\ (\zeta_o, t)$ may be determined by using a heat balance equation near the interface of the earth and the atmosphere. However, no soil temperature measurements were available for this study. Therefore, $\theta\ (\zeta_o, t)$ is specified from the available observed values at the lowest level. The lowest level at which the measurements were

made is about 3 m. Therefore, the temperature near the surface is assumed to be about 1.5^{o} higher than that observed at 3 m. This assumption should not be used under nocturnal conditions as inversions are generally present during night.

5.2.5 Initial Conditions

The initial potential temperature profile is obtained by hand-smoothing the observed potential temperature profile. The initial wind components are $u = u_g$ and $v = v_g$. The geostrophic components u_g and v_g are obtained by averaging (in space) the observed wind speed and wind direction profiles between 1000 m and 2000 m heights. The observed time of these profiles must be the same or nearly the same as that of the initial potential temperature. Alternatively these components can be specified from upper air charts.

5.3 RESULTS AND DISCUSSION

Using the model described earlier, wind and temperature profiles within the PBL observed near the GCOS site on three different days in 1977 were simulated. While discussing and comparing these results with observations, one should bear in mind the model's assumption of homogeneous surface and the departure of the actual site from homogeneity. A description of the actual site can be found in Slawson et al[12] (1978). From that description the observational site appears

to be considerably non-homogeneous. Consequently, in the real case the wind and temperature profiles are influenced by the horizontal and vertical advection. Also, they are influenced by unsteadiness and the baroclinicity of the large scale flow.

A discussion of the present model's results, and a comparison of them with the observation are given below.

March 26, 1977. The large scale wind on this day was nearly west-southwesterly (i.e. nearly normal to the Athabasca river valley). The wind components used for the initialization of the model are $u = 6.13$ m s^{-1} and $v = 4.14$ m s^{-1}. These are obtained from the wind speed and wind direction profiles observed at 0902 MST.

The initial potential temperature profile used (was also obtained at 0902 MST) is shown in Figure 5.1. It can be seen from this figure that the atmosphere was stably stratified. Over the next two hours the temperature distribution changed very little, except below about 400 m height. This is mainly due to surface heating. The predicted profiles agree quite well with the observed profiles over most of the region. However, near the 550 m height the predicted profile at 1100 MST is somewhat colder than the corresponding observed one. The reason for this may be downward vertical velocities, which were ignored by the model. A similar discrepancy between the observed and predicted potential temperature profiles may be noted even at

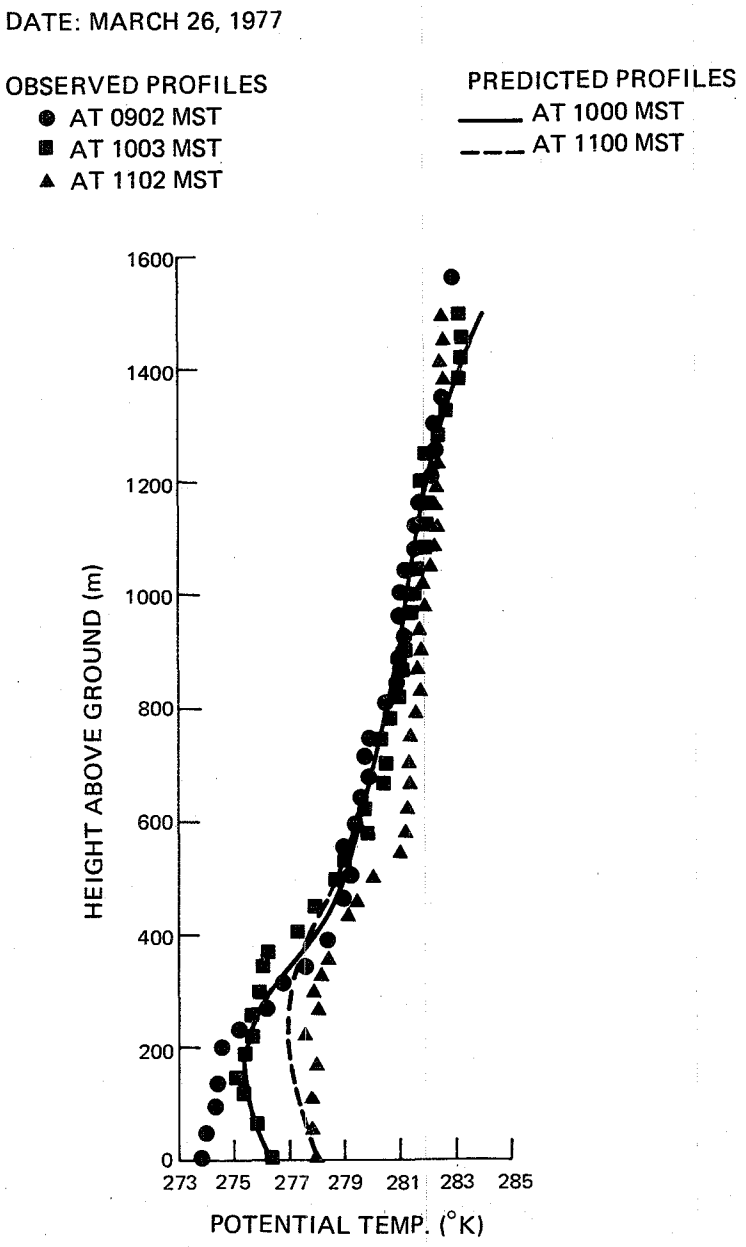

Figure 5.1. Observed and predicted potential temperature profiles (March 26, 1977.)

later times (see Figures 5.2 and 5.3). Incorporation of penetrative convection into the model may improve the results somewhat even though vertical velocities cannot be included. At still later time, i.e. at 1600 MST, both the observed and predicted profiles agree very well, except near the top boundary (Figure 5.4). Since the atmosphere was nearly neutrally stratified at this time, vertical velocities had no effect on the temperature distribution. This may be the main reason for the remarkable agreement between the observed and predicted potential temperature profiles in Figure 5.4.

Observed and predicted profiles of wind speed and wind direction are presented in Figures 5.5 and 5.7. Referring to Figure 5.5, it may be noted that the predicted and observed wind speed profiles at around 1000 MST show similar features. However the observed wind speeds below about 600 m height are lower. Below this height the observed wind direction profiles (see Figure 5.5) show considerable scatter. The predicted profile is in very good agreement with the observed profiles above the 600 m height. Below that height, it is difficult to draw any definite conclusions because of the large scatter in the observational data. At around 1100 MST (see Figure 5.6), and 1300 and 1400 MST both the observed and predicted wind speed profiles show, once again, similar features although the observed wind speeds are lower than those predicted. The observed and predicted wind direction profiles at 1100 MST do not agree below about 900 m height. However, at 1300 and 1400 MST the predicted and observed wind

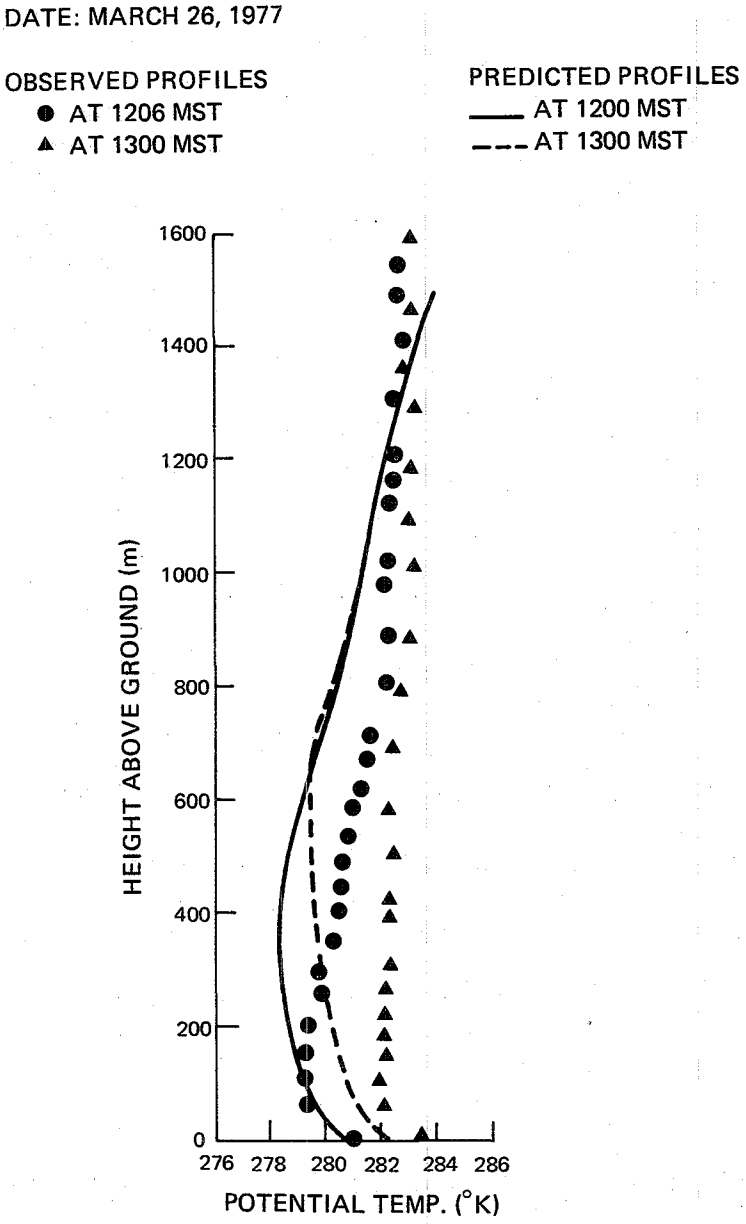

Figure 5.2. Observed and predicted potential temperature profiles (March 26, 1977).

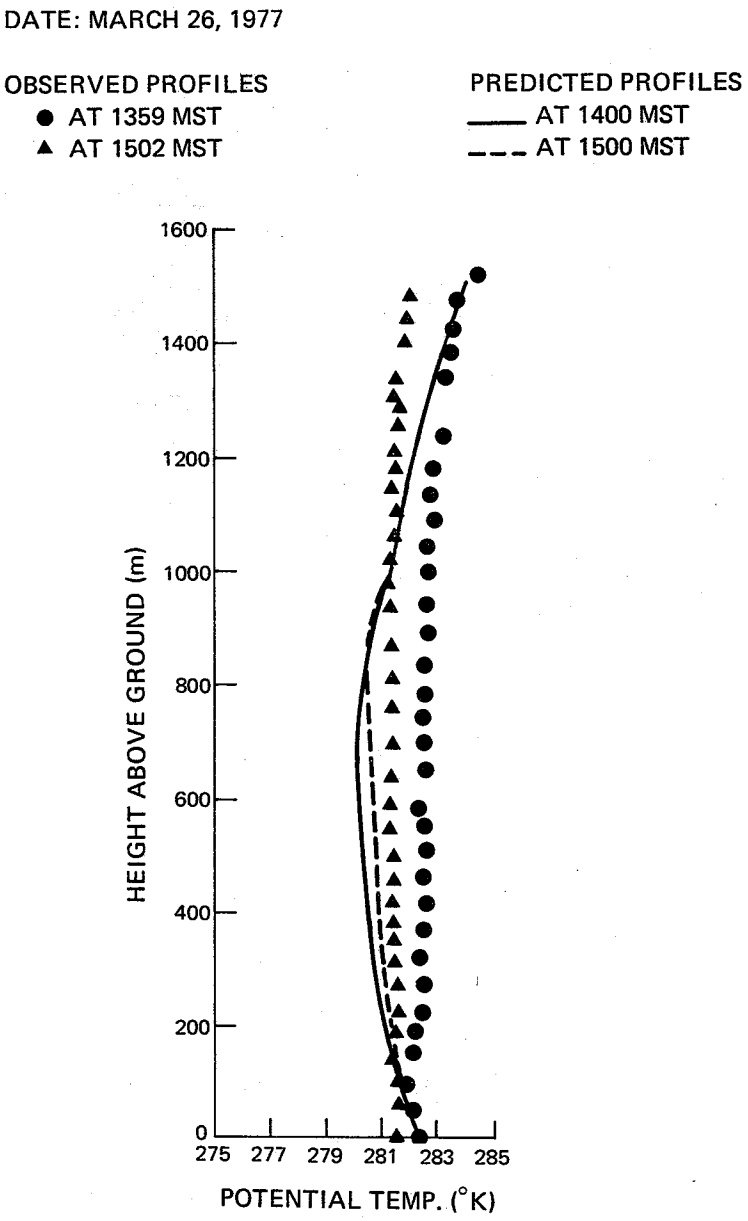

Figure 5.3. Observed and predicted potential temperature profiles (March 26, 1977).

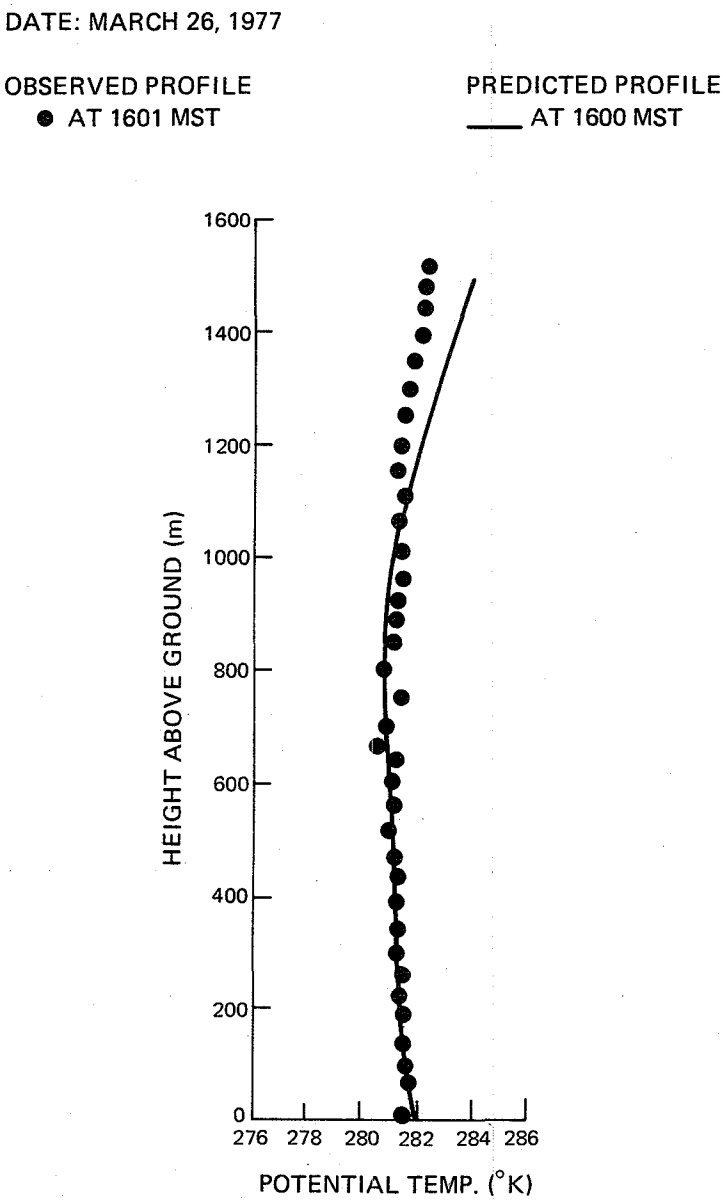

Figure 5.4. Observed and predicted potential temperature profile (March 26, 1977).

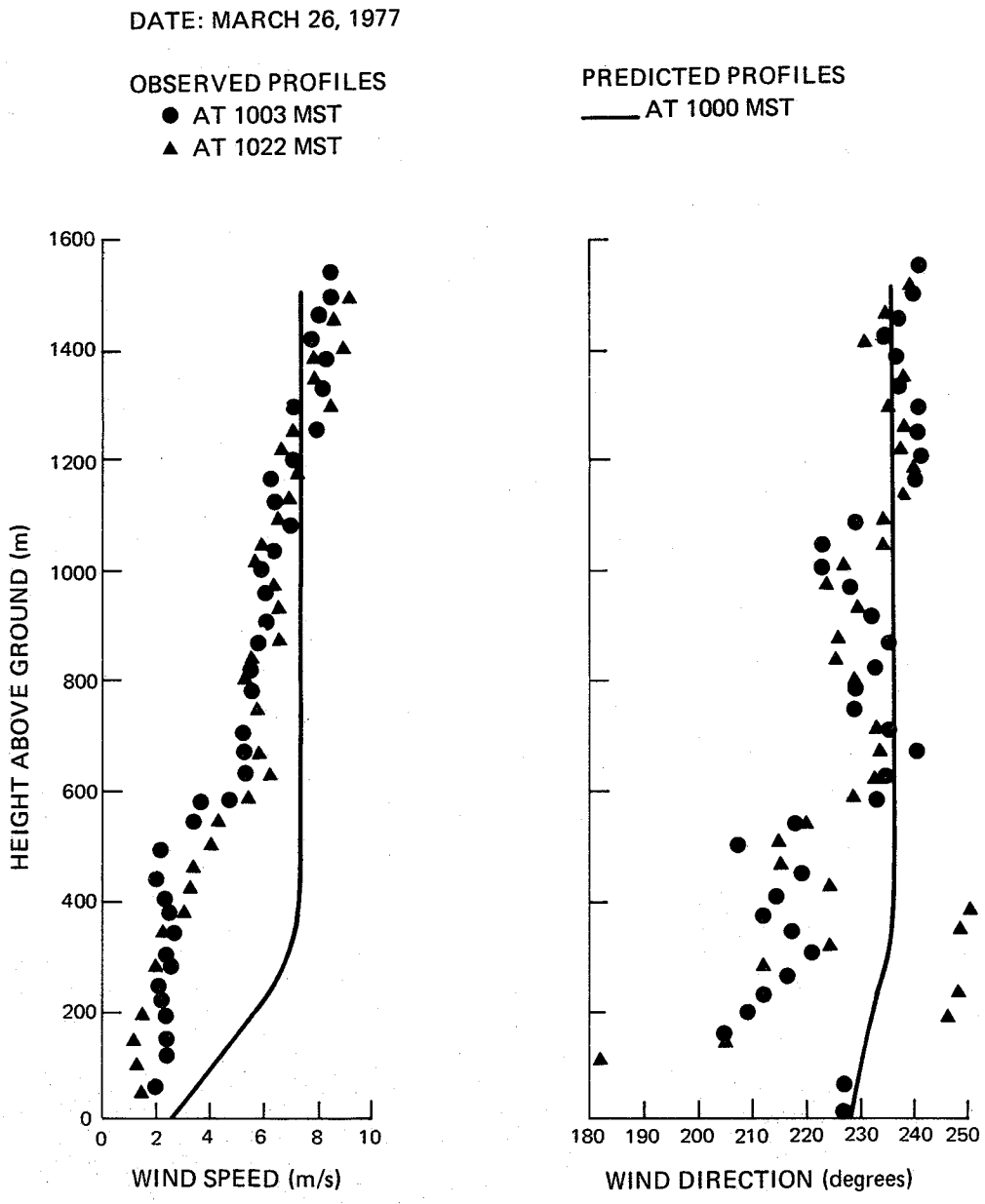

Figure 5.5. Observed and predicted wind profiles (March 26, 1977).

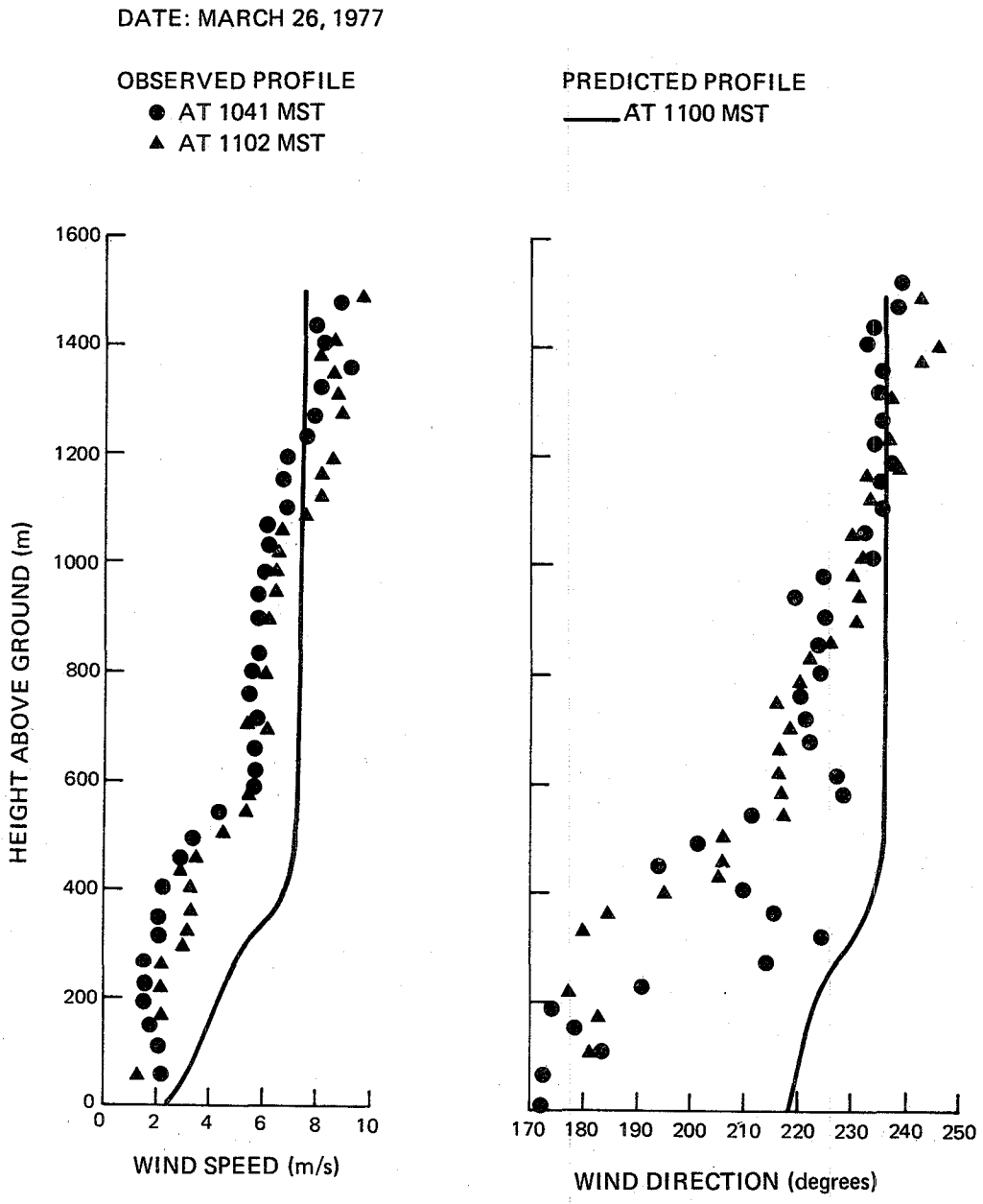

Figure 5.6. Observed and predicted wind profiles (March 26, 1977).

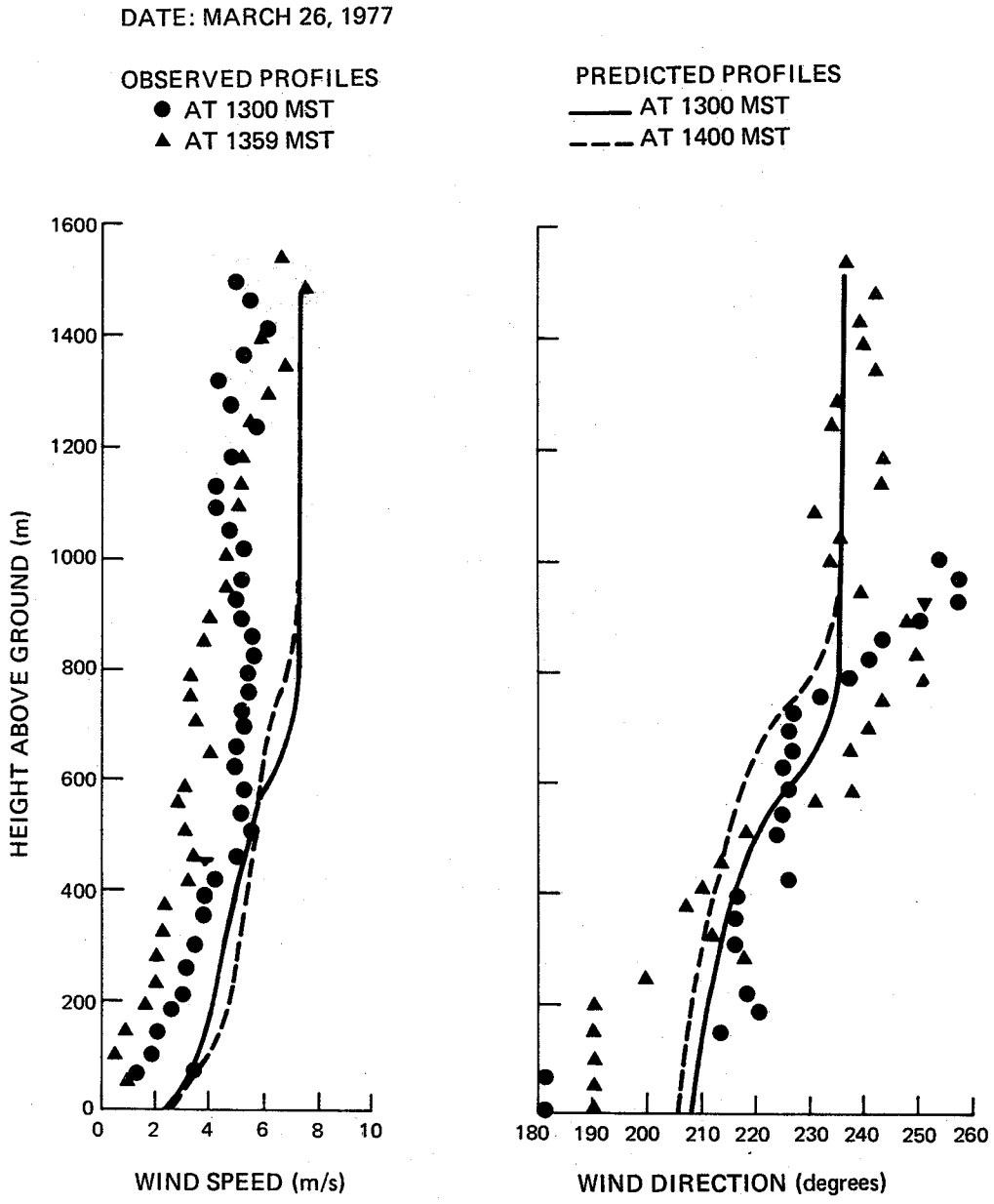

Figure 5.7. Observed and predicted wind profiles (March 26, 1977).

direction profiles (see Figure 5.7) show good agreement, except in a shallow layer of about 150 m height near the surface. The scatter near the surface in the observed data may partly be due to observational errors and partly due to non-homogeneity introduced by the Athabasca river and valley.

July 16, 1977. The large scale wind on this day was nearly southerly. The wind components used initially as input are $u = 1.26$ m s^{-1} and $v = 8.41$ m s^{-1}. The initial temperature profile used as input was observed at 0602 MST. It is shown in Figure 5.8. Referring to this figure it can be seen that the atmosphere is slightly stably stratified over most of the region, except between 100 m and 300 m heights where a stronger stability can be observed. These conditions prevailed for at least the next 2 to 2½ hours. The predicted profiles (see Figure 5.8) are in excellent agreement with the observed ones. During the next three hours (see Figure 5.9) the predicted potential temperature profiles tend to be cooler than the observed ones. However, both the observed and predicted profiles show the same trend. The predicted temperature profiles continue to be cooler (see Figure 5.10) over the next 2 hours. The reason, for this discrepancy, appears to be warming up of the atmosphere by large scale advection of heat. Referring to Figures 5.8 through 5.10, one can notice that the observed potential temperature at 1500 m height is increased by about $2^{o}K$ (i.e. from about $294^{o}K$ to $296^{o}K$) over a period of 5 hours. This increase is probably due to changes in synoptic

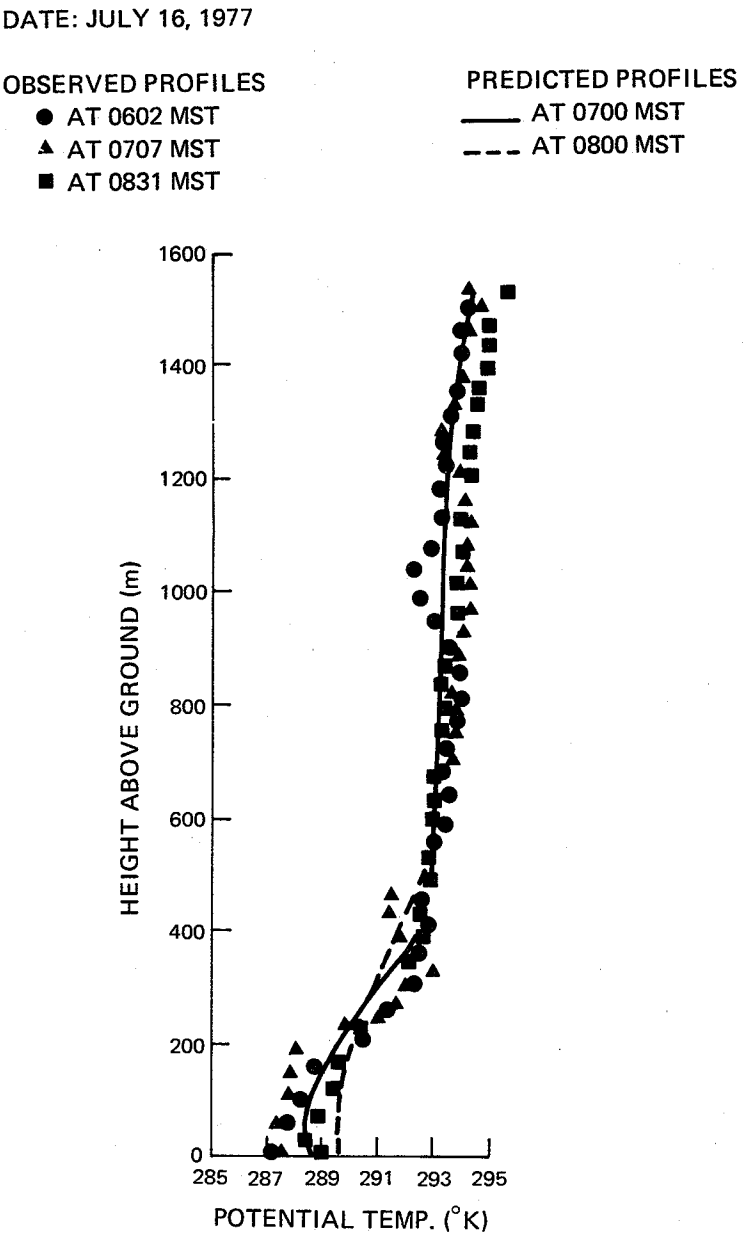

Figure 5.8. Observed and predicted potential temperature profiles (July 16, 1977).

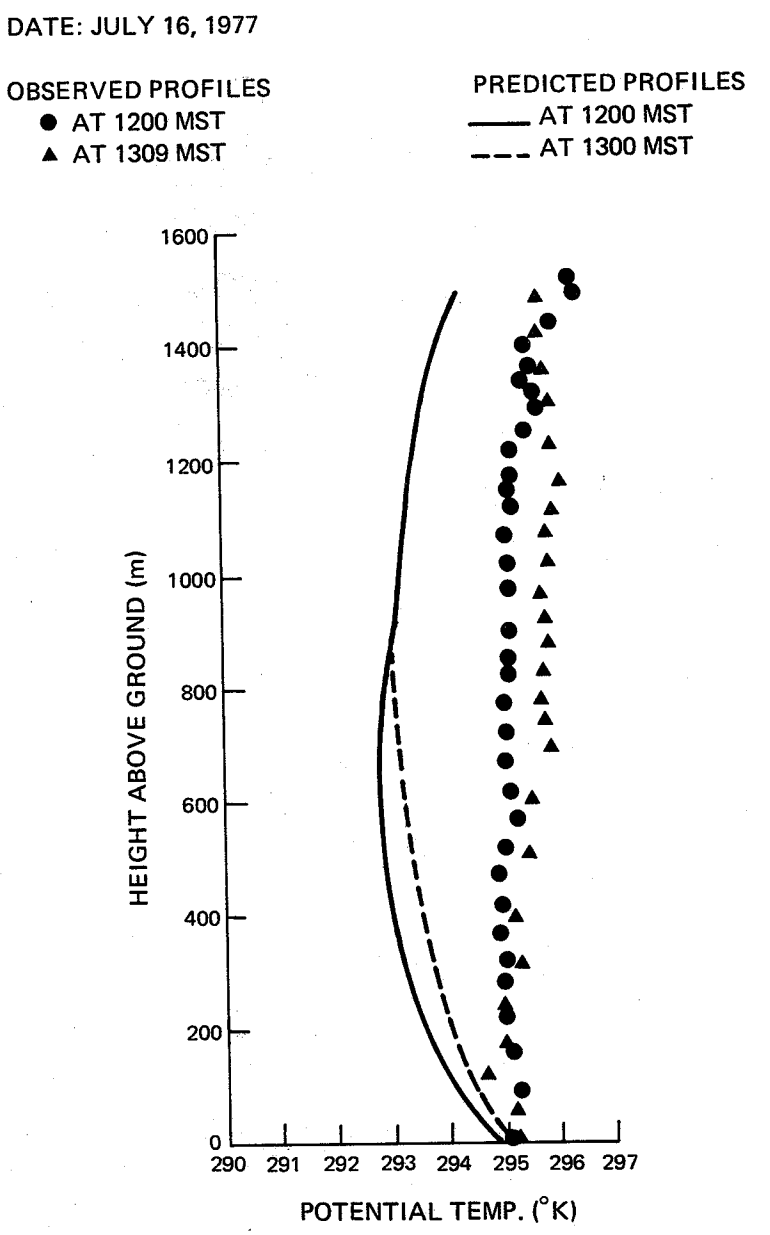

Figure 5.10. Observed and predicted potential temperature profiles (July 16, 1977).

conditions as mentioned above and appears as a deviation between the predicted and observed profiles.

The predicted and observed profiles of wind speed and wind direction are shown in Figure 5.11 through 5.13. The measured wind profile at 0707 MST is missing between about 500 m to 700 m. Also, it appears to be suspect below this height. Except for this, there is a very good agreement between the measured and predicted profiles of wind (both in speed and direction) at all levels except very near the surface as can be seen from these figures (i.e. Figures 5.11 through 5.13). It may be noted here, that the computed wind direction profile at 1300 MST is nearly coincident with that at 1200 MST and, hence, is not shown in the figure.

July 20, 1977. On this day the large scale atmosphere is considerably unsteady as can be seen from Figure 5.14. The wind varied from westerly to southwesterly. The wind speed changed from about 4.5 m s^{-1} to about 7 m s^{-1} over a period of 7 hours. In spite of the unsteadiness in large scale conditions, this day was chosen for the simulation in order to assess the model's performance under such conditions.

Two cases were modeled. Case A uses fixed top boundary conditions. For case B the top boundary conditions are specified as a function of time.

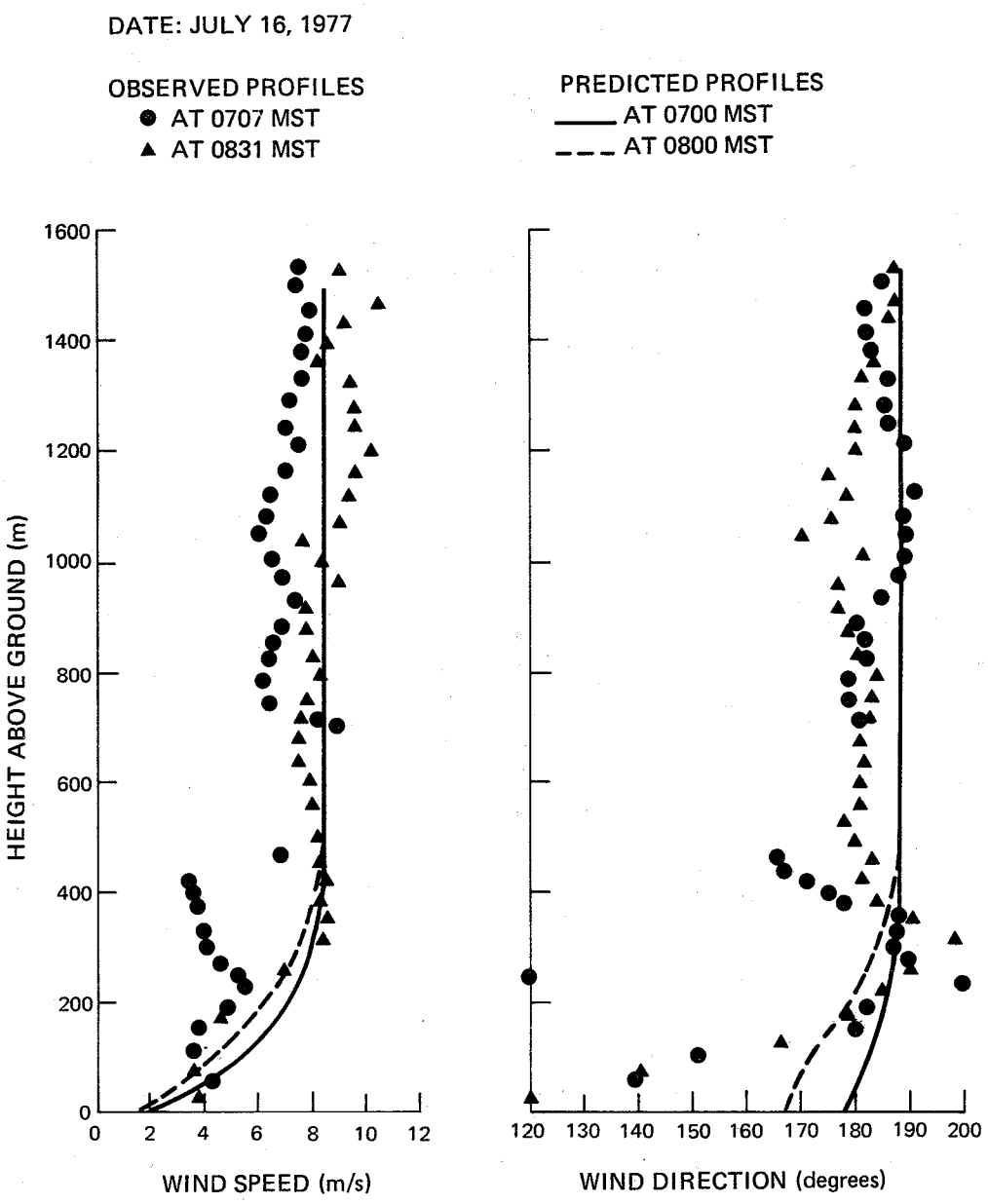

Figure 5.11. Observed and predicted wind profiles (July 16, 1977).

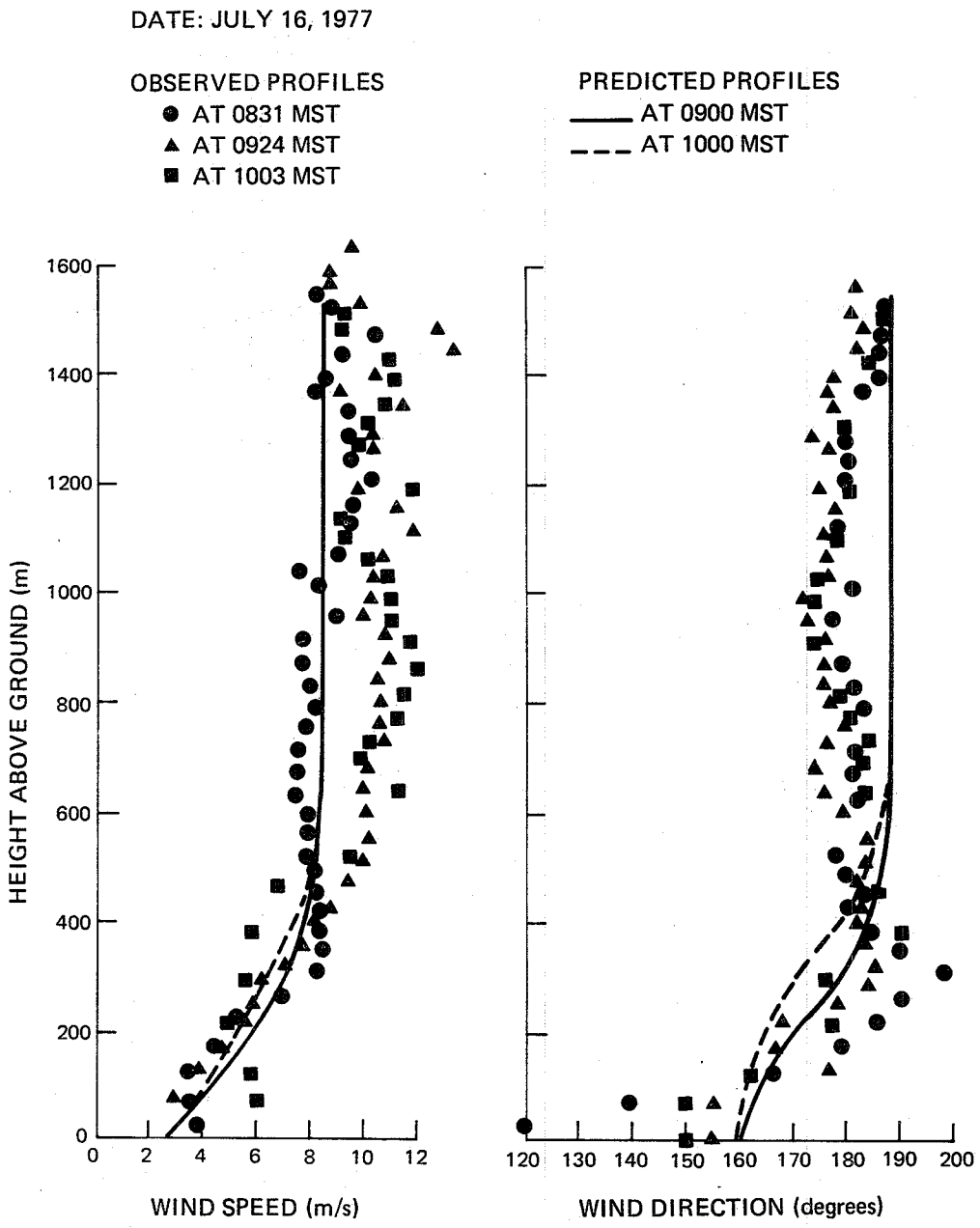

Figure 5.12. Observed and predicted wind profiles (July 16, 1977).

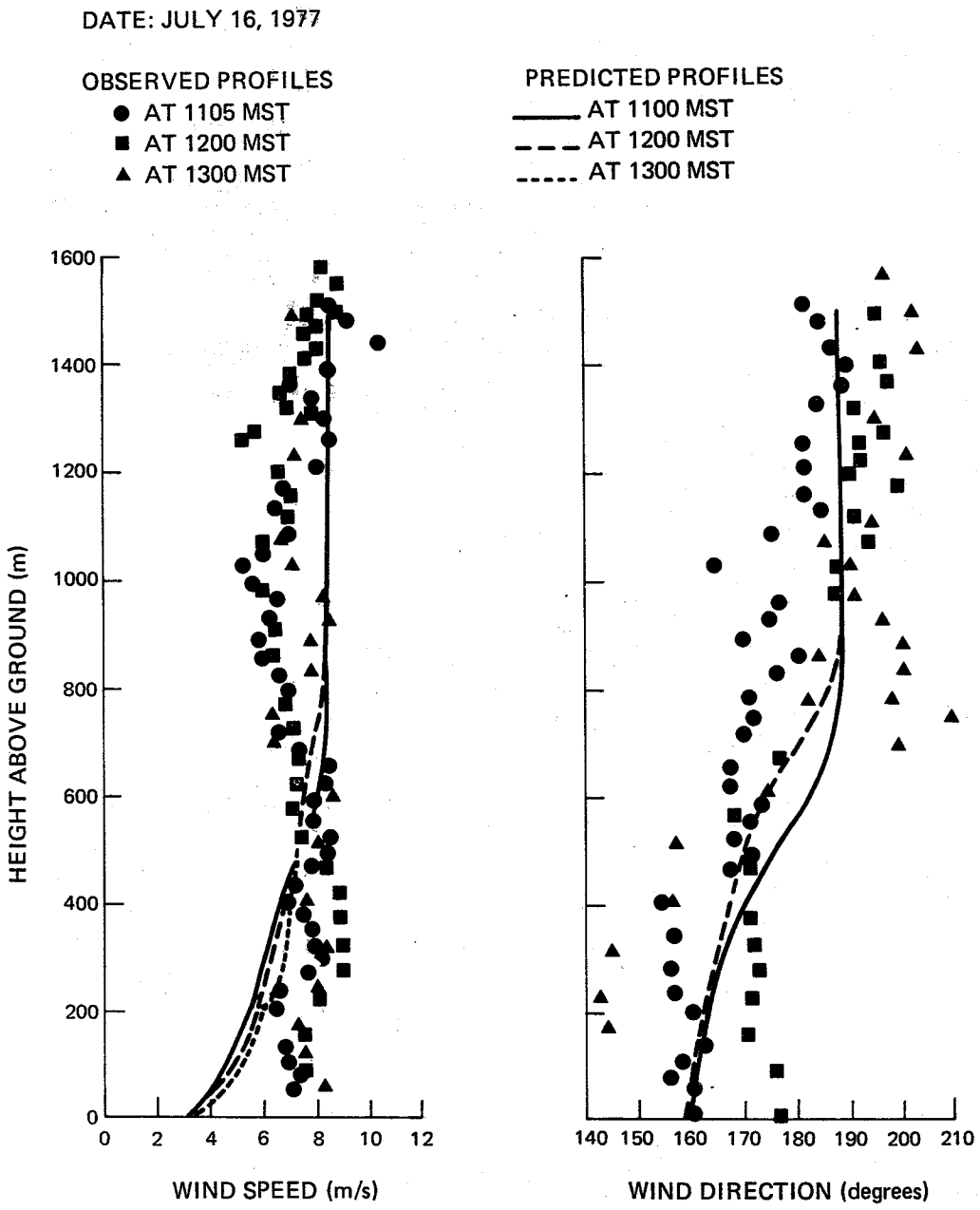

Figure 5.13. Observed and predicted wind profiles (July 16, 1977).

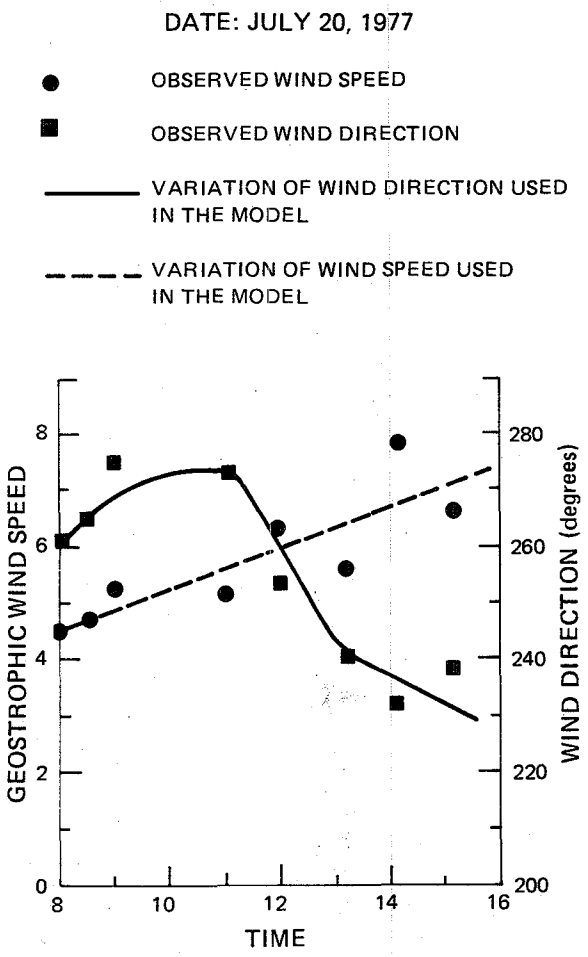

Figure 5.14. Variation of geostrophic wind with time (July 20, 1977).

The initial conditions are, of course, the same for both cases. The initial potential temperature profile was observed at 0804 MST. This profile can be seen in Figure 5.15. In this figure can also be seen the observed and predicted temperature profiles at about 0900 MST for both cases. The predicted profiles, for both the cases as can be seen from this figure, are in excellent agreement with the observed ones. The predicted and observed potential temperature profiles during the next 3 hours are shown in Figure 5.16. The predicted profiles in both the cases agree quite well with the observed ones at all levels except between 100 m and 400 m levels. At 1400 and 1500 MST the predicted temperature profiles (see Figure 5.17) are cooler by about 2 to $3^{o}K$ above 600 m level. Once again, neglect of vertical velocities and horizontal advection may be responsible for the discrepancy.

The predicted and observed wind profiles are shown in Figures 5.18 through 5.22. Referring to Figure 5.18, it can be seen that the predicted wind speed profile in case B agrees well with the observed one over most of the levels. In case A, the agreement is not good below the 900 m level. However, in both cases the predicted profiles below 200 m level (i.e. near the surface) do not agree with the observed ones. The wind direction profiles also do not agree with the measured ones at lower levels. However, at higher levels the predictions showed improvement. At 1100 MST (Figure 5.19), at 1200 MST (Figure 5.20) and at 1300 MST (Figure 5.21) the predicted wind speeds

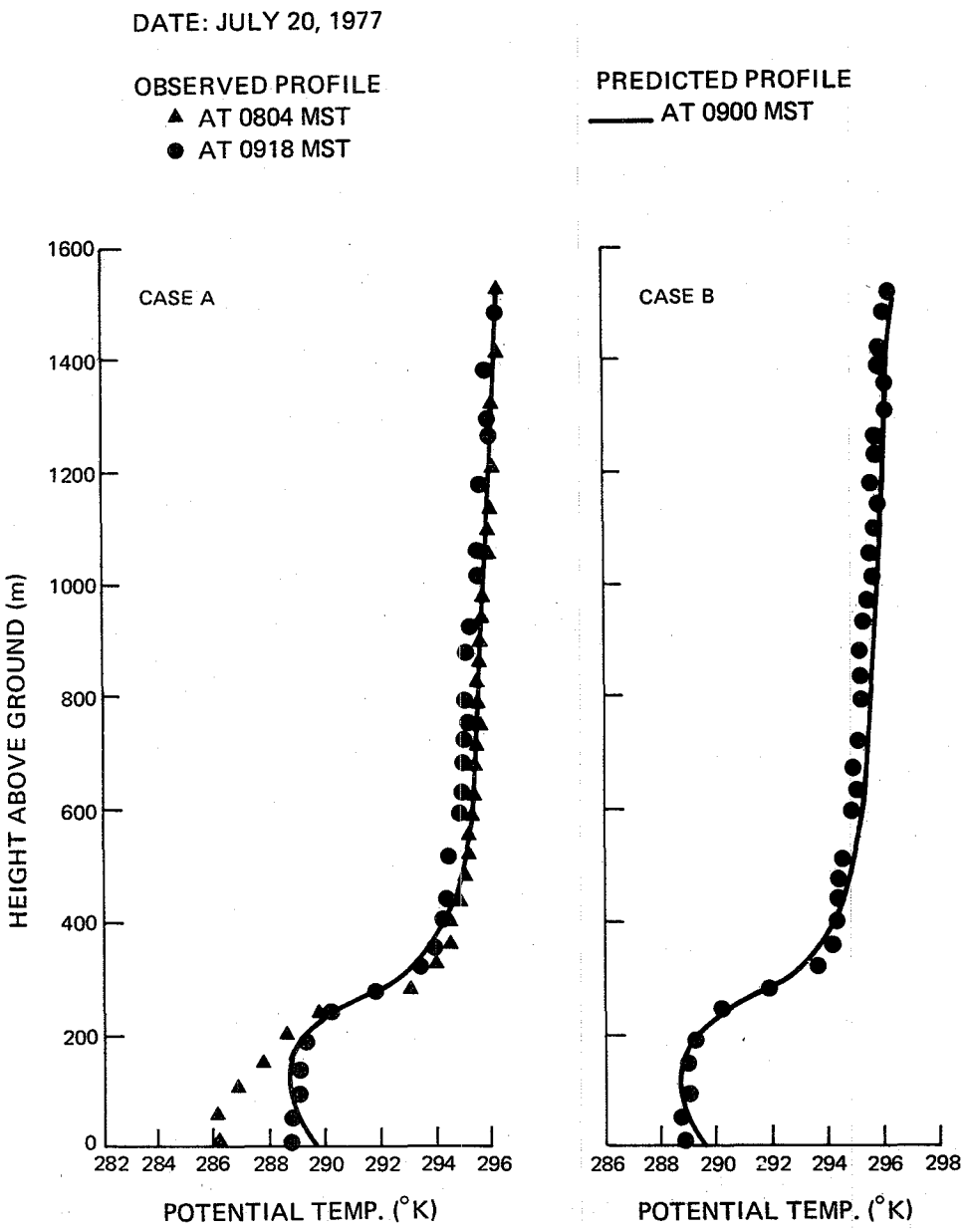

Figure 5.15. Observed and predicted potential temperature profiles (July 20, 1977).

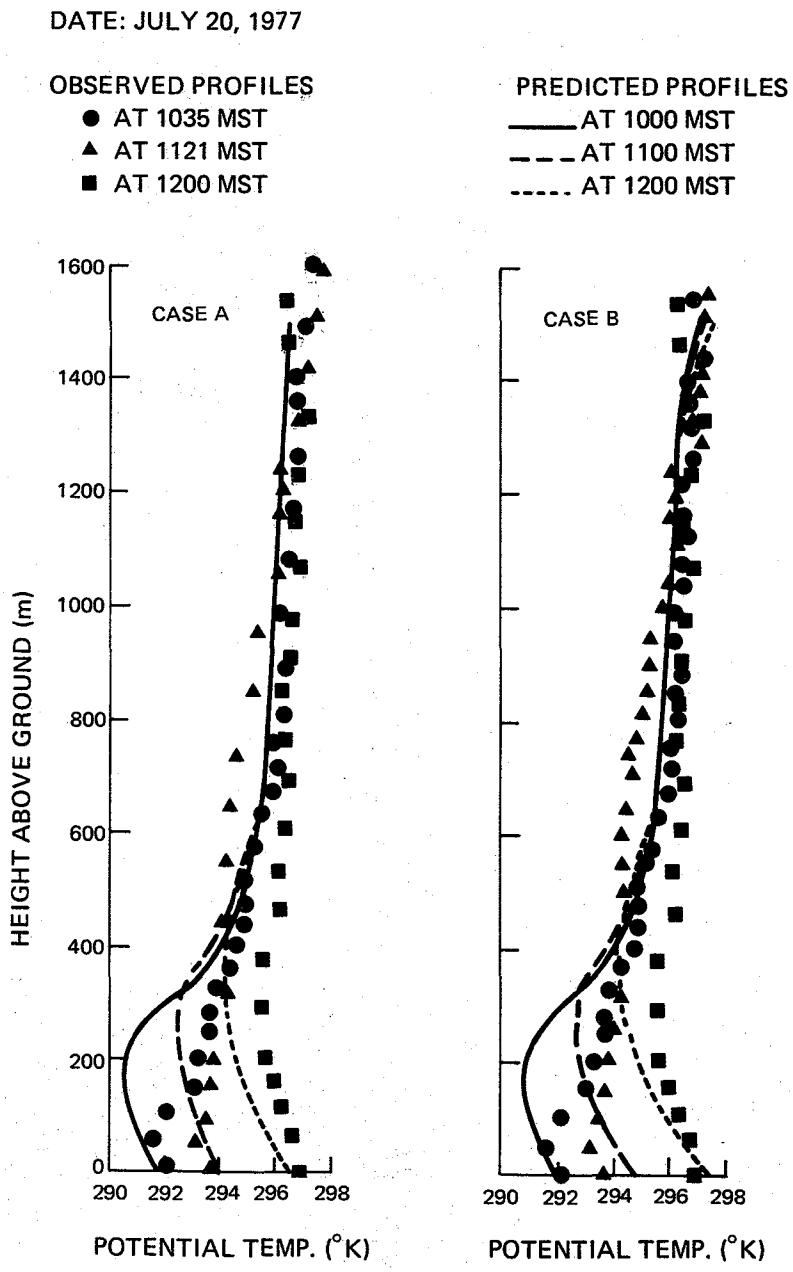

Figure 5.16. Observed and predicted potential temperature profiles (July 20, 1977).

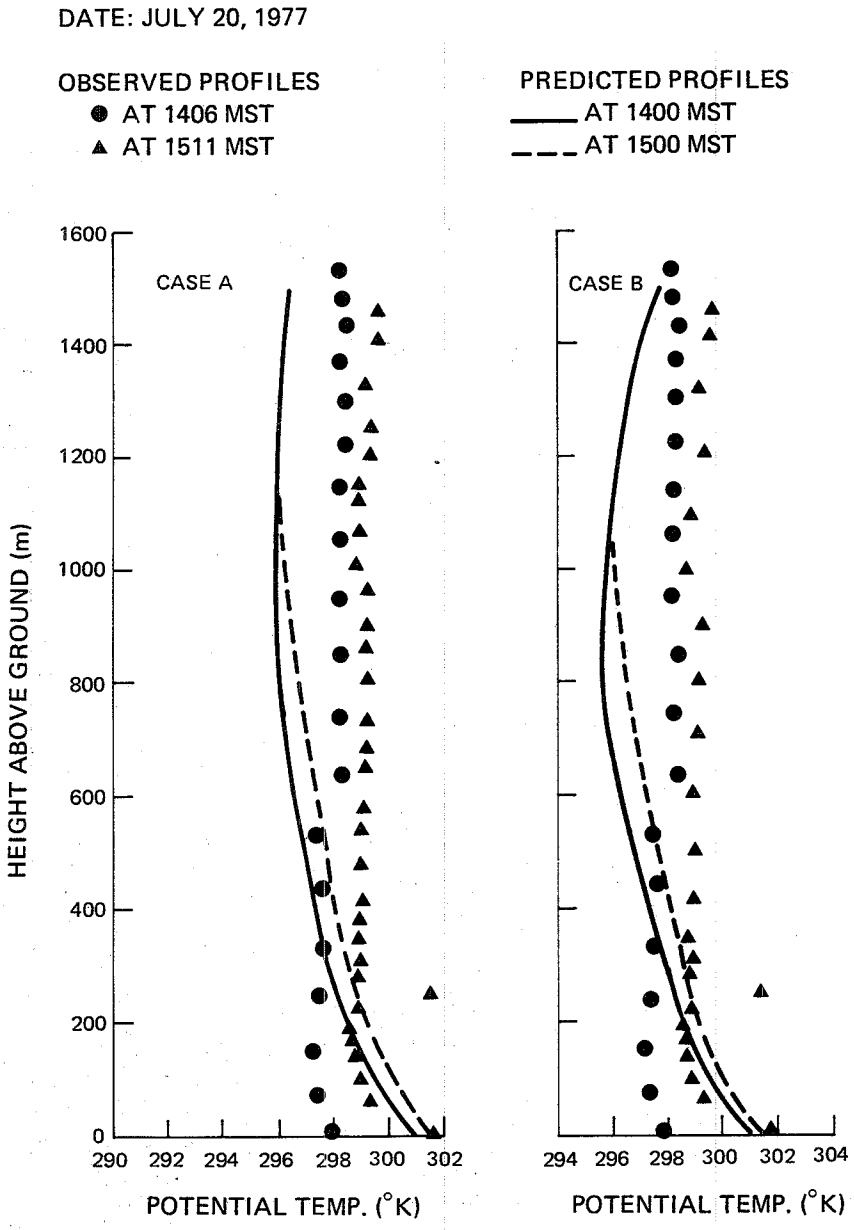

Figure 5.17. Observed and predicted potential temperature profiles (July 20, 1977).

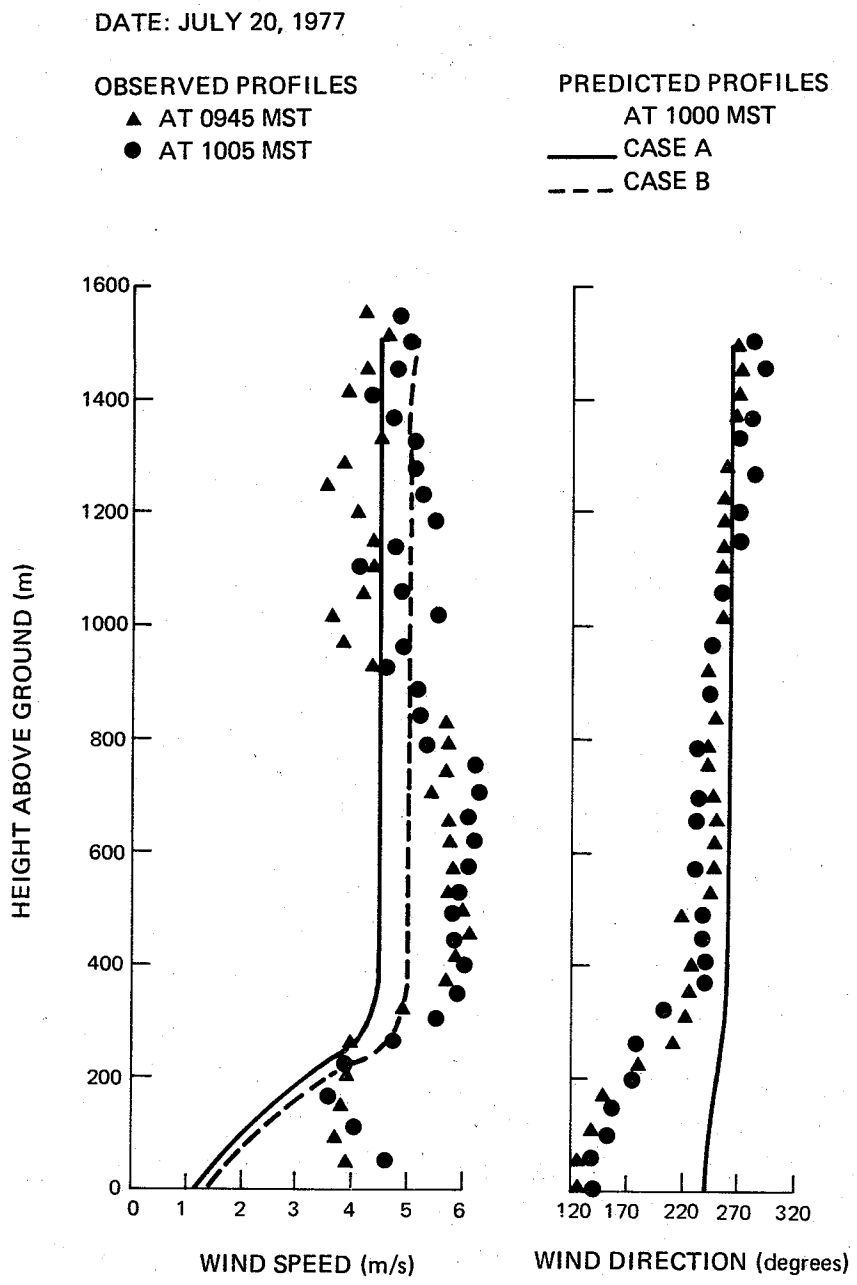

Figure 5.18. Observed and predicted wind profiles (July 20, 1977).

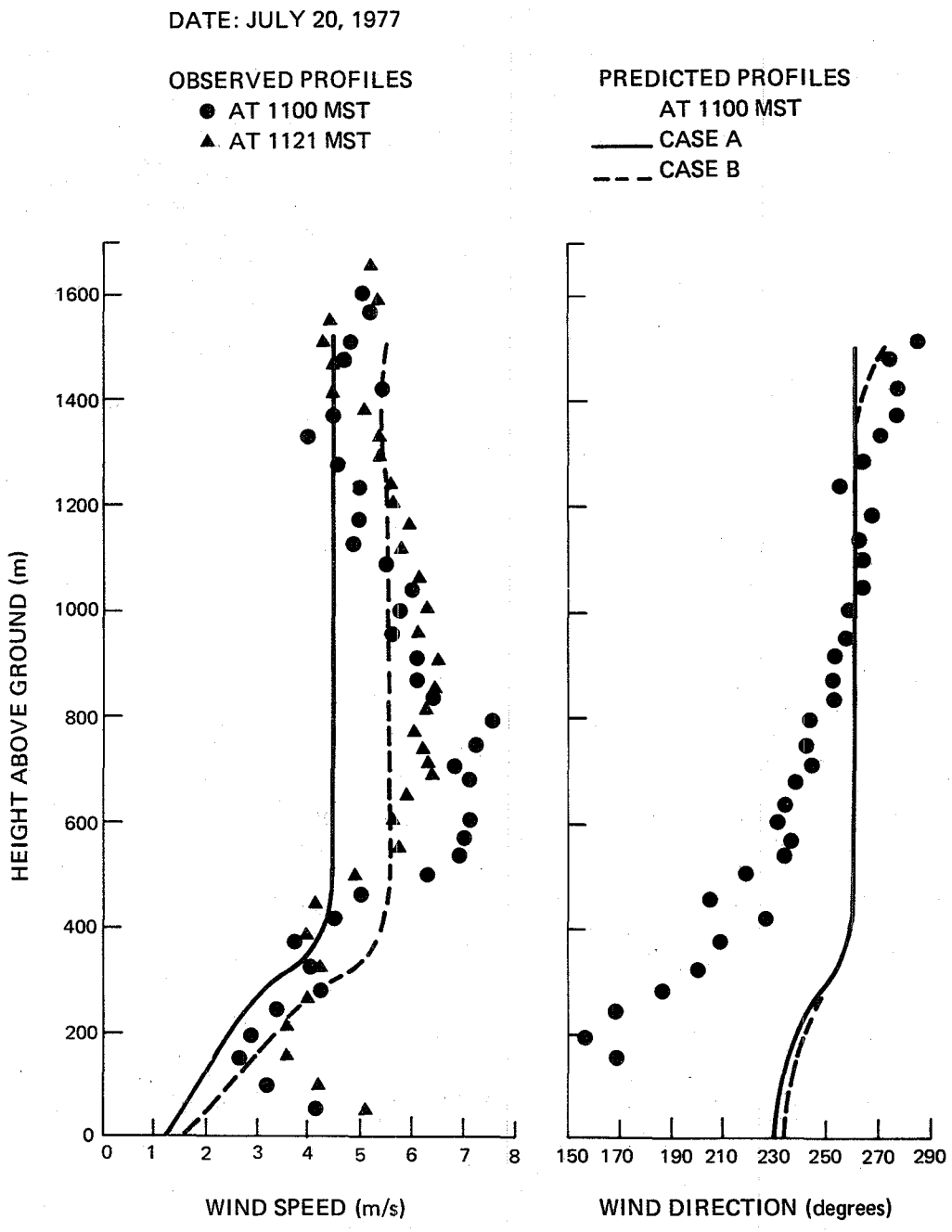

Figure 5.19. Observed and predicted wind profiles (July 20, 1977).

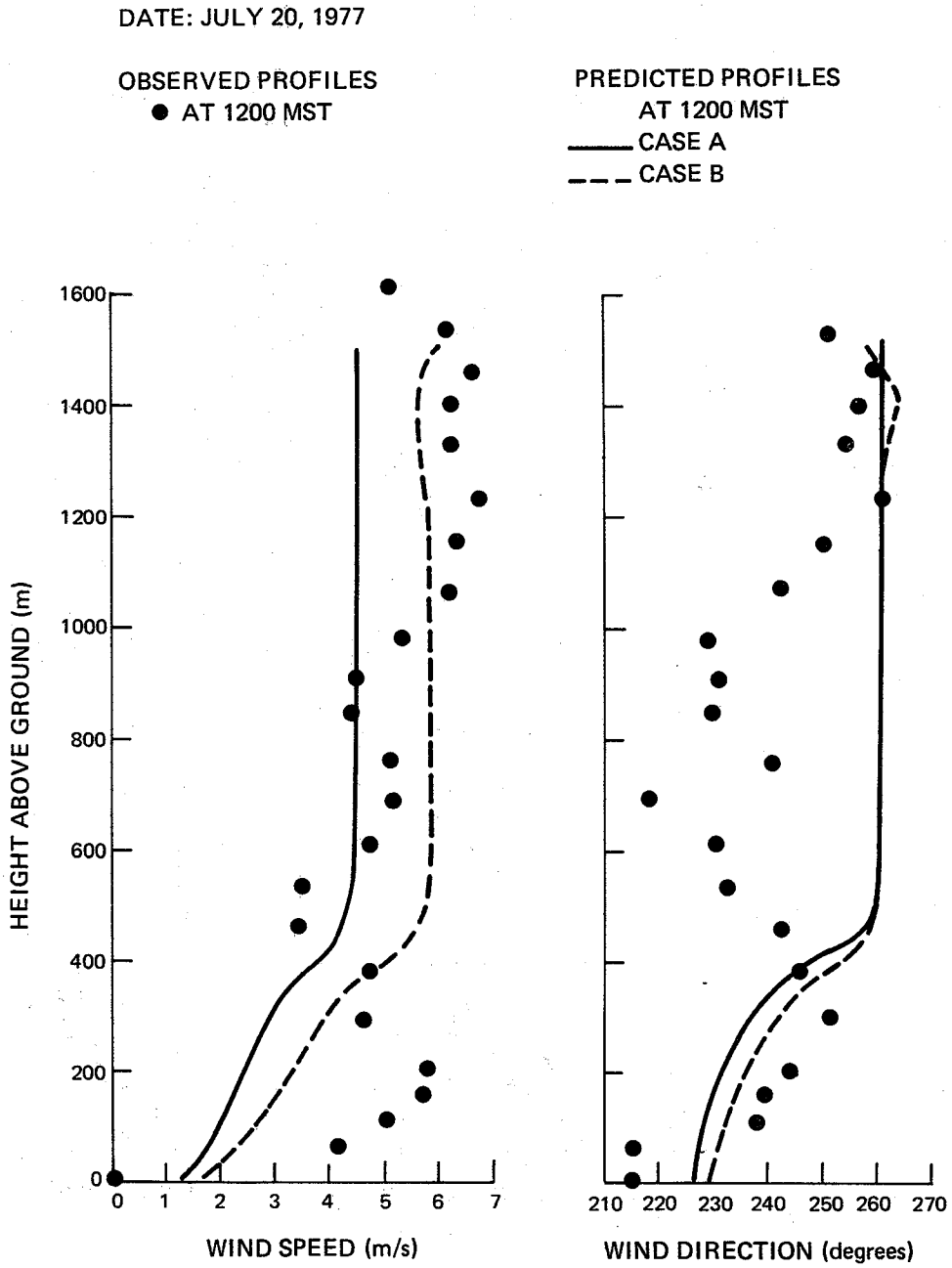

Figure 5.20. Observed and predicted wind profiles (July 20, 1977).

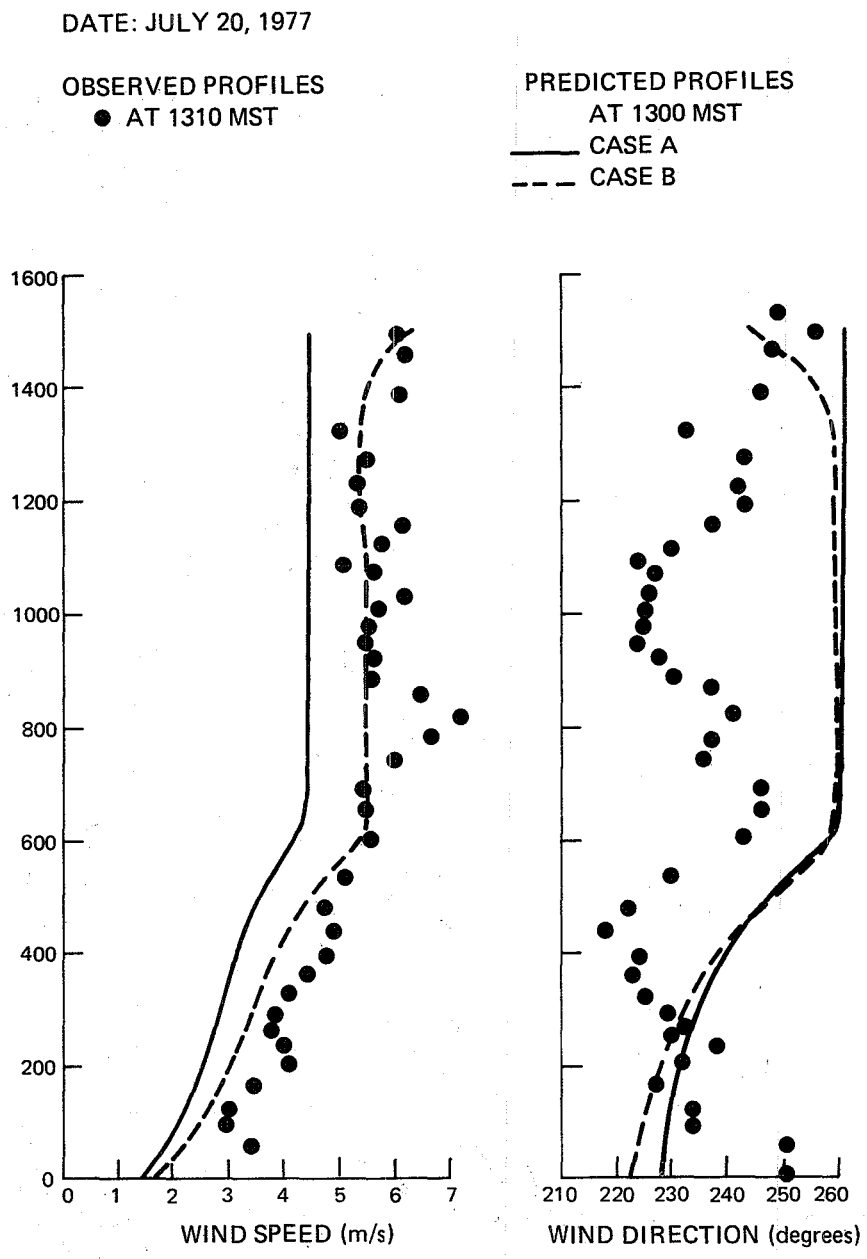

Figure 5.21. Observed and predicted wind profiles (July 20, 1977).

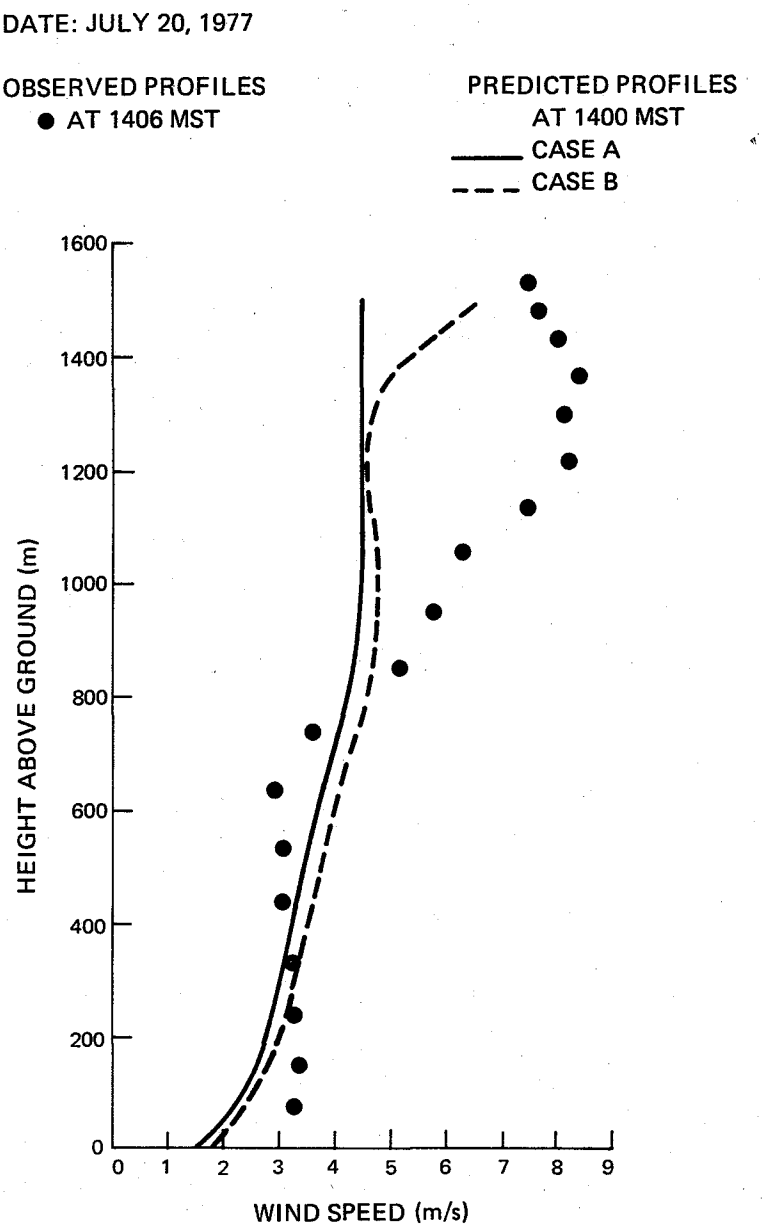

Figure 5.22. Observed and predicted wind profiles (July 20, 1977).

in case B are nearly in agreement with the measured ones over most of the region, except at lower levels. Case A did not fare well. However, both cases failed in predicting the wind direction profiles. One should, however, note that there is considerable scatter in the observed data, which prevents one from drawing any definite conclusions. In Figure 5.22, are shown observed and predicted wind speed profiles at 1400 MST. It appears that the predicted profiles in both cases agree with the observed one up to 900 m level. Above that level there is considerable disagreement between the predicted and observed ones. In general, the predictions for this day are not as good as those for the other two days for which the model made predictions.

5.4 SUMMARY AND CONCLUDING REMARKS

A one-dimensional planetary boundary layer model, whose performance was tested against observed data is described here. The model consists of a constant flux layer near the surface, and a transition layer above it. The top boundary conditions are specified from large scale atmospheric conditions. In determining the surface temperature as a function of time, a desirable approach is to solve a heat budget equation near the earth atmosphere interface. However such a step would require soil temperature data, which were not available for this study. Hence, the surface temperature as a function of time was specified by making use of the temperature observed at the 3 m level.

The model was tested using data obtained on 3 days in 1977. On two of these days the variations near the top boundary of the model are small. The model's predictions for these days are quite good, when one takes into account the errors in observational data and the departure of the observational site from homogeneity. The model's predictions for the remaining day on which the conditions at the top boundary varied significantly are not as good as those for the other two days.

Introduction of baroclinic and penetrative convection effects into the model is desirable. It is recommended that in any future application of the model to this site such a step be taken. Use of the soil layer, in addition to the constant flux and transition layers, in order to determine surface temperature is also recommended. Since the model in its original form (see Maddukuri 1977) accounted for this layer, only soil temperature measurements are needed for initialization and inclusion in the one-dimensional model. Efforts to include the nonhomogeneous effects, probably empirically using the site-specific data, may also be made. Of course, the nonhomogeneous effects may be taken into account using a multi-dimensional model. However, such a step would be considerably more expensive.

If this model is to form the basis for an operational model, it is suggested that the above improvements be made to it and then the model tested against more of the observed data.

6. CONCLUSIONS

The objective of the work described in this report was to further analyze the 1977 field study data given in Slawson et al (1978) in order to investigate and develop a predictive plume rise and dispersion model that could be subsequently applied to the Syncrude plume.

Various integral plume rise models were investigated and we came to the conclusion that a numerical integration model that does not employ the Boussinesq assumption, best described the observed plume behavior under both linear and non-linear atmospheric wind and temperature fields.

In a Gaussian dispersion model, the prediction of the effective stack height is well known to be very important to a successful prediction of point of impact concentrations. Thus, the prediction of the final plume rise height in stable, neutral and unstable (convective) atmospheres is required. The numerical plume rise model recommended here adequately predicts the final plume rise in stable atmospheres. However, although some progress was made on a simple empirical formulation for the final rise in near-neutral atmospheres, further work is required. Also, since anything other than a flat terrain effects the plume impact zone, inclusion of terrain specific to the Syncrude plume is required in any subsequent Syncrude plume dispersion model.

The re-analysis of the aircraft plume transect data produced a sigma data set with less scatter than that given in Slawson et al (1978). The resulting sigmas are fairly well represented by the typing scheme of Briggs (1973) in the absence of significant cross-wind shear. A simple empirical formulation was found that describes the observed quantitative effect of shear enhanced diffusion due to cross-wind shear on the lateral standard deviation of (Gaussian) plume spread. The direct incorporation of plume distortion due to cross-wind shear into a modified Gaussian plume model appears to predict the correct trends but further comparison with observations and a sensitivity analysis of the model is required.

A one-dimensional planetary boundary layer model was developed which shows some promise of adequately predicting the essential features of the wind and temperature fields some six hours in advance. However, non-homogeneity of terrain, albedo and large scale pressure impose significant restrictions on the use of a one-dimensional model. Improvement in a planetary boundary layer model's performance can be expected with the inclusion of convective penetration and baroclinicity.

Comparisons of a simple Gaussian plume dispersion model which incorporates the work on plume rise and sigma specification above, may form the basis for a subsequent Syncrude plume dispersion model.

7. RECOMMENDATIONS

As a result of the research and development work outlined in this report a number of recommendations are given below that may hopefully further the development of a successful site-specific predictive plume dispersion model for the Syncrude plant:

(1) The recommended plume rise model as well as any others should be tested against a limited set of time-mean plume observations of the Syncrude plume. Successful comparisons between observations and predictions will add further confidence to the plume rise model as well as offer an opportunity for any necessary refinement specific to the Syncrude plume. Appreciation of measurement errors will define limits for evaluating a model's performance.

(2) Measurement of final plume rise by aircraft or remote sensing in near-neutral and convective atmospheric conditions are needed in order to understand and successfully formulate the final rise.

(3) An investigation into the importance of terrain to the predictions of ground level concentrations for the Syncrude plume is needed.

(4) Continued efforts to both improve and increase the meteorological and climatological data base is required. More accurate wind and temperature profiles are required in order to further improve mixing height and planetary boundary layer models for the tar sands area. Also, tests on the homogeneity of the wind and temperature fields should be conducted at least to distances from the source where maximum ground level concentrations are expected.

(5) Any further programs for the measurement of the standard deviations of plume spread should be more statistically comprehensive. Thus, the use of proven remote sensing systems such as particle LIDAR and or at least two aircraft simultaneously sampling the plume is recommended. Also, additional work on the specification of sigmas should incorporate bi-vane and ΔT measurements from a suitable meteorological tower, so that currently available theoretical sigma typing schemes may be improved and or used.

(6) Where possible, continuous fixed monitoring of ground level concentrations should be made for subsequent model refinement and validation. A full scale field program designed specifically for validation of the Syncrude plume model should ultimately be undertaken.

(7) In addition to the above, there are many research areas one may further pursue in which the existing data base may prove fruitful in the better understanding of plume diffusion processes. Some of these are: (a) the investigation of the plume penetration of elevated inversions and the subsequent diffusion to ground level, (b) the quantitative formulation of the effects of cross-wind shear on plume spread, (c) investigation of the effects of terrain on ground level concentrations specific to the G.C.O.S. plume.

REFERENCES

1. G.I. Taylor (1945): Dynamics of a mass of hot gas rising in air. USAEC Report MDDC-919, LADC-276.

2. G.A. Briggs (1975): Plume rise predictions. Presented at the AMS workshop in Meteorology and Environmental Assessment. Boston Sept. 29-Oct. 3, 1975.

3. D.P. Hoult, J.A. Fay, L.J. Forney (1969): A theory of plume rise compared with field observations. J. Air Pollution Control Assoc., 19, 585.

4. M.P. Escudier (1972): Aerodynamics of a burning turbulent jet in a cross-flow. Comb. Sci. and Tech., 4, 293.

5. R. Jordinson (1965): Flow in a jet normal to the wind. Imperial College, Aeronautics Dept., Paper No. 35.

6. G. Abraham (1971): The flow of round, buoyant jets issuing vertically into ambient fluid flowing in a horizontal direction. Delft Hydraulics Lab., Publication No. 81.

7. G. Ooms (1972): A new method for the calculation of the plume path of gases emitted by a stack. Atmos. Environment, 6, 899.

8. P.R. Slawson, personal communication.

9. B.R. Morton, G.I. Taylor, J.S. Turner (1956): Turbulent gravitational convection from maintained and instantaneous sources. Proc. Roy. Soc. A284, 1.

10. P.R. Slawson, G.T. Csanady (1967): On the mean path of buoyant, bent-over chimney plumes. J. Fluid Mech., 28, 311.

11. G.A. Davison, P.R. Slawson, S.G. Djurfors (1978): A plume dispersion study at Mildred Lake, Alberta. Proc. of 9th NATO International Tech. Meeting on Air Pollution Modelling and its Application. Toronto, Aug. 28-31, 1978.

12. P.R. Slawson, G.A. Davidson, W. McCormick, G. Raithby (1978): A study of the dispersion characteristics of the G.C.O.S. plume. Syncrude Canada Limited Report.

13. J. Halitsky (1961): Single camera measurement of smoke plumes. Int. J. of Air and Water Pollution, 4, 185.

14. J.A. Fay, M. Escudier, D.P. Hoult (1970): A correlation of field observations of plume rise. J. Air Pollution Control Ass., 20, 391.

15. P.R. Slawson (1978): Observations and predictions of natural draft cooling tower plumes at Paradise Steam Plant, Atmos. Environment, 72, 1713.

16. S.R. Hanna (1972): Rise and condensation of large cooling tower plumes, J. Appl. Meteorology, 11, 793.

17. A.C. McMillan (1977): Nanticoke diffusion study--1976, Ontario Hydro, Res. Div. Report, No. 77-432-K.

18. G.C. Edwards (1977): Lidar and photographic observations of plume rise and dispersion at the Nanticoke Generating Station, MaSc T hesis, Mech. Eng. Dept., University of Waterloo.

19. G. Howroyd (1979): The mesoscale diffusion of plumes released from tall stacks at large industrial sources, PhD Thesis, Mech. Eng. Dept., University of Waterloo.

20. W. McCormick (1979): Comparison of a plume dispersion model with observations from a large industrial stack, MaSc Thesis, Mech. Eng. Dept., University of Waterloo.

21. F. Pasquill (1976): Atmospheric dispersion parameters in Gaussian plume modelling. Part II. Possible requirements for change in the Turner Workbook values U.S. EPA Report, EPT - 600/4-76-030b. Res. Triangle Park, North Carolina 12pp.

22. R.R. Draxler (1976): Determination of atmospheric diffusion parameters. Atm. Env., 10, 99-105.

23. D.B. Turner: Workbook of atmospheric dispersion estimates, U.S. EPA 1970.

24. D.S. Davison, E.D. Leavitt: Analysis of AOSERP plume sigma data, Intera Environmental Consultants Ltd., Unpublished report.

25. F.A. Gifford: Turbulent diffusion typing schemes -.A review. Nuclear Safety, 17, 68. 1976.

26. J.L.G. Nillson: A preliminary analysis of data collected in plumes from steam plant stacks by an airborne SO_2 analyzer, TVA, Air Quality Branch, 1975.

27. C.H.B. Priestley (1959): Turbulent transfer in the lower atmosphere. The University of Chicago Press, 130pp.

28. P.J. Roache (1972): Computational fluid dynamics, Revised printing, 1976, Hermosa Publishers, Alburquerque, N.M., U.S.A. 446pp.

29. P.A. Taylor (1969): The planetary boundary layer above a change in surface roughness, J. Atmos. Sci., 26, 432-440.

30. M.A. Estoque, C.M. Bhumralkar (1970): A method for solving the planetary boundary layer equations, Boundary-Layer Meteorol., 1, 169-194.

31. P. Laasonen (1949): Uber eine methode sur losung der warmeleitungsgleichung, Acta Mathematica, 81, 309.

32. C.S. Maddukuri (1977): Air flow over an urban area: Some numerical experiments with a two-dimensional time dependent boundary layer model. PhD Thesis, York University, Toronto, 137pp.

33. C.S. Maddukuri, P.R. Slawson, M.B. Danard: The applications of a two-dimensional numerical model of the planetary boundary layer to the Nanticoke Region on the north shore of Lake Erie, Boundary-Layer Meteorology, 15 (1978) 163-179.

34. G.T. Csanady (1973): Turbulent diffusion in the environment, 248pp. D. Reidel Pub. Co., Dordrecht, Holland.

35. J.C. Doran, T.W. Horst, P.W. Nickola (1978): Experimental observations of the dependence of lateral and vertical dispersion characteristics on source height, Atmos. Env. V12, pp. 2259-2263.

36. R.G. Lamb (1979): The effects of release height on material dispersion in the convective planetary boundary layer, 4th Symp. on Turb., Diffusion and Air Poll., A.M.S., Jan. 13-18, Reno, Nevada.

37. F.A. Gifford (1975): Atmospheric dispersion models for environment pollution application, Lect. on Air Poll., American Met. Soc.

38. K.K. DeBower, B.R. Eppright, and J.D. Stuart (1979): An air dispersion model for primary aluminum reduction plant emissions. 4th Symp. on Turb. and Diff., and Air Poll. A.M.S. Jan. 15-18, Reno, Nevada.

39. S.R. Hanna (1978): A review of the influence of new boundary layer results on diffusion prediction techniques, A.T.D.L. Cont. #78/5.

40. S.G. Djurfors, D. Netterville (1978): Buoyant plume rise in non-uniform wind conditions. J. Air Pollution Control Assoc., 28, 780.

Conditions of Use

Slawson, P.R., G.A. Davidson and C.S. Maddukuri, 1980. Dispersion modeling of a plume in the tar sands area. Syncrude Canada Ltd., Edmonton, Alberta. Environmental Research Report 1980-1. 316 pp.